

Characterisation of Low Velocity Impact Response in Composite Laminates

Zeng Shen

A thesis submitted in partial fulfilment of the requirements of the University of
Hertfordshire for the degree of Doctor of Philosophy

The programme of research was carried out in the School of Engineering and
Technology, University of Hertfordshire

November 2014

Abstract

A major concern affecting the efficient use of composite laminates in aerospace industry is the lack of understanding of the effect of low-velocity impact (LVI) damage on the structural integrity. This project aims to develop further knowledge of the response and damage mechanisms of composite laminates under LVI, and to explore the feasibility of assessing the internal impact damage with a visually inspectable parameter.

The response and damage mechanisms of composite laminates under LVI have been investigated experimentally and numerically in this project. Various parameters including the laminates thickness, lay-up configuration, repeated impact, and curing temperature have been examined. The concept and the phenomena of delamination threshold load (DTL) have been assessed in details. It was found that DTL exists for composite laminates, but the determination of the DTL value is not straightforward. There is a suitable value of range between the impact energy and the laminates stiffness/thickness, if the sudden load drop phenomenon in the impact force history is used to detect the DTL value. It is suggested that the potential menace of the delamination initiation may be overestimated. The composite laminates tested in this project demonstrate good damage tolerance capacity due to the additional energy absorption mechanism following the delamination initiation. As a result, the current design philosophy for laminated composite structure might be too conservative and should be reassessed to improve the efficiency further.

To explore the feasibility of linking the internal damage to a visually inspectable parameter, quasi-static indentation (QSI) tests have been carried out. The dent depth, as a visually inspectable parameter, has been carefully monitored and assessed in relation to the damage status of the composite laminates. It is proposed that the damage process of composite laminates can be divided into different phases based on the difference in the increasing rate of dent depth. Moreover, the internal damage has been examined under the optical microscope (OM) and the scanning electron microscope (SEM). Residual compressive strength of the damaged specimen has been measured using the compression-after-impact (CAI) test. The results further confirm the findings with regard to the overestimated potential menace of the delamination initiation and the proposed damage process assumption. The proposed damage process assumption has great potential to improve the efficiency and accuracy of both the analytical prediction and the structural health monitoring for damages in composite laminates under low-velocity impact.

Acknowledgements

I would like to express my sincere gratitude to my supervision team, Dr. Yigneg Xu and Prof. Andreas Chrysanthou, for their dedicated guidance and support throughout the project. It would be impossible for me to bring the project to a success without their professional help, encouragement and patience.

I would like to thank the technical support team at the School of Technology & Science, in particular to Dr. William Tiu, Dr. Phil Green, Dr. Anatoli Babutskyi, Mr. Pete Thomson and Mr. Dave Smith for their excellent technical support.

Many thanks also go to my friends and colleagues for sharing happiness with me. And my particular thank goes to Sisi Yang for being the love of my life.

Finally, I would like to thank my parents Fujia Shen and Li Zeng for their understanding, belief in me, and the financial support throughout the project.

Dedication

I dedicate this work to my late grand mother, who left me one year ago. Her endless love and encouragement make me be tough to overcome the difficulties throughout the project.

Contents

Abstract.....	I
Acknowledgements	II
Dedication	III
List of Figures.....	VIII
List of Tables	XV
Nomenclature	XVI
CHAPTER 1 Introduction	1
1.1 Background	1
1.2 Aims and Objectives	2
1.3 Outline of the Thesis	3
CHAPTER 2 Literature Review	4
2.1 An Overview of Composite Material	4
2.1.1 Historical Development of Composite Material.....	4
2.1.2 Classification of Composite Material	7
2.1.3 Advantages and Limitations of Composite Material	8
2.2 An Introduction to Composite Laminates	9
2.2.1 Characterisation of Composite Laminates.....	9
2.2.2 Lay-up of Composite Laminates	10
2.2.3 Mechanical Analysis of Composite laminates.....	11
2.3 Composite Laminates under Low-velocity Impact	16
2.3.1 Definition of Low-velocity Impact.....	17
2.3.2 Classification of Low-velocity Impact Tests.....	18
2.3.3 Failure Modes of Composite Laminates under Low-velocity Impact.....	19
2.3.4 Failure Criteria of Composite Laminates	24

2.4 Delamination Initiation and Propagation of Composite Laminates	31
2.4.1 Experimental Detection of Delamination Initiation	31
2.4.2 Analytical Prediction on Delamination Threshold Load	34
2.4.3 Numerical Simulation of Delamination.....	35
2.5 Composite Laminates under Quasi-static Indentation	42
2.5.1 Contact Models of Composite Laminates	42
2.5.2 Similarity between Contact Responses of Composite Laminates under LVI and QSI	49
2.5.3 Contact Laws of Composite Laminates under QSI	52
2.6 Summary	57
CHAPTER 3 Research Strategy	59
CHAPTER 4 Derivation of Mechanical Properties of UD Material.....	63
4.1 Composite Plate Fabrication	63
4.2 Specimen Preparation and Test Set-up.....	67
4.2.1 Specimen Geometry and Set-up of Tensile Property Test	68
4.2.2 Specimen Geometry and Set-up of Shear Property Test	70
4.3 Test Results	73
4.3.1 Tensile Property Test.....	73
4.3.2 Shear Property Test	78
4.4 Summary	81
CHAPTER 5 Results of Composite Laminates under LVI.....	84
5.1 Instrumented Drop-weight Test	84
5.1.1 Specimen Preparation and Test Set-up	84
5.1.2 Effect of Thickness on Impact Response of Composite Laminates	93
5.1.3 Effect of Repeated Impact on Impact Response of Composite Laminates	99
5.1.4 Effect of Lay-up Configuration on Impact Response of Composite Laminates ...	105

5.1.5 Effect of Curing Temperature on Impact Response of Composite Laminates.....	109
5.2 Numerical Simulation	114
5.2.1 Model Creation without Consideration of Damage Mechanism	115
5.2.2 Simulation Results without Consideration of Damage Mechanism	119
5.2.3 Model Generation with Consideration of Damage Mechanism	125
5.2.4 Preliminary Simulation Results with Consideration of Damage Mechanism	136
5.3 Summary	144
CHAPTER 6 Results of Composite Laminates under QSI.....	147
6.1 Instrumented Quasi-static Indentation Test.....	147
6.1.1 Quasi-static Indentation Test Set-up.....	147
6.1.2 Composite Laminates under a Continuous Indentation Approach	150
6.1.3 Comparison between Results of QSI and LVI Tests.....	151
6.1.4 Composite Laminates under a Step-by-step Indentation Approach	153
6.1.5 Dent Depth Measurement.....	158
6.1.6 Back-face Displacement Measurement	161
6.2 Compression-after-impact Test	163
6.2.1 Compression-after-impact Test Set-up.....	164
6.2.2 CAI Test	165
6.3 Internal Damage Characterisation.....	169
6.3.1 Optical Microscope Observation Set-up.....	169
6.3.2 Optical Microscope Observation Results	170
6.3.3 Scanning Electron Microscope Observation Set-up.....	174
6.3.4 Scanning Electron Microscope Observation Results.....	175
6.4 Numerical Simulation	180
6.4.1 Model Creation	180
6.4.2 Simulation Results.....	183
6.5 Result of Analytical Prediction	188

6.5.1 Hertz Contact Theory based Contact Model	188
6.5.2 Elastoplastic Response based Contact Model	190
6.6 Summary	192
CHAPTER 7 Discussion	195
7.1 Reliable Detection of DTL	195
7.2 Potential Menace of Delamination Initiation	198
7.3 Damage Process Assumption	201
CHAPTER 8 Conclusions and Recommended Work.....	205
8.1 Conclusions	205
8.2 Recommended Work.....	209
References.....	211
Appendix I Un-filtered Impact Force History.....	221
Appendix II Derivation of ABD Matrix.....	223
Appendix III Analytical Prediction by Hertz Contact Law Based Contact Model	229
Appendix IV Analytical Prediction by Elastoplastic Response Based Contact Model .	230
Appendix V Publication List.....	232

List of Figures

Figure 2.1 Examples of natural composite materials.....	5
Figure 2.2 Applications of modern composite materials [2].	6
Figure 2.3 Chronological variation of the relative importances of materials [16].....	6
Figure 2.4 Schematic illustration of polymer, metal, and ceramic matrix composite materials [7].	7
Figure 2.5 Schematic illustration of fibre, particulate, and flake reinforced composite materials [5].....	8
Figure 2.6 Specific strength and modulus of general engineering materials [19].	9
Figure 2.7 Schematic illustration of (a) the UD composite laminates [5] and (b) the woven composite laminates.	10
Figure 2.8 Schematic illustration of the applied stresses for determining compliance matrix of a lamina [15].....	12
Figure 2.9 Schematic illustration of (a) on-axis and (b) off-axis configurations [15].....	14
Figure 2.10 Laminates stacking sequence nomenclature [5].	15
Figure 2.11 Schematic illustration of common impact test rigs [4].....	18
Figure 2.12 Cross-section view of the impact damaged composite laminates [46].....	19
Figure 2.13 Schematic illustration of the low-velocity impact damage natures in a composite laminates [11].....	20
Figure 2.14 Schematic illustration of different damage patterns [4].	21
Figure 2.15 (a) Top and side views of the delamination area from C-scan observations [46]; (b) schematic illustration of delamination [4]; (c) ideal model of delamination [46].	22
Figure 2.16 Schematic illustration of fibre failure modes.	23
Figure 2.17 Impact force history of a composite laminates subjected to low-velocity impact [14].	32
Figure 2.18 (a) Damage area vs. incident energy, and (b) damage area vs. impact force for a large number of composite laminates with different thicknesses, plate sizes, and support conditions [11].	33
Figure 2.19 Impact force histories of composite laminates caused by (a) the small mass impactor and (b) the large mass impactor under same impact energy level [72]. 33	

Figure 2.20 Schematic illustration of the tie-break interface contact in normal direction [78].	36
Figure 2.21 Schematic illustration of three delamination fracture modes [79].	36
Figure 2.22 Cohesive element pre-inserted positions in the practical simulation model [12].	37
Figure 2.23 Principle of the cohesive zone model [84].	38
Figure 2.24 Traction-separation law for mode I (a) and mode II/III (b) fractures [85].	38
Figure 2.25 Schematic illustration of the 2D elements model in the virtual crack closure method [93].	39
Figure 2.26 Virtual crack closure technique for the 2D four-node elements model [93].	40
Figure 2.27 Methods to determine the critical strain energy release rates [94].	41
Figure 2.28 Relationship between the cohesive element and the frictional contact [12].	42
Figure 2.29 Schematic illustration of the classification of contact responses [74].	43
Figure 2.30 Schematic illustration of the one-dimensional contact model for a ballistic response [72].	43
Figure 2.31 Schematic illustration of the three-element spring-dashpot contact model for a ballistic response [107].	44
Figure 2.32 Schematic illustration of the contact model for a small mass contact response [72].	45
Figure 2.33 Schematic illustration of impactor (a) before and (b) during indentation of a plate [73].	46
Figure 2.34 Comparison between (a) large mass and (b) small mass contact responses [73].	47
Figure 2.35 Schematic illustration of the contact model for a large mass contact response [108].	47
Figure 2.36 Schematic illustration of the modified contact model of a large mass contact considering delamination in the plate [74].	48
Figure 2.37 Comparison of indentation and impact force vs. displacement relations [109].	49
Figure 2.38 Comparison of the impact and indentation induced delamination area vs. maximum force relations [104].	50
Figure 2.39 Comparison of the impact and indentation tests in relationships between load level and (a) damage area, (b) damage width, and (c) dent depth [110].	50
Figure 2.40 Knee point phenomenon in variation of dent depth vs. indentation force [111].	51
Figure 2.41 Schematic illustration of the contact between a composites plate and a rigid sphere indenter [115].	53

Figure 2.42 Schematic illustration of the contact between a half-space and a rigid sphere indenter [115].	54
Figure 2.43 Stress-strain relation for the elastoplastic analysis [4].	54
Figure 2.44 Schematic illustration of the indentation of a thin laminates supported by a rigid substrate [4].	55
Figure 3.1 Research strategy flowchart.	59
Figure 4.1 Hand lay-up of the composite plate.	63
Figure 4.2 Schematic diagram of the vacuum bagging.	64
Figure 4.3 Prepared vacuum bagging and composite plates under the required vacuum pressure for curing.	65
Figure 4.4 (a) Composite curing autoclave and (b) its control system.	66
Figure 4.5 Autoclave curing cycle used to fabricate composite plates [125].	66
Figure 4.6 Two types of specimens in tensile test.	68
Figure 4.7 Hounsfield 50kN universal test machine and the computer aided data acquisition system.	69
Figure 4.8 Tensile test specimen with the multidirectional strain gauges bonded.	70
Figure 4.9 Schematic illustration of specimen for the interlaminar shear strength test.	71
Figure 4.10 Preparation of ILSS test specimens.	71
Figure 4.11 Schematic illustration of the in-plane shear modulus test specimen.	72
Figure 4.12 Tested specimens after reaching the tensile strengths.	74
Figure 4.13 Test results of the longitudinal tensile test specimens with strain gauge bonded.	76
Figure 4.14 Test results of the transverse tensile test specimens with strain gauge bonded.	77
Figure 4.15 Schematic illustration of the measurements of the specimen width and the failed area length.	78
Figure 4.16 Specimens failed under the interlaminar shear stress.	79
Figure 4.17 Test results of the in-plane shear test specimens.	80
Figure 5.1 Curing cycles with the normal and the changed curing temperatures.	85
Figure 5.2 Schematic illustration of the drop-weight impact test specimen [119].	86
Figure 5.3 Schematic illustration of the impact support fixture [119].	87
Figure 5.4 CEAST drop-weight test rig.	88
Figure 5.5 Schematic illustration of an impact force acquisition system.	89

Figure 5.6 Calibration of the impactor with strain gauge bonded.	90
Figure 5.7 Test data of the impactor calibration and its resulting calibration curve.	90
Figure 5.8 Recorded data of a strain gauge indicator calibration and its resulting calibration curve.	91
Figure 5.9 Impact force history of a 4mm specimen under 9J impact energy.....	92
Figure 5.10 Filtered impact force histories of 4mm specimens with cross-ply lay-up configuration.	93
Figure 5.11 Filtered impact force histories of 5mm specimens with cross-ply lay-up configuration.	95
Figure 5.12 Filtered impact force histories of 2mm specimens with cross-ply lay-up configuration.	96
Figure 5.13 Filtered impact force histories of 3mm specimens with cross-ply lay-up configuration.	97
Figure 5.14 Filtered impact force histories of test specimens with various thicknesses under 6J impact energy level.....	98
Figure 5.15 Filtered first and repeated impact force histories of 2mm specimens with cross-ply lay-up configuration.	99
Figure 5.16 Filtered first and repeated impact force histories of 4mm specimens with cross-ply lay-up configuration.	100
Figure 5.17 Filtered first and repeated impact force histories of 5mm specimens with cross-ply lay-up configuration.	101
Figure 5.18 Filtered first and repeated impact force histories of 3mm specimens with cross-ply lay-up configuration.	102
Figure 5.19 Comparison between filtered impact force histories of 4mm specimens with cross-ply and quasi-isotropic lay-up configurations.	105
Figure 5.20 Filtered first and repeated impact force histories of 4mm specimens with quasi-isotropic lay-up configuration.	106
Figure 5.21 Comparison between filtered impact force histories of 2mm specimens with cross-ply and quasi-isotropic lay-up configurations.	107
Figure 5.22 Filtered first and repeated impact force histories of 2mm specimens with quasi-isotropic lay-up configuration.	108
Figure 5.23 Comparison between filtered impact force histories of 4mm specimens cured at 195°C and 180°C.....	110

Figure 5.24 Comparison between filtered impact force histories of 4mm specimens cured at 165°C and 180°C.....	111
Figure 5.25 Filtered first and repeated impact force histories of 4mm specimens cured at 195°C.....	111
Figure 5.26 Filtered first and repeated impact force histories of 4mm specimens cured at 165°C.....	112
Figure 5.27 Filtered repeated impact force histories of 4mm specimens cured at 165°C and 195°C.....	113
Figure 5.28 Input data for the 2mm laminates with cross-ply lay-up configuration in MAT_117_COMPOSITE_MATRIX material card.	117
Figure 5.29 Initial condition of the projectile in the FE simulation.....	118
Figure 5.30 Geometry model for the FE simulation of the 2mm laminates under low-velocity impact.....	119
Figure 5.31 Computed displacement of the 3mm laminates under 6J impact energy level. .	120
Figure 5.32 Simulation result of the model with 60×40 mesh scheme for laminates.	120
Figure 5.33 Determination of impact force history from a simulation result.	121
Figure 5.34 Unfiltered simulation results of impact force histories of 3mm laminates under various impact energy levels.....	122
Figure 5.35 Comparison between simulation results employing ABD matrix modelling strategy and test results: (a) 4mm and (b) 5mm laminates.	123
Figure 5.36 Comparison between simulation results and test results for 3mm laminates.....	125
Figure 5.37 Schematic illustration of the stack of 11 laminas to simulate the 4mm quasi-isotropic laminates.	126
Figure 5.38 Geometry model for the FE simulation of the 4mm laminates under low-velocity impact.....	127
Figure 5.39 Input data for +45° prepreg in MAT_54/55 material card.	128
Figure 5.40 Schematic illustration of different material axis defining methods in MAT_54/55 material model.....	132
Figure 5.41 Input data for the tie-break contact card.....	134
Figure 5.42 Simulation models with different mesh schemes for the laminates.	136
Figure 5.43 Comparison between experimental result and simulation results obtained from models with different plate mesh schemes.	137
Figure 5.44 Simulation models with different mesh densities for the impactor.....	138

Figure 5.45 Comparison between experimental result and simulation results obtained from models with different mesh densities for impactor.	139
Figure 5.46 Comparison between simulation results employing modelling strategy with consideration of damage mechanisms and test results.....	139
Figure 5.47 Literature simulation results: (a) an impact event with preload [103]; and (b) a simulation using thin shell element and tie-break contact [81].	140
Figure 5.48 Simulation result of the simulation model with 12J impact energy.	141
Figure 5.49 Simulation result of the modified simulation model with 12J impact energy....	142
Figure 5.50 Comparison between test result and simulation results with different impact contact definitions.	143
Figure 6.1 Schematic illustration of the quasi-static indentation test [120].	148
Figure 6.2 Instrumented quasi-static indentation test facility.....	148
Figure 6.3 Depth dial gauge to measure dent depth.....	150
Figure 6.4 Indenter displacement curves of 2mm and 4mm specimens under the continuous loading approach.	150
Figure 6.5 Comparison between LVI and QSI test results of 2mm specimens.	152
Figure 6.6 Comparison between LVI and QSI test results of 4mm specimens.	153
Figure 6.7 Indenter displacement histories of a 4mm specimen under the step-by-step loading approach.	154
Figure 6.8 Indenter displacement histories of a 2mm specimen under the step-by-step loading approach.	154
Figure 6.9 Determination of overall indenter displacement histories of (a) 2mm and (b) 4mm specimens under the step-by-step loading approach.....	156
Figure 6.10 Comparison among indenter displacement histories of 4mm and 2mm specimens under continuous and step-by-step loading approaches.....	157
Figure 6.11 Indentation force vs. dent depth/indenter displacement of a 4mm specimen....	158
Figure 6.12 Indentation force vs. dent depth/indenter displacement of a 2mm specimen....	160
Figure 6.13 Result of total indentation of a 4mm specimen.	161
Figure 6.14 Schematic illustration of total indentation.....	162
Figure 6.15 Comparison between permanent back-face deformation and dent depth.....	163
Figure 6.16 (a) Schematic illustration of the support fixture suggested by test standard [121]; (b) the support fixture used in practice.	165
Figure 6.17 Top and side views of a failed specimen after a CAI test.	166

Figure 6.18 Summary of CAI test results.	167
Figure 6.19 Motic microscope system and its built-in Moticam camera.....	170
Figure 6.20 Optical microscope observation results of the reference specimen and the specimen loaded up to 3.8kN.....	171
Figure 6.21 Optical microscope observation results of the specimens loaded up to 4.2kN and 6.5kN.....	172
Figure 6.22 Optical microscope observation results of the specimens loaded up to 7kN, 8kN and 11kN.....	173
Figure 6.23 Facilities used in SEM observation: (a) SEM and (b) sputter coater.	175
Figure 6.24 SEM image of the reference specimen.	176
Figure 6.25 SEM images of the specimen loaded up to 3.8kN.....	176
Figure 6.26 SEM images of the specimen loaded up to 4.2kN.....	177
Figure 6.27 Comparison between delaminations in the specimens subjected to 6.5kN and 7kN loads.	178
Figure 6.28 SEM image of the specimen loaded up to 8kN.	179
Figure 6.29 SEM observation result of the specimen loaded up to 11kN.	179
Figure 6.30 Geometry model for the indentation event of the 4mm thick laminates.	181
Figure 6.31 Meshed 4mm thick plate and indenter in simulation.....	182
Figure 6.32 Material properties outline of the nonlinear M21 resin.....	182
Figure 6.33 Input data for a typical 0.1mm displacement control.	183
Figure 6.34 Simulation results obtained from different models with different plate mesh schemes.	184
Figure 6.35 Simulation results of models with 2mm and 4mm plate thicknesses.	185
Figure 6.36 Comparison between results achieved from numerical simulation and experimental test for the 2mm specimen.	186
Figure 6.37 Comparison between results achieved from numerical simulation and experimental test for the 4mm specimen.	187
Figure 6.38 Comparison between analytical prediction and experimental measurement.	189
Figure 6.39 Comparison between analytical prediction and experimental measurement: (a) 2mm and (b) 4mm composite laminates.	191
Figure 7.1 SEM image of the initial delamination propagate tip.....	199
Figure 7.2 CAI test results of various 4mm specimens suffered different maximum loads..	200
Figure 7.3 Damage process assumption for (a) 4mm and (b) 2mm specimens.	202

List of Tables

Table 4.1 Dimensions of the tensile strength specimens	73
Table 4.2 Tensile strength of M21/T700 UD material	74
Table 4.3 Dimensions of tensile test specimens with strain gauge bonded	75
Table 4.4 Longitudinal Young's modulus and major Poisson's ratio of M21/T700 UD material.....	76
Table 4.5 Transverse Young's modulus and minor Poisson's ratio of M21/T700 UD material	78
Table 4.6 Dimensions of the interlaminar shear strength test specimens	79
Table 4.7 Interlaminar shear strength of M21/T700 UD material	79
Table 4.8 Dimensions of the in-plane shear modulus test specimens.....	80
Table 4.9 In-plane shear modulus of M21/T700 UD material.....	81
Table 4.10 In-plane shear strength of M21/T700 UD material.	81
Table 4.11 Summary of tensile and shear properties of M21/T700 UD material.....	82
Table 4.12 Summary of compressive properties and fracture mechanics of M21/T700 UD material [125, 126]	82
Table 5.1 Lay-up configurations of the impact test specimens	85
Table 5.2 MAT_54/55 input parameter definitions and values [122]	128
Table 6.1 Summary of specimens prepared for CAI tests and the corresponding applied loads	164
Table 7.1 Summary of DTL values of different composite laminates.....	196

Nomenclature

Latin Symbols	Description	Unit
A	damage area predicted by fibre failure criterion	mm ²
A_0	fibre failure interaction area associated with the measured tensile strength	mm ²
$A_1, A_2, A_3, A_4, B_1, B_2, C_{12}$	seven independent strength parameters	
A_{ij}	component of the extensional stiffness matrix	
B_{ij}	component of the extensional-bending coupling matrix	
C	a curve fit coefficient determined by impact curve	
d	diameter of impactor	mm
D	bending stiffness; opening gap inside cohesive zone	N/m mm
D_{ij}	component of the bending stiffness matrix	
D_j	relative distance between two coincident nodes	mm
D^*	effective bending stiffness of an orthotropic laminates	N/m
D_n^*	effective bending stiffness of an orthotropic laminates with n delaminations	N/m
e_c	history variable for fibre failure in compression	
e_d	history variable for matrix failure in compression	
e_f	history variable for fibre failure in tension	
e_m	history variable for matrix failure in tension	
E_i	elasticity modulus in i -direction; impact energy	GPa J
E_f	flexural modulus	GPa
E_1^d	reduced longitudinal modulus	
E_{TI}^*	effective modulus of transversely isotropic material	GPa
F	contact force	N
F_{bs}	bending and shear contribution load	N
F_i, F_{ij}, F_{ijk}	corresponding material strength parameters	
F_m	membrane load	N

F_{mbs}	total load on plate	N
G_{ij}	shear modulus in ij -plane	GPa
G_I	energy release rate in mode I	J/m ²
G_{IC}	critical energy release rate in mode I	J/m ²
G_{II}	energy release rate in mode II	J/m ²
G_{IIC}	critical energy release rate in mode II	J/m ²
G_{III}	energy release rate in mode III	J/m ²
G_{IIIC}	critical energy release rate in mode III	J/m ²
G_T	total energy release rate	J/m ²
G_{12}^d	reduced shear modulus	GPa
h	laminates thickness	mm
I_1, I_2, I_3, I_4	stress invariants under a rotation about the fibre direction	
k	the k^{th} layer	
k_b	bending stiffness	N/m
k_{bs}	bending and shear contribution stiffness	N/m
k_c	contact stiffness by Hertz contact law	N/m
k_m	membrane stiffness	N/m
k_s	shear stiffness	N/m
k^*	effective contact stiffness; contact stiffness of a half-space	N/m N/m
K	shear factor of laminates	
K_1	cohesive stiffness	N/m
K_2	contact stiffness	N/m
K_α	contact stiffness	N/m
K_{ij}	penalty stiffness	N/m
L	unsupported length	mm
m	plate mass per unit area	g/m ²
M	indenter mass	g
M_x, M_y	bending moment per unit length	N
M_{xy}	twisting moment per unit length	N
M_p^*	effective plate mass	g

n_d	number of delamination interfaces	
n_d^*	number of delamination interfaces starting from the laminates back face	
N	layers of laminates	
N_x, N_y	normal force per unit length	N/m
N_{xy}	shear force per unit length	N/m
P	impact force	N
P_{cr}	critical impact force	N
P_i	adhesive nodal force in i -direction	N
q	constant	
Q_α	effective out-of-plane stiffness	N/m
Q_{ij}	component of the stiffness matrix of an on-axis configuration	
\bar{Q}_{ij}	component of the stiffness matrix of an off-axis configuration	
r	radius of contact area; transverse coordinate used in elastoplastic contact model	mm mm
R	radius of indenter tip	mm
R_c	radius of contact area	mm
R_i	radius of indenter	mm
R_p	radius of plastic zone	mm
S	shear strength	MPa
S_{ij}	component of the compliance matrix; shear strength in ij -plane	GPa
S^*	effective shear stiffness of an orthotropic laminates	N/m
S_n^*	effective shear stiffness of an orthotropic laminates with n delaminations	N/m
t	laminates thickness	mm
t_p	clustering thickness including the thickness of layers with the same fibre orientation	mm
v_0	initial velocity of impactor	m/s
w	laminates width	mm
w_c	global plate deflection of point c	mm
w_i	impactor mass centre displacement	mm

w_o	global plate deflection of point o	mm
w_p	laminates back-surface deflection	mm
w_ℓ, u_ℓ	nodal displacements at the nodal point ℓ in the upper crack face	mm
w_{ℓ^*}, u_{ℓ^*}	nodal displacements at the nodal point ℓ^* in the lower crack face	mm
X_c	longitudinal compressive strength	MPa
X_i	shearing force at nodal point i close to the crack tip	N
X_t	longitudinal tensile strength	MPa
Y_c	transverse compressive strength	MPa
Y_t	transverse tensile strength	MPa
Z_c	material yield strength	MPa
Z_i	opening force at nodal point i close to the crack tip	N
Δa	length increment	mm
Δu_ℓ	shearing displacement at the two nodal points ℓ	mm
Δw	deflection difference between points o and c	mm
Δw_ℓ	opening displacement at the two nodal points ℓ	mm
ΔE	energy required to extend crack	J

Greek Symbols	Description	Unit
α	relative displacement; contact indentation	mm mm
α_c	indentation depth of point c	mm
α_o	indentation depth of point o	mm
α_o^*	centre indentation of corresponding half-space	mm
β	shape parameter of Weibull distribution for the property degradation	
γ	fracture energy	J
γ_{ij}	shear strain in ij -plane	
ε	strain	
ε_c	ultimate compressive strain	
ε_i	normal strain in i -direction	

ε_S	ultimate shear strain	
ε_{X_c}	longitudinal ultimate compressive strain	
ε_{X_t}	longitudinal ultimate tensile strain	
ε_{Y_c}	transverse ultimate compressive strain	
ε_{Y_t}	transverse ultimate tensile strain	
ε_{zz}	transverse normal strain	
$\dot{\varepsilon}$	strain rate	
θ	rotation angle of an off-axis configuration; angle between the material principal axis and the load direction	degree degree
θ_0	an arbitrary initial angle	degree
θ_k	orientation of the k^{th} layer of a laminates	degree
ν	Poisson's ratio	
ν_{ij}	negative ratio of the normal strain in j -direction to the normal strain in i -direction	
σ	flexural strength	MPa
σ_i	normal stress in i -direction	MPa
τ_{ij}	shear stress in ij -plane	MPa
τ_{max}	transverse shear strength	MPa

Abbreviations

ABD	stiffness matrix
AFRL	Air Force Research Laboratory
AMCS	autoclave management & control system
BVID	barely visible impact damage
CAI	compression-after-impact
CDM	continuum damage mechanics
CFRP	carbon fibre reinforced plastic
CZM	cohesive zone model
DCB	double cantilever beam
DTL	delamination threshold load

ECT	edge-cracked torsion
ENF	end-notched flexure
FEA	finite element analysis
FRP	fibre reinforced polymer
IKE	initial kinetic energy
ILSS	interlaminar shear strength
LEFM	linear elastic fracture mechanics
LVI	low-velocity impact
MMB	mixed-mode bending
OM	optical microscope
PFM	progressive failure model
PTFE	poly tetra fluoro ethylene
QI	quasi-isotropic
QSI	quasi-static indentation
SEM	scanning electron microscope
UD	unidirectional
VCCT	virtual crack closure technique

CHAPTER 1 Introduction

This chapter consists of three sections. The first section gives a brief introduction of the value and industrial relevance of the proposed research in the project. Project aims and objectives are defined in the second section. The final section of the chapter outlines the structure of the thesis.

1.1 Background

Modern composite materials have been extensively used in high-performance structural applications, such as the aeronautical, automotive and marine industries, since the 1970s [1]. The excellent specific strength/stiffness, high corrosion resistance, long fatigue life and good design flexibility of advanced carbon fibre reinforced plastic (CFRP) composites have distinguished them from the traditional metallic materials.

The usage of composite material in the most recent aircraft such as the Boeing B787 and the Airbus A350 has exceeded more than 50 percent of the structural weight of the aircraft [2, 3]. However, the potential weight saving offered by the advanced material is still restricted by the current conservative design philosophy. This conservative approach is mainly associated with the underestimated allowable design strength due to the concern about the effect of low-velocity impact (LVI) damage on the performance of composite laminates. Out-of-plane impact by foreign objects, such as runway debris and dropped tools, is expected to occur during the operation, manufacturing, maintenance and service of composite component. In most cases, this type of impact leaves damage that is hardly detectable by visual inspection; such damage is referred to barely visible impact damage (BVID). It is generally accepted that such internal impact damages may significantly reduce the structural performance of composite laminates and grow under service loads [4-9].

Compared with conventional metallic structures, composite laminates structures are more susceptible to impact damage due to the inherent brittleness of both the carbon fibre and the epoxy resin matrix. Different damage modes including matrix crack, delamination, and fibre breakage can be introduced into the composite laminates and interacted with each other, resulting in complicated damage mechanisms. Among the low-velocity impact induced damages, delamination is the dominant failure mode and may cause severe degradation of the

structural strength when the structure is under a compressive load. When the propagating tip of the matrix crack reaches the brittle interface, the high stress concentration may cause debonding of the adjacent layers with different fibre orientations and initiate delamination. Extensive research has been carried out to understand the mechanism of delamination and the effect of delamination on the performance of composite laminates [10-12]. It has been reported that there exists a delamination threshold load (DTL) for composite laminates [10, 13, 14]. When an impact load exceeds the DTL, the area of delamination will increase significantly and thus lead to a large reduction of the residual compressive strength of the delaminated laminates. However, due to the complexity of the failure mechanisms associated with composite laminates, the reliable assessment of damage resistance and damage tolerance of composite laminates remains a major challenge to the aerospace industry. Further research is therefore required to understand the concept of DTL and its effect on the material behaviour under low-velocity impact to improve the conservative design philosophy of composite laminates.

This project also focused on the study of delamination initiation through the investigation of the contact behaviour of composite laminates under both low-velocity impact and quasi-static indentation (QSI) loading conditions. The impact response and damage mechanisms of composite laminates under low-velocity impact will be investigated by considering the effect of the delamination initiation. The detection and prediction of the DTL will be assessed. The feasibility of relating internal damage to the dent depth through visual inspection has also been explored.

1.2 Aims and Objectives

The project has following two aims:

1. To develop further knowledge of the impact response and damage mechanisms of composite laminates under low-velocity impact.
2. To explore the feasibility of assessing the internal damage with a visually inspectable parameter.

To achieve above aims, the contact behaviour of composite laminates under LVI and QSI loading conditions has been investigated through experimental, numerical, and analytical studies to achieve the following objectives:

1. To gain a good knowledge of the behaviour of composite laminates under low-velocity impact through a comprehensive literature review.
2. To conduct a series of detailed investigations of the impact response and the detection/prediction of delamination threshold load of composite laminates under low-velocity impact.
3. To establish a relation between indentation depth and internal damage through the investigation of the static response of composite laminates under quasi-static indentation loading condition.
4. To simulate the contact force history and the initiation of delamination of composite laminates subjected to low-velocity impact and quasi-static indentation loading.
5. To characterise the effect of damage on the residual compressive strength of composite laminates through the compression-after-impact (CAI) test, optical microscope (OM), and scanning electron microscope (SEM) observations.

1.3 Outline of the Thesis

This thesis presents the research work carried out between October 2010 and October 2014 for the PhD project titled “Characterisation of low-velocity impact response in composite laminates”. It consists of eight chapters. Chapter 1 gives a brief introduction of the background associated with the project and defines the project aims and objectives. Chapter 2 is a comprehensive review of the concept, theories, techniques, and key findings in the field related to the project. Chapter 3 explains the research strategy employed in the project. The fabrication of composite plates and the derivation of the basic mechanical properties of the unidirectional (UD) material are described in Chapter 4. Chapter 5 and 6 present detailed investigations, which were conducted in experimental, numerical and analytical approaches, on the impact behaviour of composite laminates under low-velocity impact and the contact response of composite laminates under quasi-static indentation load. Results achieved from the project are analysed and discussed from a project point of view in Chapter 7 to establish the relations among them. Chapter 8 summarises the key results achieved in the project and the areas where further work is required.

CHAPTER 2 Literature Review

This chapter details the existing research, techniques and theories related to the work carried out in this project. Topics of composite material, composite laminates, low-velocity impact damage mechanisms, delamination threshold load and quasi-static indentation behaviour of composite laminates are reviewed and discussed.

2.1 An Overview of Composite Material

Composite material is a structural material typically constructed from at least two constituents with significantly different properties. The constituents are combined at a microscopic or macroscopic level and have a distinct interface between each other. This combination produces a material possessing more desirable properties, such as improved stiffness-to-weight and strength-to-weight ratio, long fatigue life, and high electrochemical corrosion resistance, which are not attainable with the individual constituent [5, 6, 15]. These advantages have made the composite materials a very broad and important class of engineering materials; the world annual production of composite materials (over 10 million tons) has been increasing 5-10% per annum in recent years [7].

2.1.1 Historical Development of Composite Material

Many natural biological materials are effective composite materials, due to a combination of two or more components in many cases. Bamboo, bone and celery are good examples of cellular natural composite; while muscle tissue is a kind of multidirectional natural fibre composite as shown in Figure 2.1 [7, 15].

Composite materials have been exploited throughout human history. Inspired by natural composite materials, the ancient civilizations mixed two or more components to reinforce the mixture. For instance, the Ancient Egyptians introduced glued laminated wood and papier-mache (1500 B.C.) [5] and the Inca and Mayan civilizations strengthened bricks and pottery with plant fibres [15].

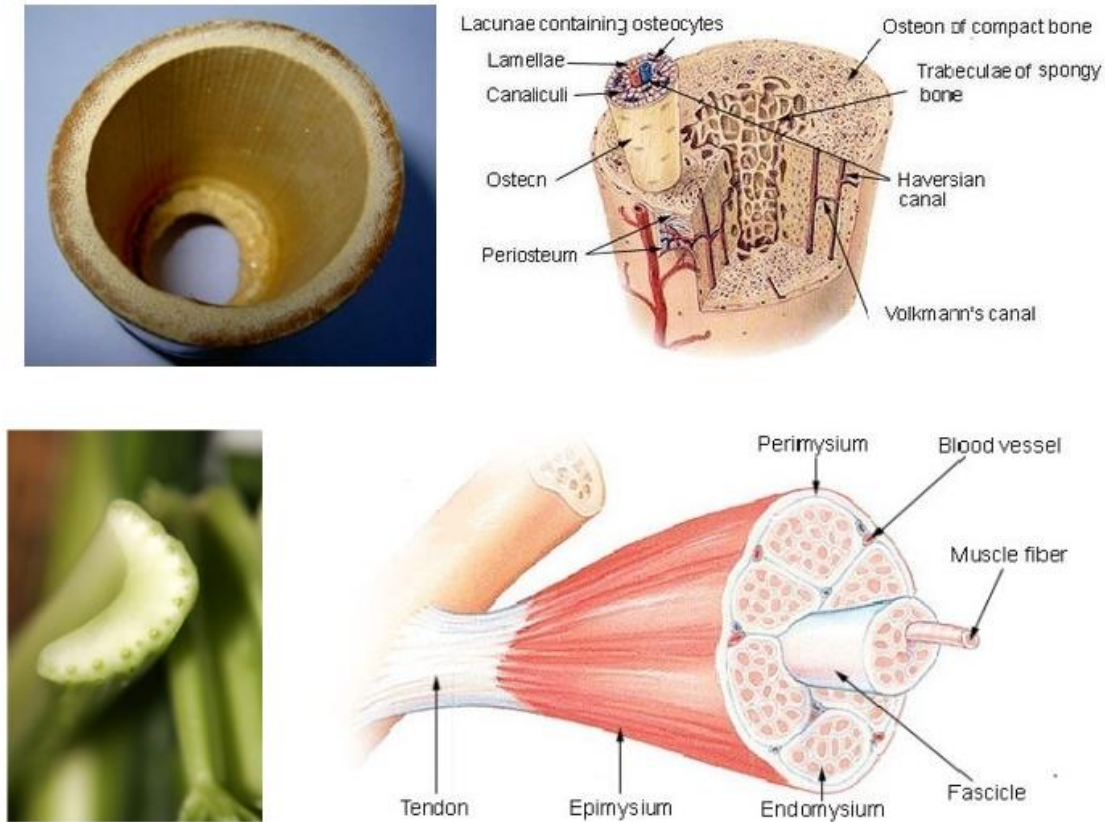


Figure 2.1 Examples of natural composite materials.

Advanced composite materials have been manufactured and applied to the modern marine, automotive and aerospace industries since the early 20th century. Glass fibre reinforced resin, commonly called fibre-glass, has been applied in boat and missile construction since it was first made in the 1930s. The applications of modern composite materials made significant progress in 1970s, due to the development of new fibres, such as carbon, boron, and aramid, and new composite systems with matrices made from metal and ceramic [1]. These new-generation high-strength composite materials proved to be the ideal alternative materials to meet the extreme requirements of performance in the aerospace industry. As Airbus claimed in the A350 XWB launch press conference [2], over 50% of the airframe by weight, including wings, hybrid fuselage, empennage and belly fairing, is made of advanced composite materials, such as carbon/epoxy and graphite/titanium, as shown in Figure 2.2. The extensive application of composites on the A350XWB has reduced its weight significantly, resulting in better fuel efficiency and up to 8% lower operating costs than its competing Boeing 787 Dreamliner.

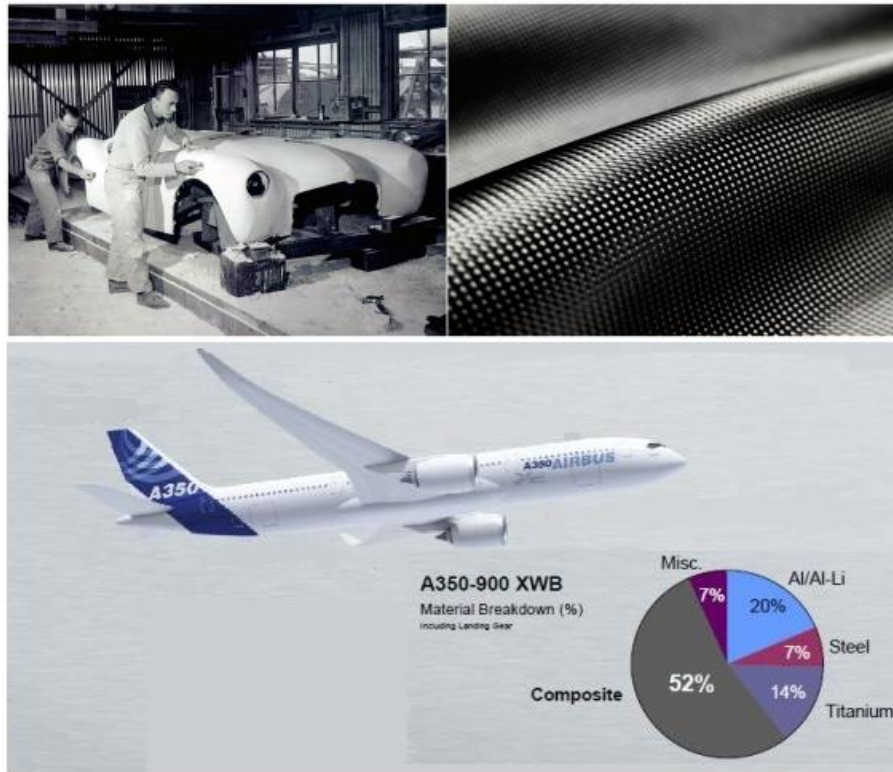


Figure 2.2 Applications of modern composite materials [2].

Ashby [16] summarised the historical development and extrapolated the expectative progression of composite materials compared with other three most commonly used materials, metal, polymer/elastomer and ceramic/glass, considering the relative importance of each group, which is presented in Figure 2.3.

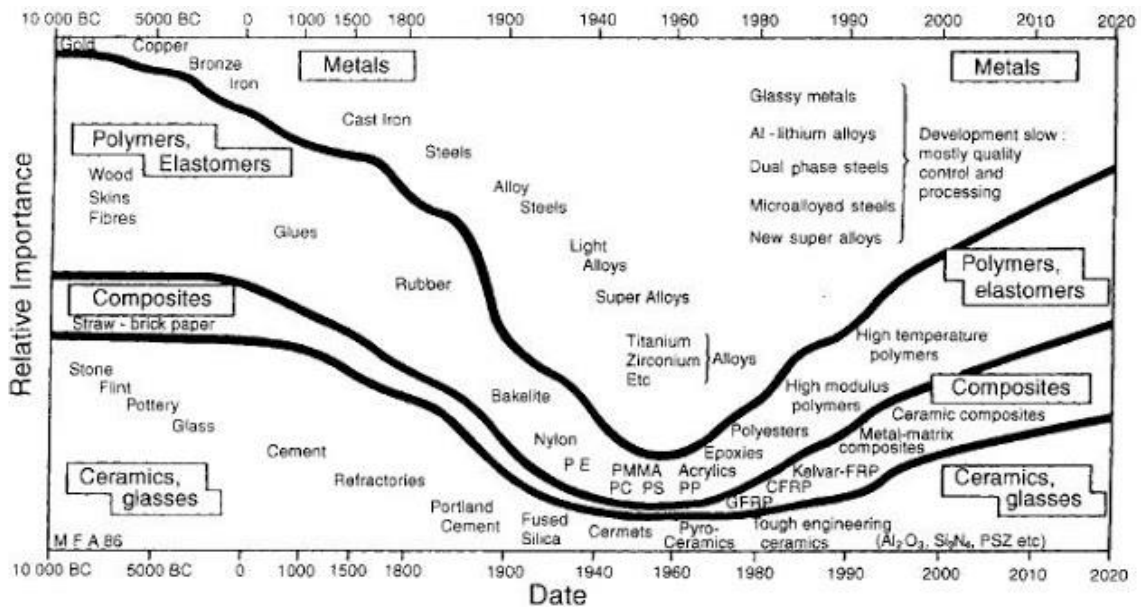


Figure 2.3 Chronological variation of the relative importance of materials [16].

It should be noted that the relative importance of each material in Figure 2.3 is not associated with any specific unit of measure; it only reflects the importance weighting factor of each material group at different ages. This helps to explain the steady growth of polymer/elastomer, composite, and ceramic/glass since 1960s. The steady growth can be attributed to the innovations (from both manufacturing and analysis viewpoints) of these advanced materials including high modulus polymers, carbon fibre and ceramic composite. Meanwhile, the progress of metal has faced its bottleneck after the dramatic development since the first industrial revolution.

2.1.2 Classification of Composite Material

A composite material generally consists of a discontinuous phase embedded within a continuous phase. The discontinuous phase is the *reinforcement* which is much stronger and stiffer than the continuous phase termed as *matrix* [7, 15, 17].

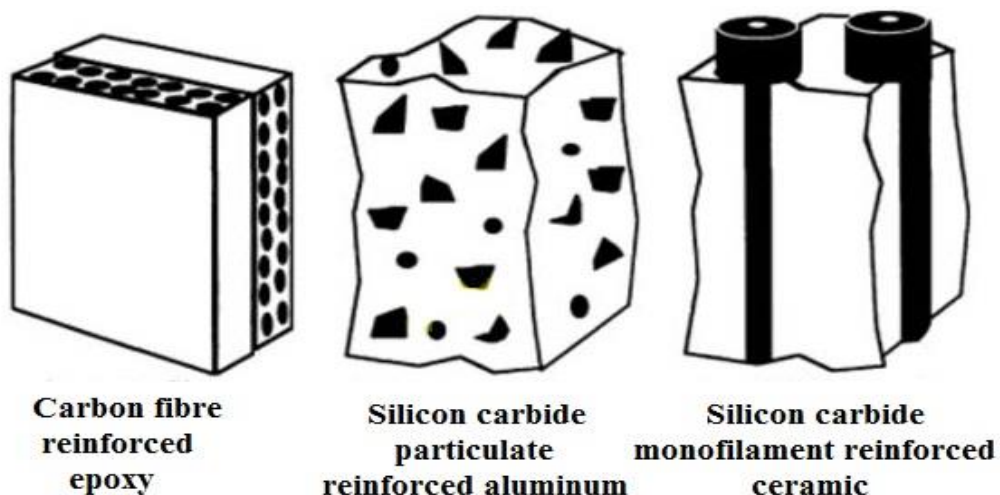


Figure 2.4 Schematic illustration of polymer, metal, and ceramic matrix composite materials [7].

Based on the difference in reinforcements and matrixes, two methods are commonly applied in classifying composite materials. In one way, composite materials are divided into three principle categories based on the matrix material type: polymer, metal and ceramic based composites as illustrated in Figure 2.4 [7]. On the other hand, the geometry of the reinforcement is used to classify the composite materials into fibre, particulate, and flake reinforced composites as illustrated in Figure 2.5 [5, 15].

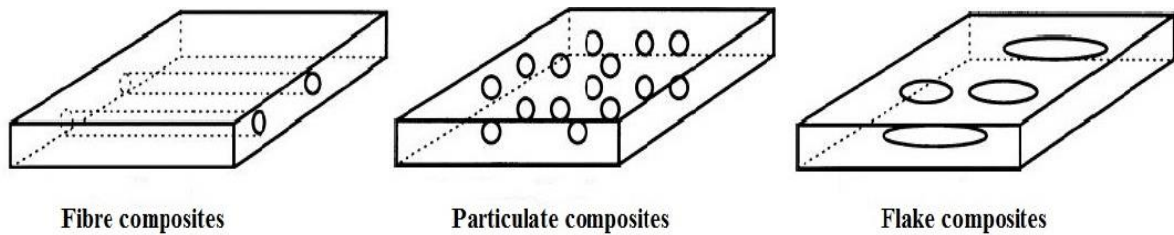


Figure 2.5 Schematic illustration of fibre, particulate, and flake reinforced composite materials [5].

Currently, fibre reinforced polymer (FRP) matrix composite is one of the most extensively used composite groups in aerospace industry. The reinforcement fibre can be produced from a range of materials, such as glass, aramid, boron, carbon and graphite. Polyester, polyamide, polypropylene, phenolic and epoxy are commonly used as matrices. Although the high strength-to-weight and stiffness-to-weight ratios of the fibre reinforced composite system are mainly determined by the reinforcements, the matrix is still required due to the inherent brittleness of the fibre reinforcement. The matrix binds fibres together and isolates them from each other; the matrix transfers the load from fibre to fibre and protects them from environmental attack; the matrix also carries the shear stress in the composite and restricts the initiation and propagation of cracks [8].

2.1.3 Advantages and Limitations of Composite Material

Compared with conventional materials such as steel, aluminium and titanium alloys, the carbon fibre reinforced epoxy composite material offers superior specific strength (strength/density) and specific modulus (modulus/density) as shown in Figure 2.6. As a consequence, the composite material has its unique advantages in the application of aircraft structure [7, 9, 17-19].

In addition to the high strength and stiffness to density ratios, several other outstanding benefits provided by composite material also attract the engineers, designers and manufacturers in aerospace industry. For instance, the ability to optimise mechanical properties by adjusting the lay-ups of composite material improves the design flexibility; the excellent fatigue and electrochemical corrosion resistance of composite material increases the operation stability; the part consolidation of composite material also reduces the assembly cost and time [19].

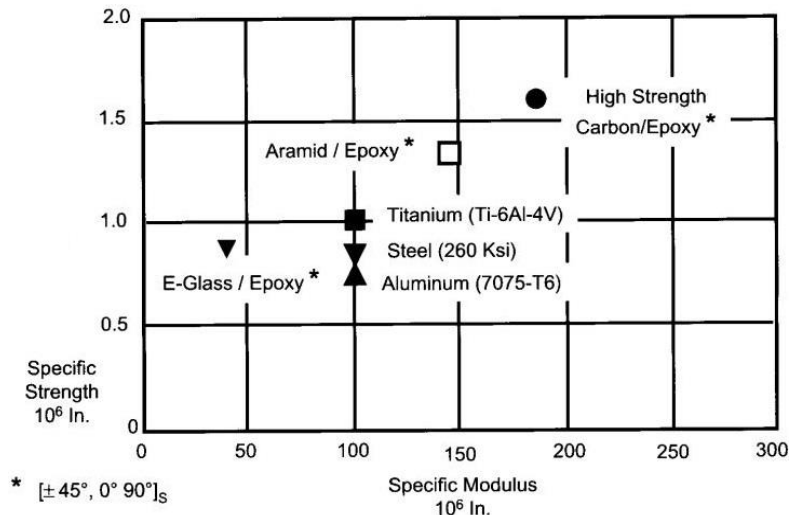


Figure 2.6 Specific strength and modulus of general engineering materials [19].

It is however worth noticing that the fibre reinforced composites are typically anisotropic. The low transverse and through-thickness strengths of fibre reinforced composite need to be considered in design and analysis [6-8, 17, 18]. Compared with conventional structural materials, the following limitations still restrict the further application of composite material:

- High fabrication cost of composites material.
- Complicated design and analysis of anisotropic composites.
- Complexity in failure mechanisms and detection of internal damage.
- Expensive and complicated repair of damaged composite structure.

2.2 An Introduction to Composite Laminates

Composite laminates, a typical form of composite material, has been used increasingly in aerospace industry as a result of its superior mechanical properties. But insufficient understanding of the failure mechanisms under low-velocity impact is a major concern which limits its further applications. A detailed understanding of its structural performance is to fully exploit the potentials of composite laminates.

2.2.1 Characterisation of Composite Laminates

Composite laminate is constructed by stacking laminas in the thickness direction, as illustrated in Figure 2.7. A lamina is typically a thin fibre reinforced composite layer which

has either a unidirectional (UD) fibre orientation as illustrated in Figure 2.7(a), or a woven fibre configuration as illustrated in Figure 2.7(b) [5]. Specific procedures, including filament winding, autoclave curing and resin transfer moulding, are involved to bond the laminas together depending on different matrix materials.

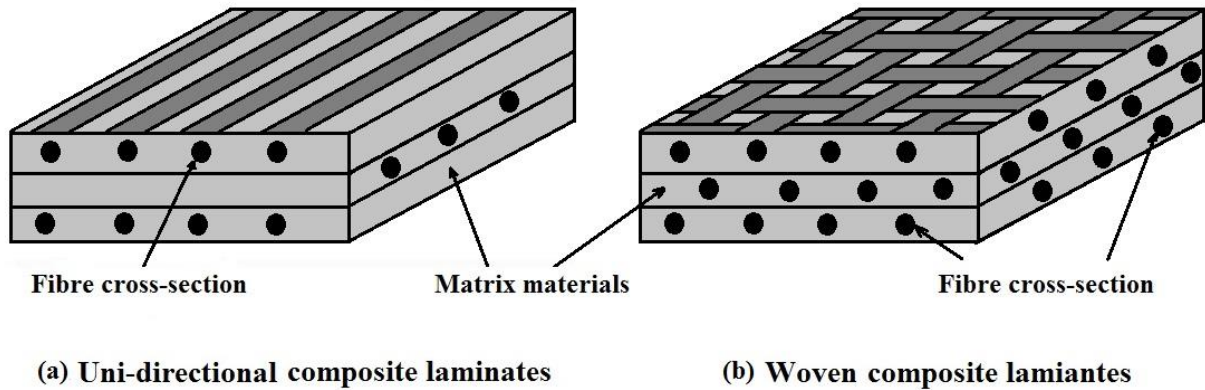


Figure 2.7 Schematic illustration of (a) the UD composite laminates [5] and (b) the woven composite laminates.

2.2.2 Lay-up of Composite Laminates

It is well-established that the lay-up configuration of composite laminates can be adjusted to achieve the desired mechanical properties including in-plane structural stiffness/strength and out-of-plane impact resistance [5, 15, 20]. Laminated woven composite material can be generally treated as a quasi-isotropic material since the fibres are weaved together in each lamina. On the contrary, composite laminates made of unidirectional laminas normally is anisotropic due to different principal material axis of individual lamina. The lay-up configuration of composite laminates made of UD laminas can be divided into following categories in order to achieve required material performance [17]:

- Unidirectional laminates: multiple layered UD laminates with orthotropic mechanical properties (*e.g.* $[0]_4$ and $[90]_8$).
- Symmetric laminates: multidirectional laminates with pairs of laminas of the same fibre orientation, material, and thickness; the laminas are stacked symmetrically with respect to the mid-ply of laminates (*e.g.* $[\pm 45/0/90]_5$).
- Antisymmetric laminates: multidirectional laminates with pairs of laminas of the opposite fibre orientation but same material and thickness stacked symmetrically with respect to the mid-ply of laminates (*e.g.* $[+45/-45/+45/-45]$).

- Cross-ply laminates: symmetrical or antisymmetrical laminates only has laminae oriented at 0° and 90° (e.g. $[0/90]_s$, $[0/90/0/90]$).
- Angle-ply laminates: symmetrical or antisymmetrical laminates with pairs of laminae oriented at $\pm\theta$ (e.g. $[\pm 45]_s$, $[+30/-30/+30/-30]$).
- Quasi-isotropic laminates: a laminates constructed by the following manners in order to gain the in-plane isotropic properties (e.g. $[\pm 45/0/90]_s$).

1). minimum 3 layers;

2). all layers have identical orthotropic material properties and thickness;

3). the orientation of the k^{th} layer of an N -layer laminates can be generated by an arbitrary initial angle θ_0 :

$$\theta_k = \frac{k\pi}{N} + \theta_0 \quad (2.1)$$

In practice, the mechanical properties of fibre reinforced composite laminates sometimes need to be quickly estimated. Hart-Smith [21] suggested an empirical prediction, termed as Ten-Percent Rule, to estimate the fibre-dominated in-plane strength and stiffness of laminated composites based on the rule of mixtures of 0° , $\pm 45^\circ$, and 90° fibre orientations. In this rule, the primary 0° laminae are considered to contribute 100 percent of its longitudinal strength and modulus to the resultant mechanical properties of laminates, while the secondary laminae (90° & $\pm 45^\circ$) are credited with only 10% of the reference strength and modulus in the estimation of overall mechanical properties. In the latest articles [22, 23], the Ten-Percent Rule has been extended beyond its prior restriction to select fibre patterns by introducing the implicit lamina failure envelope and increasing the transverse failure strain of fibre. It should be noticed that this simplification is only valid for the highly orthotropic materials.

2.2.3 Mechanical Analysis of Composite laminates

The overall performance of composite laminates can be estimated accurately through detailed mechanical analysis as described in comprehensive literatures [4, 5, 7, 15]. The compliance and stiffness matrices of individual unidirectional lamina are firstly determined, followed by the study of the overall performance of composite laminates considering the thickness and lay-up configuration of laminates.

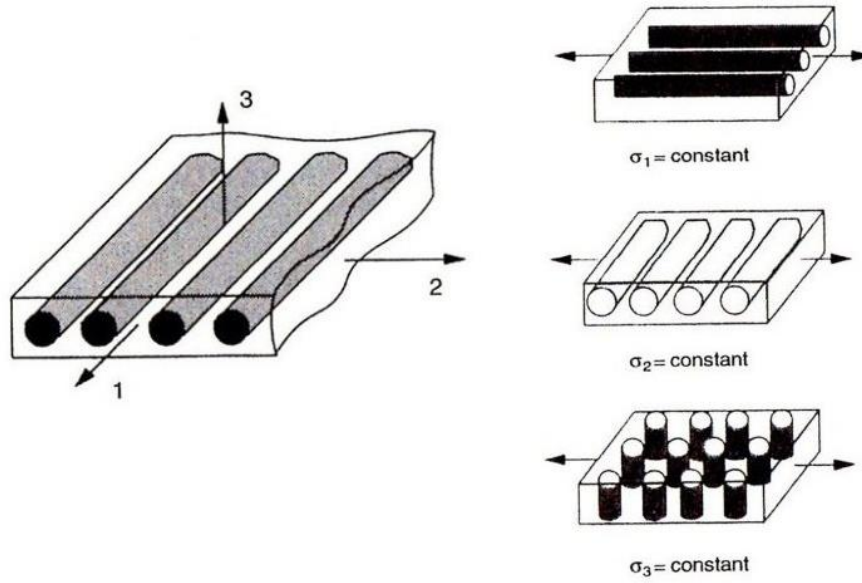


Figure 2.8 Schematic illustration of the applied stresses for determining compliance matrix of a lamina [15].

In the study of Staab [15], normal stresses are applied to the unidirectional lamina in the principal directions of orthotropic material to determine the relationship of compliance matrix to engineering elasticity constants of a lamina as illustrated in Figure 2.8. The relationships between strains in the 1, 2, and 3-directions, termed as ε_1 , ε_2 , and ε_3 , and the only nonzero applied normal stress, σ_1 , are expressed as

$$\varepsilon_1 = \frac{\sigma_1}{E_1} \quad \varepsilon_2 = \frac{-v_{12}\sigma_1}{E_1} \quad \varepsilon_3 = \frac{-v_{13}\sigma_1}{E_1} \quad (2.2)$$

where, E_i is the elasticity modulus in the i -direction; v_{ij} is defined as the negative ratio of the normal strain in the j -direction to the normal strain in the i -direction, when the only normal load is applied in the i -direction.

Similarly, the strains developed with the only nonzero stress component, σ_2 , are

$$\varepsilon_1 = \frac{-v_{21}\sigma_2}{E_2} \quad \varepsilon_2 = \frac{\sigma_2}{E_2} \quad \varepsilon_3 = \frac{-v_{23}\sigma_2}{E_2} \quad (2.3)$$

Under the 3-direction normal nonzero stress, σ_3 , the strains are expressed as

$$\varepsilon_1 = \frac{-v_{31}\sigma_3}{E_3} \quad \varepsilon_2 = \frac{-v_{32}\sigma_3}{E_3} \quad \varepsilon_3 = \frac{\sigma_3}{E_3} \quad (2.4)$$

The compliance matrix, $[S]$, can be established by combining the above results and recalling the relation $\{\varepsilon_i\} = [S_{ij}]\{\sigma_{ij}\}$ as

$$\begin{aligned}
 S_{11} &= \frac{1}{E_1} & S_{12} &= \frac{-\nu_{21}}{E_2} & S_{13} &= \frac{-\nu_{31}}{E_3} \\
 S_{21} &= \frac{-\nu_{12}}{E_1} & S_{22} &= \frac{1}{E_2} & S_{23} &= \frac{-\nu_{32}}{E_3} \\
 S_{31} &= \frac{-\nu_{13}}{E_1} & S_{32} &= \frac{-\nu_{23}}{E_2} & S_{33} &= \frac{1}{E_3}
 \end{aligned} \tag{2.5}$$

The shear terms, S_{44} , S_{55} , and S_{66} , are determined for complete compliance matrix by applying pure shear stresses in the 2-3, 1-3, and 1-2 planes. In principle, the inexistence of shear-extension coupling simplified the matter as

$$S_{44} = \frac{1}{G_{23}} \quad S_{55} = \frac{1}{G_{13}} \quad S_{66} = \frac{1}{G_{12}} \tag{2.6}$$

where, G_{ij} is the shear modulus corresponding to a shear stress applied to the ij -plane.

Therefore, the compliance matrix is expressed as

$$[S] = \begin{bmatrix} S_{11} & S_{21} & S_{31} & 0 & 0 & 0 \\ S_{12} & S_{22} & S_{32} & 0 & 0 & 0 \\ S_{13} & S_{23} & S_{33} & 0 & 0 & 0 \\ 0 & 0 & 0 & S_{44} & 0 & 0 \\ 0 & 0 & 0 & 0 & S_{55} & 0 \\ 0 & 0 & 0 & 0 & 0 & S_{66} \end{bmatrix} = \begin{bmatrix} \frac{1}{E_1} & -\frac{\nu_{12}}{E_1} & -\frac{\nu_{13}}{E_1} & 0 & 0 & 0 \\ -\frac{\nu_{21}}{E_2} & \frac{1}{E_2} & -\frac{\nu_{23}}{E_2} & 0 & 0 & 0 \\ -\frac{\nu_{31}}{E_3} & -\frac{\nu_{32}}{E_3} & \frac{1}{E_3} & 0 & 0 & 0 \\ 0 & 0 & 0 & \frac{1}{G_{23}} & 0 & 0 \\ 0 & 0 & 0 & 0 & \frac{1}{G_{31}} & 0 \\ 0 & 0 & 0 & 0 & 0 & \frac{1}{G_{12}} \end{bmatrix} \tag{2.7}$$

The stiffness matrix, $[Q]$, is obtained by inverting the compliance matrix. The individual stiffness coefficient, Q_{ij} , is expressed in terms of the engineering elasticity constants as

$$\begin{aligned}
 Q_{11} &= E_1(1 - \nu_{23}\nu_{32})/\Delta & Q_{22} &= E_2(1 - \nu_{31}\nu_{13})/\Delta & Q_{33} &= E_3(1 - \nu_{12}\nu_{21})/\Delta \\
 Q_{12} &= E_2(\nu_{12} + \nu_{32}\nu_{13})/\Delta = E_1(\nu_{21} + \nu_{31}\nu_{23})/\Delta & Q_{44} &= G_{23} \\
 Q_{13} &= E_3(\nu_{13} + \nu_{12}\nu_{23})/\Delta = E_1(\nu_{31} + \nu_{21}\nu_{32})/\Delta & Q_{55} &= G_{13} \\
 Q_{23} &= E_3(\nu_{23} + \nu_{21}\nu_{13})/\Delta = E_2(\nu_{32} + \nu_{12}\nu_{31})/\Delta & Q_{66} &= G_{12}
 \end{aligned} \tag{2.8}$$

where,

$$\Delta = 1 - \nu_{12}\nu_{21} - \nu_{23}\nu_{32} - \nu_{31}\nu_{13} - 2\nu_{13}\nu_{21}\nu_{32}$$

The current stiffness matrix is only applicable for the analysis of an on-axis configuration as shown in Figure 2.9(a). A new matrix, $[\bar{Q}]$, is required in the analysis of an θ angle lamina with an off-axis configuration shown in Figure 2.9(b).

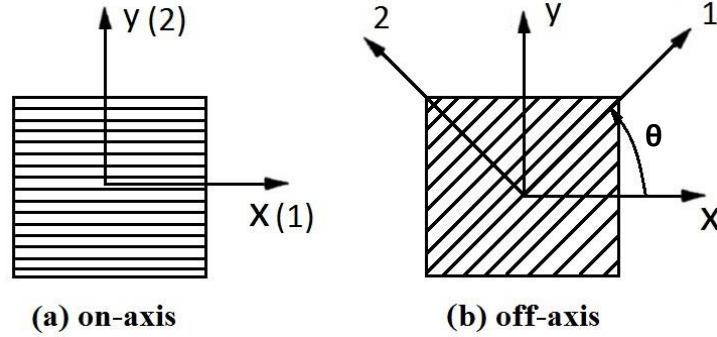


Figure 2.9 Schematic illustration of (a) on-axis and (b) off-axis configurations [15].

The expanded form of the stress-strain relationship is [15]

$$\begin{Bmatrix} \sigma_x \\ \sigma_y \\ \sigma_z \\ \tau_{yz} \\ \tau_{xz} \\ \tau_{xy} \end{Bmatrix} = \begin{bmatrix} \bar{Q}_{11} & \bar{Q}_{12} & \bar{Q}_{13} & 0 & 0 & \bar{Q}_{16} \\ \bar{Q}_{12} & \bar{Q}_{22} & \bar{Q}_{23} & 0 & 0 & \bar{Q}_{26} \\ \bar{Q}_{13} & \bar{Q}_{23} & \bar{Q}_{33} & 0 & 0 & \bar{Q}_{36} \\ 0 & 0 & 0 & \bar{Q}_{44} & \bar{Q}_{45} & 0 \\ 0 & 0 & 0 & \bar{Q}_{45} & \bar{Q}_{55} & 0 \\ \bar{Q}_{16} & \bar{Q}_{26} & \bar{Q}_{36} & 0 & 0 & \bar{Q}_{66} \end{bmatrix} \begin{Bmatrix} \varepsilon_x \\ \varepsilon_y \\ \varepsilon_z \\ \gamma_{yz} \\ \gamma_{xz} \\ \gamma_{xy} \end{Bmatrix} \quad (2.9)$$

where, σ_x , σ_y and σ_z are the normal stress in the corresponding direction, respectively; τ_{yz} , τ_{xz} and τ_{xy} are the shear stress in the corresponding plane, respectively; ε_x , ε_y and ε_z are the normal strain in the corresponding direction, respectively; γ_{yz} , γ_{xz} and γ_{xy} are the shear strain in the corresponding plane, respectively.

Each stiffness coefficient, \bar{Q}_{ij} , is expressed as

$$\begin{aligned} \bar{Q}_{11} &= Q_{11}m^4 + 2(Q_{12} + 2Q_{66})m^2n^2 + Q_{22}n^4 \\ \bar{Q}_{12} &= (Q_{11} + Q_{22} - 4Q_{66})m^2n^2 + Q_{12}(m^4 + n^4) \\ \bar{Q}_{13} &= Q_{13}m^2 + Q_{23}n^2 \\ \bar{Q}_{16} &= (Q_{11} - Q_{12} - 2Q_{66})m^3n - (Q_{22} - Q_{12} - 2Q_{66})mn^3 \\ \bar{Q}_{22} &= Q_{11}n^4 + 2(Q_{12} + 2Q_{66})m^2n^2 + Q_{22}m^4 \\ \bar{Q}_{23} &= Q_{13}n^2 + Q_{23}m^2 \end{aligned} \quad (2.10)$$

$$\bar{Q}_{26} = (Q_{11} - Q_{12} - 2Q_{66})mn^3 - (Q_{22} - Q_{12} - 2Q_{66})m^3n$$

$$\bar{Q}_{33} = Q_{33} \quad \bar{Q}_{36} = (Q_{13} - Q_{23})mn$$

$$\bar{Q}_{44} = Q_{44}m^2 + Q_{55}n^2 \quad \bar{Q}_{45} = (Q_{55} - Q_{44})mn$$

$$\bar{Q}_{55} = Q_{55}m^2 + Q_{44}n^2 \quad \bar{Q}_{66} = (Q_{11} + Q_{22} - 2Q_{12})m^2n^2 + Q_{66}(m^2 - n^2)^2$$

where,

$$m = \cos \theta \text{ and } n = \sin \theta$$

Once the stiffness and compliance matrices of an individual unidirectional lamina are determined, the overall performance of composite laminates can be estimated based on the thickness and lay-up configuration. Each lamina is assigned a reference number and a z-coordinate to identify the location in the coordinate system as shown in Figure 2.10.

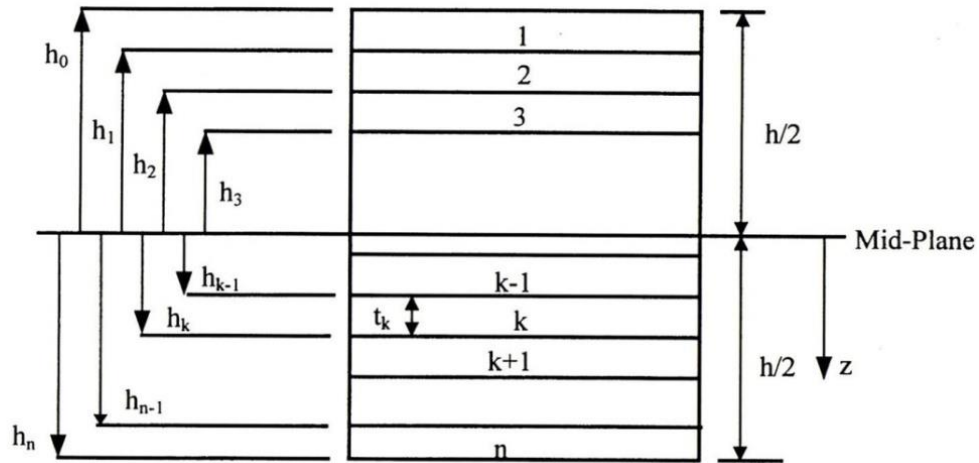


Figure 2.10 Laminates stacking sequence nomenclature [5].

Therefore, the stress for k^{th} lamina can be determined by following relation

$$\begin{Bmatrix} \sigma_x \\ \sigma_y \\ \tau_{xy} \end{Bmatrix}_k = \begin{bmatrix} \bar{Q}_{11} & \bar{Q}_{12} & \bar{Q}_{16} \\ \bar{Q}_{12} & \bar{Q}_{22} & \bar{Q}_{26} \\ \bar{Q}_{16} & \bar{Q}_{26} & \bar{Q}_{66} \end{bmatrix}_k \left(\begin{Bmatrix} \varepsilon_x^0 \\ \varepsilon_y^0 \\ \gamma_{xy}^0 \end{Bmatrix} + z \begin{Bmatrix} k_x \\ k_y \\ k_{xy} \end{Bmatrix} \right) \quad (2.11)$$

The resulting force and moment in the laminates can be written in matrix form as [15]

$$\begin{Bmatrix} N_x \\ N_y \\ N_{xy} \end{Bmatrix} = \sum_{k=1}^n \int_{h_{k-1}}^{h_k} \begin{Bmatrix} \sigma_x \\ \sigma_y \\ \tau_{xy} \end{Bmatrix} dz \quad \begin{Bmatrix} M_x \\ M_y \\ M_{xy} \end{Bmatrix} = \sum_{k=1}^n \int_{h_{k-1}}^{h_k} \begin{Bmatrix} \sigma_x \\ \sigma_y \\ \tau_{xy} \end{Bmatrix} z dz \quad (2.12)$$

where,

N_x, N_y = normal force per unit length

N_{xy} = shear force per unit length

M_x, M_y = bending moment per unit length

M_{xy} = twisting moment per unit length

Combining them together, gives

$$\begin{bmatrix} N_x \\ N_y \\ N_{xy} \end{bmatrix} = \begin{bmatrix} A_{11} & A_{12} & A_{16} \\ A_{12} & A_{22} & A_{26} \\ A_{16} & A_{26} & A_{66} \end{bmatrix} \begin{bmatrix} \varepsilon_x^0 \\ \varepsilon_y^0 \\ \gamma_{xy}^0 \end{bmatrix} + \begin{bmatrix} B_{11} & B_{12} & B_{16} \\ B_{12} & B_{22} & B_{26} \\ B_{16} & B_{26} & B_{66} \end{bmatrix} \begin{bmatrix} k_x \\ k_y \\ k_{xy} \end{bmatrix} \quad (2.13)$$

$$\begin{bmatrix} M_x \\ M_y \\ M_{xy} \end{bmatrix} = \begin{bmatrix} B_{11} & B_{12} & B_{16} \\ B_{12} & B_{22} & B_{26} \\ B_{16} & B_{26} & B_{66} \end{bmatrix} \begin{bmatrix} \varepsilon_x^0 \\ \varepsilon_y^0 \\ \gamma_{xy}^0 \end{bmatrix} + \begin{bmatrix} D_{11} & D_{12} & D_{16} \\ D_{12} & D_{22} & D_{26} \\ D_{16} & D_{26} & D_{66} \end{bmatrix} \begin{bmatrix} k_x \\ k_y \\ k_{xy} \end{bmatrix}$$

where,

$$[A_{ij}] = \sum_{k=1}^n [(\bar{Q}_{ij})]_k (h_k - h_{k-1}) \quad i, j = 1, 2, 6 \text{ extensional stiffness matrix}$$

$$[B_{ij}] = \frac{1}{2} \sum_{k=1}^n [(\bar{Q}_{ij})]_k (h_k^2 - h_{k-1}^2) \quad i, j = 1, 2, 6 \text{ extensional-bending coupling matrix}$$

$$[D_{ij}] = \frac{1}{3} \sum_{k=1}^n [(\bar{Q}_{ij})]_k (h_k^3 - h_{k-1}^3) \quad i, j = 1, 2, 6 \text{ bending stiffness matrix}$$

The loads and moments of a composite laminates can be expressed in matrix form, after integration, as

$$\begin{Bmatrix} N_x \\ N_y \\ N_{xy} \\ M_x \\ M_y \\ M_{xy} \end{Bmatrix} = \begin{bmatrix} A_{11} & A_{12} & A_{16} \\ A_{12} & A_{22} & A_{26} \\ A_{16} & A_{26} & A_{66} \\ B_{11} & B_{12} & B_{16} \\ B_{12} & B_{22} & B_{26} \\ B_{16} & B_{26} & B_{66} \end{bmatrix} \begin{Bmatrix} \varepsilon_x^0 \\ \varepsilon_y^0 \\ \gamma_{xy}^0 \\ k_x \\ k_y \\ k_{xy} \end{Bmatrix} \quad (2.14)$$

The form of equation often can be simplified as $\begin{Bmatrix} N \\ M \end{Bmatrix} = \begin{bmatrix} A & B \\ B & D \end{bmatrix} \begin{Bmatrix} \varepsilon^0 \\ k \end{Bmatrix}$ (2.15)

2.3 Composite Laminates under Low-velocity Impact

Impact damage is one of the crucial concerns in the design, manufacture, and maintenance of composite laminates. The failure mechanisms of composite laminates are much more

complex compared with conventional metallic material. Different damage modes may occur at both interlaminar and intralaminar levels and interact with each other. The failure mechanisms of composite laminates are generally classified as either low-velocity impact induced damage or high-velocity impact induced damage. The low-velocity impact damage, which is the most difficult to be detected in practice, will be focused in the current study.

2.3.1 Definition of Low-velocity Impact

The definition of low-velocity impact is still under debate among leading researchers in the field due to the uncertain transition between low-velocity impact and high-velocity impact. On one hand, a commonly accepted one is suggested by Cantwell and Morton [24] under which the impact velocity is up to 10 m/s considering the height limit of test facility (such as drop-weight tower). On the other hand, Abrate stated in his review book [4] that the impact speed of an low-velocity impact event should be less than 100 m/s.

Sjoblom *et al.* [25] and Shivakumar *et al.* [26] insisted that the upper limit of low-velocity impact vary from 1 to 10 meters per second depending on the material properties of target and the mass and stiffness of impactor. The impact response is dominated by the stress wave propagation through material. Very localised damage and energy dissipation are induced by high-velocity impact as a result of the lack of response time and negligible boundary condition effect. On the contrary, low-velocity impact event generates an entire structural response and in consequence more energy is absorbed elastically, as a result of a long enough impact duration. Davies and Robinson [27] defined the low-velocity impact not only simply by a numerical limit, but by the material property, in which case the through-thickness stress wave effect on the stress distribution is negligible. A cylindrical zone under the impactor is considered to undergo a uniform strain, as the stress wave propagating through the plate, which gives the ultimate compressive strain, ε_c , as [27]

$$\varepsilon_c = \frac{\text{transition impact velocity}}{\text{speed of sound in the material}} \quad (2.16)$$

Several researchers [28, 29] suggested that the type of impact can also be categorized by the existence of damage types. Low-velocity impact damage is characterised by delamination and matrix crack; whereas high velocity impact is dominated by fibre breakage and penetration.

In conclusion, considering the maximum impact velocity studied in this project is less than 10 m/s, and therefore the studied impact falls in the category of low-velocity impact.

2.3.2 Classification of Low-velocity Impact Tests

An impact test should be selected properly to replicate the actual loading condition to be experienced by structure in practice, and introduce the damage modes and failure mechanisms likely to occur.

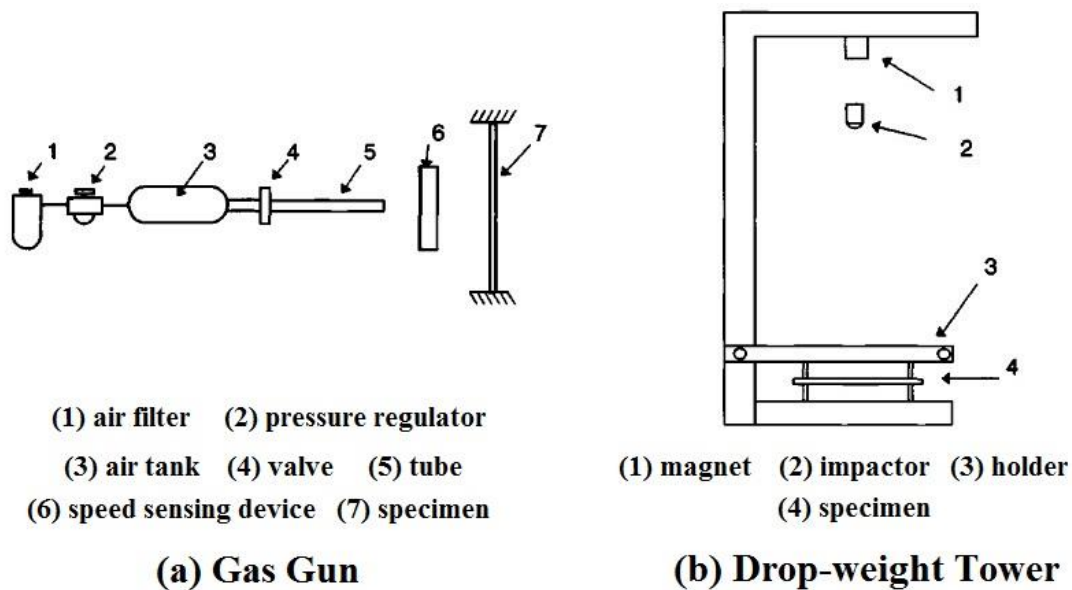


Figure 2.11 Schematic illustration of common impact test rigs [4].

Two types of impact tests are commonly employed in investigations [30-40], although many details of the actual test apparatus may differ. Gas gun test, as illustrated in Figure 2.11(a), is suitable to simulate the impact events with small mass and high-velocity projectiles, such as the runway debris impact on aircraft during its take-off and landing. Drop-weight test, as illustrated in Figure 2.11(b), is used extensively to simulate the low-velocity impact condition caused by larger projectile that may occur when tools are accidentally dropped on composite structure. Although the hemisphere is the most commonly used shape of impactor, the changeability of the geometries of impactor and target is still one of the benefits associated with the drop-weight test. Mitrevski and co-workers [41-43] conducted their detailed studies on the effect of impactor shape on the impact response and damage mechanisms of composite laminates.

In addition, pendulum-type and cantilevered-type systems are also used to generate low-velocity impact. As Cantwell and Morton suggested in their review paper [24], the pendulum-type test system was used by many early impact studies. The information about the energy absorption and dissipation in the composite can be gained by using the pendulum-type test method. Lal [44, 45] used the cantilevered impactor, by pulling back and then releasing a flexible beam with a steel ball mounted at the end, to produce a low-velocity impact.

2.3.3 Failure Modes of Composite Laminates under Low-velocity Impact

Kaw [5] suggested that the failure of composite laminates may not be catastrophic. It is much more possible that some layers fail firstly and the laminates continues to take more loads until the entire laminates fails. The failure process is quite complex, involving both intralaminar damage mechanisms, including matrix crack and fibre fracture, and interlaminar damage mechanisms, such as delamination and penetration.

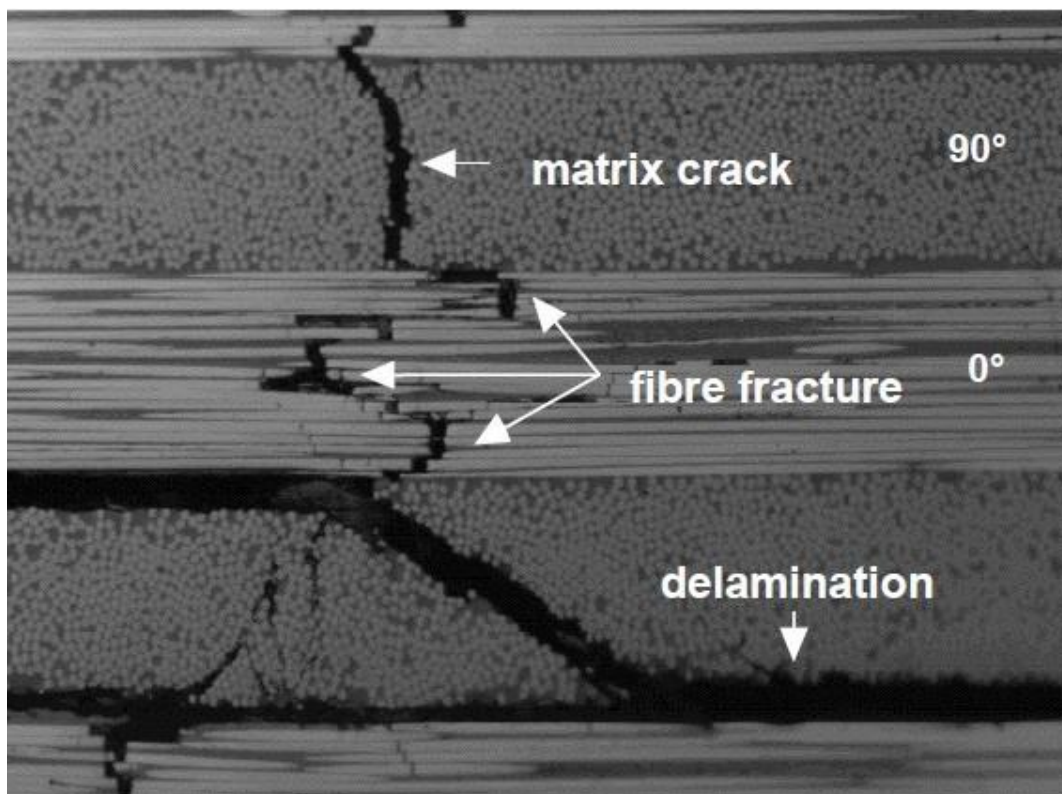


Figure 2.12 Cross-section view of the impact damaged composite laminates [46].

Matrix crack as illustrated in Figure 2.12 occurs parallel to the fibre direction due to tensile, compressive, and shear stresses induced by the low-velocity impact [47]. Delamination is the separation between layers with different fibre orientations as shown in Figure 2.12, and

triggered by the interlaminar stress due to the bending stiffness mismatch between adjacent layers [48]. Fibre fracture generally occurs under higher load after matrix crack and delamination. The fibre breaks under high tensile stress and buckles under high compression load [47]. Penetration is a macroscopic damage and occurs when the laminates failure reaches a catastrophic level which is not common in the low-velocity impact event [49]. Numerous researches have been conducted in order to achieve comprehensive understanding on the damage initiation and propagation of composite laminates under low-velocity impact.

Matrix Crack

Abrate [4] suggested that the distribution of matrix cracks was complicated and difficult to be predicted accurately. The prediction of the complex pattern is not essential since matrix crack does not significantly affect the performance of laminates. Matrix damage, including matrix crack and debonding between fibre and matrix, is the inception of other failure mechanisms and may induce delamination at the interface [4].

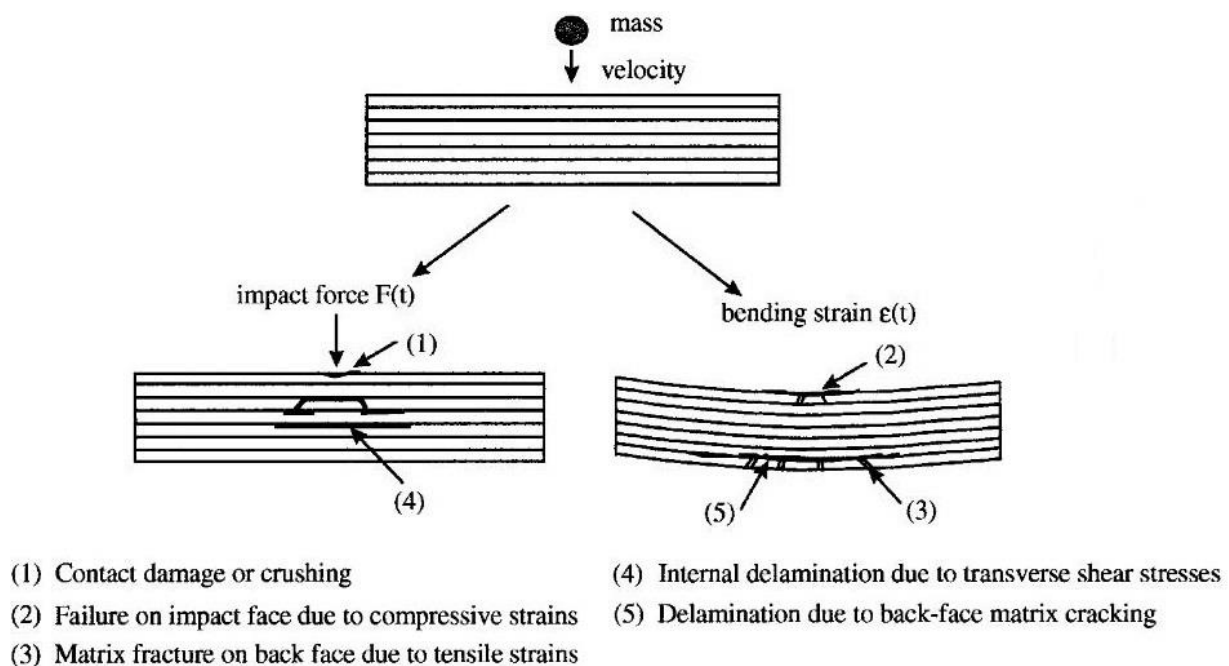


Figure 2.13 Schematic illustration of the low-velocity impact damage natures in a composite laminates [11].

Zhang [11] reported a typical damage pattern of composite laminates under low-velocity impact as shown in Figure 2.13. The highly localized contact damage (refer to notation 1 in Figure 2.13), named as crushing, appears close to the contact surface under the impactor and may extend into the target plate within 2 or 3 layers. It depends on the Hertz type contact

force and transverse material stiffness of the top layer. The matrix cracks on the impact face start at the edge(s) of the impactor (refer to notation 2 in Figure 2.13) and are at an angle of approximately 45° from the mid-surface. These shear cracks are caused by high transverse shear stress/compressive bending strain through the material [4, 50]. The vertical matrix cracks on the lower face (refer to notation 3 in Figure 2.13) are termed as tensile cracks. These cracks are introduced by high in-plane normal stress/tensile bending strain which are related to the flexural deformation of laminates [4, 51]. The internal delamination near the mid-plane (refer to notation 4 in Figure 2.13) and the delamination near the back surface (refer to notation 5 in Figure 2.13) are triggered by either shear crack or tensile crack, respectively. Once the sharp crack tips reach the interfaces, the stress concentration at interface may initiate the delamination [52].

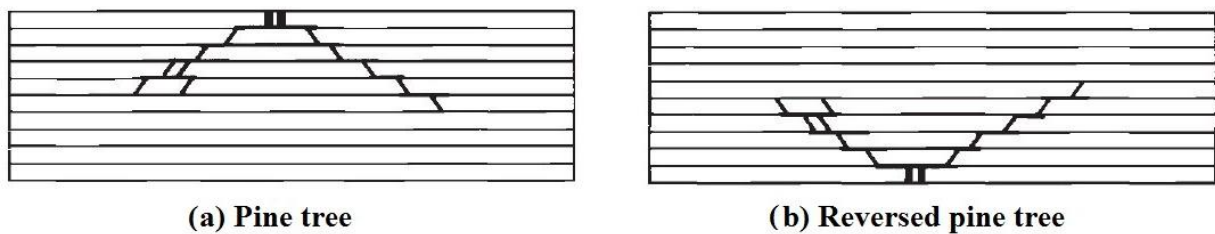


Figure 2.14 Schematic illustration of different damage patterns [4].

Abrate [4] and Cantwell *et al.*[53] reached similar conclusions about the geometry effect on matrix crack type and its distribution. The laminates thickness is proved to be the key factor. The thick specimen is stiffer and introduces transverse shear crack in the upper layers firstly due to higher contact force, resulting in the pine tree distribution damage pattern as shown in Figure 2.14(a). In contrast, the tensile cracks in the lower layers are more likely to be introduced in thin laminates by the excessive transverse deflection and subsequent membrane effects. The matrix crack and delamination are distributed in a reversed pine tree pattern as illustrated in Figure 2.14(b).

Delamination

Delamination, an interlaminar failure mode, plays a dominant role in the damage and energy dissipation of composite laminates subject to low-velocity impact. Delamination and matrix crack interact with each other and contribute to up to 60% degradation in compressive strength of composite laminates [4, 10, 12].

Experimental studies [10, 11, 48, 54] consistently report that delamination only occurs at the interface between layers with different fibre orientations as a result of the Poisson's ratio and bending stiffness mismatches between adjacent layers. Figure 2.15 presents the studies on the delamination shape.

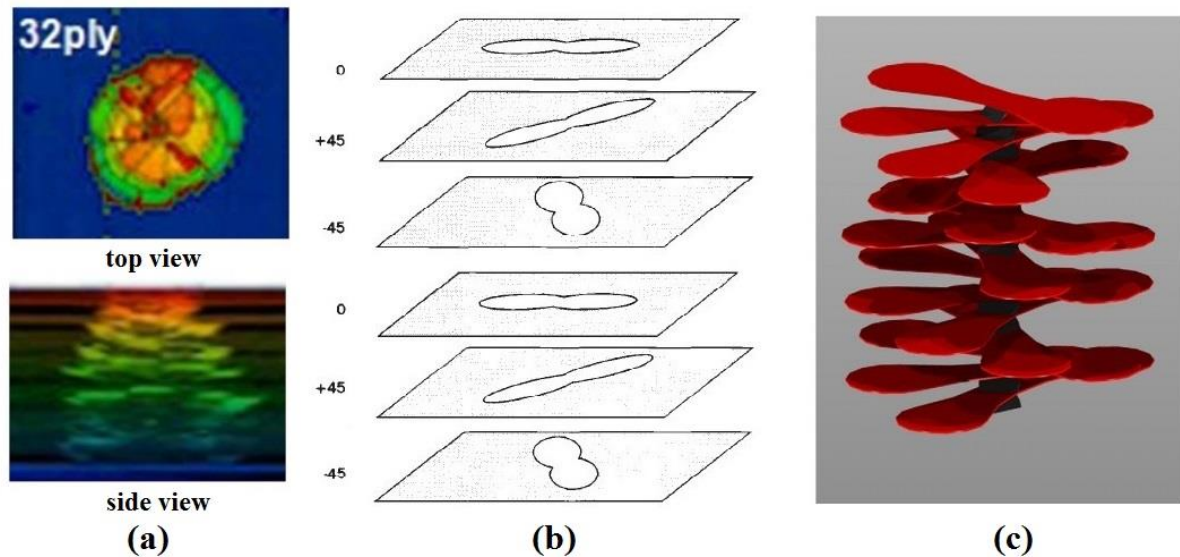


Figure 2.15 (a) Top and side views of the delamination area from C-scan observations [46]; (b) schematic illustration of delamination [4]; (c) ideal model of delamination [46].

The top and side views of a delaminated 32-ply laminates from the C-scan observations are shown in Figure 2.15(a). The top-view C-scan observation suggests the entire delamination area has a circular projection shape. Meanwhile, the side-view result indicates the delamination area is combined by several delaminations at different interfaces. The back surface of laminates tends to have larger delamination area than that at the top-surface. The individual delamination area is often in a 'peanut' shape with its major axis oriented in the direction of fibres in the lower layer at the interface as illustrated schematically in Figure 2.15(b). In the computer generated ideal model of delamination as shown in Figure 2.15(c), a spiral staircase is used to characterise the delamination distribution. It is however necessary to notice that delamination shapes often are quite irregular and the orientations become rather difficult to be ascertained. Therefore, the delamination area measured from C-scan observation, as a projection of all damaged interfaces on a single plane, is commonly used as a key parameter in the study of low-velocity induced delamination.

Liu [48] reported that the bending stress was the major cause of delamination. Sun and Joshi [28] concluded that delamination was initiated by the shear crack in upper layer, the

transverse shear crack in middle layer, and the vertical bending crack in lower layer. The initiation of delamination is believed to be associated with a critical value of impact force, named as the delamination threshold load. A detailed review of the work by a number of researchers in the area of delamination initiation and propagation will be presented in Section 2.4.

Fibre Fracture

Matrix crack can be considered as the precursor of delamination causing significant reduction in the residual strength of composite laminates under low impact energy. The initiation of fibre fracture can be considered as the precursor of catastrophic failure of composite laminates (such as penetration) under relative high impact energy. The fibre fracture generally occurs later than the matrix crack and delamination in the failure process of impacted composite laminates, as a result of the brittle fibre losing the protection provided by matrix. The damaged matrix cannot transfer the loads to fibre uniformly, which may cause the high stress concentration. There are two main kinds of fibre failure modes including the tensile fibre breakage and compressive fibre buckling as illustrated in Figure 2.16.

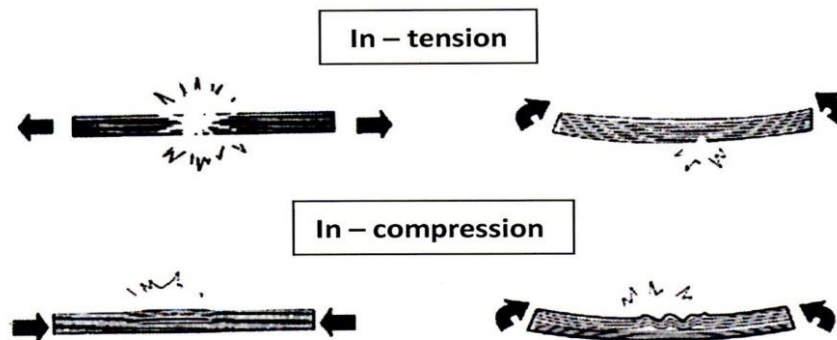


Figure 2.16 Schematic illustration of fibre failure modes.

Richardson and Wisheart suggested in their review paper [47] that the in-tension fibre breakage was introduced by high bending stress on the non-impacted surface; the in-compression fibre buckling was introduced by the high local contact stress and indentation effect under impactor. Dorey [55] also presented a simple prediction of the energy required for the back-surface flexural induced fibre fracture as

$$\text{Energy} = \frac{\sigma^2 wtL}{18E_f} \quad (2.17)$$

where, σ is the flexural strength, E_f is the flexural modulus, w is the laminates width, L is the unsupported length, and t is the laminates thickness.

However, the accurate prediction of fibre fracture is a challenging task and depends on the modelling of all damage modes, including matrix crack and delamination, with the consideration of interactions among them in the progressive damage development.

Penetration

Penetration is a catastrophic failure mode of composite laminates subjected to a high velocity/energy impact as a result of fibre fracture. It is the research focus of the ballistic impact response of composite laminates, while this macroscopic failure mode may also occur in some low-velocity impact events with high impact energy level.

Efforts have been made to predict the initiation of penetration. Some researchers [53, 56] suggested that the threshold penetration energy of composite laminate was not a linear function of the laminates thickness and rised rapidly with the increase of specimen thickness. In contrast, other researchers reported that the threshold penetration energy was proportional to specimen thickness. Dorey [55] belongs to the latter group and presented the prediction of the energy absorbed by penetration:

$$\text{Energy} = \pi\gamma td \quad (2.18)$$

where, γ is the fracture energy, t is the specimen thickness, and d is the diameter of impactor.

2.3.4 Failure Criteria of Composite Laminates

The material strength is the material capability to resist failure. A failure criterion of composite material cannot however be simply defined by material strength due to the material anisotropy. There are three principal directions of an orthotropic composite laminates, which may cause the principal stress direction different from the principal strain direction. Moreover, composite laminate has different strengths in different directions. As a result, the maximum strength may not correspond to the critical loading condition. Therefore, the failure criterion of composite laminates must be determined based on a proper comparison between the practical stress field and allowable stress.

Numerous failure criteria of composite laminates based on different phenomenological considerations have been suggested. The maximum stress and strain criteria are the earliest ones and are improved further by many researchers in their modified failure criteria.

Maximum Stress Criterion

Erdogan *et al.* [57] proposed the maximum stress criterion assuming the failure occurs when any of the stress components along the principal material direction exceeds the corresponding strength in that direction. The failure criterion is expressed as

under tension

$$\left. \begin{array}{l} \sigma_1 \geq X_t \\ \sigma_2 \geq Y_t \\ |\tau_{12}| \geq S \end{array} \right\}$$

under compression

$$\left. \begin{array}{l} |\sigma_1| \geq X_c \\ |\sigma_2| \geq Y_c \end{array} \right\} \quad (2.19)$$

where, σ_1 , σ_2 , τ_{12} , X_t , Y_t , X_c , Y_c , and S are the longitudinal stress, transverse stress, shear stress, longitudinal tensile strength, transverse tensile strength, longitudinal compressive strength, transverse compressive strength and shear strength, respectively.

In practice, the stress components along the material principal axis (σ_1 , σ_2 , and τ_{12}) are usually unknown. But the stress components in the non-principal direction, such as σ_x , σ_y , and τ_{xy} , are determinable. By introducing the angle θ between the material principal axis and the load direction, the maximum stress criterion can be rewritten as

$$\left. \begin{array}{l} \sigma_x \geq \frac{X_t}{\cos^2 \theta} \quad \left(|\sigma_x| \geq \frac{X_c}{\cos^2 \theta} \right) \\ \sigma_x \geq \frac{Y_t}{\sin^2 \theta} \quad \left(|\sigma_x| \geq \frac{Y_c}{\sin^2 \theta} \right) \\ \sigma_x \geq \frac{S}{|\sin \theta \cos \theta|} \end{array} \right\} \quad (2.20)$$

Therefore, the material strength in the θ direction can be determined as the maximum value σ_x by Equation 2.20.

Maximum Strain Criterion

The maximum strain criterion, which is similar to the maximum stress failure criterion, is believed to be firstly applied in advanced fibre-reinforced polymer composites by Waddoups [58] in 1960s. In this criterion, the failure is assumed to occur when any of the strain components along the material principal axis exceeds the corresponding ultimate strain in that direction. The failure criterion is expressed as

under tension

$$\left. \begin{aligned} \varepsilon_1 &\geq \varepsilon_{X_t} \\ \varepsilon_2 &\geq \varepsilon_{Y_t} \\ |\gamma_{12}| &\geq \varepsilon_S \end{aligned} \right\}$$

under compression

$$\left. \begin{aligned} |\varepsilon_1| &\geq \varepsilon_{X_c} \\ |\varepsilon_2| &\geq \varepsilon_{Y_c} \end{aligned} \right\} \quad (2.21)$$

where, ε_1 , ε_2 , and γ_{12} are the longitudinal strain, transverse strain, and shear strain in material principal axis, respectively. ε_{X_t} , ε_{Y_t} , ε_{X_c} , ε_{Y_c} , and ε_S are the longitudinal ultimate tensile strain, transverse ultimate tensile strain, longitudinal ultimate compressive strain, transverse ultimate compressive strain and ultimate shear strain, respectively.

Similarly, the maximum strain criterion can also be rewritten by introducing the rotational angle θ and the Poisson's ratios (ν_{12} and ν_{21}) to determine the maximum stress in the θ direction.

$$\left. \begin{aligned} \sigma_x &\geq \frac{X_t}{\cos^2\theta - \nu_{12}\sin^2\theta} & \left(|\sigma_x| \geq \frac{X_c}{\cos^2\theta - \nu_{12}\sin^2\theta} \right) \\ \sigma_x &\geq \frac{Y_t}{\sin^2\theta - \nu_{21}\cos^2\theta} & \left(|\sigma_x| \geq \frac{Y_c}{\sin^2\theta - \nu_{21}\cos^2\theta} \right) \\ & \sigma_x \geq \frac{S}{|\sin\theta \cos\theta|} \end{aligned} \right\} \quad (2.22)$$

In general, both the maximum stress and maximum strain criteria are the mostly used ones in practice due to their simplicities. They are among the few criteria that can identify the failure mode, although the prediction is sometimes not very reliable. The theoretical prediction and experimental result may differ significantly due to the simplification and lack consideration on the interactions among the failure modes. Consequently, the modifications of these failure criteria are required for composite laminates.

Tsai-Hill Failure Criterion

Hill [59] extended the application of the von Mises criterion for the isotropic material to the orthotropic material, assuming the plastic deformation was dominated by the incompressibility, and the tensile and compressive strengths were equal ($X_t = X_c = X$, and $Y_t = Y_c = Y$). The Tsai-Hill failure criterion of an orthotropic unidirectional plate is expressed as

$$\frac{\sigma_1^2}{X^2} - \frac{\sigma_1\sigma_2}{X^2} + \frac{\sigma_2^2}{Y^2} + \frac{\tau_{12}^2}{S_{12}^2} = 1 \quad (2.23)$$

where, S_{12} is the shear strength in the 1-2 plane. And the orthotropic laminates will fail when the left of the expression is equal or greater than 1.

Hoffman Failure Criterion

Hoffman [60] modified the Tsai-Hill failure criterion in order to predict the failure in the orthotropic laminates with different tensile and compressive strength ($X_t \neq X_c$, and $Y_t \neq Y_c$). The Hoffman failure criterion is expressed as

$$\frac{\sigma_1^2 - \sigma_1\sigma_2}{X_t X_c} + \frac{\sigma_2^2}{Y_t Y_c} + \frac{X_c - X_t}{X_t X_c} \sigma_1 + \frac{Y_c - Y_t}{Y_t Y_c} \sigma_2 + \frac{\tau_{12}^2}{S_{12}^2} = 1 \quad (2.24)$$

The orthotropic laminates will fail when the left of the expression is equal or greater than 1.

Tsai-Wu Failure Criterion

Tsai and Wu [61] proposed a failure criterion for the anisotropic composite laminates based on the following equation

$$F_i \sigma_i + F_{ij} \sigma_i \sigma_j + F_{ijk} \sigma_i \sigma_j \sigma_k + \dots = 1 \quad (2.25)$$

where, $i, j, k, \dots = 1, 2, 6, \dots$; F_i , F_{ij} , and F_{ijk} are the corresponding material strength parameters. The failure will be introduced into composite when the value is equal or greater than 1.

In practice, only the first two terms are used in the failure criterion shown as

$$F_i \sigma_i + F_{ij} \sigma_i \sigma_j = 1 \quad (2.26)$$

In the matrix form

$$(F_1 F_2 F_6) \begin{Bmatrix} \sigma_1 \\ \sigma_2 \\ \sigma_3 \end{Bmatrix} + (\sigma_1 \sigma_2 \sigma_6) \begin{bmatrix} F_{11} & F_{12} & F_{16} \\ F_{12} & F_{22} & F_{26} \\ F_{16} & F_{26} & F_{66} \end{bmatrix} \begin{Bmatrix} \sigma_1 \\ \sigma_2 \\ \sigma_6 \end{Bmatrix} = 1 \quad (2.27)$$

There are nine strength parameters to be determined in the criterion. The material strength is expected to be independent on changing the sign of shear stress σ_6 (τ_{12}). Therefore, the shear stress related strength parameters should be zero due to the symmetry of stress tensor, which gives

$$F_6 = F_{16} = F_{26} = 0 \quad (2.28)$$

Substituting these strength components into Equation 2.27, and thus the failure criterion is expressed as

$$F_1 \sigma_1 + F_2 \sigma_2 + F_{11} \sigma_1^2 + F_{22} \sigma_2^2 + F_{66} \sigma_6^2 + 2F_{12} \sigma_1 \sigma_2 = 1 \quad (2.29)$$

Six independent strength parameters of F_1 , F_2 , F_{11} , F_{22} , F_{66} , and F_{12} , are required to be experimentally determined. Parameters, F_1 , F_2 , F_{11} , F_{22} , and F_{66} , can be determined by the axial tensile/compressive, and shear tests along the material principal axis. The interacted parameter, F_{12} , should be determined from a biaxial test, supposing $\sigma_1 = \sigma_2 = \sigma_0$, and $\sigma_6 = 0$. The strength parameters are expressed as

$$\left. \begin{aligned} F_1 &= \frac{1}{X_t} - \frac{1}{X_c} & F_2 &= \frac{1}{Y_t} - \frac{1}{Y_c} \\ F_{11} &= \frac{1}{X_t X_c} & F_{22} &= \frac{1}{Y_t Y_c} & F_{66} &= \frac{1}{S^2} \\ F_{12} &= \frac{1}{2\sigma_0^2} \left[1 - \left(\frac{1}{X_t} - \frac{1}{X_c} + \frac{1}{Y_t} - \frac{1}{Y_c} \right) \sigma_0 - \left(\frac{1}{X_t X_c} + \frac{1}{Y_t Y_c} \right) \sigma_0^2 \right] \end{aligned} \right\} \quad (2.30)$$

Pipes and Cole [62] reported a good agreement between the Tsai-Wu model predictions and the experimental results by conducting the off-axis strength tests on boron/epoxy composites. Moreover, the Tsai-Wu failure criterion has been available in most of the commercial FEM software, *e.g.* MAT-55 in LS-DYNA, due to its better accuracy and higher efficiency.

Hashin's Failure Criterion

Hashin [63] proposed a specific criterion to predict the failure in the transversely isotropic material (*e.g.* the unidirectional composite laminates). Unlike the Tsai-Wu criterion, which is a phenomenological failure criterion, the choice of quadratics in the Hashin's failure criterion is based on the physical reasons and not on curve fitting considerations.

Considering the coordinate transformations, the stress invariants under a rotation about the fibre direction (axis-1) are [63]

$$I_1 = \sigma_1, I_2 = \sigma_2 + \sigma_3, I_3 = \tau_{23}^2 - \sigma_2\sigma_3, I_4 = \tau_{12}^2 + \tau_{13}^2 \quad (2.31)$$

Thus the most general transversely isotropic quadratic approximation is [63]

$$A_1 I_1 + B_1 I_1^2 + A_2 I_2 + B_2 I_2^2 + C_{12} I_1 I_2 + A_3 I_3 + A_4 I_4 = 1 \quad (2.32)$$

Seven independent strength parameters of $A_1, A_2, A_3, A_4, B_1, B_2,$ and C_{12} are involved in the failure criterion. Different modes of failure may expect different sets of independent parameters, for the fibre failure

$$A_1 I_1 + B_1 I_1^2 + A_3 I_3 + A_4 I_4 = 1$$

and for the matrix failure

$$A_2 I_2 + B_2 I_2^2 + A_3 I_3 + A_4 I_4 = 1 \quad (2.33)$$

The failure criteria for different failure modes can be expressed as

tensile fibre failure for $\sigma_1 \geq 0$

$$\left(\frac{\sigma_1}{X_t}\right)^2 + \frac{\tau_{12}^2 + \tau_{13}^2}{S_{12}^2} = \begin{cases} \geq 1 & \text{failure} \\ < 1 & \text{no failure} \end{cases}$$

compressive fibre failure for $\sigma_1 < 0$

$$\left(\frac{\sigma_1}{X_c}\right)^2 = \begin{cases} \geq 1 & \text{failure} \\ < 1 & \text{no failure} \end{cases}$$

tensile matrix failure for $\sigma_2 + \sigma_3 \geq 0$

$$\frac{(\sigma_2 + \sigma_3)^2}{Y_t^2} + \frac{\tau_{23}^2 - \sigma_2\sigma_3}{S_{23}^2} + \frac{\tau_{12}^2 + \tau_{13}^2}{S_{12}^2} = \begin{cases} \geq 1 & \text{failure} \\ < 1 & \text{no failure} \end{cases}$$

compressive matrix failure for $\sigma_2 + \sigma_3 < 0$

$$\left[\left(\frac{Y_c}{2S_{23}}\right)^2 - 1\right] \left(\frac{\sigma_2 + \sigma_3}{Y_c}\right) + \frac{(\sigma_2 + \sigma_3)^2}{4S_{23}^2} + \frac{\tau_{23}^2 - \sigma_2\sigma_3}{S_{23}^2} + \frac{\tau_{12}^2 + \tau_{13}^2}{S_{12}^2} = \begin{cases} \geq 1 & \text{failure} \\ < 1 & \text{no failure} \end{cases} \quad (2.34)$$

Further modifications [64, 65] based on these criteria have made the Hashin's criterion to be one of the most widely involved failure criteria in the commercial FEM software.

Chang-Chang Failure Criterion

Chang-Chang failure criterion [66] is based on a progressive damage model and capable of predicting damage in laminates with arbitrary fibre orientations. The failure criterion is proposed by a nonlinear material model with consideration of accumulated damage in laminates.

For the tensile fibre failure, where $\sigma_1 \geq 0$

$$e_f^2 = \left(\frac{\sigma_1}{X_t}\right)^2 + \left(\frac{\tau_{12}}{S_{12}}\right)^2 = \begin{cases} \geq 1 & \text{failure} \\ < 1 & \text{no failure} \end{cases}$$

For the compressive fibre failure, where $\sigma_1 < 0$

$$e_c^2 = \left(\frac{\sigma_1}{X_c}\right)^2 = \begin{cases} \geq 1 & \text{failure} \\ < 1 & \text{no failure} \end{cases}$$

For the tensile matrix failure, where $\sigma_2 \geq 0$

$$e_m^2 = \left(\frac{\sigma_2}{Y_t}\right)^2 + \left(\frac{\tau_{12}}{S_{12}}\right)^2 = \begin{cases} \geq 1 & \text{failure} \\ < 1 & \text{no failure} \end{cases}$$

For the compressive matrix failure, where $\sigma_2 < 0$

$$e_d^2 = \left(\frac{\sigma_2}{2S_{12}}\right)^2 + \left(\frac{\tau_{12}}{S_{12}}\right)^2 + \left[\left(\frac{Y_c}{2S_{12}}\right)^2 - 1\right] \frac{\sigma_2}{Y_c} = \begin{cases} \geq 1 & \text{failure} \\ < 1 & \text{no failure} \end{cases} \quad (2.35)$$

where, e_f , e_c , e_m , and e_d are the history variables for fibre and matrix failures in tension and compression, respectively.

When matrix failure occurs in a layer, the transverse modulus E_2 and Poisson's ratio ν_{12} (ν_{21}) are reduced to zero. However, the longitudinal modulus E_1 is unchanged. For the existence of fibre failure in a layer, the material degradation within the damaged area depends on the size of damage. Both the transverse modulus and Poisson's ratio are reduced to zero, but the degraded longitudinal modulus and shear modulus (G_{12}) are expressed as follow

$$E_1^d = \exp \left[- \left(\frac{A}{A_0} \right)^\beta \right] E_1$$

$$G_{12}^d = \exp \left[- \left(\frac{A}{A_0} \right)^\beta \right] G_{12} \quad (2.36)$$

where, E_1^d and G_{12}^d are the reduced longitudinal and shear modulus, respectively. A is the damage area predicted by the fibre failure criterion, and A_0 is the fibre failure interaction area associated with the measured tensile strength. β is the shape parameter of the Weibull distribution for property degradation.

Chang-Chang failure criterion is capable of assessing the failure modes, damage area, material degradation, residual strength and failure load. Therefore, most commercial FEM software contains the material type associated with this failure criterion. For instance, MAT-54 material model in LS-DYNA used in this project uses Chang-Chang failure criterion and will be described in Section 5.2.3.

2.4 Delamination Initiation and Propagation of Composite Laminates

As has been discussed above, delamination is the dominant failure mode in composite laminates subjected to low-velocity impact and will cause a large reduction in the post-impact compressive strength [4, 10, 13, 14, 67]. The relationship between the delamination area measured from ultrasonic scan and the initial kinetic energy (IKE) of impactor has been documented in many investigations [48, 68-70]. There is however no clear energy threshold for delamination initiation as the delamination size increases with the impact energy. Meanwhile, several studies [10, 13, 14] have indicated that the initiation of delamination can be related to a critical load named as delamination threshold load (DTL). It is believed that the impact will not initiate any delamination if the peak impact force is below the delamination threshold load. Instantaneous delamination will occur when the peak impact load is above the DTL. Therefore, an accurate detection and prediction of delamination initiation is extremely important for the damage characterisation of composite laminates under low-velocity impact.

2.4.1 Experimental Detection of Delamination Initiation

It has been widely reported that the DTL value can be detected through an experimental investigation, assuming the first sudden drop of impact force in the impact force history as the sign of delamination initiation. This sudden load drop is due to the sudden reduction in the

stiffness of laminates under the impactor as a result of the unstable damage development [10, 11].

Sjoblom [25] stated that the overall laminates stiffness was not dramatically affected by the presence of matrix crack during the impact event. But the matrix crack tips may act as the initiation points for delamination that can significantly reduce the stiffness of laminates. Therefore, the sudden load drop in the impact force history can detect the initiation of delamination experimentally.

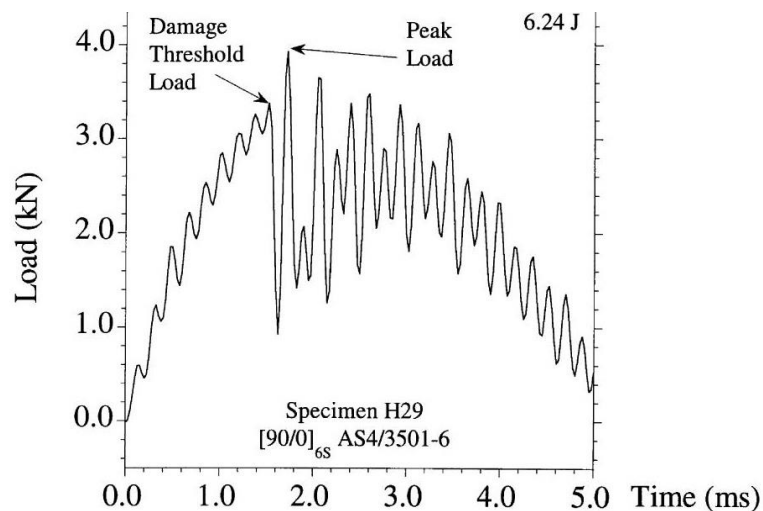


Figure 2.17 Impact force history of a composite laminates subjected to low-velocity impact [14].

Figure 2.17 shows the load history for a 24 ply graphite/epoxy laminates subjected to a 6.24J impact [14]. A clear sudden load drop occurs at around 3.4kN which is lower than the peak impact load of 4.0kN.

Zhang [11] conducted a series of impact tests with a wide range of composite laminates specimens made of Ciba-Geigy 6376C-HTA carbon fibre prepreg. The specimens have three different plate thicknesses, two different plate sizes, and simply supported and clamped boundary conditions. The damage area measured by the ultrasonic scan is plotted against the incident energy and the impact force as shown in Figure 2.18. The test results proved the existence of a threshold load, but not threshold energy for the initiation of delamination. The test results suggest that DTL value is an intrinsic property of composite laminates dominated by the laminates thickness, and independent of the laminates size and boundary condition.

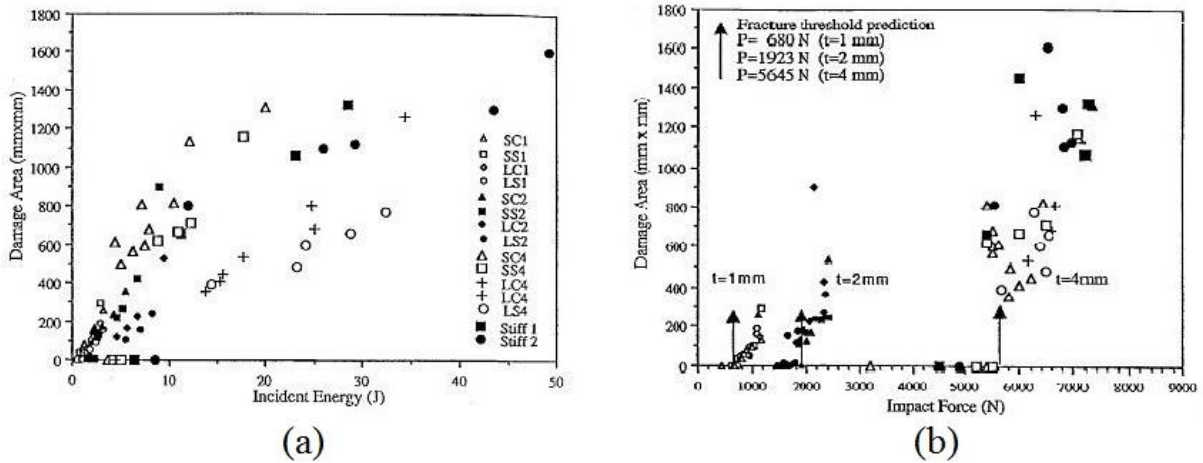


Figure 2.18 (a) Damage area vs. incident energy, and (b) damage area vs. impact force for a large number of composite laminates with different thicknesses, plate sizes, and support conditions [11].

Davies *et al.* [71] obtained similar results in their impact tests conducted on the woven fabric glass/polyester laminates specimens with different thicknesses and sizes. They also suggested that the damage force map was not only effective in detecting the delamination initiation, but also in monitoring the delamination propagation.

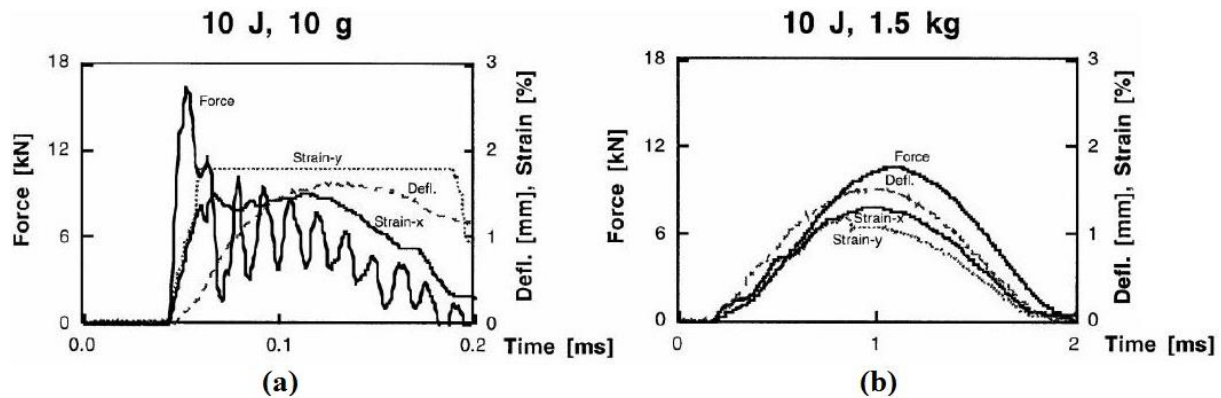


Figure 2.19 Impact force histories of composite laminates caused by (a) the small mass impactor and (b) the large mass impactor under same impact energy level [72].

However, Olsson [13, 72-74] indicated that the laminates size and boundary condition affected the response of composite laminates as shown in Figure 2.19. Figure shows that the accurate detection of delamination initiation through experimental approach is dependent on the contact duration which is dominated by different contact response models. The detailed contact response models will be discussed in Section 2.5.1.

2.4.2 Analytical Prediction on Delamination Threshold Load

The delamination threshold load of composite laminates can also be predicted through an analytical approach. An empirical relation between delamination threshold load and laminates thickness was suggested by Schoeppner *et al.* [14] using approximately 500 low-velocity impact force histories from the Air Force Research Laboratory (AFRL) low-velocity impact database and is expressed as follows

$$DTL = C t^{3/2} \quad (2.37)$$

where, C is a curve fit coefficient determined by the impact curves; t is the laminates thickness. Equation 2.37 indicates that the DTL for the initial delamination is proportional to $t^{3/2}$.

Sjoblom [75] predicted the similar trend by proposing a simple material strength model including several more parameters governing the critical force

$$P_{cr} = (2\pi\tau_{max} t)^{3/2} d^{3/4} k_C^{-1/2} \quad (2.38)$$

where, P_{cr} is the critical impact force, τ_{max} is the transverse shear strength, d is the diameter of a spherical impactor, and k_C is the contact stiffness determined by a Hertz contact law based contact model. The detailed contact model will be reviewed in Section 2.5.3.

Davies and Zhang [10, 11] proposed a fracture mechanics based model by introducing the critical energy release rate in mode II, G_{IIC} , at the boundary of a central circular delamination [27] to predict the threshold load. In their model, the quasi-isotropic laminate was simplified as isotropic; and the through-thickness-distributed delamination was idealized to a single mid-plane delamination with an axisymmetric circular shape. The critical impact force, P_{cr} , for a quasi-isotropic laminate is given by

$$P_{cr}^2 = \frac{8\pi^2 E_f t^3 G_{IIC}}{9(1-\nu^2)} \quad (2.39)$$

where, E_f and ν are the flexural modulus and Poisson's ratio, respectively. It is worth noticing that the critical force predicted by Equation 2.39 is independent of the delamination size since the radius of the axisymmetric circular delamination is not considered in the prediction. This scenario indicates that the delamination would occur at the threshold load, but the induced delamination area would still be indeterminate.

Olsson *et al.* [13] further developed the prediction by considering the delamination through thickness, which is defined as

$$F_{dn_d}^{\text{stat}} = \pi \sqrt{\frac{32DG_{IIC}}{n_d+2}} \quad (2.40)$$

where, D is the bending stiffness of composite laminates, n_d is the number of delamination interfaces. When the value of n_d is equal to 1, the current prediction is equivalent to the prediction suggested by Davies and Zhang [10, 11].

Gonzalez and co-workers [76] proposed a modified prediction considering the layer clustering effect in composite laminates, which is

$$F_{dn_d^*}^{\text{stat}} = 4\pi\sqrt{2D^*G_{IIC}} \left(-1 + \frac{t^3}{(t-n_d^*t_p)^3 + n_d^*t_p^3} \right)^{-1/2} \quad (2.41)$$

where, n_d^* is the number of delamination interfaces starting from the back face of laminates, D^* is the effective bending stiffness of an orthotropic laminates, and t_p is the clustering thickness including the thickness of layers with the same fibre orientation. They suggested that the layer clustering effect may lower the damage resistance of composite laminates under low-velocity impact. The reduction in threshold load is attributed to the decreased number of interfaces with different fibre orientations where delamination is expected to occur. Consequently, larger delamination areas may be introduced into fewer interfaces by higher interface shear stress between different layer groups due to bigger bending stiffness mismatch.

2.4.3 Numerical Simulation of Delamination

Over the years, extensive efforts have been made in simulating the initiation and propagation of delamination in composite laminates. Finite element analysis (FEA), as the most extensively used method, shows great capability to simulate the delamination when it has been applied properly.

Tay [77] reviewed the development in simulating delamination employing FEA method from 1990 to 2001. Several advanced models and elements, which can speed up FEA computations, are described with their advantages and applications. Among these analytical advances, the tie-break interface contact and cohesive zone element method are the most commonly used approaches to simulate the delamination in composite laminates.

Borg *et al.* [78] suggested the initiation and propagation of delamination could be simulated by monitoring the force-displacement relation between pairs of coincident nodes employing the stress based tie-break interface contact. In the FEA method, the delamination path is restricted to a presumed adhesive interface; the coincident nodes along the interface are used to initially tie the material on each side of the interface. The principle of tie-break contact is shown in Figure 2.20.

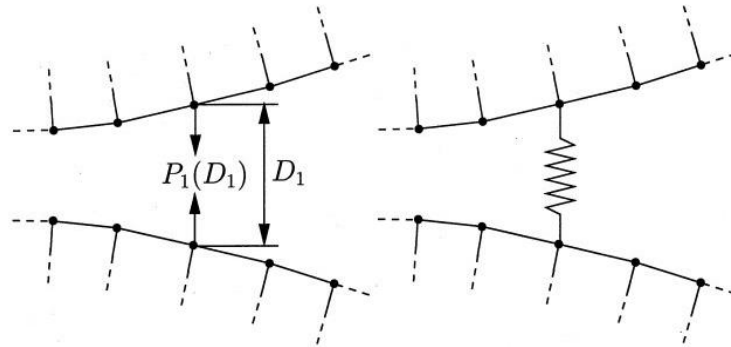


Figure 2.20 Schematic illustration of the tie-break interface contact in normal direction [78].

The linear elastic fracture mechanics (LEFM) based penalty formulation associated with the interface contact is

$$P_i = K_{ij} D_j \quad (2.42)$$

where, P_i and D_j are the adhesive nodal force in i -direction and the relative distance between the two coincident nodes, respectively. K_{ij} is the penalty stiffness, which is only valid up to a maximum adhesive force. The delamination will be propagated when the limitation is exceeded.

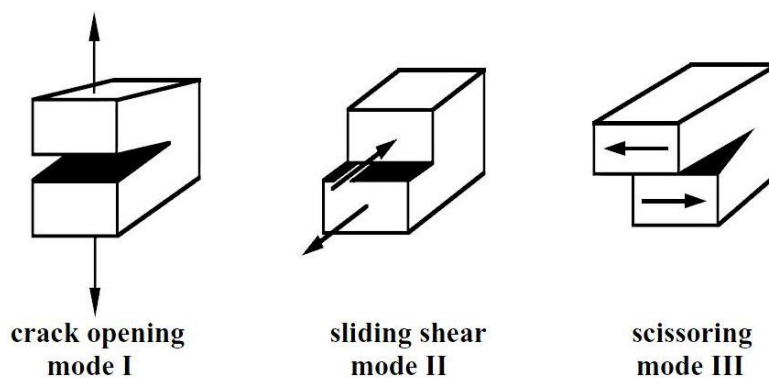


Figure 2.21 Schematic illustration of three delamination fracture modes [79].

It is worth noting that delamination can be caused by a combination of three basic fracture modes shown in Figure 2.21. Mode I opening is caused by the peel stress, while modes II and III deformations are driven by the interlaminar shear stresses [79]. The penalty stiffness, K_{ij} , in Equation 2.42 should therefore be a diagonal matrix which complies with the interpretation of the penalty formulation as three orthogonal springs [78].

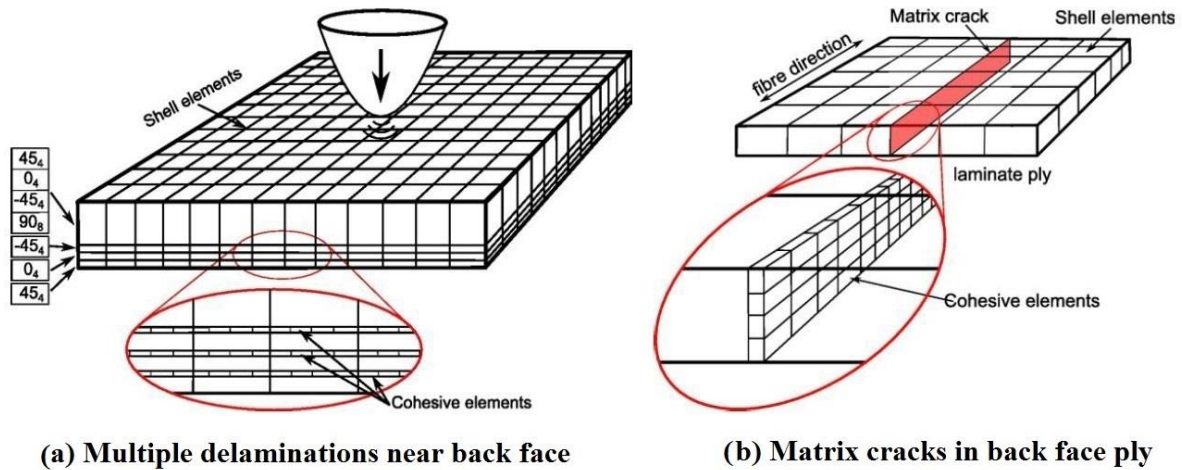


Figure 2.22 Cohesive element pre-inserted positions in the practical simulation model [12].

The cohesive zone model (CZM) is firstly proposed by Hillerborg *et al.* [80] in order to predict the delamination in composite laminates. The cohesive zone model treats delamination as a gradual phenomenon in which the separation takes place across the extended cohesive zone with the adhesive traction force. The cohesive zone element does not represent any physical material. It is used to determine the cohesive forces induced by the separation of material elements [81]. The cohesive zone element can be inserted between layers with different fibre orientations to simulate the interface delamination as shown in Figure 2.22(a), and placed within the lamina plane to simulate the in-plane matrix crack as shown in Figure 2.22(b) [12].

It is noticed that the initiation and propagation of delamination can be simulated by the cohesive zone model which employs traction-separation law, although uncertainties exist in the sensitivity of simulation results to the traction-separation law [82, 83].

Figure 2.23 illustrates the principle feature of a cohesive zone model [84]. The adhesive stress increases to its maximum while the crack tip approaches the end of the cohesive zone; and the adhesive stress is a simple function of opening gap, D , inside the cohesive zone

$$\sigma_c = \sigma(D) \quad (2.43)$$

The adhesive stress is zero when the crack is fully open.

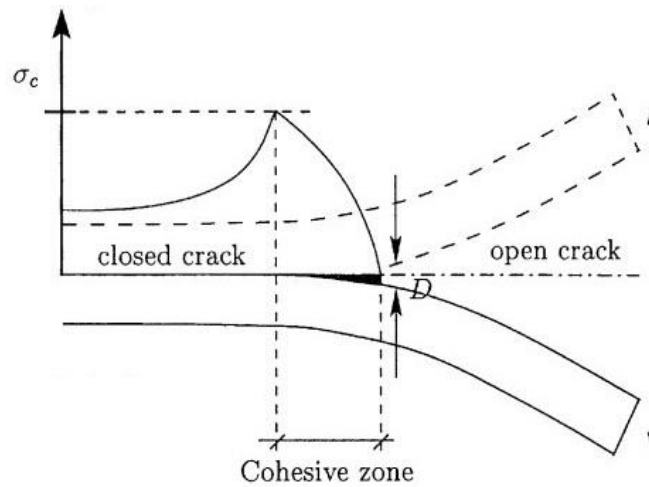


Figure 2.23 Principle of the cohesive zone model [84].

Various traction-separation laws are available in literatures and can be classified into bilinear [85-87], trapezoidal [88], parabolic [89], and exponential [90, 91]. Aymerich *et al.* [85] proposed a popular bilinear traction-separation law under mode I and mode II/III as illustrated in Figure 2.24 to simulate multiple delaminations in cross-ply laminates.

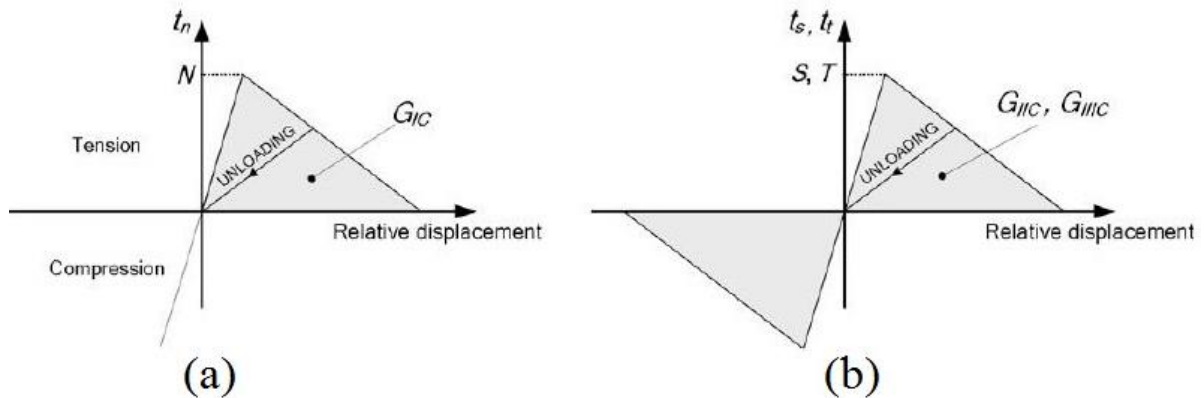


Figure 2.24 Traction-separation law for mode I (a) and mode II/III (b) fractures [85].

In this bilinear cohesive law, the normal (mode I) and the tangential (mode II/III) adhesive tractions are related to the corresponding separation, or the relative displacement, between the upper and lower cohesive surfaces. This implies that the area under the traction-separation curve can be considered as the energy required to delaminates the cohesive interface. As illustrated in Figure 2.24, an initial linear increasing stage is included in the traction-

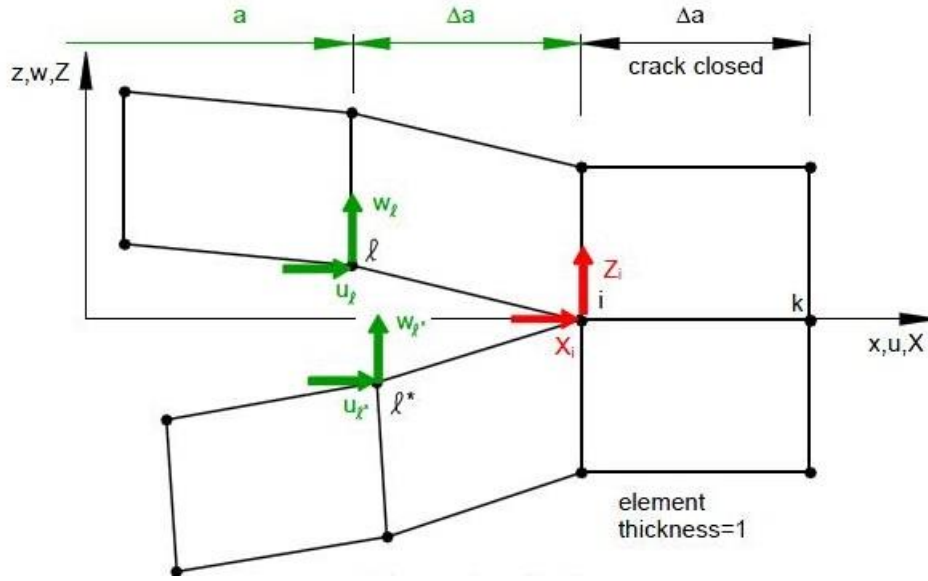


Figure 2.26 Virtual crack closure technique for the 2D four-node elements model [93].

The energy release rates in mode I and mode II, G_I and G_{II} , are calculated for the 2D model with 4-node elements as shown in Figure 2.26

$$G_I = -\frac{1}{2\Delta a} \cdot Z_i \cdot (w_\ell - w_{\ell^*}) \quad \text{and} \quad G_{II} = -\frac{1}{2\Delta a} \cdot X_i \cdot (u_\ell - u_{\ell^*}) \quad (2.45)$$

where, w_ℓ , u_ℓ , w_{ℓ^*} , and u_{ℓ^*} are the nodal displacements at the nodal point ℓ in the upper crack face and nodal point ℓ^* in the lower crack face, respectively.

Therefore, the total energy release rate, G_T , is calculated from the individual mode components as

$$G_T = G_I + G_{II} + G_{III} \quad (2.46)$$

where, G_{III} can be obtained in a similar way to G_{II} based on a 3D analysis. G_{III} is zero for the 2D analysis.

The critical strain energy release rate, named as fracture toughness, can be determined by an experimental approach. The pure mode I fracture toughness, G_{IC} , can be determined by the double cantilever beam (DCB) test [95] as illustrated in Figure 2.27(a). The pure mode II fracture toughness, G_{IIC} , can be obtained using 3 or 4 points end-notched flexure (ENF) tests [96-98] as illustrated in Figure 2.27(b) & Figure 2.27(c). The mixed-mode I/II fracture toughness, $G_{IC/IIIC}$, can be measured from mixed-mode bending (MMB) test [99] as illustrated

in Figure 2.27(d). If the pure mode III fracture toughness, G_{IIIc} , is required, the edge-cracked torsion (ECT) test [100, 101] can be used.

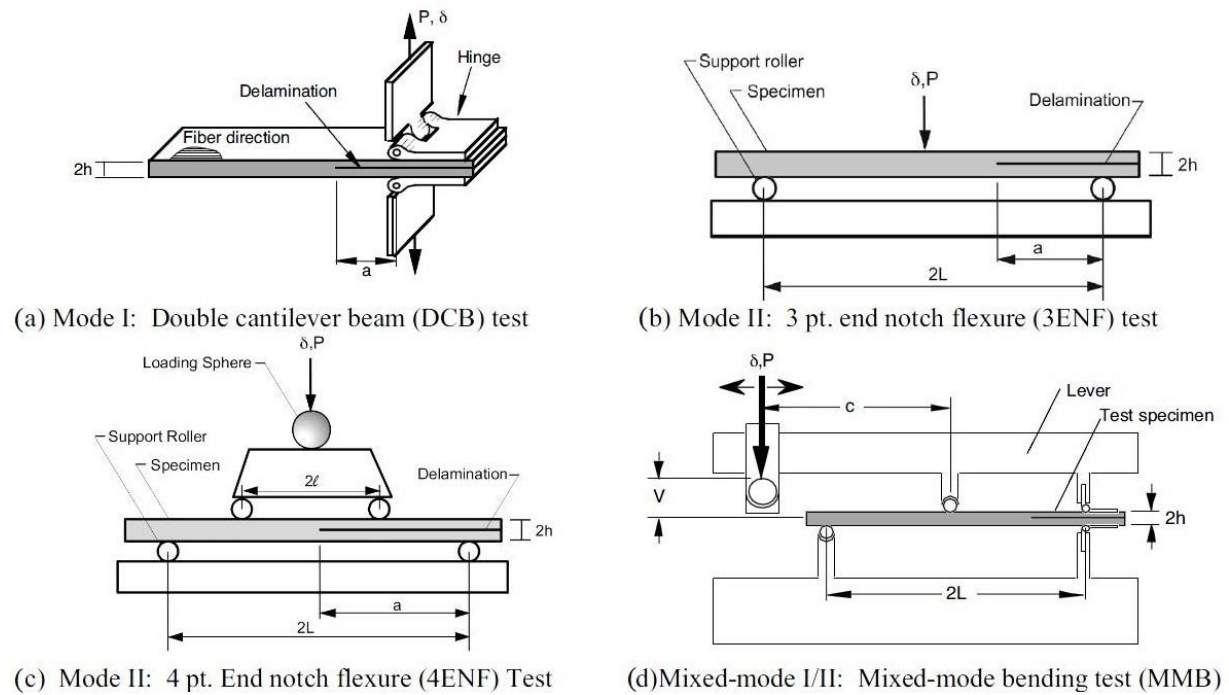


Figure 2.27 Methods to determine the critical strain energy release rates [94].

Cohesive zone model has been employed by numerous applications to simulate the delamination in composite laminates. Zhang et al. [12] developed a numerical model using cohesive element to predict the low-velocity impact induced force and damage in composite laminates. The cohesive element is governed by a bilinear traction-separation law with the introduction of a new contact stiffness spring alongside the cohesive stiffness spring in the model to account for the frictional force between the contact pair as shown schematically in Figure 2.28. The low-velocity impact event is modelled as a quasi-static indentation case to save the computation cost. The similarity between the LVI and QSI has been observed and will be reviewed in details in Section 2.5.2.

Hadavinia *et al.* [81, 102] carried out researches to predict the delamination of impacted composite structures by numerical simulation approach. Different models, including thick shell elements with cohesive interface, solid elements with cohesive interface and thin shell element with tiebreak contact, are developed. The FEA results in terms of force and energy show good correlations to the experimental test results in literature. It is however noticed that the numerical simulation results are strongly influenced by several parameters, in particular, the element size, the number of shell sub-laminates and the contact stiffness scale factor.

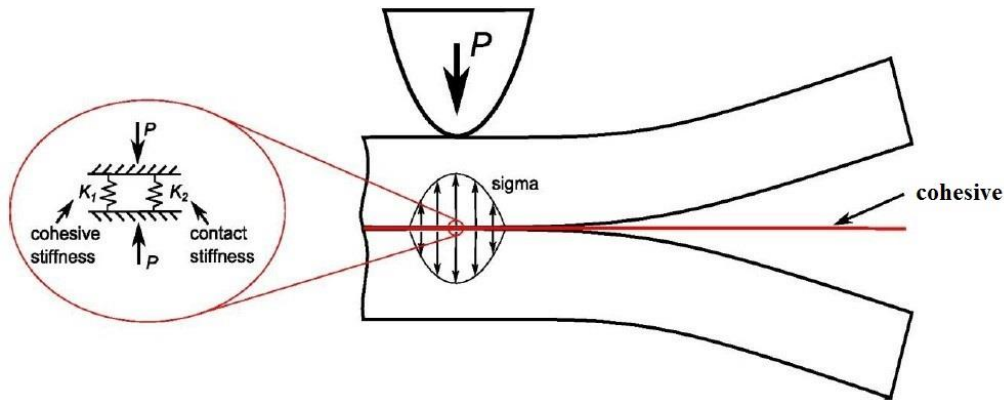


Figure 2.28 Relationship between the cohesive element and the frictional contact [12].

Heimbs and his colleagues [39, 103] predicted the low-velocity impact response of compressively pre-loaded composite laminates using a cohesive element model with the commercial explicit finite element code LS-DYNA. The prediction shows a good agreement with the experimental data in terms of force/energy plots and the evaluated damage profile. Similar to the work of Hadavinia *et al.* [81, 102], simulation results are strongly dependent on the simulation parameters, which adds the complexity of FE simulation of impact damage of composite laminates under low-velocity impact.

2.5 Composite Laminates under Quasi-static Indentation

A number of studies [25, 49, 104, 105] have indicated that the low-velocity impact and quasi-static indentation cause a similar contact response of composite laminates in terms of the induced damage and the residual strength. In most cases, the low-velocity impact introduced by a large mass impactor can be treated as a quasi-static indentation event [72, 74]. As a result, the contact response of composite laminates under QSI has been investigated in order to achieve a comprehensive understanding of the damage mechanisms in composite laminates. The application of the quasi-static indentation test method to study the low-velocity impact event has been proved to be popular and successful due to the simplicity and reliability in obtaining required results from the easily controlled quasi-static indentation process.

2.5.1 Contact Models of Composite Laminates

The structural models for contact events between composite laminates and foreign objects, which are used to simulate the motion of the projectile, the dynamics of the target, and the

local indentation in the contact zone, are the fundamental for understanding the contact response and predicting the induced damage [106]. A number of contact models to characterise the responses of composite laminates are available in the literature.

Olsson [72-74] suggested that the contact response of composite laminate was governed by the impactor-plate mass ratio, not the impact velocity. It is explained by the fact that different contact durations may generate different contact responses of composite laminates as illustrated in Figure 2.29.

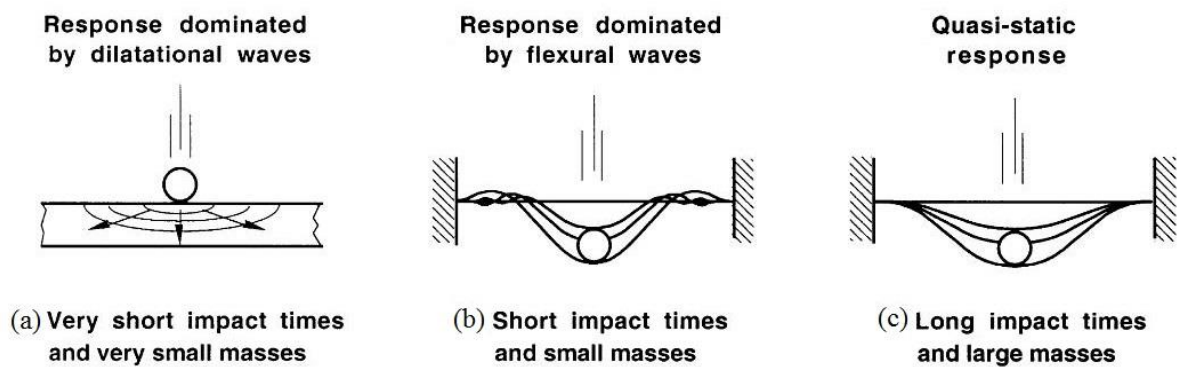


Figure 2.29 Schematic illustration of the classification of contact responses [74].

An impactor with very small mass and contact time causes a ballistic response dominated by through-the-thickness wave propagation as shown in Figure 2.29(a). An impactor with moderately small mass and contact time causes a small mass response dominated by shear and flexural waves as shown in Figure 2.29(b). An impactor with much larger mass than the mass of the target plate and much longer contact time than the time needed by shear and flexural waves to reach the boundaries of the target plate causes a quasi-static response dominated by the lowest natural frequency of the structure as shown in Figure 2.29(c).

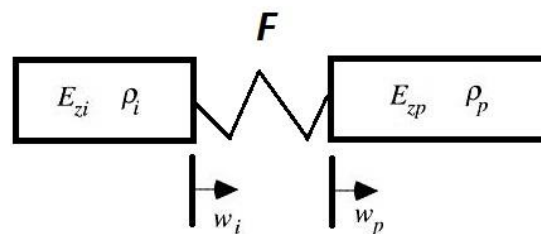


Figure 2.30 Schematic illustration of the one-dimensional contact model for a ballistic response [72].

It is reported that the ballistic response is not influenced by the plate size and boundary conditions, and the corresponding damage is easily detectable in most cases. Olsson [72] proposed a simplified one-dimensional contact model as shown schematically in Figure 2.30 to predict the ballistic response.

The contact force, F , and the relative displacement, α , are related as

$$F = K_\alpha \alpha^q = K_\alpha (w_i - w_p)^q \quad (2.47)$$

where, w_i and w_p are the impactor mass centre displacement and laminates back-surface deflection, respectively. The constant, q , is equal to $3/2$ according to the Hertz theory of contact between the composite plate and a hemispherical indenter. K_α is the contact stiffness, which is derived by

$$K_\alpha = \frac{4}{3} Q_\alpha \sqrt{R}$$

where, R is the radius of the indenter tip; and Q_α . The effective out-of-plane stiffness is given by

$$Q_\alpha = \frac{Q_{zp}Q_{zi}}{Q_{zi}+Q_{zp}} \quad \text{and} \quad Q_z = E_z/(1 - \nu_{rz}\nu_{zr})$$

where, indexes i and p refer to the indenter and plate; E and ν are Young's modulus and Poisson's ratio, respectively.

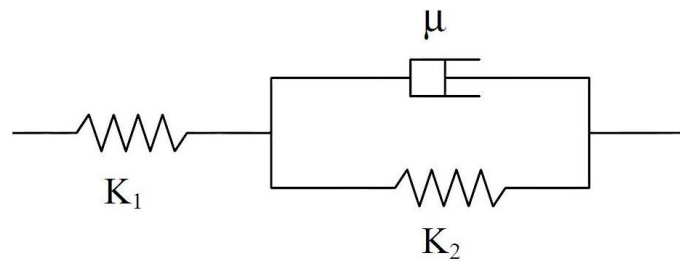


Figure 2.31 Schematic illustration of the three-element spring-dashpot contact model for a ballistic response [107].

Lim *et al.* [107] proposed a three-element contact model to characterise the ballistic response, including two Hooke springs and a Newtonian dashpot as shown schematically in Figure 2.31.

The stress-strain relation of the ballistic contact model is described by

$$\left(1 + \frac{K_2}{K_1}\right) \sigma + \frac{\mu}{K_2} \dot{\sigma} = K_2 \varepsilon + \mu \dot{\varepsilon} \quad (2.48)$$

where, K_1 , K_2 , and μ are the semi-empirically derived constants of the springs and the dashpot, respectively. σ is the stress. ε and $\dot{\varepsilon}$ are the strain and strain rate, respectively. Good correlation of the analytical prediction to the experimental data is achieved, in terms of the ballistic limit, residual velocity, energy absorption and transverse deflection of the laminates [107].

More efforts have been focused on the contact models of other response types, including the small mass response and large mass response since the damage caused by these responses is difficult to detect. The small mass response is governed by flexural and shear waves with no input from the boundary condition as the impact finishes before the stress wave reaches the boundary of the plate. Figure 2.32 shows a contact model proposed by Olsson [72, 73] for a small mass response.

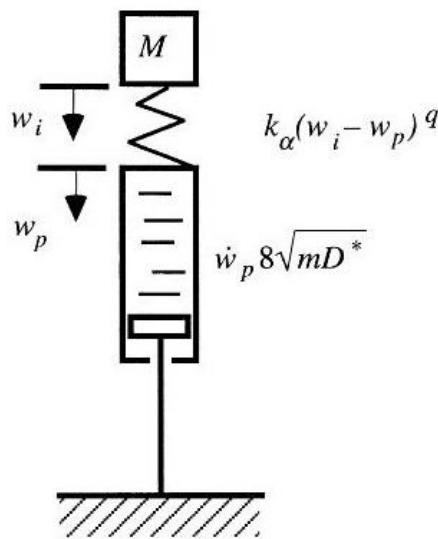
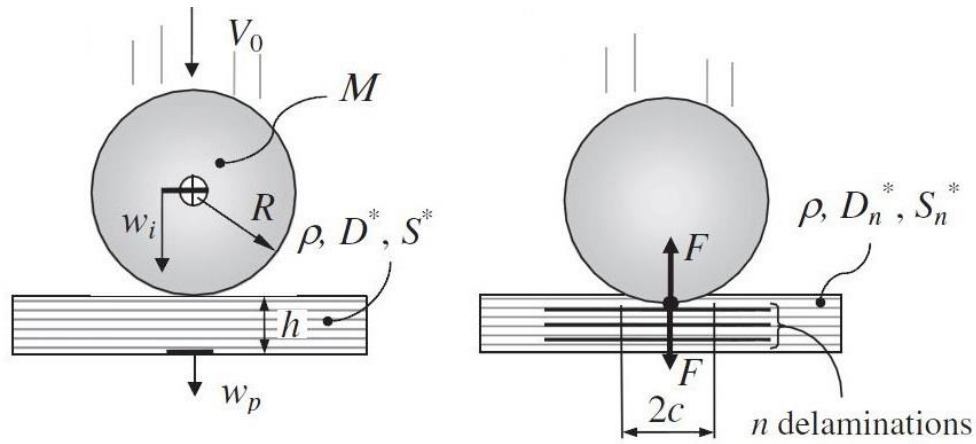


Figure 2.32 Schematic illustration of the contact model for a small mass contact response [72].

In this model, the plate mass per unit area, m , and the effective bending stiffness of the orthotropic laminates, D^* , are introduced to account for the propagation wave effect. The plate effective stiffness is approximately determined by

$$D^* \approx \sqrt{D_{11}D_{22}(A + 1)/2} \quad \text{where, } A = (D_{12} + 2D_{66})/\sqrt{D_{11}D_{22}} \quad (2.49)$$



(a) contact model before indentation (b) contact model during indentation

Figure 2.33 Schematic illustration of impactor (a) before and (b) during indentation of a plate [73].

In Olsson's recent paper [73], the small mass contact model is further developed to account for the effect of the delamination as illustrated in Figure 2.33. The effective bending stiffness of an orthotropic laminates with n delaminations, D_n^* , is defined as

$$D_n^* = D^*/(n + 1)^2 \quad (2.50)$$

and the effective shear stiffness of an orthotropic laminates with n delaminations, S_n^* , defined as

$$S_n^* = S^* \quad \text{where,} \quad S^* \approx KG_{rz}h$$

where, K is the shear factor of the laminates and is $\approx 5/6$ for homogeneous plates. The shear stiffness is therefore independent of the delamination. The delamination size, load, and deflection history can be predicted by the small mass contact model.

The large mass contact response, as a quasi-static contact event, occurs when the impactor mass is more than one quarter of the plate weight [72]. It has been experimentally demonstrated that the large mass impactor causes a relatively smaller contact load and a significantly smaller damage than small mass impactor with the same initial energy. Moreover, the load and the deflection are more or less in phase in the contact response of a quasi-static contact, while they are out of phase during a small mass contact as shown in Figure 2.34 [72].

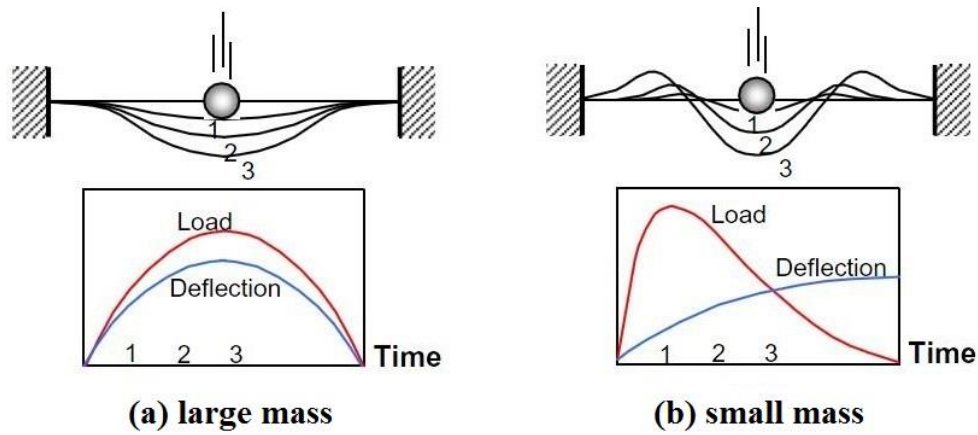


Figure 2.34 Comparison between (a) large mass and (b) small mass contact responses [73].

Shivakumar [108] proposed a two degree-of-freedom spring-mass model for the large-mass contact response considering the shear and membrane effects as shown schematically in Figure 2.35.

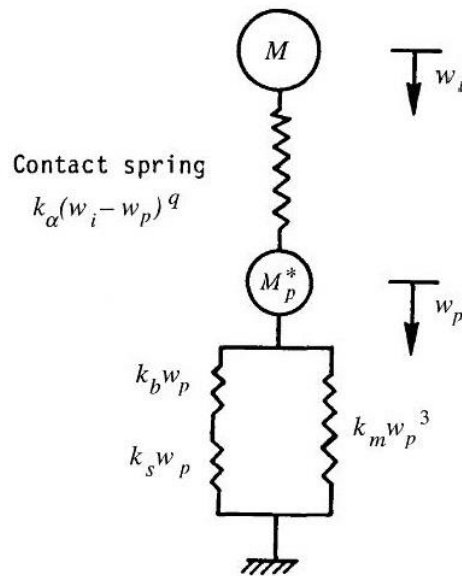


Figure 2.35 Schematic illustration of the contact model for a large mass contact response [108].

M is the indenter mass. M_p^* is the effective plate mass, which is taken as one-fourth of the total mass of the plate. There is a Hertz contact law based spring to connect those two masses. The bending stiffness, k_b , the shear stiffness, k_s , and membrane stiffness, k_m , are also introduced in the model to generate the forces induced by the bending, shear, and membrane

deformations of the plate, respectively. However, the material damping, plate damage, and surface friction are not considered in the model.

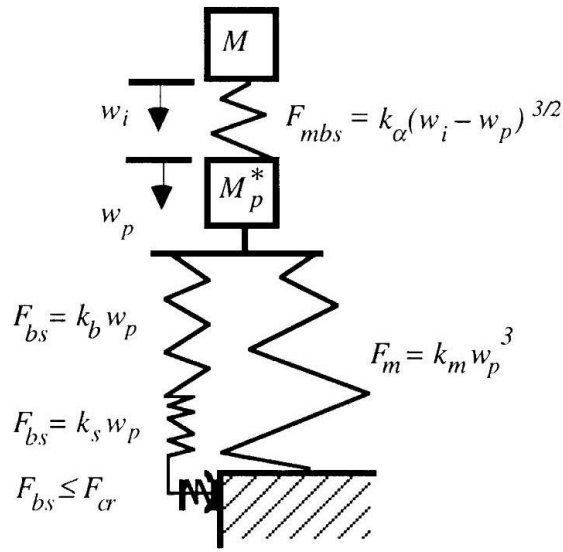


Figure 2.36 Schematic illustration of the modified contact model of a large mass contact considering delamination in the plate [74].

Olsson [74] proposed a modified contact model with the consideration of the reduced bending stiffness caused by delamination. The modified model as shown in Figure 2.36 is suitable for the case, in which the plate is unable to support a load larger than the delamination threshold load, F_{cr} , given by Equation 2.40.

The total load on the plate, F_{mbs} , is the sum of the bending and shear contribution load, F_{bs} , and the membrane load, F_m ,

$$F_{mbs} = F_m + F_{bs} \quad (2.51)$$

where,

$$F_m = k_m w_p^3 \quad \text{and} \quad F_{bs} = k_{bs} w_p \leq F_{cr}$$

where,

$$\frac{1}{k_{bs}} = \frac{1}{k_b} + \frac{1}{k_s}$$

In general, the large mass low-velocity impact on composite laminates can be treated as a quasi-static indentation event due to the similar contact response. The detailed researches on

the similarity between the contact responses of composite laminates under LVI and QSI will be reviewed in the next section.

2.5.2 Similarity between Contact Responses of Composite Laminates under LVI and QSI

Brindle and Zhang [109] compared the reaction force versus deflection curves of a 32-ply quasi-isotropic composite laminates by conducting low-velocity impact tests (at impact energy of 20J and 30J) and a quasi-static indentation test. The QSI and LVI test results agree well as shown in Figure 2.37. The sudden load drop, which represents the initiation of damage, and the ultimate load, which represents the catastrophic damage, can be both obtained from the LVI and QSI test results with an engineering application acceptable difference (less than 15%). Thus, the similarity between the low-velocity impact and quasi-static indentation in terms of the damage characterisation has been proved.

Kaczmarek *et al.* [104] conducted a comparative study of the damage detected by a ply-by-ply ultrasonic scan method on a quasi-isotropic composite laminates after a quasi-static indentation and a low-velocity impact, respectively. The delamination areas are plotted against the maximum force as shown in Figure 2.38.

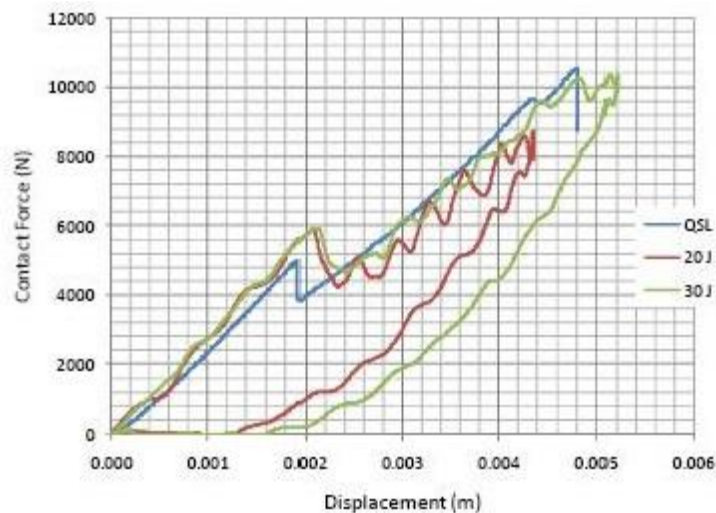


Figure 2.37 Comparison of indentation and impact force vs. displacement relations [109].

Similar delamination growth behaviours were observed under the two loading modes. Both tests were capable to capture two important features of the response of the laminates to the contact force: delamination threshold and fact damage propagation threshold. The damage

area vs. maximum contact force relations are in good agreements, especially within the relative lower maximum force region where the delamination initiated.

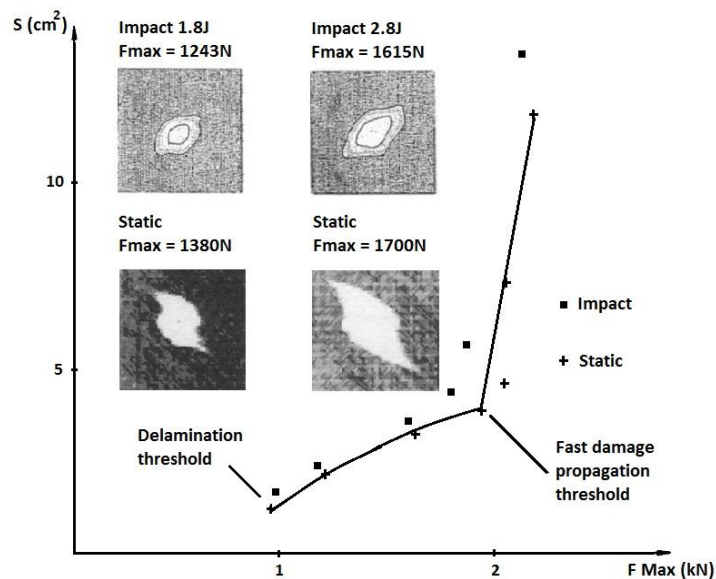


Figure 2.38 Comparison of the impact and indentation induced delamination area vs. maximum force relations [104].

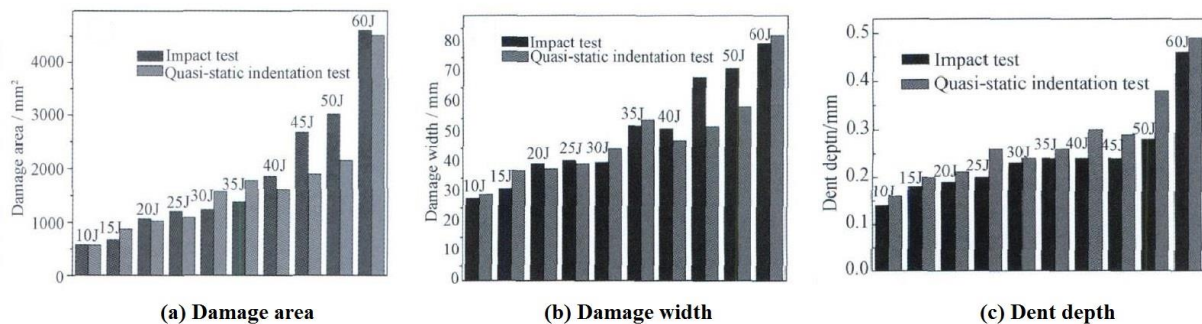


Figure 2.39 Comparison of the impact and indentation tests in relationships between load level and (a) damage area, (b) damage width, and (c) dent depth [110].

Yan *et al.* [110] carried out a series of QSI and LVI tests on the foam core sandwich composites, in order to determine the relationships between load level and various damage parameters including the damage area as shown in Figure 2.39(a), damage width as shown in Figure 2.39(b), and dent depth as shown in Figure 2.39(c). A good correlation of the test results between QSI and LVI tests has been established, although the correlation of damage area and damage width to load level is not as good as the correlation of dent depth to load level. This indicates that the dent depth can be the most suitable damage parameter when the LVI test is replaced by the QSI test to investigate the impact response of composite laminates

under low-velocity impact. The quasi-static indentation test can be used as an alternative to investigate the low-velocity impact damage mechanisms of composite laminates.

Chen *et al.* [111] conducted detailed studies on using the dent depth as a damage parameter to characterise the failure mechanisms of composite laminates subjected to static indentation. The knee point phenomenon in the variation of dent depth against the indentation force is obvious as shown in Figure 2.40. Before the knee point, the dent depth increases slowly and almost linearly. Once the knee point is reached, or the indentation force exceeds a certain load, a sharp increase in dent depth is observed. This rapid increase in dent depth is attributed to the fibre breakage. After the plastic failure occurred in the resin near the contact surface, the brittle fibre will lose the protection provided by the relatively ductile resin.

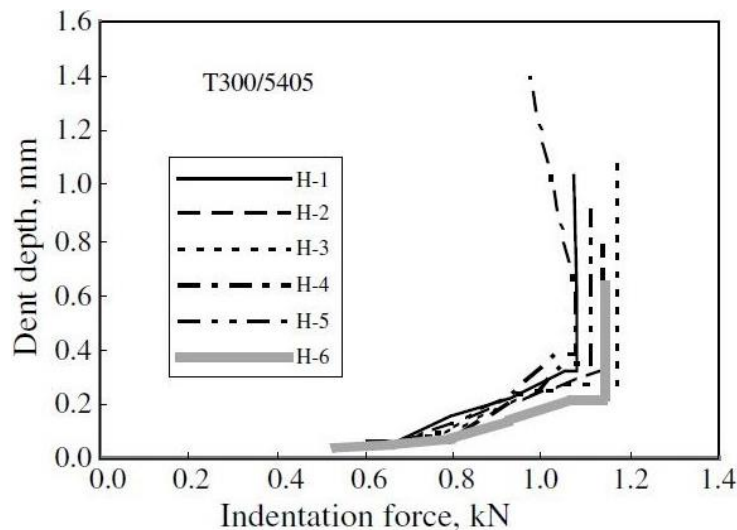


Figure 2.40 Knee point phenomenon in variation of dent depth vs. indentation force [111].

In one word, the similarity between contact responses of composite laminates under low-velocity impact and quasi-static indentation has been established, especially for the damage characterisation. Therefore, the quasi-static indentation method can be used to represent the low-velocity impact event in most cases. This will save the research cost and obtain some important data efficiently and accurately. The dent depth, as the key damage parameter, is closely linked to the contact force in the characterisation of the damage mechanisms of composite laminates. Contact law plays a key role in the study of contact behaviour of composite laminates under QSI and will be reviewed in the next section.

2.5.3 Contact Laws of Composite Laminates under QSI

The Hertz contact law [112] is a classic contact theory to characterise the contact behaviour between homogeneous isotropic bodies. A variety of modifications has been made in order to extend the application of the classic contact law to composite laminates.

Yang and Sun [113] proposed one of the most widely used contact laws based on the Hertz contact theory to solve the contact problems between a composite laminates and a rigid sphere indenter. The modified contact law is expressed as

$$F = k_C \alpha^{1.5} \quad (2.52)$$

where, F is the contact force, α is the contact indentation, and the Hertz contact stiffness, k_C , is approximated by

$$k_C = \frac{4}{3} \sqrt{R} E_3$$

where, E_3 is the Young's modulus of the upper layer in the thickness direction, and R is the radius of the rigid spherical indenter. In Yang and Sun's contact law, it is assumed that the material remains to be linear elastic; even if the permanent deformation has been introduced into the contact zone at relatively low contact forces [4]. Further, the laminates thickness effect has not been taken into account by the current contact law since the isotropic modulus of elasticity is replaced by the orthotropic modulus in the thickness direction.

Turner [114] proposed a modified contact law for transversely isotropic materials, such as the quasi-isotropic composite laminates, by replacing the isotropic modulus with a combination of the transversely isotropic properties. Thus relationship between the contact force and the contact indentation is expressed as

$$F = \frac{4\sqrt{R}E_{TI}^*}{3} \alpha^{1.5} \quad (2.53)$$

where, E_{TI}^* is the effective modulus of transversely isotropic material. The effective modulus E_{TI}^* and contact stiffness, k^* , are derived as follows

$$E_{TI}^* = \frac{2}{\alpha_1 \alpha_3} \quad \text{and} \quad k^* = \frac{4}{3} \sqrt{R} E_{TI}^* \quad (2.54)$$

where,

$$\alpha_1 = \sqrt{\frac{E_x/E_z - \nu_{xz}^2}{1 - \nu_{xy}^2}}, \alpha_2 = \frac{1 + (E_x/2G_{xz} - 1) - \nu_{xz}(1 + \nu_{xy})}{1 - \nu_{xy}^2}, \text{ and } \alpha_3 = \frac{1 - \nu_{xy}}{G_{xy}} \sqrt{\frac{\alpha_1 + \alpha_2}{2}}$$

where, E_x , E_z , G_{xy} , G_{xz} , ν_{xy} , and ν_{xz} are the three-dimensional effective constants of transversely isotropic material. Therefore, the effective modulus of the quasi-isotropic composite laminates can be determined if the three-dimensional effective elastic parameters are available.

However, the prediction of the modified Hertz contact law may still deviate considerably from the experimental results, especially for the cases with relatively large indentations. It is reasonable to ascribe such deviations to the drawbacks of the Hertz contact law since the original theory is only valid for the elastic half-space entity, not for the anisotropic plate with finite thickness. Chen *et al.* [115] modified the Hertz contact law by involving the global deflection in the contact model to consider the thickness effect as shown in Figure 2.41.

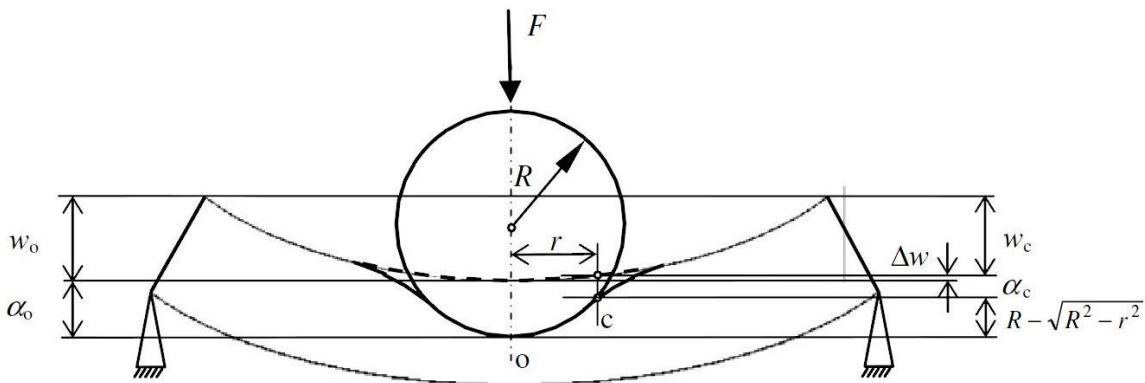


Figure 2.41 Schematic illustration of the contact between a composite plate and a rigid sphere indenter [115].

The geometrical relationship of deformation in the contact region is expressed as

$$\Delta w + \alpha_o = \alpha_c + R - \sqrt{R^2 - r^2} \quad \text{and} \quad \Delta w = w_o - w_c \quad (2.55)$$

where, subscribes o and c refer to the initial contact point, o, and the contact point, c, at the boundary of the contact area, respectively. w_o , w_c , α_o , and α_c are the global plate deflections and the indentation depth of the two points o and c, respectively. R is the indenter radius, r is the radius of the contact area, and Δw is the deflection difference between the two points.

It is further assumed that the contact force and the indentation follow the same mathematical formation as the Hertz contact law. The above contact model can be transformed into the

contact model including the half-space. Therefore, the relationship between the contact force and the indentation for model illustrated in Figure 2.42 is derived as

$$F = k^* \alpha_o^{*1.5} \quad (2.56)$$

where, k^* is the contact stiffness of the half-space, which can be determined by Equation 2.54. α_o^* is the centre indentation of the corresponding half-space, which is equal to the sum of the deflection difference between the two points, Δw , and centre indentation depth, α_o . Therefore, the deflection difference, Δw , is proved to be the key factor dominating the contact force predictions.

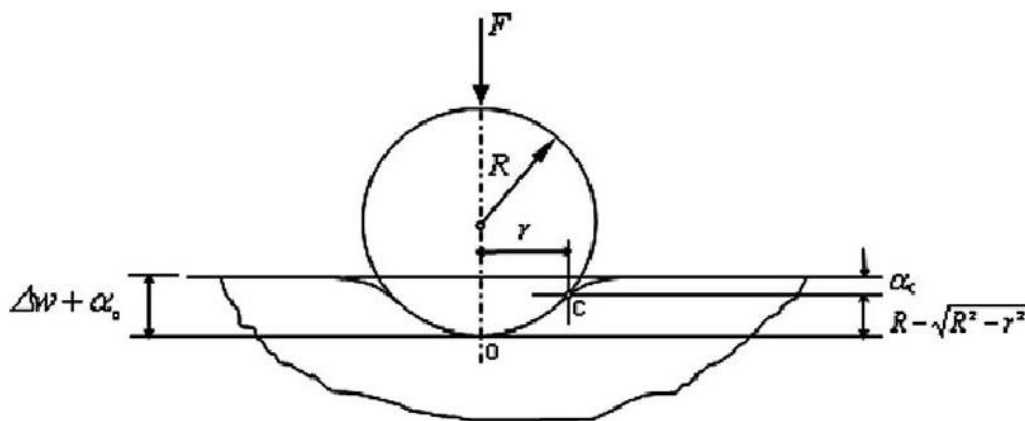


Figure 2.42 Schematic illustration of the contact between a half-space and a rigid sphere indenter [115].

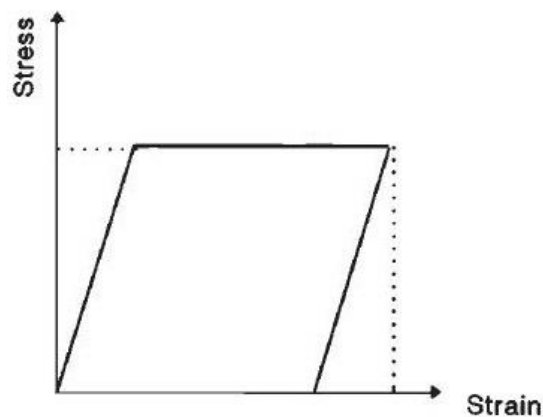


Figure 2.43 Stress-strain relation for the elastoplastic analysis [4].

In addition to these Hertz contact law based predictions, the contact law with elastoplastic model is an alternative approach to predict the contact behaviour of composite laminates. The elastoplastic contact law is based on the following rules: (1) the material behaves elastically

until the indentation exceeds a critical value; (2) the material behaviour in the transverse direction is governed by the stress-strain behaviour of the matrix as illustrated in Figure 2.43. [4].

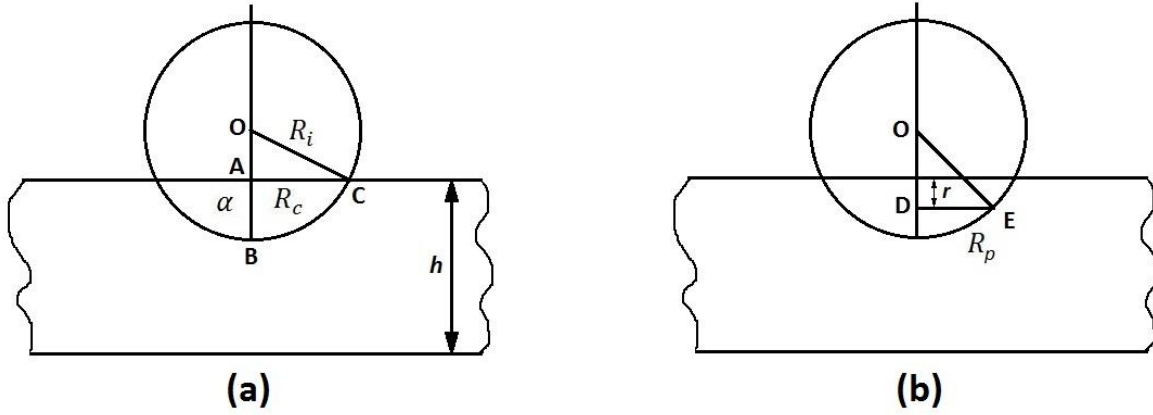


Figure 2.44 Schematic illustration of the indentation of a thin laminates supported by a rigid substrate [4].

The indentation as shown in Figure 2.44(a) is assumed to occur when a laminates of thickness h , is indented by a sphere rigid indenter under a uniaxial compression in the z -direction. A relation among the indentation, α , the radius of the indenter, R_i , and the radius of contact area, R_c , can be expressed as

$$R_c = \sqrt{2\alpha R_i - \alpha^2} \approx \sqrt{2\alpha R_i} \quad (2.57)$$

For simplicity, the second term inside the first square root of Equation 2.57 can be neglected since the indentation is much smaller than the radius of the indenter.

The displacements under the indenter can be derived from Figure 2.44(b) as

$$\delta(r) = \alpha - R_i \left[1 - \sqrt{1 - \left(\frac{r}{R_i}\right)^2} \right] \approx \alpha - \frac{r^2}{2R_i} \quad (2.58)$$

Again, the bracketed quantity can be simplified since the contact radius is much smaller than the indenter radius for small indentations.

The transverse normal strain is assumed to be uniform through the thickness and can be determined by $\varepsilon_{zz} = \delta(r)/h$. The contact force, P , is given by

$$P = \frac{2\pi E}{h} \int_0^{R_c} \delta(r) r dr \quad (2.59)$$

where, E is the modulus of elasticity in the transverse direction. Substituting Equation 2.58 and Equation 2.57 into Equation 2.59, the contact law for the elastic contact is given by

$$P = \frac{\pi E R_i}{h} \alpha^2 \quad (2.60)$$

The contact law indicates that the contact force is proportional to α^2 instead of $\alpha^{1.5}$ as demonstrated by Hertz contact law based predictions.

Moreover, the permanent indentation effects are also taken into account, by assuming the composite material is elastoplastic in the transverse direction. The stresses will reach the yield strength first in the contact centre since the largest deformations occur at the centre of the contact zone. Thus, the contact area are divided into a plastic zone of radius, R_P , and an elastic zone between R_C and R_P . Further, the stress is equal to the material yield strength, Z_C , at the boundary between the two zones. Therefore, the radius of the plastic zone, R_P , is expressed as

$$R_P = \sqrt{2R_i \left(\alpha - \frac{Z_C h}{E} \right)} \quad (2.61)$$

as long as the indentation, α , is larger than the critical indentation, α_{cr} ,

$$\alpha_{cr} = \frac{Z_C h}{E} \quad (2.62)$$

the critical indentation is related to the laminates thickness, but not a material property as assumed by the Hertz contact law based prediction.

Therefore, the contact force in the elastoplastic model is approximated as

$$P = \pi R_P^2 Z_C + \frac{2\pi E}{h} \int_{R_P}^{R_C} \delta(r) r dr \quad (2.63)$$

The contact law can be simplified as

$$P = \pi R_i Z_C (2\alpha - \alpha_{cr}) \quad \text{when } \alpha > \alpha_{cr} \quad (2.64)$$

2.6 Summary

Presented in this chapter is a review of the related research work on the failure mechanisms of composite laminates subjected to low-velocity impact. Following important statements can be made based on the literature review.

Composite materials, in particular the composite laminates, are becoming more and more important in the aerospace industry due to their advantages compared with conventional engineering alloys. However, the further application of the advanced material is restricted by the conservative design philosophy due to lack of understanding of low-velocity impact induced damage in composite laminates. Thus, developing further knowledge of damage mechanisms and impact response of composite laminates subjected to low-velocity impact is highly desirable to the industry and is one of the main focuses of this research.

The damage mechanisms of composite laminates, especially for the damage modes and corresponding failure criteria, were reviewed. Extensive researches have been conducted on the analysis and modelling of the delamination which is the dominant failure mechanism and may affect the post-impact load bearing capacity of composite laminates significantly. It is noticed that the initiation of delamination occurs consistently under a certain threshold load for a given laminates. Various analytical prediction models on the delamination threshold load have been proposed. These predictions indicate that the DTL value is influenced by the laminates thickness and the critical strain energy release rate. Further, the delamination has also been modelled with tie-break contact and cohesive zone model in the FE simulation in order to simulate the initiation and propagation of delamination.

The barely visible impact damage is a major concern in the practical operation and maintenance of composite structures. Therefore, developing an engineering approach to predict the impact damage by relating the internal damage to a visually detectable parameter is the other main focus of this research.

The quasi-static indentation test is an efficient alternative to represent the low-velocity impact response in developing such an inspection approach. The dent depth is proved to be a proper damage parameter to characterise the damage mechanisms in composite laminates. The contact force also needs to be estimated in order to relate the visually detectable parameter to the internal damage in composite laminates. Although exclusive Hertz theory or elastoplastic model based contact laws are available, the modified contact force prediction, considering

relation between the global deformation and the delamination induced stiffness degradation, is still required.

CHAPTER 3 Research Strategy

Aims of this PhD project are to develop further knowledge of the impact response and damage mechanisms of composite laminates under low-velocity impact, and to explore the feasibility of assessing the internal damage with a visually inspectable parameter. To achieve these aims, a series of investigations need to be conducted in the coordinated experimental, numerical, and analytical research work in this project.

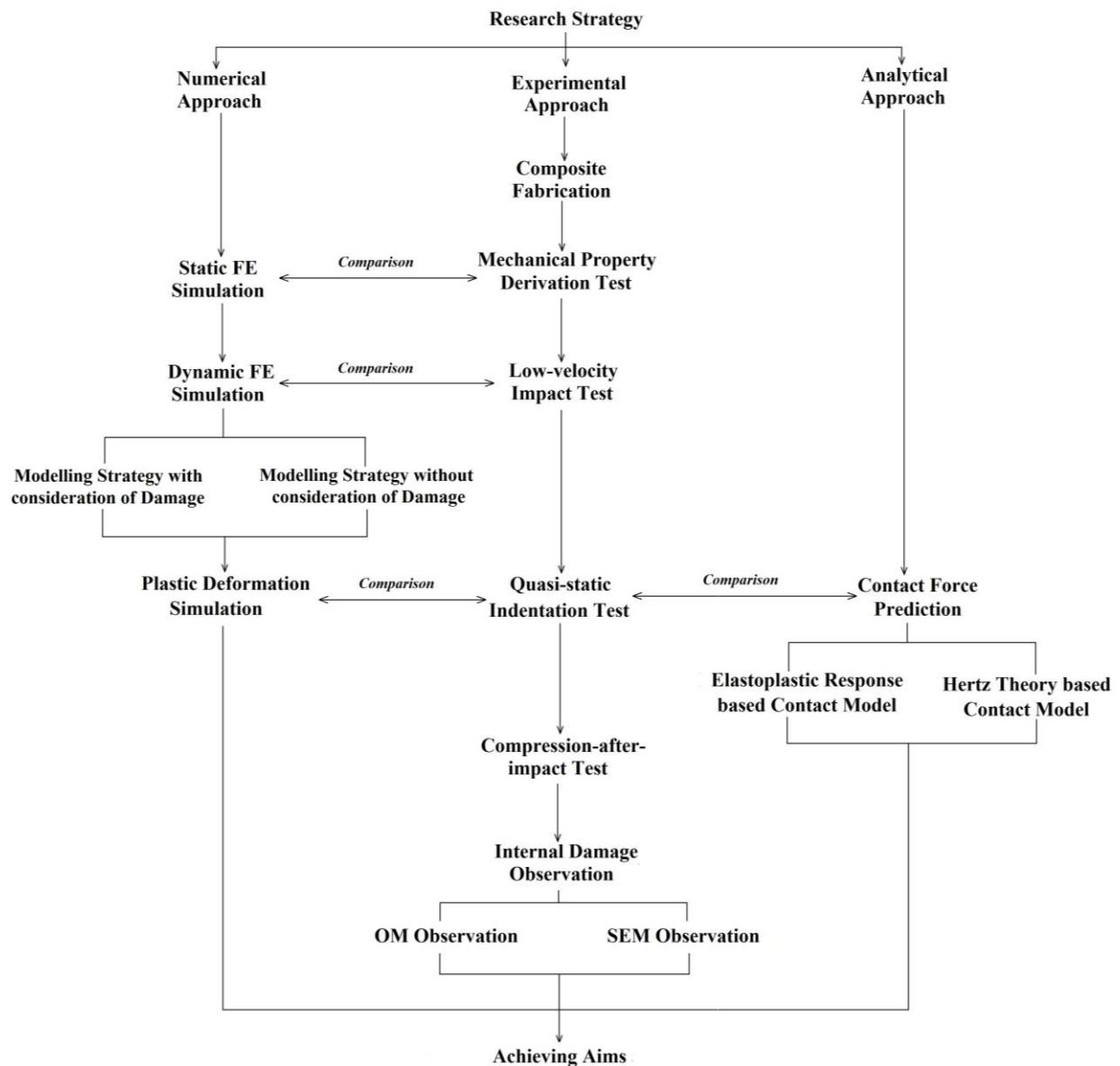


Figure 3.1 Research strategy flowchart.

Figure 3.1 shows the flowchart of the research strategy employed in this project. Only the purpose and method of the research activities are discussed in the current chapter in terms of

the feasibility and rationality of the research. The technical details, including the experimental test set-up, numerical model creation, and analytical procedure, will be described in the corresponding chapters.

In the experimental approach, the composite laminates will be firstly manufactured following the procedure involving the hand lay-up, vacuum bagging, and autoclave curing. Specimens with different geometries and lay-up configurations can be reliably prepared. Then, the basic mechanical properties of T700/M21 UD material will be determined through a number of material property derivation tests in accordance with different test standards, including ASTM D3039 [116] for the determination of tensile properties, ASTM D3846 [117] for the determination of in-plane shear strength, and ASTM D3518 [118] for the determination of in-plane shear response.

The instrumented low-velocity impact test will be conducted on the impact test specimen, in accordance with the ASTM 7136 test standard [119], to develop further understanding on the damage mechanisms and structural behaviour of composite laminates subjected to low-velocity impact. Particular attention is paid to the phenomenon of DTL and its detection based on the impact force history obtained from the drop weight test. Effects of the laminates thickness, repeated impact, lay-up configuration and residual thermal stress on the impact response of composite laminates are investigated systematically to develop further knowledge of impact response and damage mechanisms of composite laminates under low-velocity impact.

Furthermore, instrumented quasi-static indentation test will be conducted in accordance with the ASTM 6264 test standard [120]. It is based on extensive literature results [104, 109-111] that the QSI test can be an alternative method to further investigate the low-velocity impact response of composite laminates. Compared with low-velocity impact test, quasi-static indentation test can be controlled more reliably and often delivery more reliable test data. As a result, not only the first aim of this project, to develop further understanding on the damage mechanisms and structural behaviour of composite laminates under low-velocity impact, is better achieved; but also the second aim of this project, to explore an engineering applicable inspection technique to estimate the impact induced damage based on the relation between the internal damage and a visually inspectable parameter, can be reached by monitoring the dent depth variation under different indentation loads. Moreover, the back-face displacement is also measured during the indentation test, which provides further information on the

structural behaviour of composite laminates subjected to quasi-static indentation/low-velocity impact.

In order to establish relations among dent depth, residual strength, and the internal damage distribution, specimens loaded up to different loads need to be investigated by the compression-after-impact test and internal damage observation. The compression-after-impact test is carried out in accordance with the ASTM 7137 test standard [121]. The internal damage observation is conducted with the optical microscopy and the scanning electron microscopy. Based on the suggestion that the internal damage spread from the point immediately under the impact/indentation position [4], the specimen is cut along the longitudinal centreline to observe the cross-section of the internally damaged area. The OM observation with relative low magnification is firstly conducted to have a big picture of the internal damage distribution within the observed cross-section. The same cross-section will then be further examined by SEM under the guidance of the OM observation result. More information on damage mode and damage distribution at specific locations under different loading levels can be identified by the SEM observation results under high magnification.

In parallel to the experimental approach, analytical and numerical investigations will be carried out synchronously to achieve a better understanding of impact response of composite laminates under low-velocity impact.

In the numerical approach, the static FE analysis will be firstly conducted in the ANSYS Mechanical APDL 14.5 software to simulate the elastic behaviour of composite laminates under constant directional load. The simulation results are compared with the experimental results from material property derivation test. The impact event between the impactor and composite laminates will then be simulated in the ANSYS/LS-DYNA software. There are two main modelling strategies involved in the dynamic FE simulation. The modelling strategy without consideration of damage deliveries the estimation of overall structural behaviour of composite laminates by employing the ABD matrix. The ABD matrix, which is the effective stiffness matrix of composite laminates, is calculated from the mechanical properties as derived in the former experimental study and the lay-up configuration of composite laminates. The simulation based on the ABD matrix is capable of simulating the structural behaviour of the undamaged composite laminates. The numerical prediction will deviate from the experimental result when impact force exceeds the DTL since no material degradation is considered in the simulation. Therefore, simulation will be carried out with the second

modelling strategy considering the damage mechanisms. In the second modelling strategy, the failure criterion and degradation scheme are defined in the material model for each individual lamina to simulate the intralaminar damage, while the tie-break contact is used to connect the adjacent layers to simulate the interlaminar damage. The result so obtained is capable of simulating the low-velocity impact event, especially for the impact induced damage initiation and propagation [81, 103, 122]. The simulation results will be compared with the experimental result achieved from the low-velocity impact test to develop a further understanding on the damage mechanisms and structural behaviour of composite laminates under low-velocity impact.

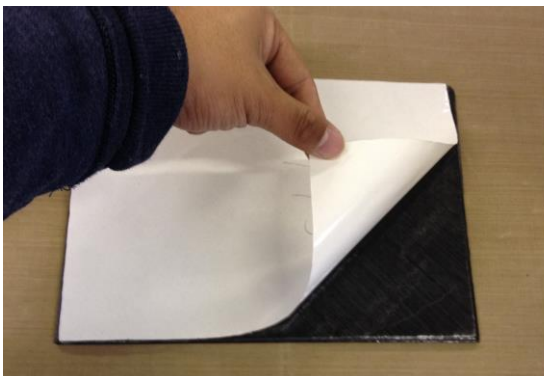
Furthermore, the quasi-static indentation response of composite laminates will be investigated in both the numerical and analytical approaches to understand the contact behaviour of composite laminates under low-velocity impact. The numerical simulation of the indentation event is conducted in the ANSYS/Workbench software. In the simulation, the plastic deformation of the indented composite laminate is of particular interest. The elastoplastic material properties of matrix material is assigned to the target entity only in the simulation model, which is based on the assumption that the structural behaviour of composite laminates in the transverse direction is governed by the material properties of matrix resin [123, 124]. The simulation result, in terms of the local plastic deformation, is capable of validating the relation between the contact force and resultant dent depth derived from the quasi-static indentation test. Moreover, the contact force will be predicted through analytical studies. Two main contact models are used: one is the elastoplastic response based contact model and the other is the Hertz contact theory based contact model. The work with the first analytical contact model is conducted based on the same assumption as employed in the numerical approach in which the indented composite laminate is simplified to an ideal material bonded to the rigid substrate and the contact response is dominated by the elastoplastic material behaviour of the matrix. The analysis with the second analytical contact model is conducted based on the Hertz contact theory in which the contact stiffness and the effective modulus are determined for the contact event. As a result, the local permanent deformation and the relatively displacement can be linked to the contact force by the analytical predictions using the two contact models, respectively. Finally, the results on the indentation behaviour of composite laminates from the experimental, numerical, and analytical studies will be compared and analysed to explore the feasibility of assessing the internal damage with a visually inspectable parameter.

CHAPTER 4 Derivation of Mechanical Properties of UD Material

Reliable data of the basic mechanical properties of unidirectional material is essential in the characterisation of low-velocity impact response of composite laminates. This chapter presents the experimental work to determine the basic mechanical properties of the UD material used in this project. Composite plates were firstly fabricated using the autoclave curing technique. Different test coupons were then prepared and tested in accordance with different test standards to determine the corresponding basic mechanical properties.

4.1 Composite Plate Fabrication

The procedure of hand lay-up, vacuum bagging, and autoclave curing were followed in the fabrication of composite plates for the coupons tested in this study. The unidirectional material is the carbon/epoxy prepreg *Hexply UD/M21/35%/268/T700GC/300* supplied by the Centre of Composites, Airbus Operations Ltd (UK).



(a) A white protective sheet is removed from a prepreg layer.



(b) A layered laminates is rolled by a hand roller.

Figure 4.1 Hand lay-up of the composite plate.

The T700/M21 UD material roll needs to be stored in a sealed moisture-proof bag at -18°C , and be removed from the refrigerator 24 hours before use to defrost [125]. The sealed moisture-proof bag only can be opened until the material temperature rises to the room temperature to prevent the condensation. The prepreg is 300mm wide and covered by a non-stick protective sheet. After curing, each layer is around 0.26mm thick [125]. A composite

dedicated scissor and a paper trimmer were used to cut the prepreg into sheets with required specifications (dimensions and fibre orientations) according to the patterns drawn on the protective sheet.

The lay-up of the laminate was carried out manually to stack the laminas in a predetermined sequence. The first lamina was laid on a clean smooth surface with the black prepreg face down, and then the white protective sheet was removed as shown in Figure 4.1(a). The next layer with the prepreg face down was carefully laid onto the adhesive prepreg face of the first layer so that the fibres were aligned in the desired direction. A hand roller was used to remove the air bubbles out of the laminates as shown in Figure 4.1(b). Moreover, the layered panel was debulked every four layers by placing the plate into a temporary vacuum bag for 15 minutes at a slightly increased temperature of around 30°C. The temporary vacuum of the stacked layers helped to minimise the presences of voids in the laminates caused by unremoved air and volatiles. The elevated temperature during debulking ensured the good adhesion between layers. All these processes were repeated until the desired lay-up configuration was achieved.

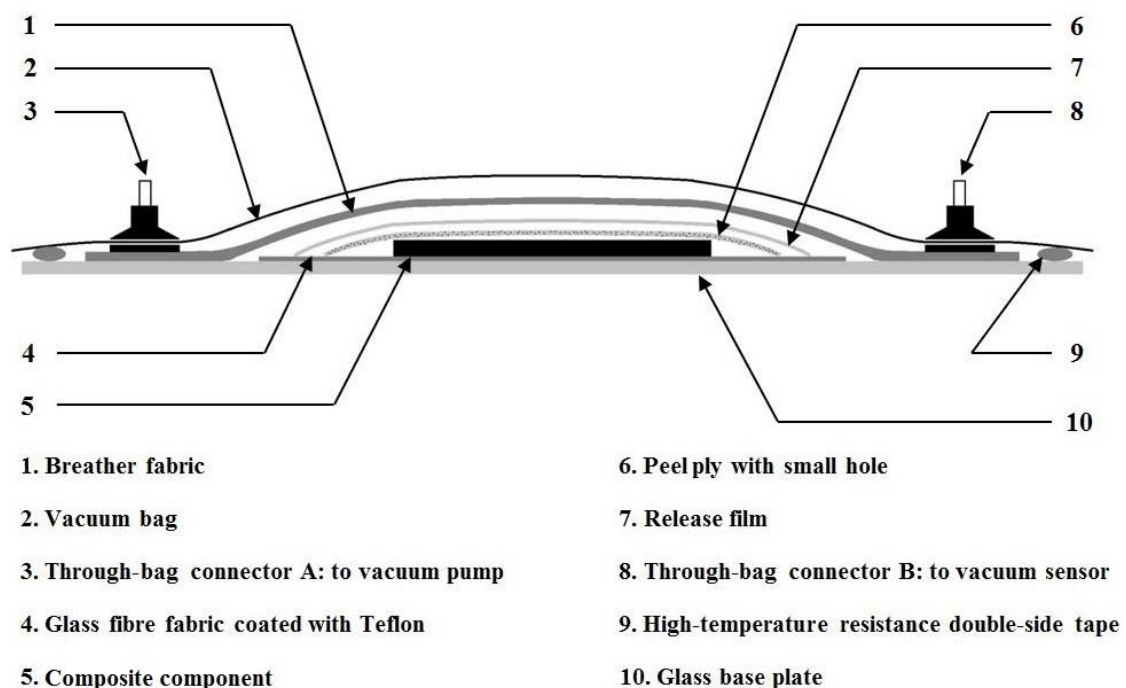
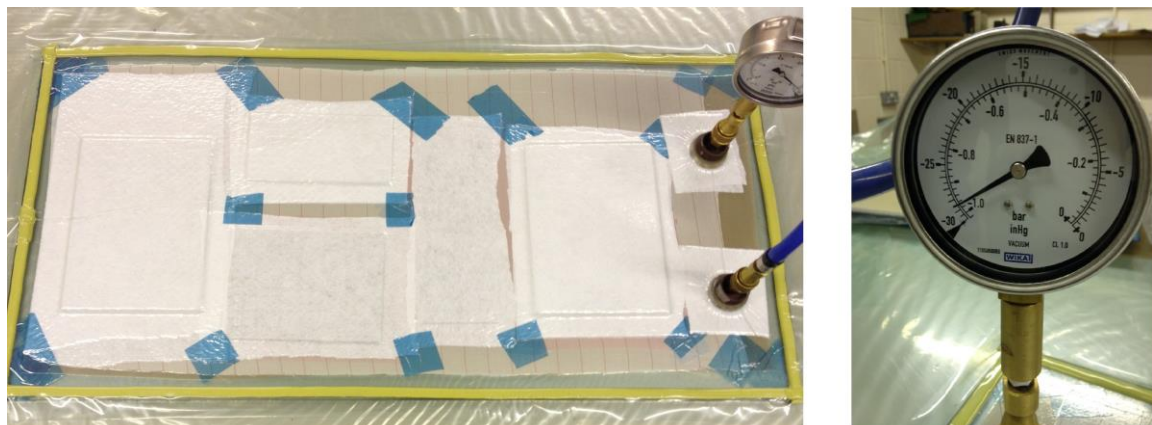


Figure 4.2 Schematic diagram of the vacuum bagging.

A breather & bleeder system was used in the vacuum bagging process in order to absorb excess resin and allow the escape of volatiles during the autoclave curing process. The

schematic diagram of the vacuum bagging is shown in Figure 4.2. A layer of glass fibre fabric coated with Teflon (PTFE) was taped to a flat and smooth glass base plate. The composite plate was placed on the non-stick Teflon coated fabric to prevent the bonding between the laminates and the glass after curing. The composite plate was also covered by a layer of peel ply with small hole, which improved the surface finishing quality of the laminates after curing and provided a path for the excess resin and escaped volatiles to go through the peel ply during curing. Another layer of release film was used to ensure the separation between the plate and the breather fabric after curing. Appropriate amount of the breather fabric was used to absorb the excess resin depends on the laminates size and thickness. Finally, the entire assembly of composite laminates and auxiliary materials was covered by the vacuum bag film. The high-temperature resistant double-side tape was used to seal the vacuum bag on all the four edges of the rectangular glass base plate. Moreover, two through-bag connectors were used to connect to the sealed vacuum bag to the vacuum pump and vacuum sensor.



(a) An assembly of composite plates and (b) Vacuum gauge indicating the required vacuum bagging ready for curing. vacuum pressure for curing.

Figure 4.3 Prepared vacuum bagging and composite plates under the required vacuum pressure for curing.

Figure 4.3(a) shows a prepared vacuum bagging under vacuum overnight and ready for curing. The vacuum pressure (-1 bar full vacuum) was measured by the vacuum gauge as shown in Figure 4.3(b). The vacuum quality was evaluated by checking whether the vacuum bag was holding pressure after turning off the vacuum pump.

The composite plates were cured by the Aeroform gas fired autoclave system at University of Hertfordshire as shown in Figure 4.4(a). The allowable working temperature and pressure of the autoclave are 200°C and 100PSI, respectively. The curing process was fully controlled by

the autoclave management & control system (AMCS) developed by AIC as shown in Figure 4.4(b). The all-digital controlled system includes four vacuum sensors and up to eight thermocouples, which provides simpler operation and improves curing reliability.

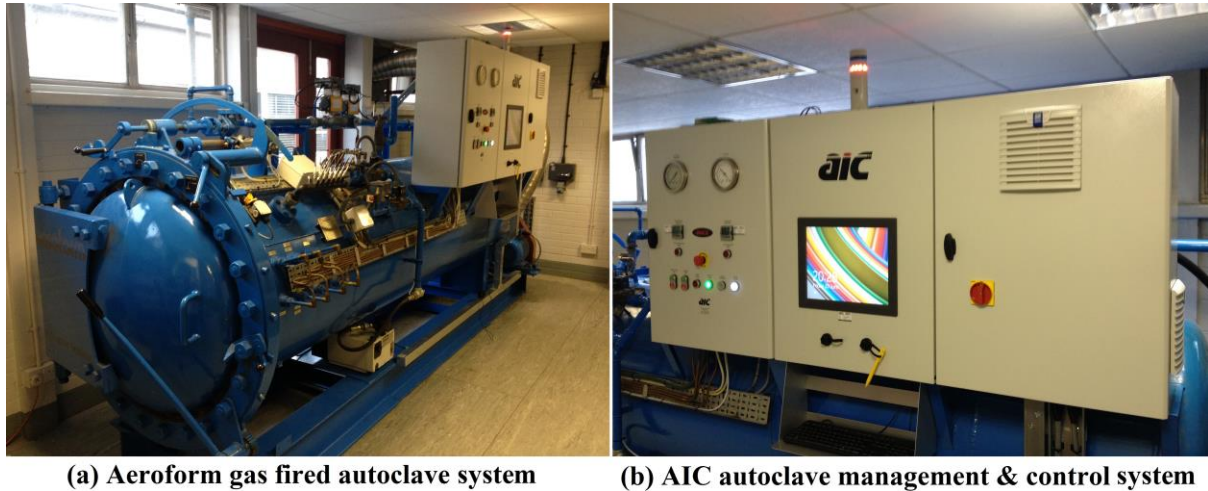


Figure 4.4 (a) Composite curing autoclave and (b) its control system.

Figure 4.5 shows the curing cycle used in this project to fabricate the composite plates [125].

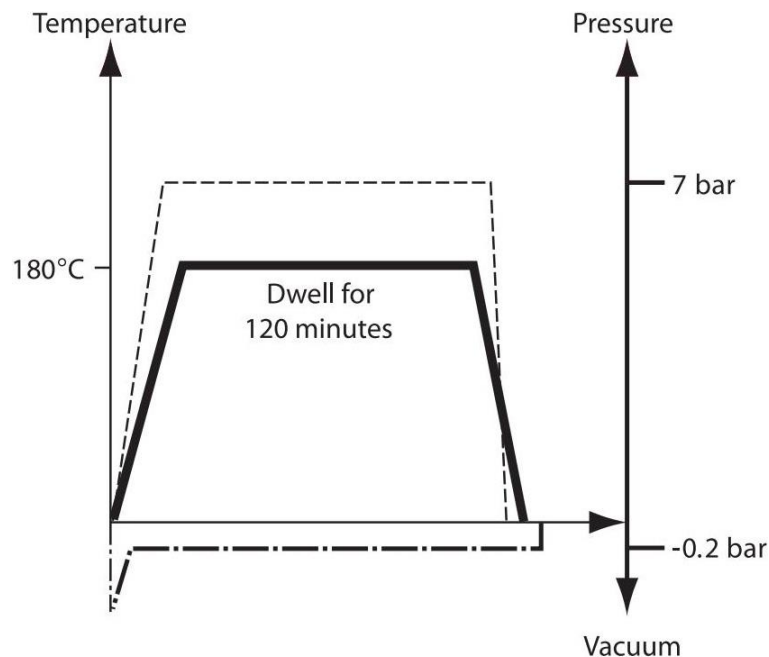


Figure 4.5 Autoclave curing cycle used to fabricate composite plates [125].

The autoclave was first pressurized to 7 bar. The vacuum pressure of the full vacuum bag (as -1 bar) was then vented to a safety value of -0.2 bar, when the autoclave pressure was reached. The autoclave was heated from room temperature to $180^{\circ}\text{C} \pm 5^{\circ}\text{C}$ at an actual component

heat-up rate of 1-2 °C/min. The curing temperature was hold for 120min \pm 5min at 180°C \pm 5°C. After the holding phase, the autoclave was cooled at an actual component cool-down rate of 2-5 °C/min. Finally, the autoclave pressure was released when the component temperature was less than 60°C.

The fabrication quality of composite plate was further checked by the cured specimen thickness and the surface visual inspection. The qualified specimen had a shining smooth surface and the mean individual lamina thickness was 0.26mm \pm 0.015mm.

4.2 Specimen Preparation and Test Set-up

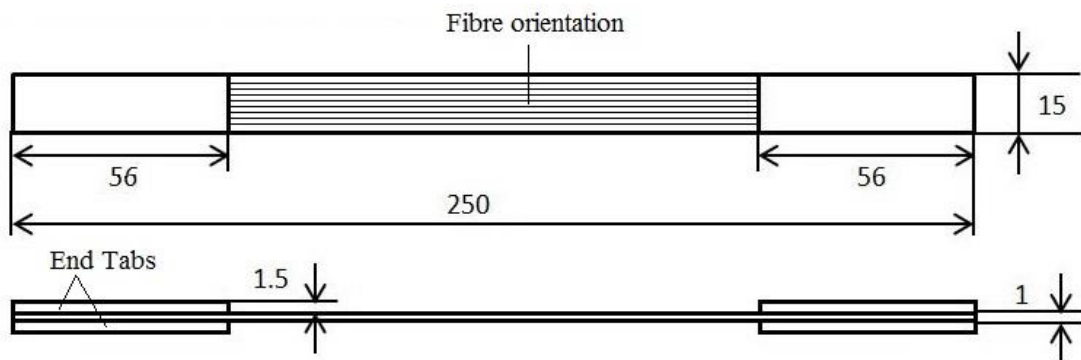
Following the fabrication procedure outlined in section 4.1, the qualified composite plates were further processed to obtain the final test coupons in accordance with different test standards.

The composite plates were cut into pieces with the required dimensions using a cutting machine with a diamond-coated saw. A consistent cutting speed of 5 mm/s was applied to improve the cutting quality and minimize the cutting induced damage. The specimen dimension was measured by a digital vernier. The dimensional tolerance was about \pm 0.5mm. Aluminium tabs were bonded on the faces of specimen ends (see Figure 4.6) by the ARALDITE[®] 420A/B two components epoxy adhesive system. The 5251-H22 aluminium alloy end taps were firstly bonded to one face of each specimen. A minimum setting period of 24 hours was required for the adhesive before bonding the end tabs to the opposite face of each specimen. Although the gripping tabs were not essentially required by the test standard, they were strongly recommended by the test standards to ensure the acceptable failure mode and location. The successful introduction of force into the specimen and the prevention of premature failure rely on the proper applications of the end tabs. Moreover, electrical strain gauges were used in some specific tests in which the specimen deformation measurement was required. The strain gauge was bonded onto the surface of the specimen at the required position. The strain gauge bonded on the test specimen was EA-13-060RZ-120/E (see Figure 4.8) with a resistance of 120 \pm 0.4% Ohms and a gauge factor of 2.09 at 24°C.

4.2.1 Specimen Geometry and Set-up of Tensile Property Test

The tensile properties of the unidirectional material were determined by a series of tensile tests in accordance with the ASTM D3039/D3039M-07 test standard [116]. The longitudinal and transverse tensile strengths were determined by using the $[0^\circ]_4$ and $[90^\circ]_8$ tensile test specimens without strain gauge bonded. The longitudinal Young's modulus and major Poisson's ratio was derived by the stress-strain relationship of the $[0^\circ]_4$ tensile test specimen with strain gauge bonded. Similarly, the $[90^\circ]_8$ tensile test specimen with strain gauge bonded was used in the derivation of the transverse Young's modulus and minor Poisson's ratio.

Longitudinal tensile test specimen $[0^\circ]_4$



Transverse tensile test specimen $[90^\circ]_8$

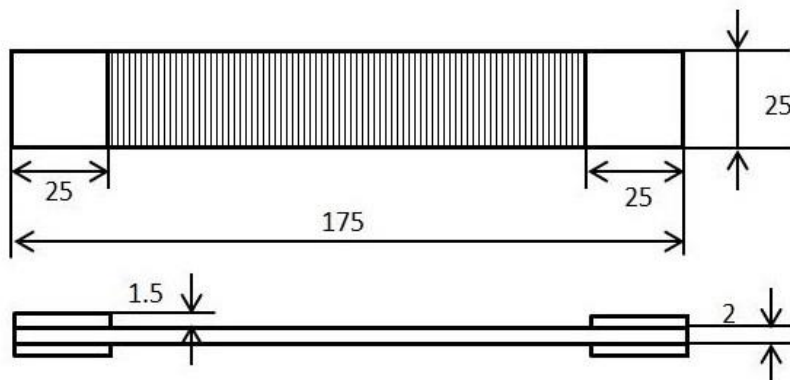


Figure 4.6 Two types of specimens in tensile test.

The standard recommended specimen geometry for the determination of the ultimate tensile strength was illustrated in Figure 4.6. To determine the longitudinal tensile strength, the $[0^\circ]_4$ tensile test specimen was loaded continuously at a constant test speed of 5 mm/min on the

Hounsfield 50kN universal test machine until the final failure. During the test, the applied force and the axial extension were automatically recorded by a data acquisition system as shown in Figure 4.7. The accuracies of the force and the extension are $\pm 0.5\%$ of the indicated values within the force and extension ranges. The longitudinal tensile strength was derived by the applied force over the cross-section area. The $[90^\circ]_8$ specimen was tested on the Hounsfield 10kN universal test machine to determine the transverse tensile strength.

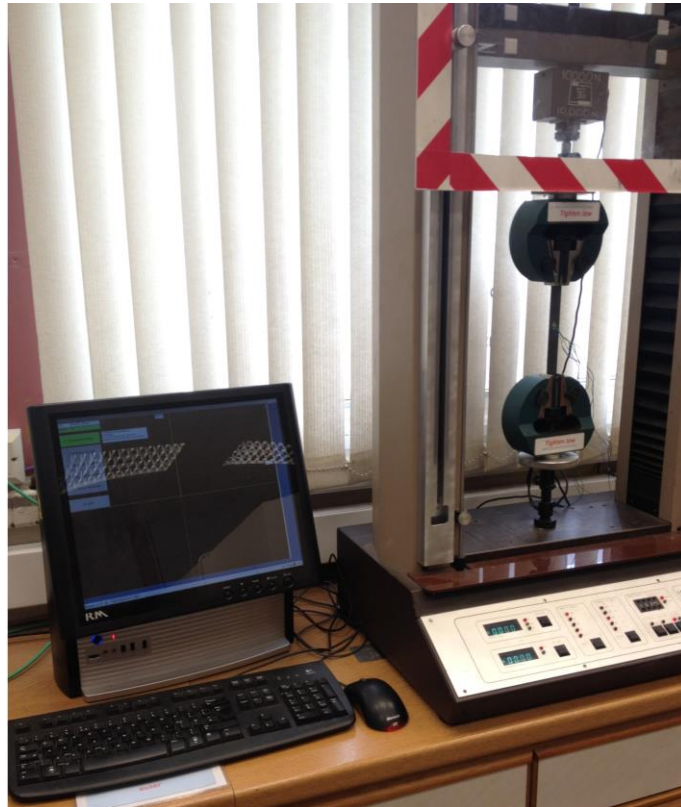


Figure 4.7 Hounsfield 50kN universal test machine and the computer aided data acquisition system.

The determination of the Young's modulus and the Poisson's ratio requires the information of the specimen deformation. Figure 4.8 shows the specimen with centre bonded 45° strain gauge rosettes to measure the specimen deformation during the tensile test. The strain gauges in axial and lateral directions were wired to the strain gauge amplifier using the quarter Wheatstone bridge connection. Moreover, the tensile test was conducted on the Hounsfield 10kN universal test machine to achieve more accurate results since the derivation of the material elasticity property only required the strain-stress relationship of the tested specimen in the elastic region.

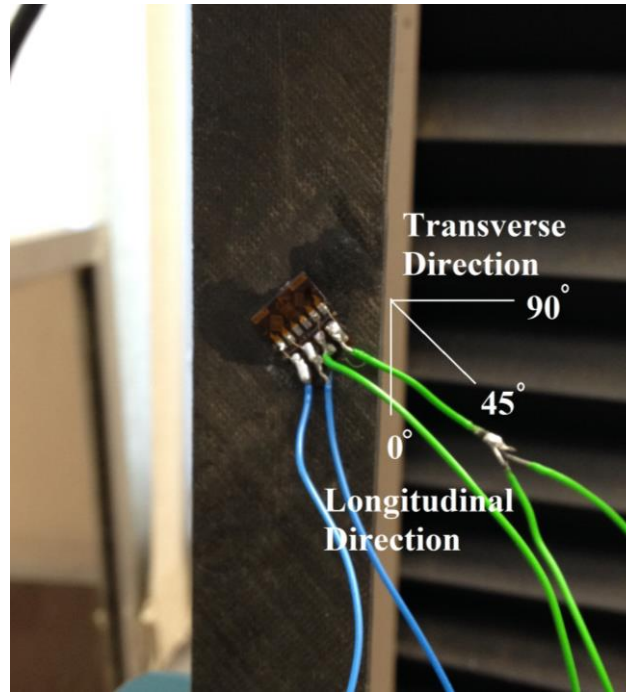


Figure 4.8 Tensile test specimen with the multidirectional strain gauges bonded.

During the test for Young's modulus and Poisson's ratio, the specimen was loaded in a step-by-step approach, in which the applied force and the axial/lateral strains were manually recorded at different loads. The longitudinal $[0^\circ]_4$ specimen was loaded up to 10kN with a step of 0.5kN to determine the longitudinal Young's modulus and the major Poisson's ratio. The transverse $[90^\circ]_8$ specimen was loaded up to 1.5kN with a load step of 0.05kN to determine the transverse Young's modulus and the minor Poisson's ratio.

4.2.2 Specimen Geometry and Set-up of Shear Property Test

The shear properties of the unidirectional material, including the interlaminar shear strength and the in-plane shear modulus/strength, were determined by a series of tests in accordance with the ASTM D3846/D3846M-02 [117] and the ASTM D3518/D3518M-01 [118] test standards.

The test specimen with two notches on the opposite faces as illustrated in Figure 4.9 was designed to determine the shear strength of the bond between the two adjacent layers (interlaminar shear strength). The specimen was prepared in accordance to the ASTM D3846 test standard with some modification to the creation of the notches.

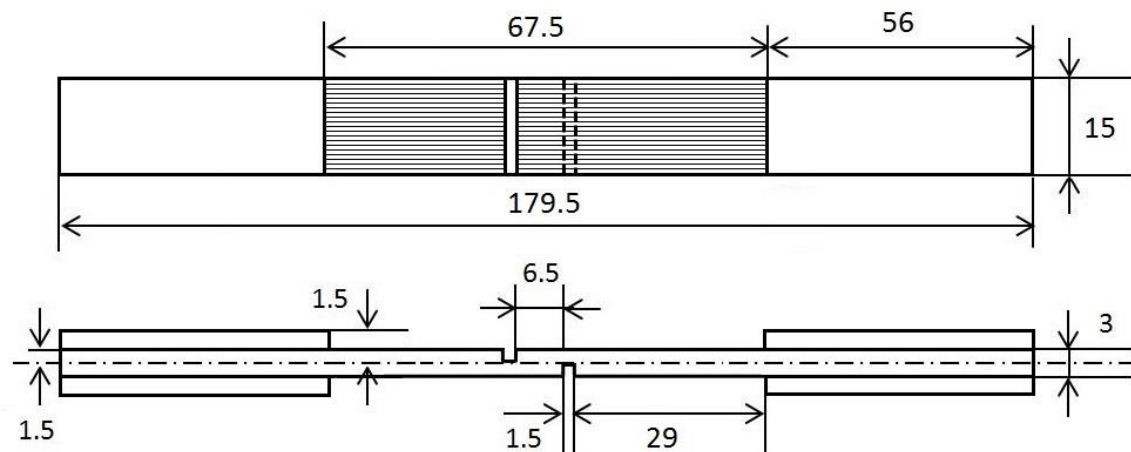
Interlaminar shear strength test specimen $[0^\circ]_{12}$ 

Figure 4.9 Schematic illustration of specimen for the interlaminar shear strength test.

The notches were originally required to be cut halfway through the thickness of the cured specimen. It was however found to be extremely difficult to achieve such precision notch by using the available cutting equipment. Therefore, it was decided to lay four individual lamina stacks (6 layers of 0° prepreg) together to achieve the structure required by the test standards. The notch was temporarily filled by a strip of the high temperature resistant double sided tape to prevent any resin spilling into the notch during curing as shown in Figure 4.10. The double sided tape strip was completely removed after the curing process to create the required notch.

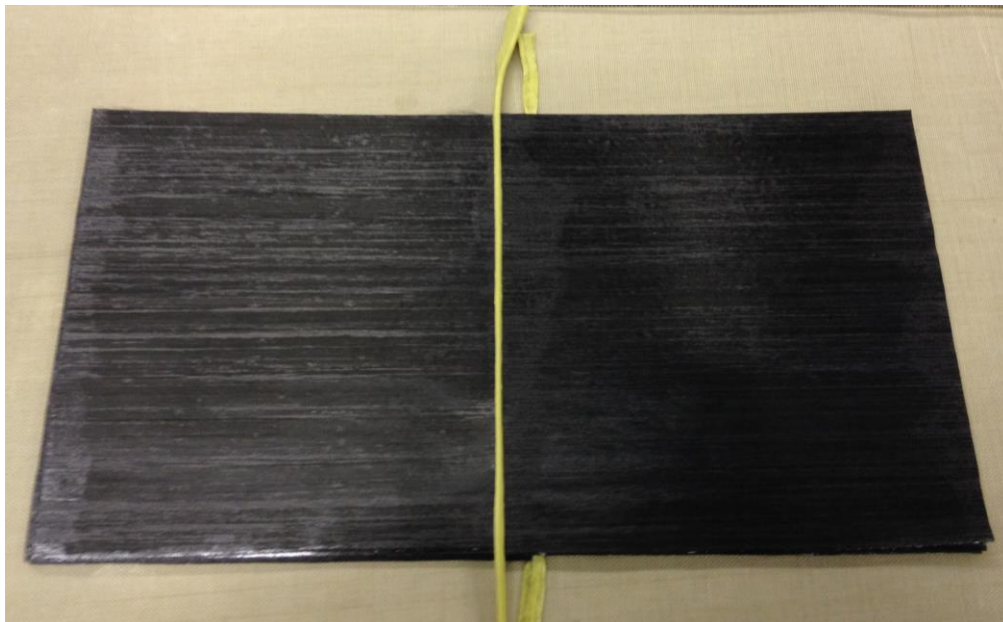


Figure 4.10 Preparation of ILSS test specimens.

The specimen was loaded continuously to the final failure in order to determine the failure load. The 10 kN Hounsfield universal test machine was used to apply the axial tensile load at a constant speed control of 1.3 mm/min. Although the compressive load was required by the original test standard, the tensile load was used to introduce the in-plane shear failure in order to prevent the possible buckling under compression. The failure plane was expected to be located along the longitudinal axis of the specimen between two centrally located notches which were halfway through its thickness on opposing faces.

In-plane shear modulus test specimen $[\pm 45^\circ]_{2s}$



Figure 4.11 Schematic illustration of the in-plane shear modulus test specimen.

Figure 4.11 shows the $[\pm 45^\circ]_{2s}$ specimen with strain gauge bonded, in accordance to the ASTM D3518 test standard, to determine the in-plane shear modulus of the unidirectional material. The test set-up was similar to the tensile test to determine the elasticity property of the material. The test specimen was loaded step-by-step up to 3kN on the Hounsfield 10kN universal test machine. During the loading process, the applied force and the axial/lateral strains were manually recorded for every 0.25kN to obtain the stress/strain curve of the unidirectional material. However, the stress and strain were calculated by:

$$\tau_{12i} = \frac{P_i}{2A} \quad \text{and} \quad \gamma_{12i} = \varepsilon_{xi} - \varepsilon_{yi} \quad (4.1)$$

where, τ_{12i} and γ_{12i} are shear stress and shear strain at i -th data point, respectively. P_i is the applied load at i -th data point. A is the specimen cross section area. ε_{xi} and ε_{yi} are the longitudinal and lateral normal strains at i -th data point, respectively.

Moreover, the $[\pm 45^\circ]_{2s}$ specimens without strain gauge bonded were loaded continuously to the final failures by the Hounsfield 50kN universal test machine. The maximum in-plane

shear stress, τ_{12} , was therefore determined by dividing the half of the maximum applied load by the cross-section area of the specimen.

4.3 Test Results

The test results for the determination of the basic mechanical properties of the unidirectional material are presented in this section. At least five specimens were tested repetitively for each test condition.

4.3.1 Tensile Property Test

The dimensions of the tensile strength test specimens were measured by a digital vernier and summarized in Table.4.1. The data listed below is the average value by taking at least five measurements at different locations.

Table 4.1 Dimensions of the tensile strength specimens

	[0°] ₄ tensile strength test specimen					[90°] ₈ tensile strength test specimen				
Specimen No.	1.6	1.7	1.8	1.9	1.10	2.6	2.7	2.8	2.9	2.10
Average width (mm)	15.08	15.18	15.05	15.21	15.21	24.63	24.52	25.02	24.72	24.70
Average thickness (mm)	1.09	1.08	1.07	1.08	1.09	2.18	2.09	2.10	2.11	2.12
Cross-section area (mm ²)	16.36	16.42	16.08	16.38	16.56	53.61	51.29	52.62	52.25	52.40

Once the geometries of the specimens were measured, the specimens were tested following the test procedure described in section 4.2.1 to determine the maximum tensile load each specimen could take.

The explosive final failure was observed during the longitudinal tensile strength test as shown in Figure 4.12(a) since all the fibres were aligned in the axial loading direction. The specimen only failed when the ultimate tensile strength was reached. However, the final failure happened to the transverse tensile strength test specimen was at a much lower load level as the loading direction was perpendicular to the fibre direction. The straight fracture section, which was parallel to the fibre direction, could be introduced into the transverse tensile

strength test specimen at any place due to the uniformly distributed tensile stress as shown in Figure 4.12(b).

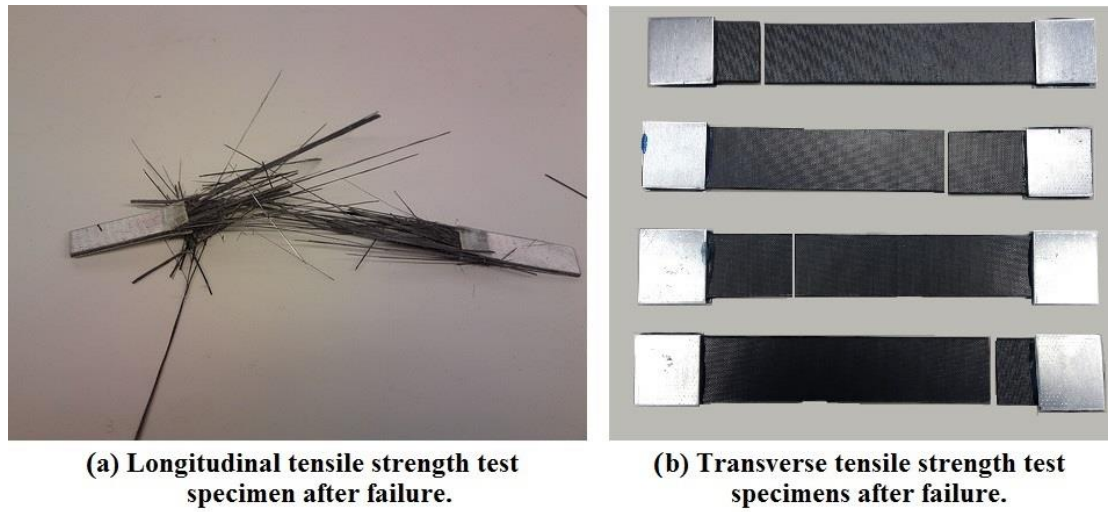


Figure 4.12 Tested specimens after reaching the tensile strengths.

Table.4.2 presents tensile strength test results including the maximum load and cross-section area for each test specimen. The average longitudinal tensile strength was 2116.60 MPa and the average transverse tensile strength was 44.60MPa.

Table 4.2 Tensile strength of M21/T700 UD material

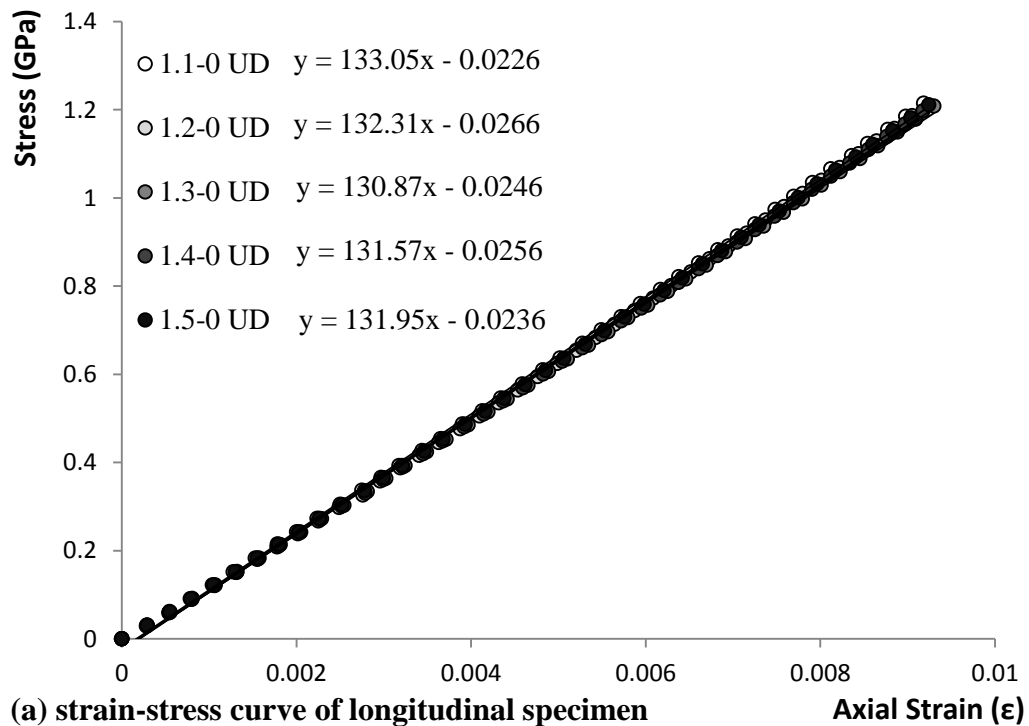
		Maximum load (N)	Cross-section area (mm ²)	Ultimate tensile strength (MPa)
[0°] ₄ tensile strength test specimen	1.6	34540	16.36	2111.02
	1.7	34917	16.42	2127.00
	1.8	33884	16.08	2107.00
	1.9	34676	16.38	2117.01
	1.10	35118	16.56	2121.01
	Average longitudinal tensile strength			2116.60
[90°] ₈ tensile strength test specimen	2.6	2470	53.61	46.07
	2.7	2290	51.29	44.64
	2.8	2272	52.62	43.18
	2.9	2375	52.25	45.46
	2.10	2288	52.40	43.67
Average transverse tensile strength			44.60	

The dimensions of the tensile test specimens with strain gauge bonded, which were used in the derivations of the elastic properties of the unidirectional material, are summarized in Table.4.3.

Table 4.3 Dimensions of tensile test specimens with strain gauge bonded

Specimen No.	[0°] ₄ specimen with strain gauge					[90°] ₈ specimen with strain gauge				
	1.1	1.2	1.3	1.4	1.5	2.1	2.2	2.3	2.4	2.5
Average width (mm)	15.39	15.46	15.33	15.19	15.43	25.48	25.37	25.34	25.26	25.42
Average thickness (mm)	1.07	1.09	1.08	1.1	1.07	2.12	2.06	2.10	2.09	2.11
Cross-section area (mm ²)	16.47	16.85	16.56	16.71	16.51	54.02	52.26	53.21	52.79	53.64

Five [0°]₄ specimens with strain gauge bonded were tested following the test procedure described in Section 4.2.1 to determine the longitudinal tensile modulus of elasticity, E_{1t} , and the major Poisson’s ratio, ν_{12} . The test results of the longitudinal tensile test specimens with strain gauge bonded are shown in Figure 4.13.



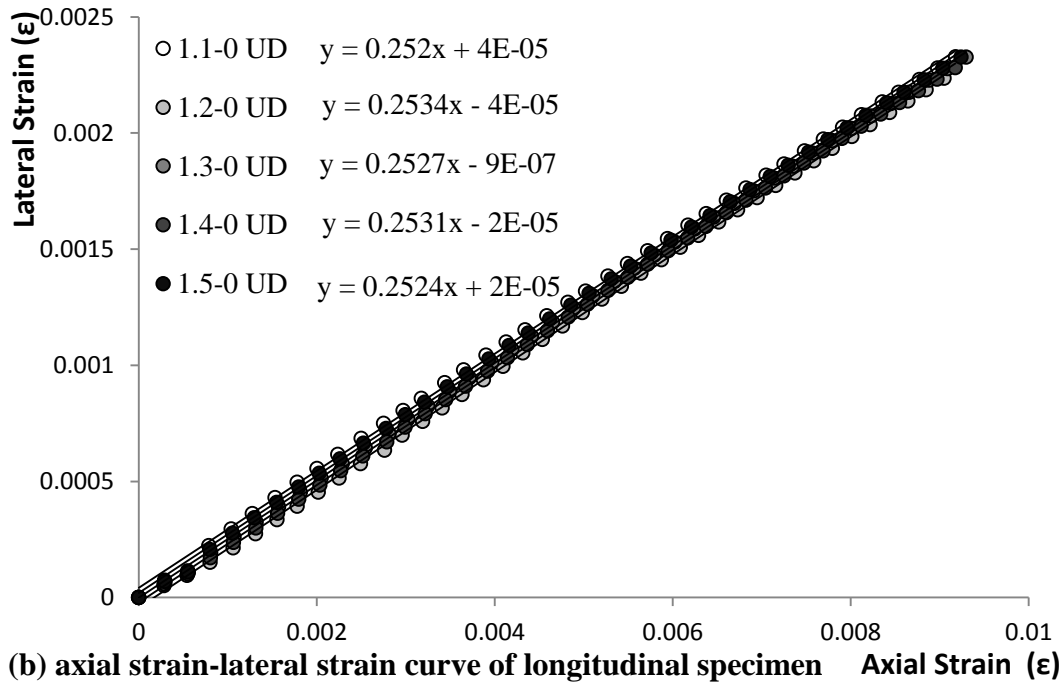


Figure 4.13 Test results of the longitudinal tensile test specimens with strain gauge bonded.

Figure 4.13(a) shows the stress-strain curves of $[0^\circ]_4$ specimens where the tensile loading was applied in the fibre direction. Figure 4.13(b) shows the relation between the axial deformations and the lateral deformations of the specimens under different loads. The major Poisson’s ratio was determined by the ratio between the lateral strain and the axial strain. The test results of different specimens in terms of the longitudinal Young’s modulus and the major Poisson’s ratio are summarized in Table.4.4.

Table 4.4 Longitudinal Young’s modulus and major Poisson’s ratio of M21/T700 UD material

$[0^\circ]_4$ specimen with strain gauge	1.1	1.2	1.3	1.4	1.5	Average value
Longitudinal Young’s modulus (GPa)	133.05	132.31	130.87	131.57	131.95	131.95
Major Poisson’s ratio	0.252	0.253	0.253	0.253	0.252	0.253

Five $[90^\circ]_8$ specimens with strain gauge bonded were tested following the test procedure described in the previous section to determine the transverse tensile modulus of elasticity, E_{2t} , and the minor Poisson’s ratio, ν_{21} . The test results of the transverse tensile test specimens with strain gauge bonded are shown in Figure 4.14.

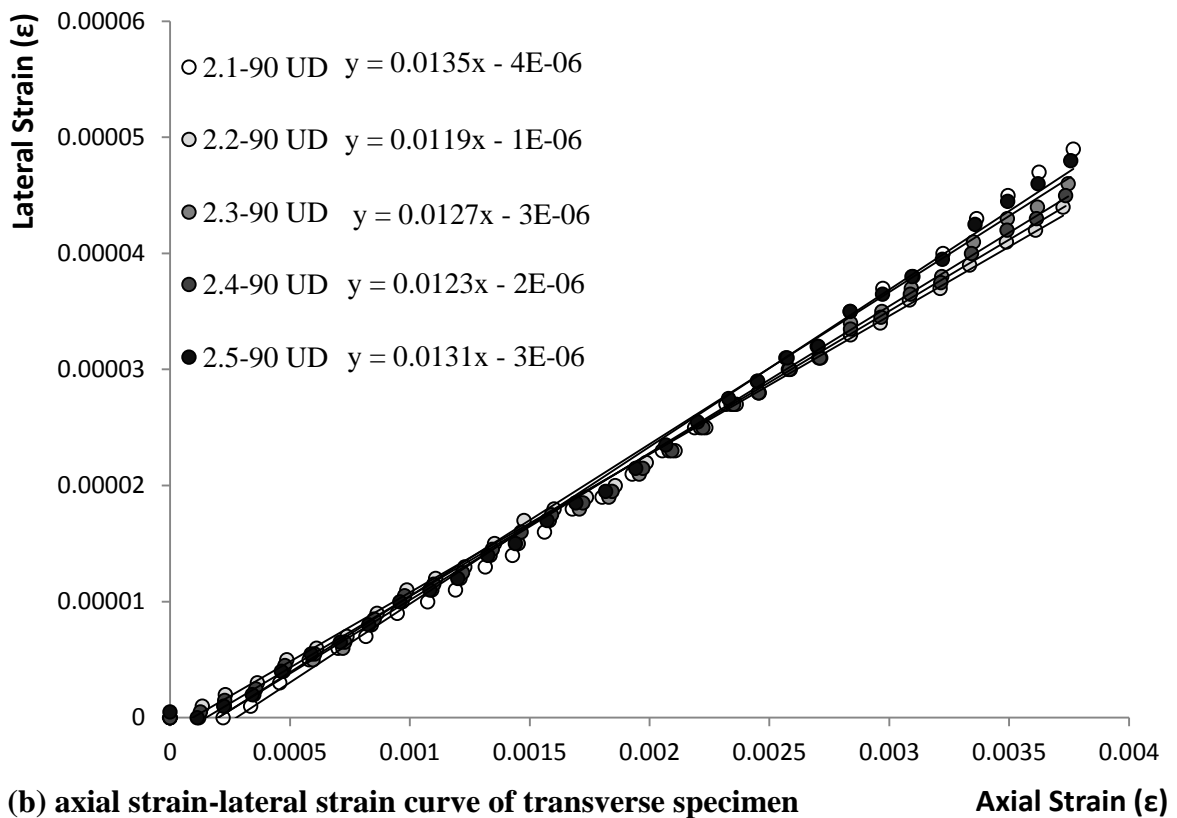
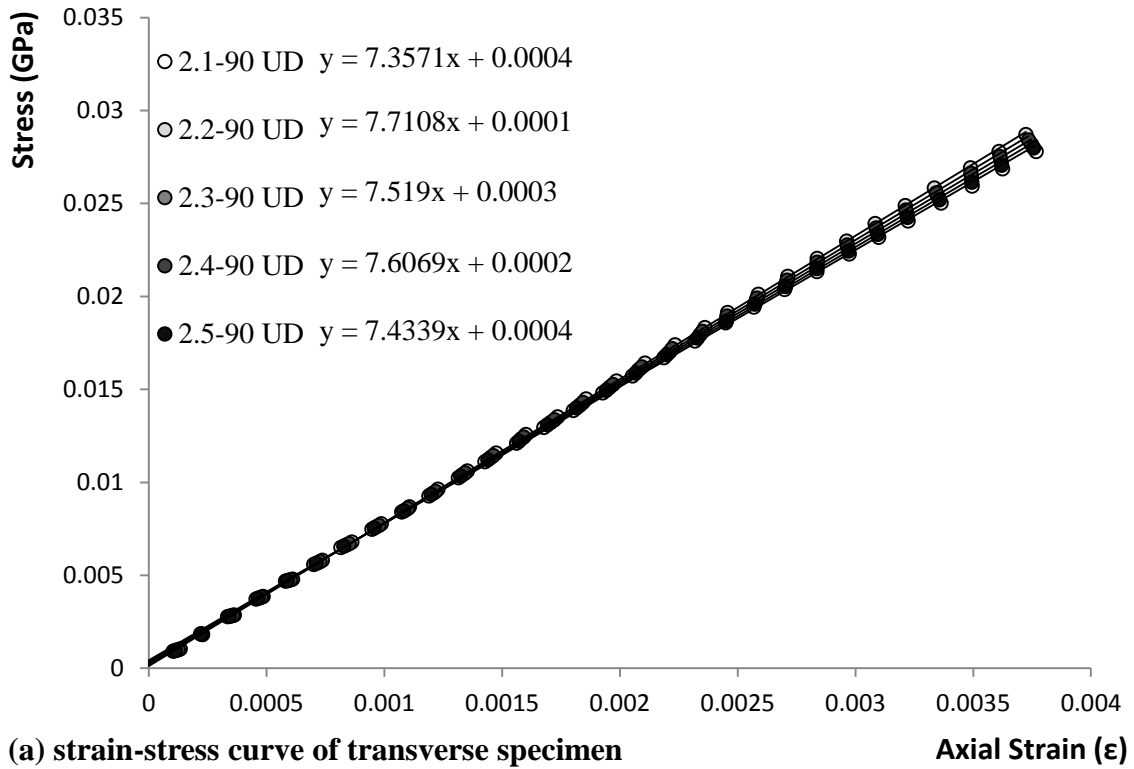


Figure 4.14 Test results of the transverse tensile test specimens with strain gauge bonded.

Figure 4.14(a) shows the stress-strain curves for $[90^\circ]_8$ specimens where the direction of the applied tensile loading is perpendicular to the fibre direction. The linear correlation was applied to the test data to obtain the linear equation between the applied stress and the axial strain. Figure 4.14(b) presents the recorded strains in both axial and lateral directions of the different test specimens under different loads. The minor Poisson's ratio was derived from the linear correlation equation in terms of the gradient of the approximate trend line. The test results of different specimens in terms of the transverse Young's modulus and the minor Poisson's ratio are summarized in Table.4.5.

Table 4.5 Transverse Young's modulus and minor Poisson's ratio of M21/T700 UD material

$[90^\circ]_8$ specimen with strain gauge	2.1	2.2	2.3	2.4	2.5	Average value
Transverse Young's modulus (GPa)	7.36	7.71	7.52	7.61	7.43	7.53
Minor Poisson's ratio	0.0135	0.0119	0.0127	0.0123	0.0131	0.0127

4.3.2 Shear Property Test

The dimensions of the notched $[0^\circ]_{12}$ specimens are summarized in Table.4.6. The width of the specimen was measured between the notches, and the length of the failed area was measured by the distance between the two notches as shown in Figure 4.15.

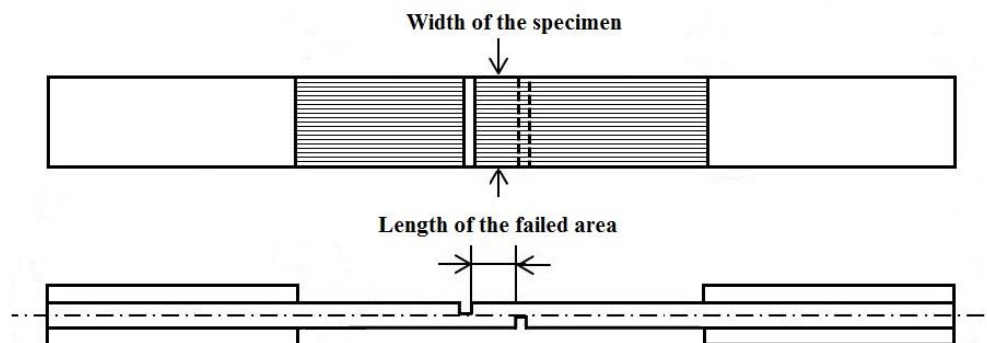


Figure 4.15 Schematic illustration of the measurements of the specimen width and the failed area length.

Five specimens were tested in accordance with the test procedure described in Section 4.2.2 to determine the failure loads. The interlaminar shear strength was calculated by dividing the

maximum applied load by the product of the width of the specimen and the length of the failed area.

Table 4.6 Dimensions of the interlaminar shear strength test specimens

[0°] ₁₂ interlaminar shear strength test specimen					
Specimen No.	ILSS-1	ILSS-2	ILSS-3	ILSS-4	ILSS-5
Average width of the specimen (mm)	14.66	14.72	15.19	14.87	14.95
Average length of the failed area (mm)	6.36	6.30	6.31	6.32	6.40
Failed area (mm ²)	93.22	92.74	95.79	93.98	95.63



Figure 4.16 Specimens failed under the interlaminar shear stress.

All the five specimens failed across the desired notched mid-section as shown in Figure 4.16. The maximum applied loads and the corresponding interlaminar shear strengths of the notched specimens are summarized in Table 4.7.

Table 4.7 Interlaminar shear strength of M21/T700 UD material

		Maximum applied load (N)	Failed area (mm ²)	Interlaminar shear strength (MPa)
[0°] ₁₂ interlaminar shear strength test specimen	ILSS-1	3875	93.22	83.14
	ILSS-2	3689	92.74	79.56
	ILSS-3	4077.5	95.79	85.13
	ILSS-4	3797	93.98	80.81
	ILSS-5	4107	95.63	85.90
	Average interlaminar shear strength			

The dimensions of the $[\pm 45^\circ]_{2s}$ test specimens which were used to determine the in-plane shear modulus and strength of the unidirectional material are summarized in Table 4.8.

Table 4.8 Dimensions of the in-plane shear modulus test specimens

	$[\pm 45^\circ]_{2s}$ in-plane shear modulus test specimen					$[\pm 45^\circ]_{2s}$ in-plane shear strength test specimen				
	3.1	3.2	3.3	3.4	3.5	3.6	3.7	3.8	3.9	3.10
Average width (mm)	24.67	24.62	24.87	24.79	24.73	25.03	24.86	25.16	25.12	25.10
Average thickness (mm)	2.05	2.07	2.10	2.06	2.12	2.09	2.11	2.09	2.10	2.12
Cross-section area (mm ²)	50.57	50.96	52.23	51.07	52.43	52.31	52.46	52.59	52.75	53.21

Five $[\pm 45^\circ]_{2s}$ specimens with strain gauge bonded were tested following the test procedure described in section 4.2.2 to determine the in-plane shear modulus of elasticity, G_{12} . The test results are shown in Figure 4.17.

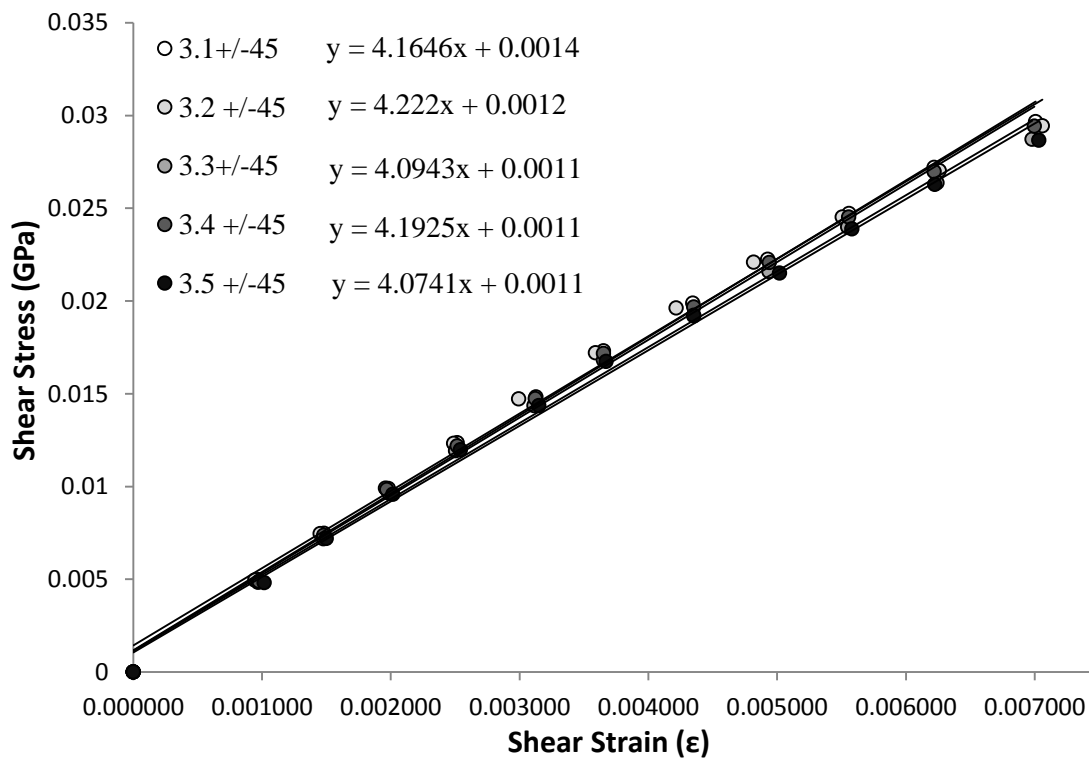


Figure 4.17 Test results of the in-plane shear test specimens.

Figure 4.17 shows the elastic parts of the shear stress-strain curves for $[\pm 45^\circ]_{2s}$ specimens under uniaxial tensile loads. Equation 4.1 was used to convert the applied load and the directional strains to the shear stress and strain. Moreover, the linear correlation was applied to the converted test data and thus the in-plane shear modulus was equal to the gradient of the linear equation. Table 4.9 summaries the shear modulus of the tested specimen.

Table 4.9 In-plane shear modulus of M21/T700 UD material

$[\pm 45^\circ]_{2s}$ in-plane shear modulus test specimen	3.1	3.2	3.3	3.4	3.5	Average value
In-plane shear modulus (GPa)	4.16	4.22	4.09	4.19	4.07	4.15

The other five $[\pm 45^\circ]_{2s}$ specimens without strain gauge bonded were tested following the test procedure described in section 4.2.2 to determine the in-plane shear strength, τ_{12} . The test results are presented in Table 4.10.

Table 4.10 In-plane shear strength of M21/T700 UD material.

	Maximum applied load (N)	Cross-section area (mm ²)	In-plane shear strength (MPa)
$[\pm 45^\circ]_{2s}$ in-plane shear strength test specimen	3.6	8950	52.31
	3.7	8889	52.46
	3.8	8834	52.59
	3.9	8971	52.75
	3.10	8924	53.21
	Average in-plane shear strength		

4.4 Summary

The tensile and in-plane shear material properties of the unidirectional materials measured by the current study are summarized in Table 4.11.

Literature results in terms of the manufacturer supplied product data [125] and the test data obtained by the conventional experimental tests presented in the literature [126] are also included in the table to provide further validation on the current test results.

Table 4.11 Summary of tensile and shear properties of M21/T700 UD material

Mechanical properties	Notation	Test result	Literature results	
			Product data	Reference data
			[125]	[126]
Longitudinal tensile modulus (GPa)	E_{1t}	131.95	148	130
Transverse tensile modulus (GPa)	E_{2t}	7.53	N/A	7.7
Longitudinal tensile strength (MPa)	σ_{1t}	2116.60	2375	N/A
Transverse tensile strength (MPa)	σ_{2t}	44.60	N/A	50
Major Poisson's ratio	ν_{12}	0.253	N/A	0.33
Minor Poisson's ratio	ν_{21}	0.0127	N/A	N/A
In-plane shear modulus (GPa)	G_{12}	4.15	4.5	4.75
In-plane shear strength (MPa)	τ_{12}	84.63	95	90
Interlaminar shear strength (MPa)	ILSS	82.91	105	N/A

Most of test results achieved in the current study agreed well with the literature results. In general, the test results differed to the literature results by around 10%. Such deviations are considered acceptable in industry due to the inherent experimental error caused by the differences in calibration of the test equipment and the preparation of the test specimen. It is noticed that the agreement between the current test result and the literature test result was slightly better than the one between the current test result and the manufacturer supplied product data. This could be attributed to the different test standards used in these experimental works. The overall test of the measurement of the tensile and shear properties of the unidirectional material has been a success. The test results will be used in the subsequent study on the low-velocity impact response of composite laminates for the project.

Table 4.12 Summary of compressive properties and fracture mechanics of M21/T700 UD material [125, 126]

Mechanical properties	Notation	Literature results	
		Product data	Reference data
		[125]	[126]
Longitudinal compressive modulus (GPa)	E_{1c}	119	100
Longitudinal compressive strength (MPa)	σ_{1c}	1465	N/A
Mode I critical energy release rate (J/m ²)	G_{Ic}	N/A	500
Mode II critical energy release rate (J/m ²)	G_{IIc}	N/A	1600

Several other material properties of the unidirectional material are required in the current study, such as the compressive property and the fracture toughness. Due to the time constraint of the project, these data have not been measure in the project. Literature results [125, 126] shown in Table 4.12 will be used when necessary.

CHAPTER 5 Results of Composite Laminates under LVI

This chapter presents the results of composite laminates subjected to low-velocity impact. The investigation was conducted in both experimental and numerical approaches to develop a further understanding of the damage mechanisms and impact response of composite laminates under low-velocity impact. Efforts were directed to the study of delamination threshold load, a load above which the significant increment of delamination and thus large residual strength degradation may occur. The effect of delamination initiation on the load bearing capacity of impacted composite laminate was re-evaluated in the current study. The re-evaluated effect of delamination initiation in composite laminates could help to improve the conservative design philosophy of composite laminates.

5.1 Instrumented Drop-weight Test

In the experimental approach, the instrumented drop weight tests were carried out on different impact test specimens at different initial kinetic energy levels. The effects of laminates thickness, lay-up configuration, repeated impact and curing temperature of laminates on the impact response and failure mechanisms of composite laminates under low-velocity transverse impact were examined.

5.1.1 Specimen Preparation and Test Set-up

A series of instrumented drop weight tests were conducted in accordance with the ASTM D7136/D7136M-05 test standard [119] in terms of the specimen preparation and test set-up.

The test specimens were made of the same carbon/epoxy composite system (Hexply T700/M21) as those tested in Chapter 4 to determine the basic mechanical properties of this UD material. The fabrication of impact test specimen was conducted in the same procedure as described in Section 4.1.

Table 5.1 shows the different lay-up configurations to study the effects of the laminates thickness and lay-up configuration on the impact response of composite laminates.

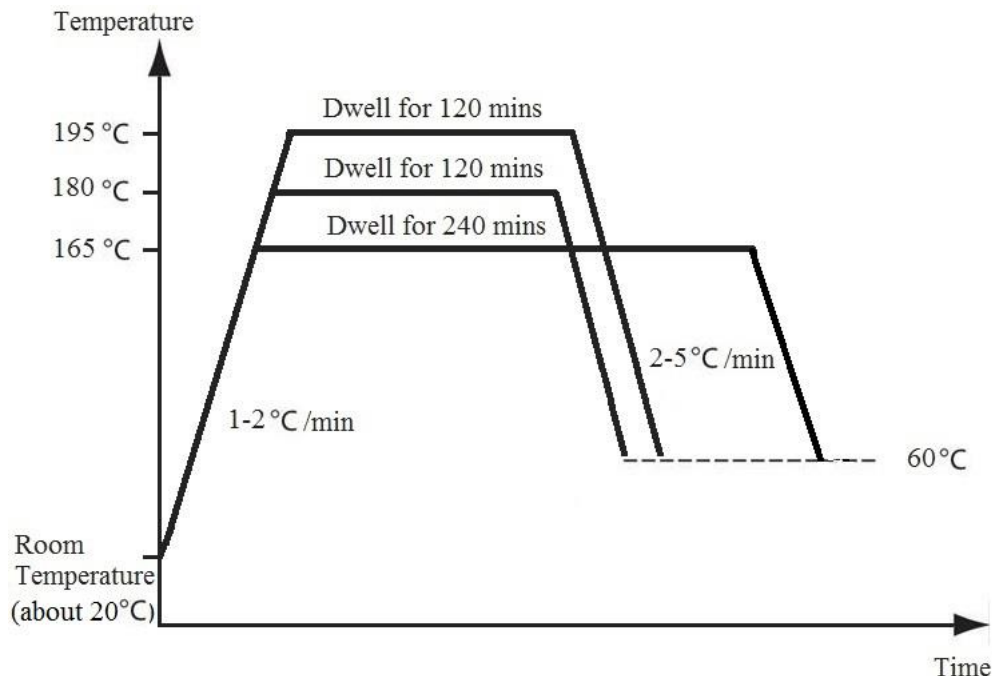
Table 5.1 Lay-up configurations of the impact test specimens

Thickness (mm)	Cross-ply lay-up	Quasi-isotropic lay-up
2	$[0/90_2/0]_s$	$[\pm 45/0/90]_s$
3	$[0_2/90_3/0]_s$	
4	$[0_2/90_3/0_2/90]_s$	$[\pm 45/0_2/90_2/\pm 45]_s$
5	$[0_2/90_3/0_2/90_2/0]_s$	

Four different laminates thicknesses (2 mm, 3 mm, 4 mm, and 5 mm) and two different lay-up types (cross-ply and quasi-isotropic) were used to prepare the impact test specimens. The lay-up configurations were determined by the following lay-up criteria of Airbus Operations Ltd (UK) [127]:

- Put +45° and -45° layers together as the top and bottom layers
- Symmetrical lay-up with no more than 3 same layers together

To investigate the effect of curing temperature on the impact response of composite laminates, different curing temperatures of 165°C, 180°C, and 195°C were used in the autoclave curing process of the 4mm quasi-isotropic specimens.

**Figure 5.1 Curing cycles with the normal and the changed curing temperatures.**

The curing cycles with the normal (180°C) and the changed (165°C and 195°C) curing temperatures are shown in Figure 5.1. The same ramp-up rates were used in all the three curing cycles to achieve the different curing temperatures. Meanwhile, the curing temperature holding period for the 195°C curing condition was set to be the same as it for the curing cycle with normal curing temperature, which was 120 minutes. However, the curing temperature holding period for the 165°C curing condition was set to 240 minutes, which is the double of the normal holding period. It is because of the complete curing of the resin takes much longer time, when the specimen is cured at a lower curing temperature. The cool-down rate for all the three curing conditions was set to 2-5 °C/min.

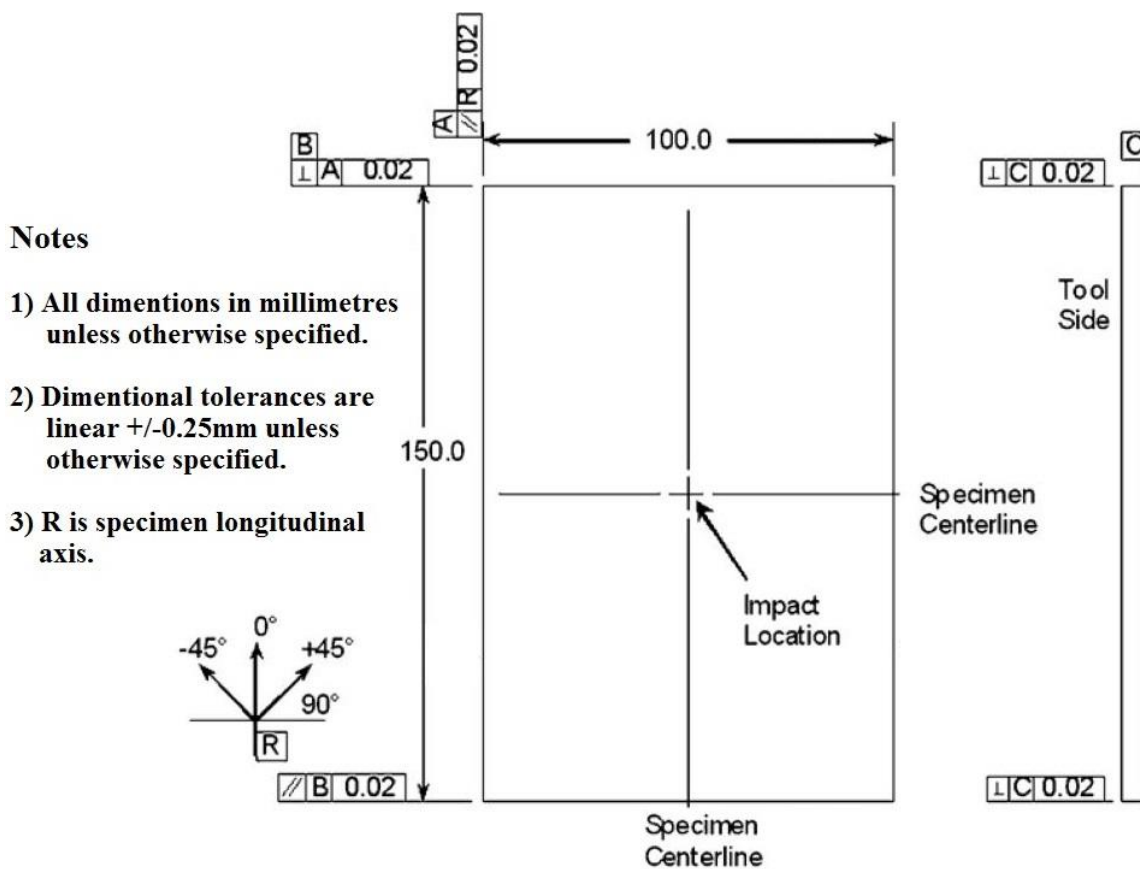


Figure 5.2 Schematic illustration of the drop-weight impact test specimen [119].

Figure 5.2 shows the schematic of the drop-weight test specimen in accordance with the ASTM test standard [119]. The cured composite plates were cut into the required shape following the same cutting procedure as described in Section 4.2. The standard required the rectangular drop-weight impact test specimen (150mm by 100mm) with the longitudinal axis in the 0° direction. Moreover, the prepared specimens were impacted under various impact

energy levels. To ensure the reliability of the test results, at least three specimens were prepared for each lay-up configuration and each impact energy level.

During the drop-weight test, the test specimen was clamped by the impact support fixture as illustrated in Figure 5.3, which was in accordance with the ASTM D7136 test standard [119]. The fixture base was a mild steel plate with dimensions of 300mm × 300mm × 24mm. There was a rectangular cut-out in the middle of the fixture base with dimensions of 125mm by 75mm. Four guiding pins were used to ensure that the impact test specimen can be positioned correctly for the test. The specimen was securely clamped in the fixture base by four toggle clamps to prevent movement during the test. The centreline of the toggle clamp was 25mm away from the shorter edge of the test specimen and the clamped rubber tip was 6mm centred from the edge of cut-out.

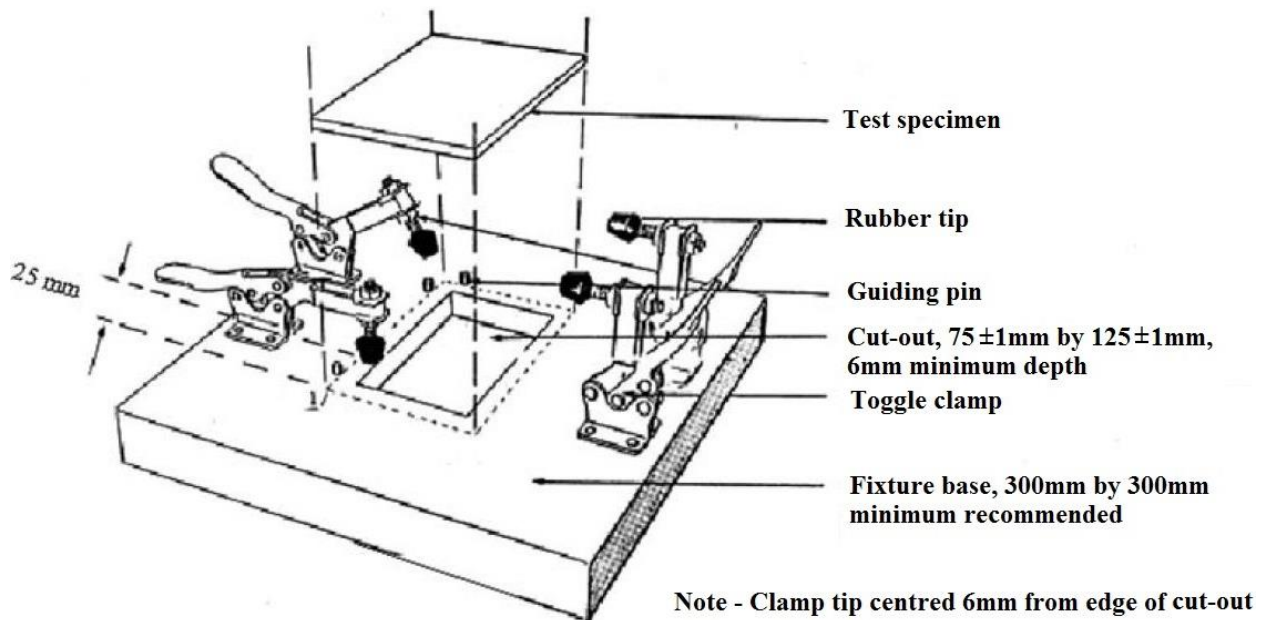


Figure 5.3 Schematic illustration of the impact support fixture [119].

The low-velocity impact test was performed by using the CEAST drop-weight test rig as shown in Figure 5.4. The impact test rig includes a drop tower, a projectile, a base to support the fixture plate and a data acquisition system. The projectile consisting of an impact rod with a semi-sphere shaped impactor head drops with the support frame. The total mass of the drop-weight was 11.8kg. The diameter of the semi-sphere shaped impactor head was 20mm. The projectile could slide freely along the two guiding rails. An electrical motor at the top of the drop tower was used to adjust the drop-weight height to achieve the required impact energy, E_i , calculated by the following equation:

$$E_i = mgh \quad (5.1)$$

where, m is the total mass of the drop-weight, g is the acceleration of the gravity, and h is the drop weight height. In order to prevent multiple impacts on the specimen, an electrical capture system was also involved in the test rig to automatically capture the rebounded projectile.

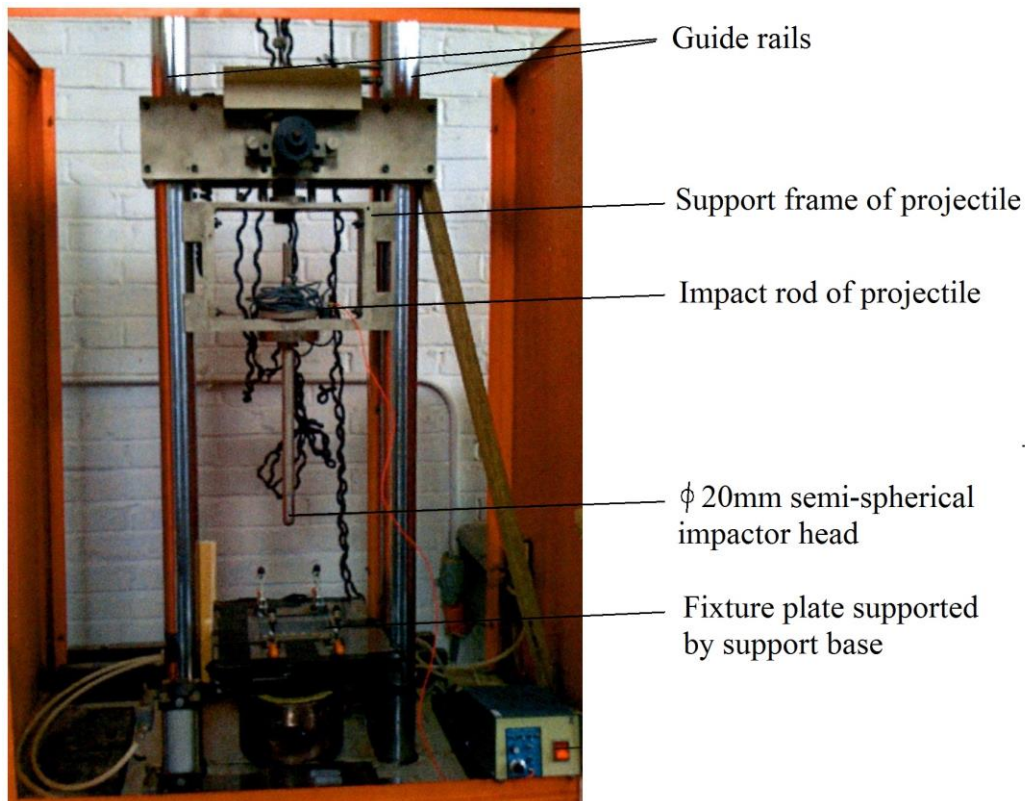


Figure 5.4 CEAST drop-weight test rig.

The impact force acquisition system is shown schematically in Figure 5.5. The principle of the impact force history acquisition system was the relation between the applied load and the deformation of the impactor head. Strain gauge was bonded close to the impactor head to detect the impactor head deformation. The strain gauge indicator was plugged into a PicoScope 3000 series PC oscilloscope to convert the analogue signal to the digital signal. The oscilloscope was then connected to a PC to record the test data and display the test result history of voltage (mV) against time (ms). The voltage displayed in the test result needed was then converted into the impact force through the calibration of the impactor and the strain gauge indicator.

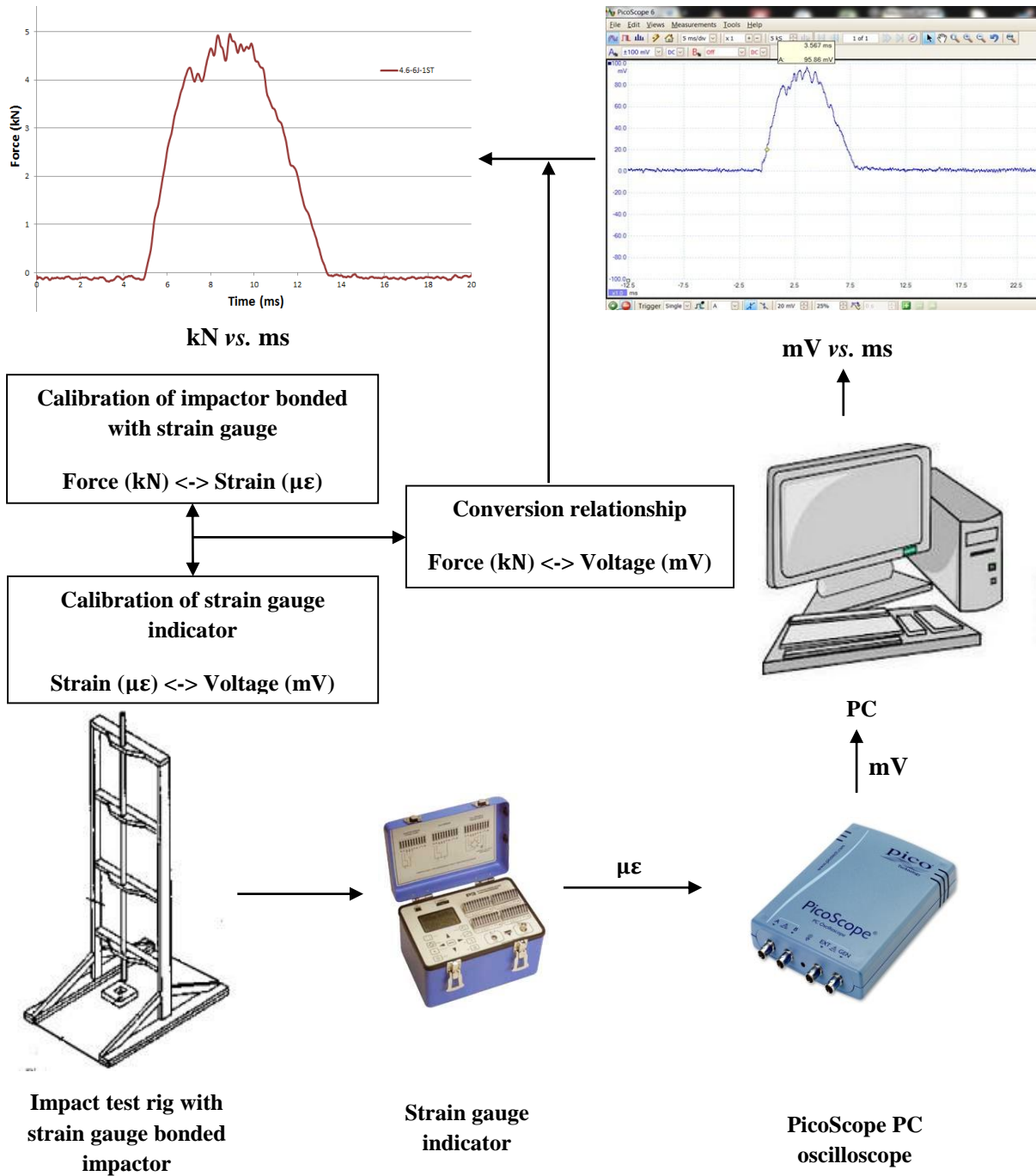


Figure 5.5 Schematic illustration of an impact force acquisition system.

The impactor was calibrated by a compression test to determine the relationship between the axial compression load and the impactor deformation. The calibration of the impactor was conducted in the Hounsfield universal test machine as shown in Figure 5.6.



Figure 5.6 Calibration of the impactor with strain gauge bonded.

The recorded test data and the resulting calibration curve are shown in Figure 5.7. The linear relationship between the impactor deformation and applied load was clear.

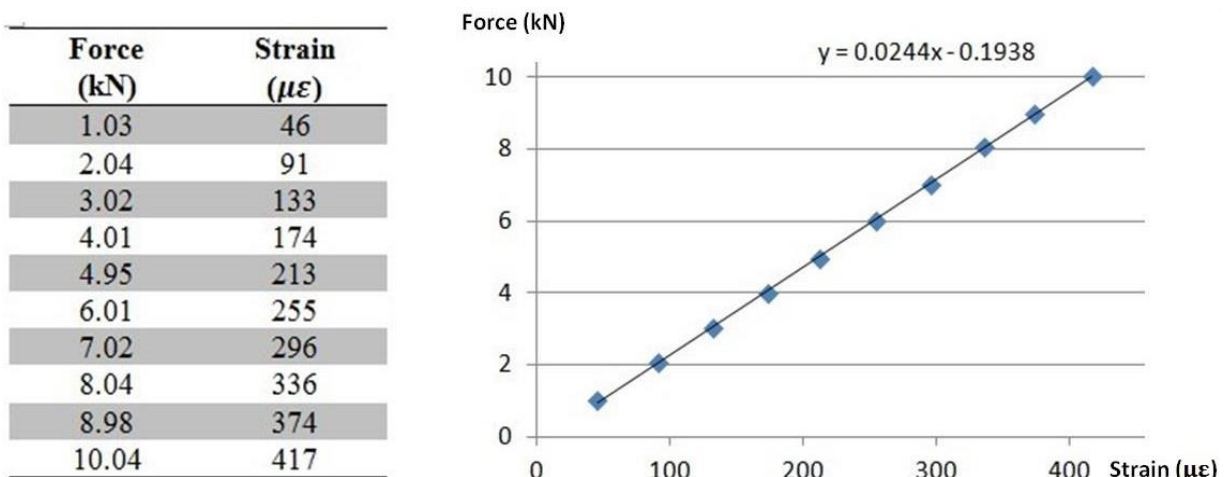


Figure 5.7 Test data of the impactor calibration and its resulting calibration curve.

In addition, the relationship between the analogue signal exported from the strain gauge indicator and the digital signal processed by the oscilloscope also needed to be carefully calibrated before each impact test due to the difference among individual strain gauge indicators. The calibration was conducted by importing different analogue signals (strain in $\mu\epsilon$)

into the oscilloscope and the digital signals (voltage in mV) recorded on PC. Figure 5.8 shows the recorded data and the resulting calibration curve.

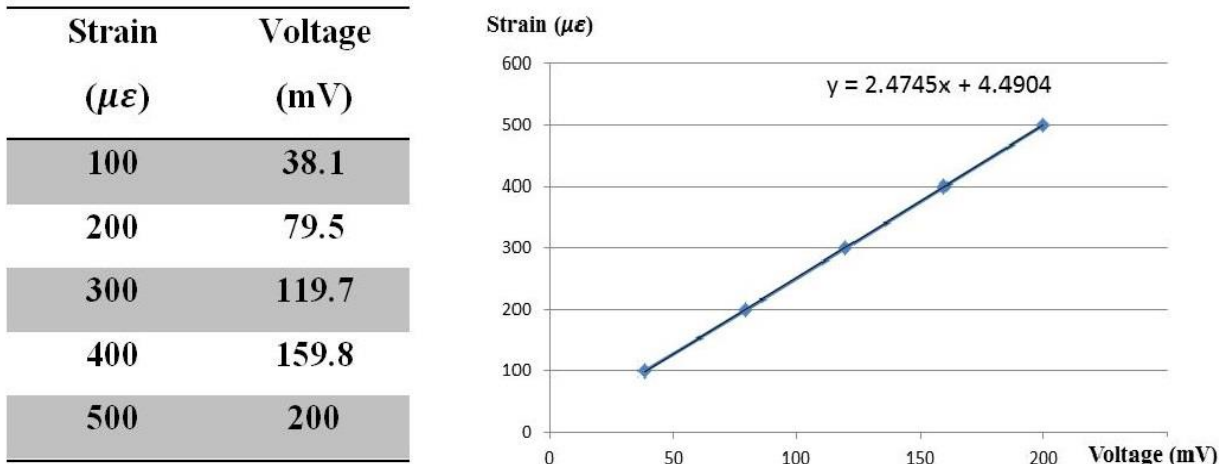


Figure 5.8 Recorded data of a strain gauge indicator calibration and its resulting calibration curve.

Therefore, the conversion between the digital signal generated by the oscilloscope and the impact force was determined by combining the calibration results of the impactor and strain gauge indicator. The relationship between the voltage and the impactor force was expressed as:

$$Y = 0.0244 \times (2.4745X + 4.4904) - 0.1938 = 0.06038X - 0.08423 \quad (5.2)$$

where, X is the voltage in mV as the digital signal generated by the PC oscilloscope, Y is the corresponding impact force in kN.

However, the impact force history, as illustrated in Figure 5.9(a) as the impact force history of the impact test conducted on a 4mm specimen under 9J impact energy, was quite noisy due to the high frequency noise and the unwanted vibrations. The high frequency noise needs to be filtered out to provide meaningful information on the impact response of the tested composite laminates.

Therefore, the raw data were filtered by LS-PREPSOT software to minimize the noise, in which a COS 108Hz filter was used. Figure 5.9(b) shows the same impact force history after the data filtering operation. The filtered impact force history was clearer than that from the unfiltered raw data. It was then possible to carry out meaningful assessment on the impact response without the disturbance of the high frequency noise.

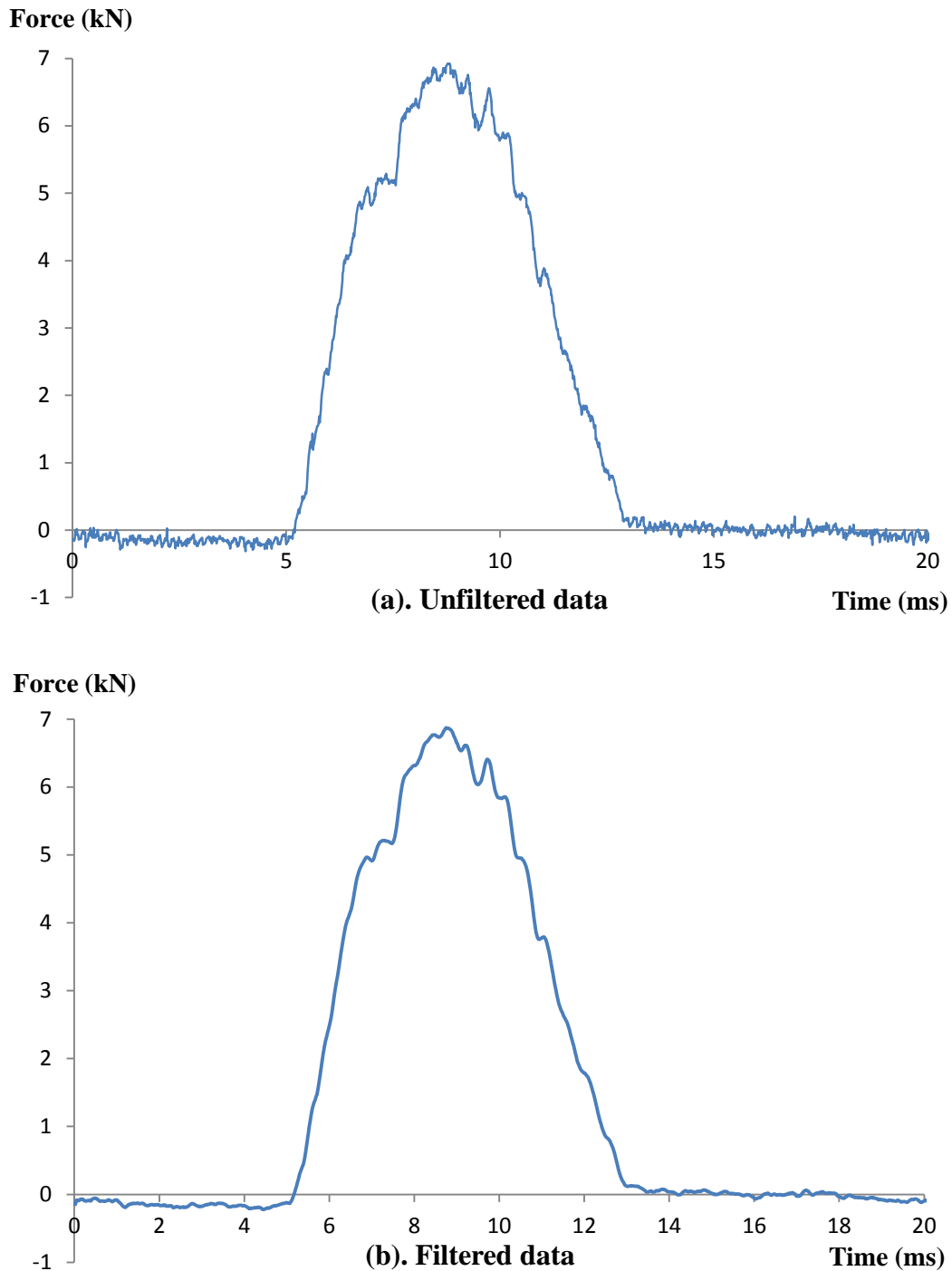


Figure 5.9 Impact force history of a 4mm specimen under 9J impact energy.

Further, the filtered impact force history, $P(t)$, was used to calculate the history of the acceleration, $a(t)$, the velocity, $v(t)$, the displacement, $d(t)$, and the energy, $E(t)$. The equations used in the calculations were shown as below:

$$a(t) = \frac{P(t)}{m} - g \quad (5.3)$$

$$v(t) = v_0 - \int a(t) dt \quad (5.4)$$

$$d(t) = \int v(t) dt \quad (5.5)$$

$$E(t) = \int d(t)P(t) dt \quad (5.6)$$

where, v_0 is the initial velocity of the projectile immediately before the impact contact.

5.1.2 Effect of Thickness on Impact Response of Composite Laminates

The impact force history of the low-velocity impact event provided important information regarding the damage initiation and propagation. It has been documented by many investigators [10, 11, 14] that the sudden load drop in impact force history was associated with the stiffness reduction of laminates due to the initiation of delamination.

In this study, detailed impact force histories were obtained under various test conditions following the test procedure as described in Section 5.1.1 to catch the possible delamination threshold load. The thickness effect on the impact response of composite laminate was explored by testing the specimens with cross-ply lay-up configurations of $[0/90_2/0]_s$ (2mm), $[0_2/90_3/0]_s$ (3mm), $[0_2/90_3/0_2/90]_s$ (4mm), and $[0_2/90_3/0_2/90_2/0]_s$ (5mm) under various impact energy levels.

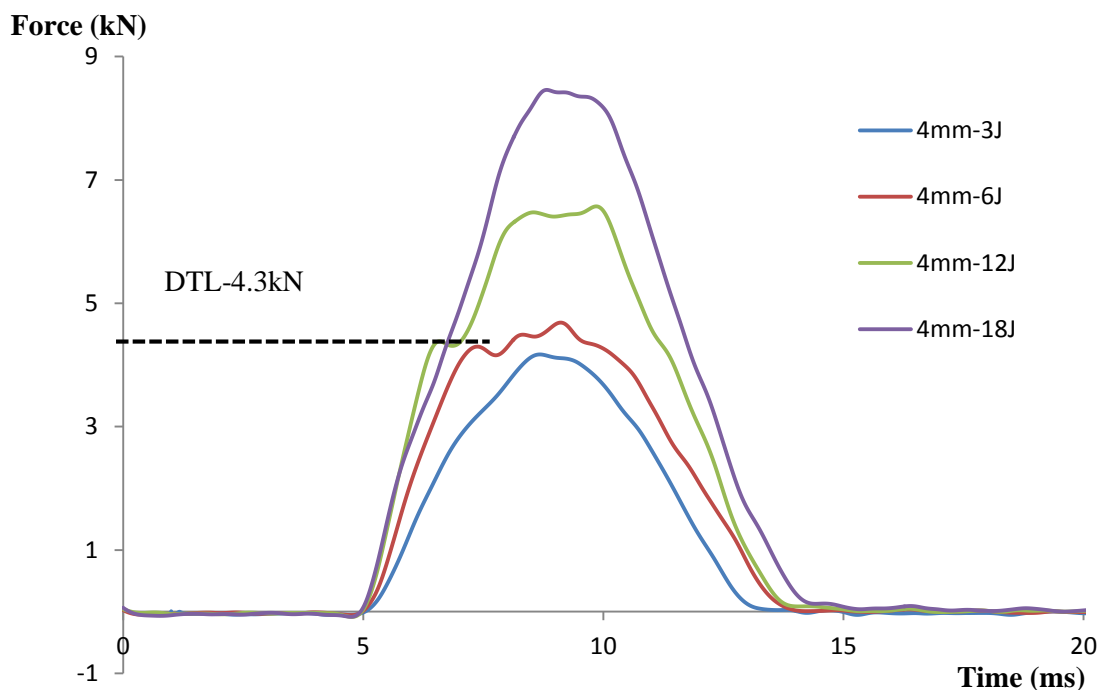


Figure 5.10 Filtered impact force histories of 4mm specimens with cross-ply lay-up configuration.

Figure 5.10 shows the filtered impact force histories of 4mm thick specimens under four different impact energy levels. The corresponding un-filtered impact force histories are also presented in Appendix I as reference. There is no noticeable fluctuation observed in the impact force history under the impact energy of 3J when the peak impact force had not exceeded a critical load. The smooth impact force history curve indicates that the impact under the impact energy of 3J caused little critical damage (*e.g.* delamination). On the contrary, clear sudden drops in the impact force can be seen for the specimens under the impact energies of 6J and 12J once the critical load had been reached. The DTL value of the 4mm thick laminates with cross-ply lay-up configuration was approximately determined as 4.3kN since the same DTL value obtained under different impact energy levels, which demonstrates that the DTL does exist for the low-velocity impact of composite laminates.

It is however interesting to note that the impact force history under a relatively higher impact energy of 18J does not show a clear dip in the impact force. The overall impact force history curve is also smoother than the ones under the impact energies of 6J and 12J with the existence of DTL clearly visible. But dramatic damages, including delamination and fibre breakage, were found in the specimen. As this observation may look like in contradictory to the concept of the DTL, tests were repeated to check the results and similar observations were obtained. Considering the current test results under 6J and 12J and the subsequent test results of specimens with different thicknesses, it was concluded that the concept of the DTL is still valid. The possible explanation for the observation under 18J impact is that the relative influence of the delamination initiation on the impact response of the specimen became less significant under relatively higher energy levels. The specimen stiffness degradation is caused by not only the delamination initiation, but also the delamination propagation and other damage types under high impact energy level. The combined effect of delamination initiation and damage propagation/other damage types under high impact energy levels may smooth out the load drop associated with delamination initiation. It is suggested that there might exist a suitable range of ratio of the impact energy to the laminates stiffness/thickness to determine the DTL reliably through the impact force history. As a result, care should be exercised in the detection of the DTL using the impact force histories.

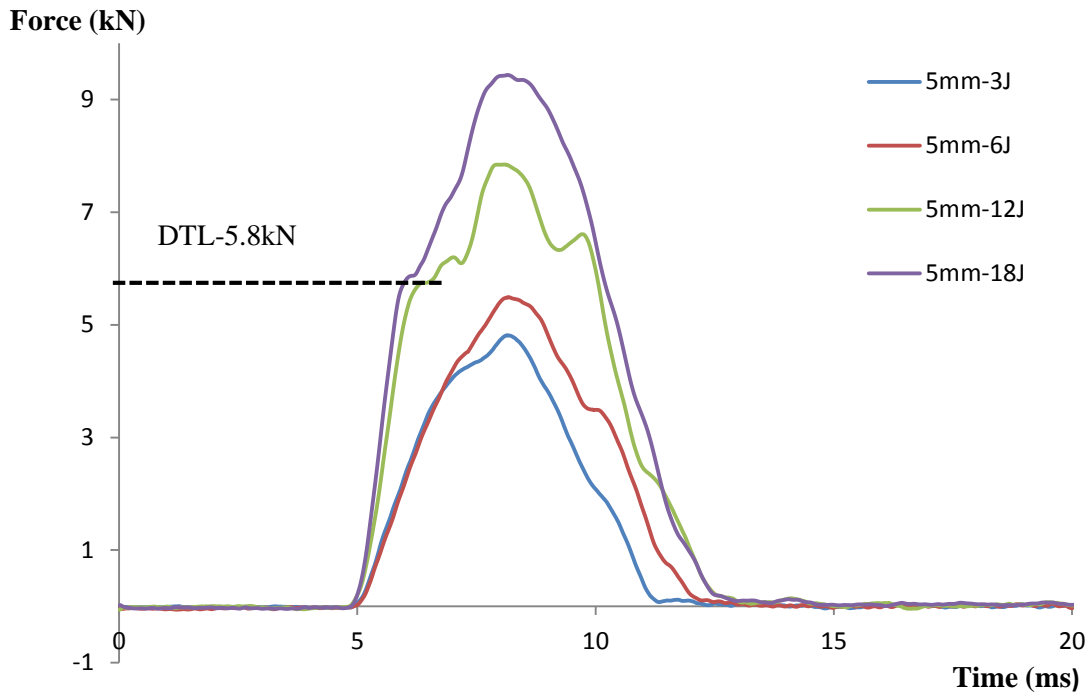


Figure 5.11 Filtered impact force histories of 5mm specimens with cross-ply lay-up configuration.

Figure 5.11 shows the filtered impact force histories of 5mm thick specimens under various impact energy levels. The corresponding un-filtered impact force histories are also presented in Appendix I as reference. Reasonable results were achieved in terms of the existence of the DTL and the overall trend in the detection of the DTL using the impact force history. The existence of the DTL is proved by the same sudden load drops observed in the 12J and 18J impact force histories. The delamination threshold load of 5mm thick specimen was determined at a higher value (around 5.8kN) than that of 4mm thick specimen (around 4.3kN), which indicates the delamination resistance of composite laminate is linked to the specimen thickness. However, it is noticed that the load dip in the 18J impact force history is not as significant as that in the 12J impact force history. This scenario supports further the previous speculation based on the 4mm specimen results that there might exist a suitable range of ratio of the impact energy to the laminates stiffness/thickness to determine the DTL reliably through the impact force history. In other words, different responses of the impacted laminates, in terms of the existence of the sudden load drop, might be triggered under the same impact energy level of 18J due to different laminates stiffnesses (thicknesses of 4mm and 5mm). Moreover, no delamination was initiated by the impact events under the relatively

lower impact energy levels of 3J and 6J since neither of the peak impact forces exceeded the delamination threshold load.

More tests were conducted on the thinner specimens with thicknesses of 2mm and 3mm to study the thickness effect on the impact response of composite laminates, especially for the existence of DTL and its detectability using the impact force histories.

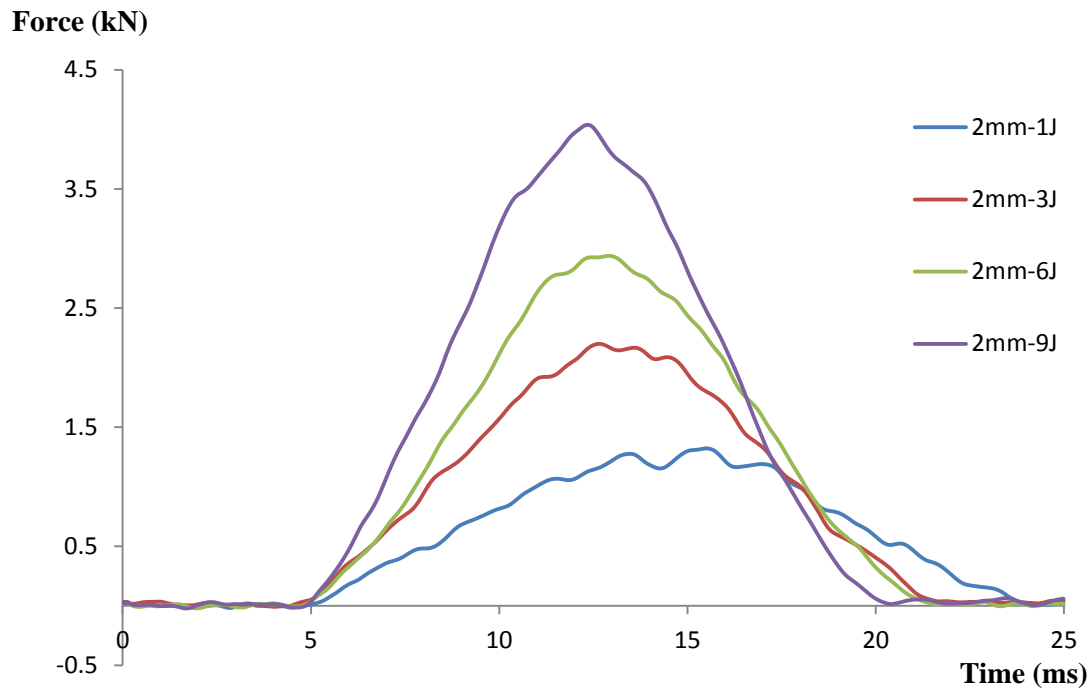


Figure 5.12 Filtered impact force histories of 2mm specimens with cross-ply lay-up configuration.

Figure 5.12 shows the filtered impact force histories of 2mm thick specimens under various impact energy levels from 1J to 9J. The corresponding un-filtered impact force histories are also presented in Appendix I as reference. It can be seen clearly that, while the maximum impact force increases with the increment of the impact energy, no clear indication of the initiation of the delamination can be reliably determined based on the impact force histories. To confirm the observations, repeated tests were carried out on the 2mm thick specimens and similar results were obtained. The possible reason is that the relatively lower stiffness of the 2mm specimen makes the thin plate more flexible than the thick one. For the case of the thin specimen subjected to the impact with relatively lower impact energy, most of the impact energy will be dissipated through the elastic deformation rather than being absorbed by the damage mechanism such as the initiation of the delamination in which case the internal stress in the laminates may not be high enough to trigger an initial delamination. For the impact

event of the thin laminates under relatively higher impact energy, damages such as delamination propagation and fibre breakage follow closely after the delamination initiation, which makes the load drop due to the initiation of the delamination less obvious and thus difficult to detect. As such, alternative method should be considered to determine the DTL for the thin laminates.

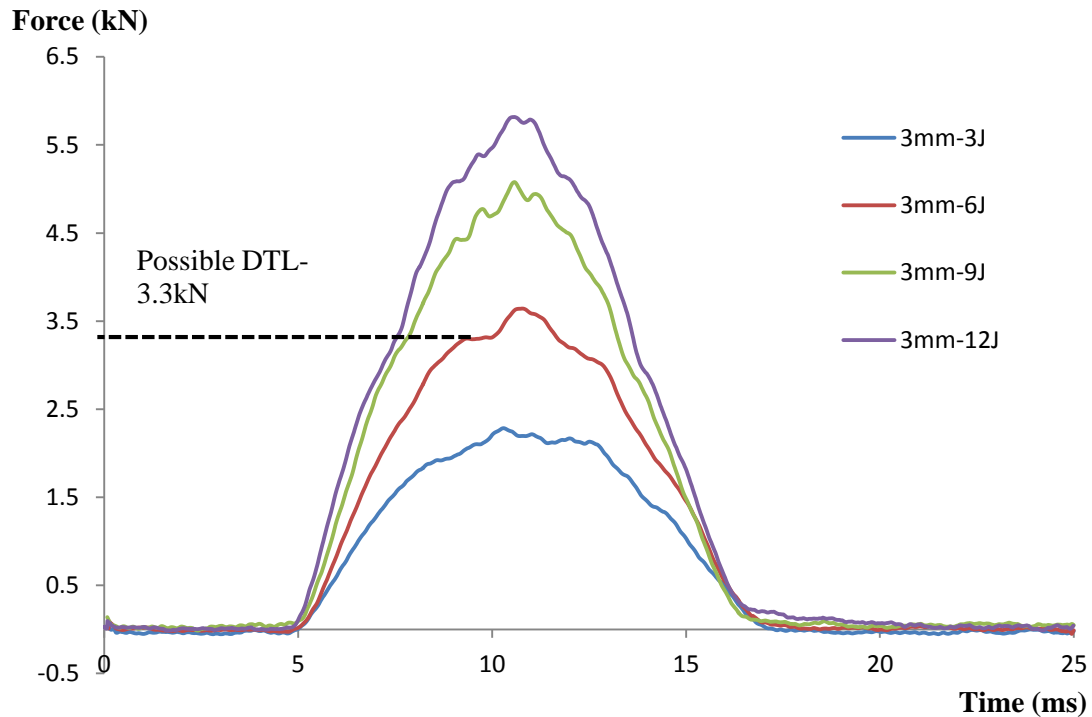


Figure 5.13 Filtered impact force histories of 3mm specimens with cross-ply lay-up configuration.

Figure 5.13 shows the filtered impact force histories of 3mm thick specimens under four impact energy levels. The corresponding un-filtered impact force histories are also presented in Appendix I as reference. It is anticipated that the impact response of 3mm specimen is somewhere between the impact responses of 2mm thin laminates and 4mm thick laminates. Although the impact force histories of 3mm specimens are smoother than the load curves of 4mm specimen, the impact force dip can still be observed at around 3.3kN in the impact force history under 6J impact energy. The load dip is however barely detectable from the impact force history under higher energy levels of 9J and 12J. It shows that the impact energy is absorbed by the combination of the elastic deformation and the damage mechanisms for the 3mm laminates. Energy absorbed by the damage mechanism becomes more significant than that absorbed by elastic deformation with the increase of laminates stiffness/thickness. It is

clear that the impact response of composite laminate is controlled by the interaction between the impact energy level and the laminates stiffness.

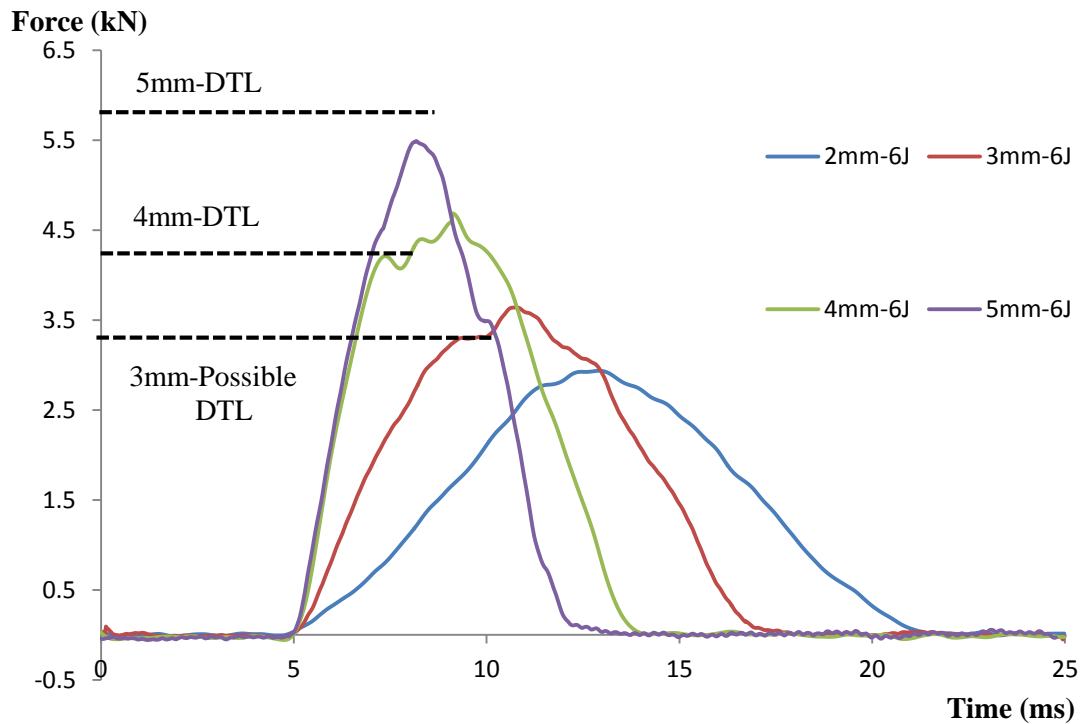


Figure 5.14 Filtered impact force histories of test specimens with various thicknesses under 6J impact energy level.

The thickness effect on the impact response of composite laminate is shown in Figure 5.14 by comparing the impact force histories of the specimens with four different thicknesses under the same impact energy level of 6J. It can be seen clearly that the peak impact force will increase when the laminates thickness is increased and the impact duration decreases with the increase of the laminates thickness. However, no obvious sudden load drop can be observed for either the thick (5mm) or the thin (2mm) specimens under the current impact energy level. For the thick specimen with 5mm thickness, the damage resistance of the laminate is high enough to prevent any delamination damage since the peak impact force is still less than the DTL value. For the thin specimen with 2mm thickness, most of the impact energy is absorbed by the elastic deformation. The bending stress in the thin laminates may not be high enough to trigger the delamination. The load dip can however be observed in the impact force histories of the specimens with 4mm and 3mm thicknesses. It further proves that the DTL can be determined through the impact force histories but special care should be taken due to the

possible existence of a suitable range of ratio of the impact energy to the laminates stiffness to determine the DTL reliably.

5.1.3 Effect of Repeated Impact on Impact Response of Composite Laminates

The effect of repeated impact on the impact response of composite laminate was investigated by conducting repeated impact on the post-impact specimen at the same impact position and under the same impact energy level. In particular, the same cross-ply specimens with four different thicknesses tested in Section 5.1.2 were experienced a repeated impact under the same impact energy level. The number of the repeated impact was set to 3 to 5, depending on the correlations among the repeated impact force histories. In the current study, the repeated impact force history curve was presented by taking the mean value of all the repeated impact test data to reflect the effect of repeated impact more reliably.

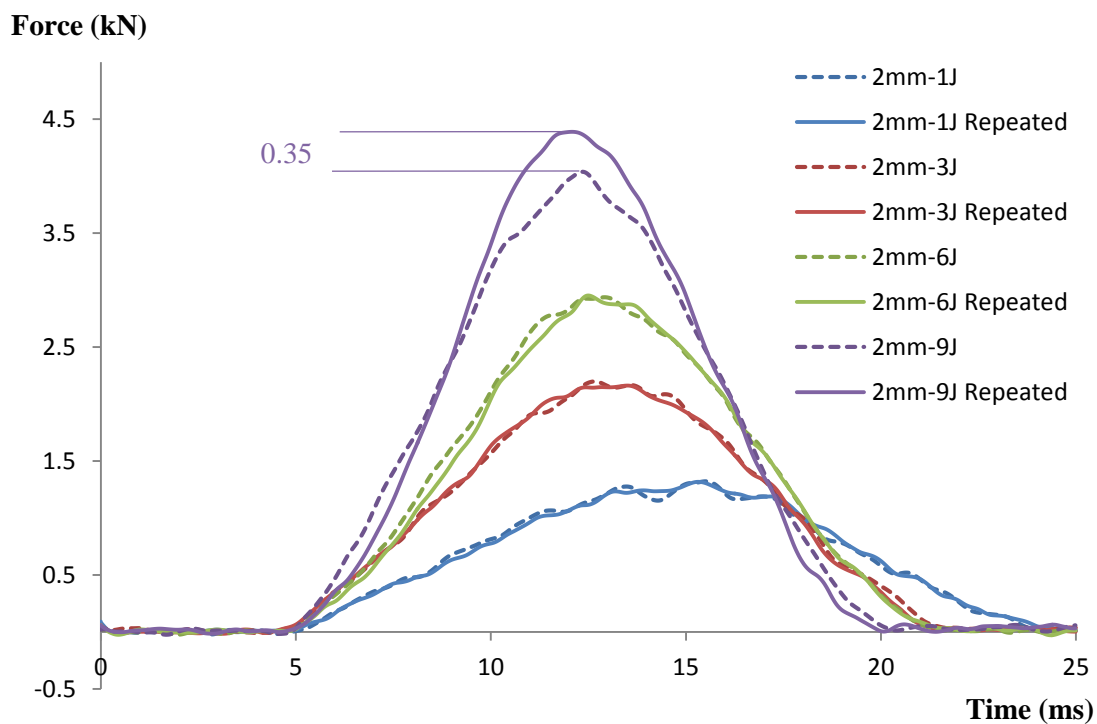


Figure 5.15 Filtered first and repeated impact force histories of 2mm specimens with cross-ply lay-up configuration.

Figure 5.15 shows the filtered first and repeated impact force histories of 2mm cross-ply specimens under various impact energy levels. It can be seen clearly that the repeated impact on the same specimen does not affect the impact duration. The repeated impact force history and the first impact force history are almost identical, especially under the relatively lower

impact energy levels of 1J, 3J, and 6J. This indicates that little damage has been introduced into the laminates by the first impact under the relatively lower energy level, which agrees well with the previous assumption that most of the impact energy is absorbed through the elastic deformation, not through the damage mechanism, in the thin laminates under the relatively lower impact energy level. It is however interesting to note that the maximum impact force has been increased by about 0.35kN (~8.7%) during the repeated impact under the relatively higher energy level of 9J. This is unexpected and tests were hence repeated. Similar results were obtained. This is clearly associated with the introduction of impact damage under the relatively higher energy. The existence of the initial delamination and other damage types in the laminates affect the impact responses of the respected impacts.

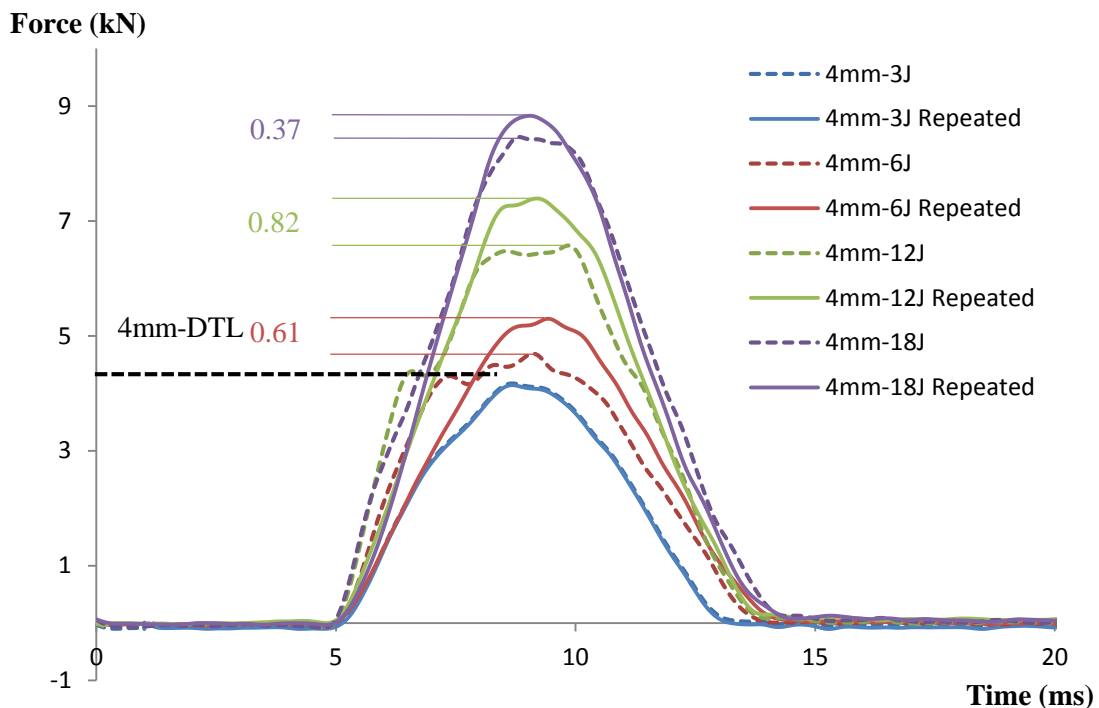


Figure 5.16 Filtered first and repeated impact force histories of 4mm specimens with cross-ply lay-up configuration.

Figure 5.16 shows a further study in the effect of the repeated impact on the impact response using 4mm specimens with cross-ply lay-up configuration under various impact energy levels. It can be seen clearly that DTL plays an important role in affecting the impact response of composite laminates under repeated impact.

For the impact case under the 3J impact energy level, the maximum load of the first impact is less than the DTL value; there is no delamination initiated by the first impact. Similar to the

observations from the 2mm specimens, the first and the repeated impact force histories are almost identical under the low impact energy of 3J. The clear difference between the first and the repeated impact force histories has also been observed for the 4mm specimens when the delamination threshold load is exceeded during the first impact under higher impact energy level. Compared with the 2mm specimen results, it is noticed that the impact force curve of the repeated impact becomes smoother in terms of the impact history of the first impact, which could indicate that there is no propagation of the initial delamination caused by the first impact during the repeated impact under the same impact energy level.

Similar to the results of the 2mm specimen, the maximum loads of the repeated impact histories under 6J and 12J was increased by 0.61kN (~13.0%) and 0.82kN (~12.5%) compared with those of the first impact histories.

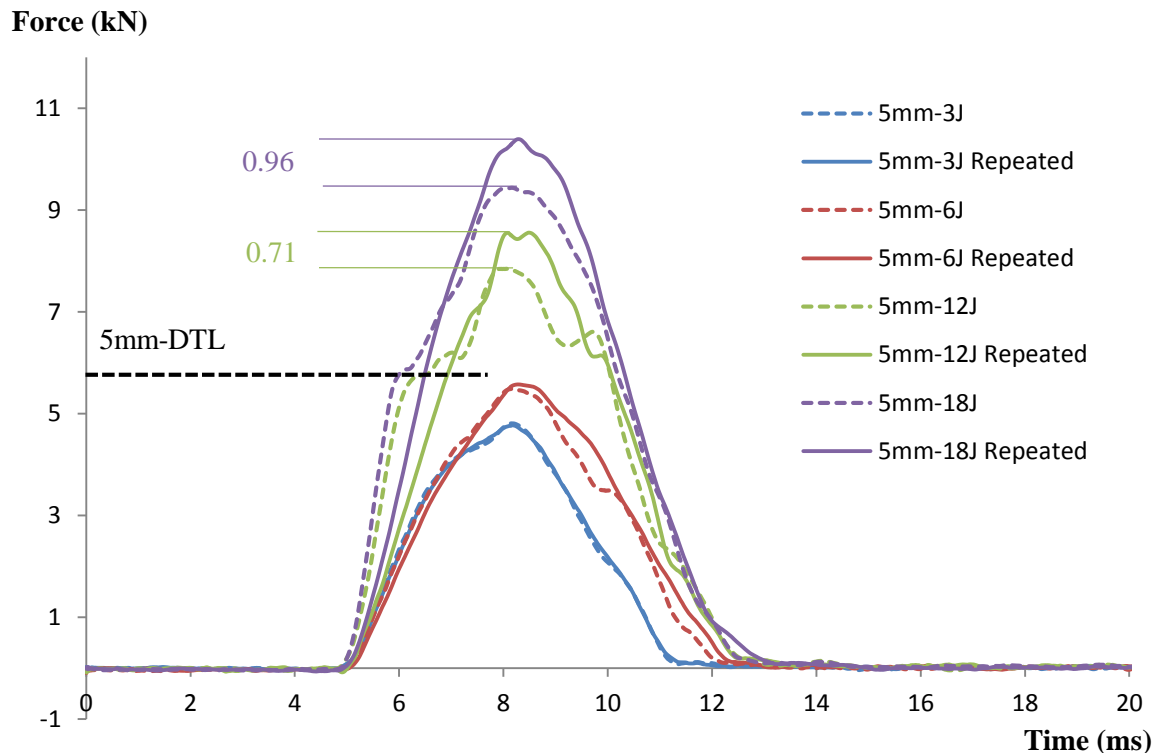


Figure 5.17 Filtered first and repeated impact force histories of 5mm specimens with cross-ply lay-up configuration.

Figure 5.17 shows the filtered first and repeated impact force histories of 5mm thick specimens with cross-ply lay-up configurations. The overall trend of the test results agrees well with the test results achieved from the 2mm and 4mm specimens. The DTL is proved to be the dominant parameter affects the correlation between the load curves of the first and the

repeated impact. If the peak force is less than the DTL (3J and 6J), the repeated impact force history matches well with the first impact force history. If the peak force is over the DTL (12J and 18J), the phenomenon of the increase of the peak force during the repeated impact appears consistently. It is worth noting that an increment of 0.96kN (~10.2%) in the impact peak force can be seen under the 18J impact energy for the 5mm specimen, which is bigger than the increment (only 0.37kN) in the 4mm specimen under the same 18J impact energy level. This indicates the effect of delamination initiation is more pronounced on the impact response of the thicker specimens. It supports further the suggestion made in the previous section that the impact response of composite laminate is dependent on the ratio of the impact energy to the specimen stiffness (thickness) and there is an applicable range to detect the DTL.

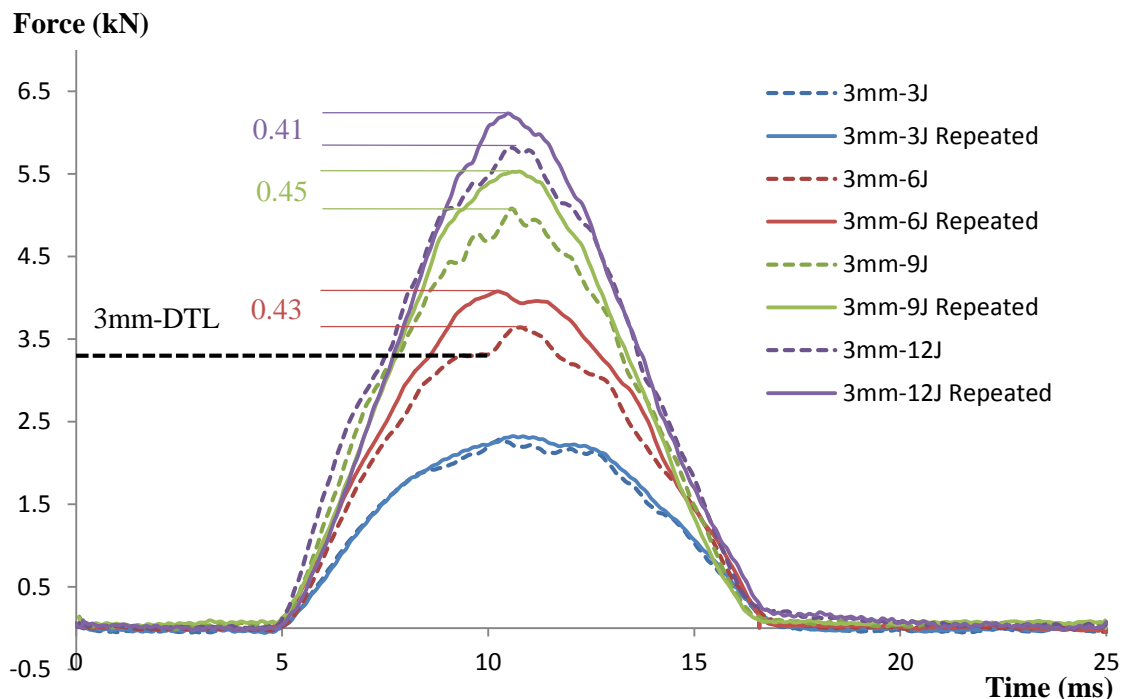


Figure 5.18 Filtered first and repeated impact force histories of 3mm specimens with cross-ply lay-up configuration.

Figure 5.18 shows the filtered first and repeated impact force histories of 3mm specimens with cross-ply lay-up configurations. Similar to the results from the specimens of different thicknesses, it can be seen clearly that the first and the repeated impact force histories under the 3J impact test condition are almost identical. The repeated impact force history deviates from the first impact force history under the impact energy of 6J, 9J, and 12J due to the delamination initiation introduced by the first impact. The increment of the peak impact force during the repeated impact is around 0.4kN (~10%), which is less than the value determined

in the studies of 4mm and 5mm specimens. This scenario supports the suggestion in the previous section that the influence of the delamination initiation on impact response of the relatively thinner laminates becomes less significant compared with that of the thicker specimens. This is due to the fact that the influence of elastic deformation and other damage forms becomes more significant for thinner specimens under the same impact energy.

Based on the results in Figure 5.15 – Figure 5.18, it suggested that the impact force history of the repeated impact under the same impact energy is very similar to the one of the first impact when the impact peak force is below DTL. While the impact duration remains the same as the one under the first impact, the impact peak force of the repeated impact is consistently higher than that of the first impact when the impact peak force exceeds the DTL.

The increase of the peak force of the impact force history during the repeated impact is however unexpected as the initiation of the delamination during the first impact is generally believed to reduce the stiffness of composite laminates, which should lead to a reduction, rather than an increase, of the impact peak force during the repeated impact under the same impact energy level. This phenomenon cannot be explained properly at the moment. One possible explanation is the effect of the thermal residual stress in the laminates generated during the curing process. The thermal residual stress may be released during the first impact when the delamination is initiated, which causes the redistribution of the internal stresses in the laminates and hence the different impact response under the same impact energy level. This argument can be supported by the effect of laminates thickness on the increase of the peak force under the repeated impact observed in the current research. The differences in the temperature and the cooling rate between the inside and outside of the laminates for the thick specimen are larger than those for the thin specimen. As a result, more thermal residual stress can be released through the initiation of the delamination in the thick specimen than that in the thin specimen. However, this preliminary explanation needs to be further validated by more impact tests conducted on different samples cured at different curing temperatures as presented in Section 5.1.5.

Another interesting observation of the test result is that the impact force history of the repeated impact under the same impact energy level becomes smoother than that of the first impact. This could be explained by the fact that the laminate is able to withstand the repeated impact without introducing any significant further delamination if the impact energy level is not too high. The elimination of the load drop in the impact force history of the repeated

impact may thus cause a higher peak force compared with the one under the first impact when load drop occurs due to the initiation of delamination. It is also interesting to note that the composite laminates tested in the current study demonstrated a good damage tolerance capacity by resisting the growth of delamination after the initiation of delamination. This could be explained by the fact that the existence of the initial delamination acts as additional sources for impact energy absorption and hence improves the damage tolerance of composite laminates under the repeated impact. The initial delamination, as a small gap at the interface of laminas with different fibre orientations, may improve the flexibility of the original brittle composite laminates and provide additional sources to absorb impact energy. The global deformation of the laminates under the repeated impact will be greater due to the initiation of delamination that will absorb extra impact energy. Additional energy will also be required to open the delamination area to a critical level before the delamination can be propagated. Hence, it makes the delamination difficult to propagate during the repeated impact under the same energy level. In one word, the increased peak force in the repeated impact force history is not caused by the increased laminates stiffness, but by the improved damage tolerance of the delaminated laminates.

It is also worth noting that the peak force increment phenomenon can be observed under a relatively higher impact energy level of 18J, although the increment is about 4.4% which is less than those (about 12.5% and 13.0%) achieved at the relatively lower energy levels. This result agrees well with the previous assumption on that the relative influence of the delamination initiation on the impact response of the specimen becomes less significant under relatively higher energy level. The specimen has been severely damaged by the impact with high impact energy but the effect of the initial delamination on the impact response of the laminate is not as significant as the ones under lower energy levels. The fact that all the specimens show an increase of the peak force under repeated impact when the peak force exceeds the DTL has nevertheless provided an alternative technique in detecting DTL. Repeated impact test should be carried out under different energy levels to determine at which level the impact force history starts to deviate from the one of the first impact. The peak impact force under this particular energy level should be the one close to DTL. This technique is particularly useful for thin specimens or thick specimens under higher impact energy in which load drop phenomenon is not obvious from the impact force history as mentioned earlier. A carefully designed repeat impact test will therefore enable the researcher to capture the DTL value of the laminates, at least the upper bound of the DTL.

5.1.4 Effect of Lay-up Configuration on Impact Response of Composite Laminates

From the previous study, it can be seen clearly that the laminates thickness strongly affects the impact response of composite laminates. Furthermore, the specimens with the thicknesses of 2mm and 4mm are considered as the representatives of the thin and the thick laminates, respectively. The specimens with the quasi-isotropic lay-up configurations of $[\pm 45/0/90]_s$ (2mm) and $[\pm 45/0_2/90_2/\pm 45]_s$ (4mm) were tested under various test conditions to study the lay-up configuration effect on the impact response of composite laminates.

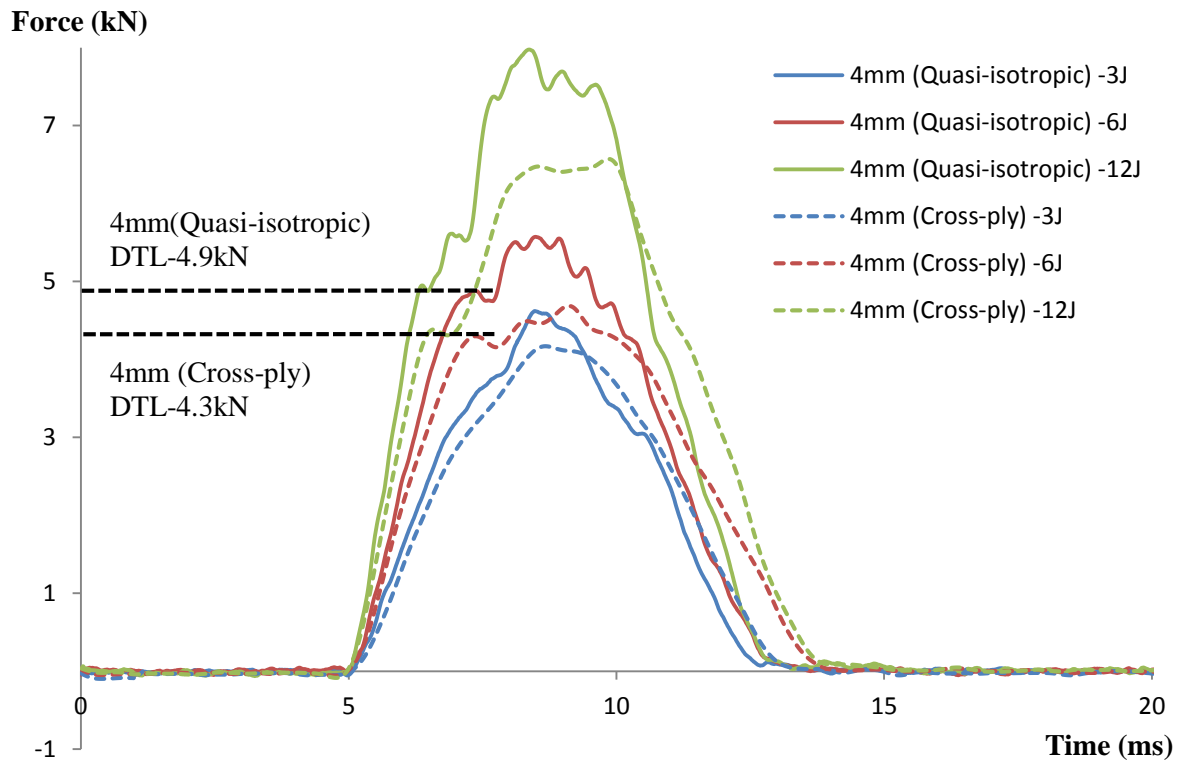


Figure 5.19 Comparison between filtered impact force histories of 4mm specimens with cross-ply and quasi-isotropic lay-up configurations.

Figure 5.19 shows the comparison between the filtered impact force histories of the 4mm thick specimens with cross-ply and quasi-isotropic lay-up configurations. It can be seen clearly that the lay-up configuration does affect the impact response of composite laminates. In general, the higher peak force and the shorter impact duration can be observed in the impact force histories of the quasi-isotropic specimens compared with those of the cross-ply specimens under the same impact energy level. The difference indicates that the quasi-isotropic specimen is stiffer than the specimen with the cross-ply lay-up configuration. This can be attributed to the smaller stiffness mismatch between the adjacent layers with the

different fibre orientations. Moreover, the sudden load drop phenomenon can also be clearly observed in the test results of 6J and 12J impacts on the quasi-isotropic specimens, which proves the existence of the delamination initiation threshold. The DTL value of the quasi-isotropic laminate is determined at around 4.9kN that is higher than the value of the cross-ply laminates (around 4.3kN). The enhanced damage resistance of the quasi-isotropic specimens is mainly due to decrease of stiffness mismatch between neighbouring layers.

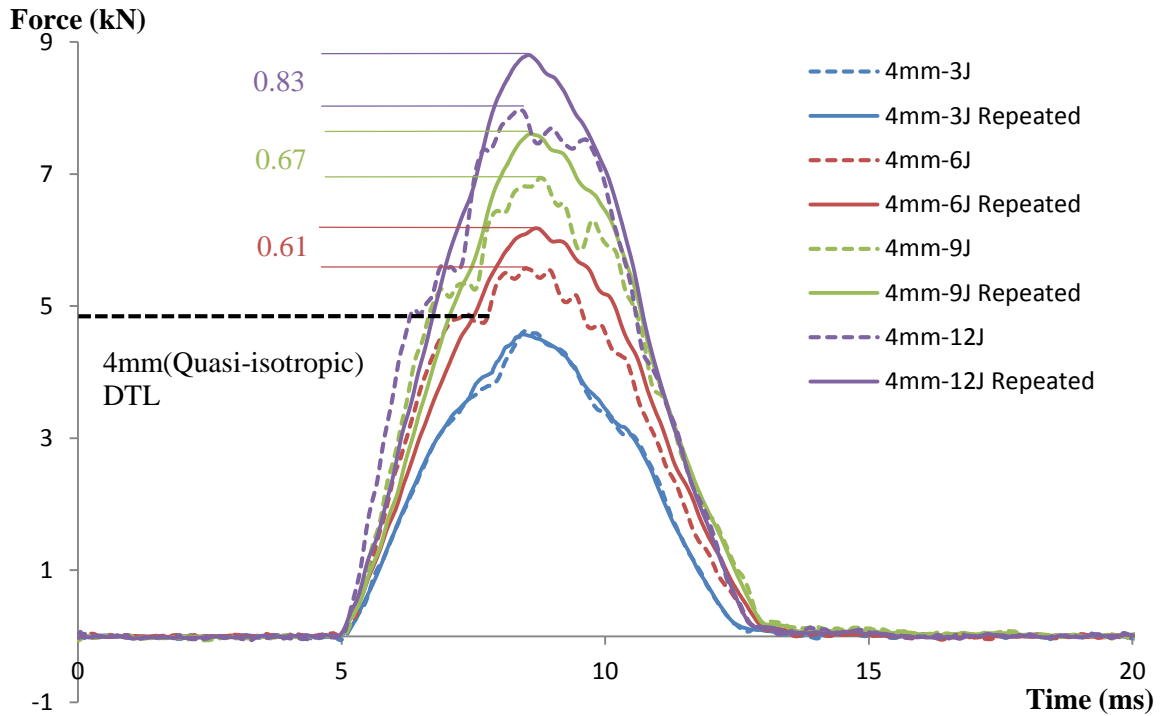


Figure 5.20 Filtered first and repeated impact force histories of 4mm specimens with quasi-isotropic lay-up configuration.

The result of the repeated impact test conducted on the 4mm quasi-isotropic specimen is shown in Figure 5.20. The overall trend in the test result is similar to that from the cross-ply specimen. The correlation between the first impact force history and the repeated impact force history is dominated by the DTL value and the peak impact force of the first impact. If the DTL value has not been exceeded in the first impact, no initial delamination will be induced by the first impact, which means the damage resistance/stiffness of the laminate has not been changed by the first impact. The damage resistance is therefore high enough and will prevent any further damage caused by the repeated impact under the same impact energy level. If the maximum force of the first impact reaches the DTL value, the repeated impact force history will significantly deviate from the first impact force history. Similar to the observation from the cross-ply laminates, the load curve of the repeated impact is smoother than the first

impact force history, which indicates that the initial delamination is not further propagated by the repeated impact under the same energy level. Moreover, the increased peak force of the repeated impact force history also indicates that the load bearing capacity of the damaged specimen is not reduced by the repeated impact under the same energy level. In other words, the resistance of the delaminated laminates to further damage is actually improved or at least not reduced if the energy level of the repeated impact is not too high.

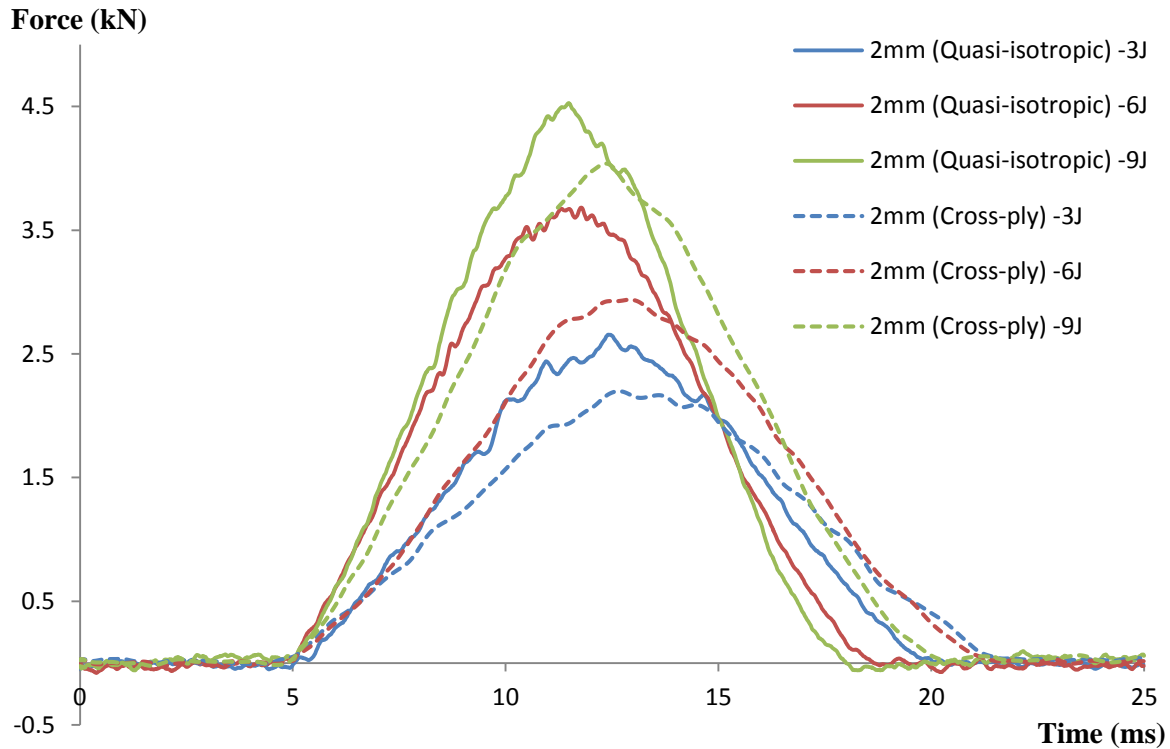


Figure 5.21 Comparison between filtered impact force histories of 2mm specimens with cross-ply and quasi-isotropic lay-up configurations.

The lay-up configuration effect on the impact response of thin composite laminate was also studied by conducting the similar investigations on the 2mm specimens with the quasi-isotropic lay-up configuration of $[\pm 45/0/90]_s$. The test results achieved from the 2mm quasi-isotropic specimens, in terms of the impact force histories, are compared with the test results of the 2mm cross-ply specimens as shown in Figure 5.21. The comparison suggests again that the lay-up configuration, or the resulting changed stiffness, does affect the impact response of composite laminates. The higher impact force and the shorter impact duration of the impact force history of the quasi-isotropic specimen indicates that the laminate is stiffer due to the balanced directional stiffness by introducing the $\pm 45^\circ$ layers into the lay-up. Furthermore, the sudden load drop phenomenon cannot be seen clearly in the test results of

the 2mm quasi-isotropic specimen, which agrees well with the previous observations on the 2mm cross-ply specimen. The effect of the initiation of delamination is proved again to be not significant on the impact response of the thin laminates.

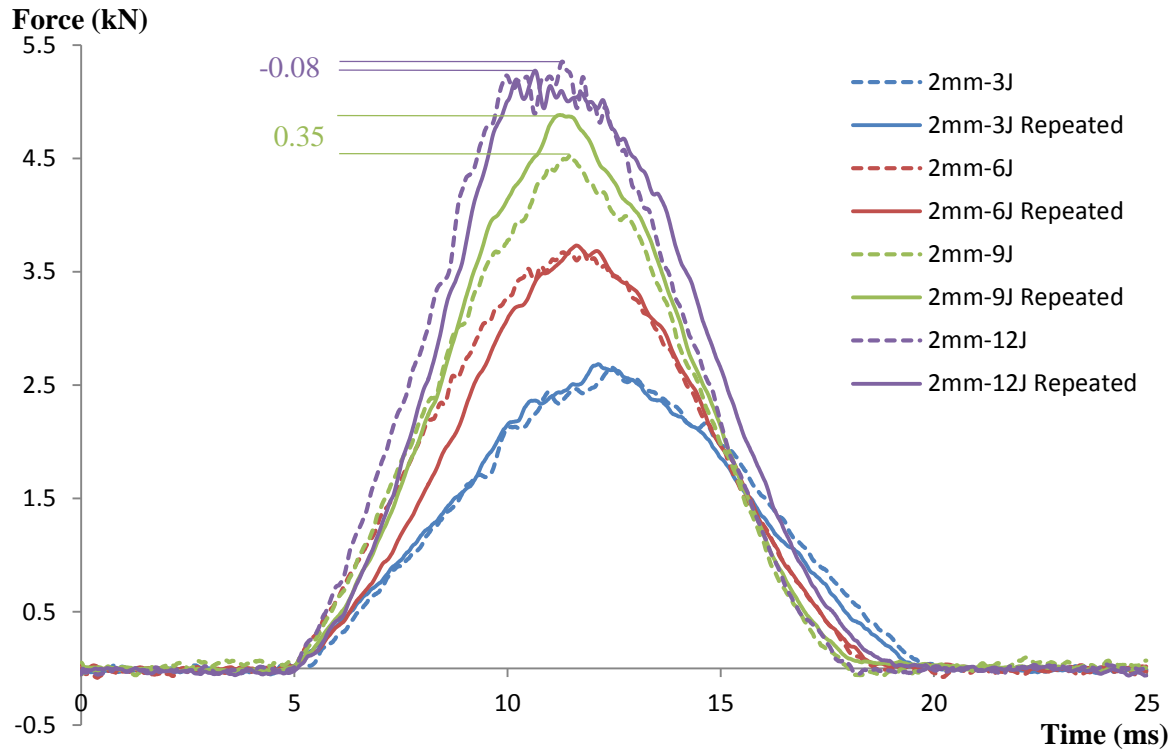


Figure 5.22 Filtered first and repeated impact force histories of 2mm specimens with quasi-isotropic lay-up configuration.

Figure 5.22 shows the filtered first and repeated impact force histories of the 2mm specimens with quasi-isotropic lay-up configuration. It can be seen clearly that the repeated impact force history fits well with the first impact force history, for the results of 3J and 6J impacts. This result further confirms that the delamination is hardly initiated in the thin laminates by the impact under the low impact energy due to the flexibility of the thin laminates. However, the initial delamination was still introduced into the thin laminates under the higher impact energy level (*e.g.* 9J). But, it should be noticed that the severe damage is also induced by the high energy impact, which occurs simultaneously with the initiation of the delamination. The severe damage causes significant reduction in the laminates stiffness. Therefore, the increment in the maximum force of the repeated impact is only around 0.35kN, which indicates the load bearing capacity enhancement caused by the existence of the initial delamination in thin laminate is not so significant as that in thick laminates. Moreover, the specimen was dramatically damaged by the first impact under the relatively high energy level

(*e.g.* 12J). The maximum impact force of the repeated impact thus decreases, as a result of the serious material degradation caused by the first impact. It is also interesting to notice that the stiffness of the dramatically damaged laminate is not further reduced by the repeated impact under the same energy level, demonstrating good damage tolerance capacity of composite laminates tested.

5.1.5 Effect of Curing Temperature on Impact Response of Composite Laminates

Some interesting findings with regard to damage resistance and damage tolerance of composite laminates under low-velocity impact have been obtained from the experimental investigations mentioned above. It is suggested that the concern on the degradation of the load bearing capacity of the damaged laminates may be overestimated. However, the phenomenon that the load bearing capacity of composite laminate has not been reduced under repeated impact still cannot be satisfactorily explained, with the major cause being associated with the initiation of delamination. It is suggested that either the released thermal residual stress in the laminates due to the delamination initiation or the new optional energy absorption mechanism introduced by the existence of the initial delamination may lead to the above phenomenon. To clarify this, tests were conducted on the specimens cured at different curing temperatures to investigate the effect of residual thermal stress, which will help to identify the dominant reason for the non-reduced load bearing capacity of the delaminated laminates.

In this study, the specimen cured at the lower curing temperature of 165°C is assumed to contain less thermal residual stress compared with the specimen cured at the normal temperature. It is related to the smaller temperature difference and the longer curing time in the curing process. On the contrary, more thermal residual stress is believed to be generated in the thick specimen cured at the higher curing temperature of 195°C. It is related to the larger difference in the thermal expansion and contraction between the inside and outside of the specimen, as a result of the larger differences in the temperature and cooling rate.

The comparison between the filtered impact force histories achieved from the 4mm quasi-isotropic specimens cured at 195°C and 180°C is shown in Figure 5.23. It can be clearly found that the change in curing temperature does affect the impact response of composite laminates, especially for the impact force. Moreover, the sudden load drop phenomenon also can be seen at around 4.3kN in the impact history of the 195°C cured specimen, which is less

than the DTL value determined from the specimen cured at 180°C. The findings indicate that both of the stiffness and the damage resistance of the laminates are decreased as a result of the increase in curing temperature.

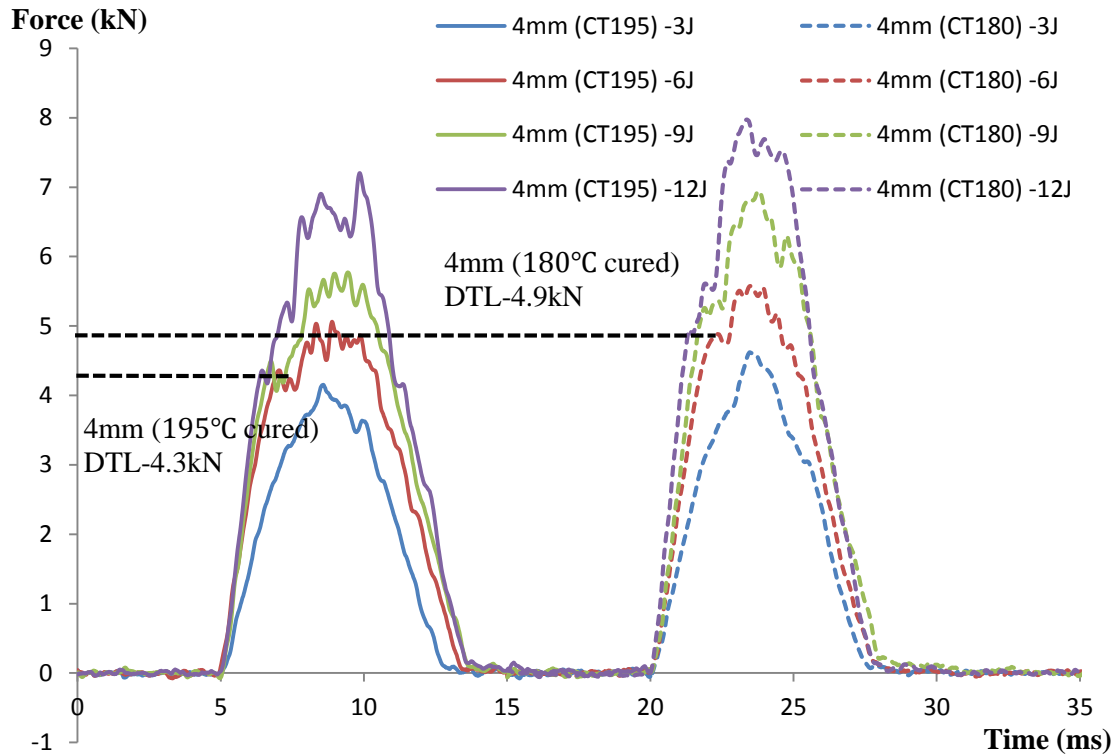


Figure 5.23 Comparison between filtered impact force histories of 4mm specimens cured at 195°C and 180°C.

Figure 5.24 shows the comparison between the filtered impact force histories of the 4mm specimens cured at 165°C and 180°C. It shows clearly that the decrease of the curing temperature causes much more significant effect on the impact response than the increase of the curing temperature. The peak impact force of the specimen cured at 165°C is much smaller than that of the specimen cured at 180°C under the same impact energy level. The impact duration of the 165°C cured specimen is also longer than that of the normal temperature cured specimen. These results indicate that the stiffness of the 165°C cured specimen is much lower than that of the 180°C cured specimen. Meanwhile, the sudden load drop phenomenon can be clearly observed in the impact force history of the 165°C cured specimen, although the load dip occurs much earlier (around 3.4kN) than the 180°C cured specimen. As a result, the initial delamination is triggered by the impact with relatively lower impact energy of 3J, due to the significant degradation of the damage resistance of the specimen cured at a lower temperature.

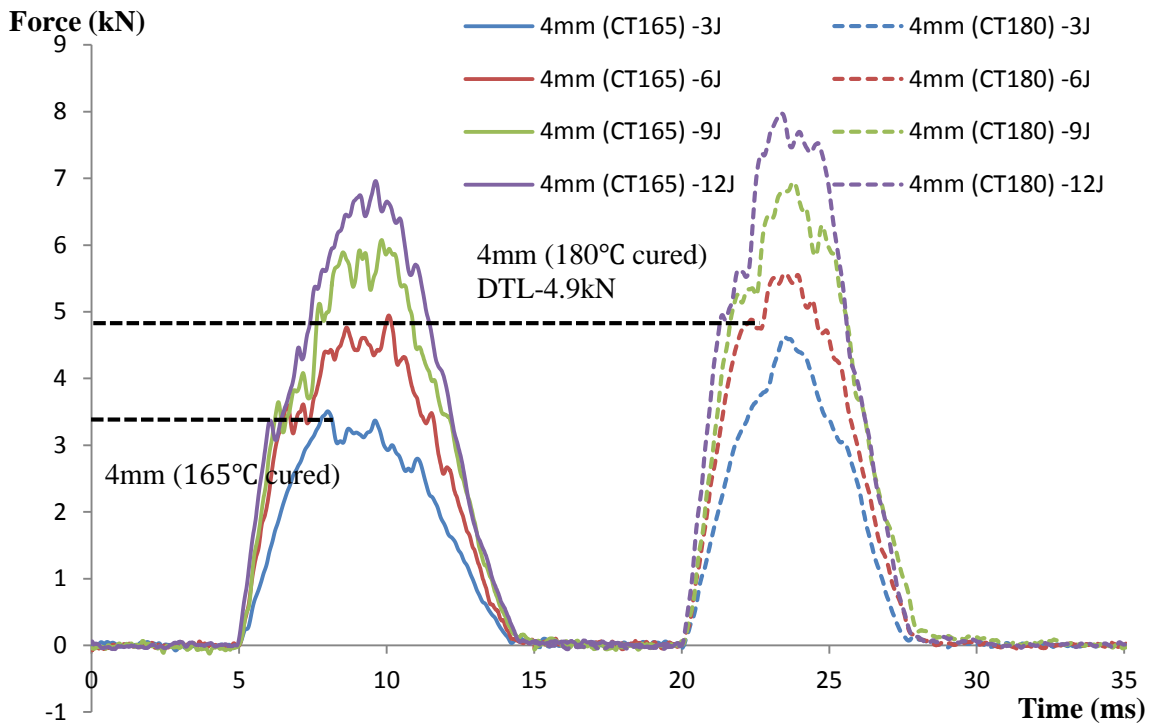


Figure 5.24 Comparison between filtered impact force histories of 4mm specimens cured at 165°C and 180°C.

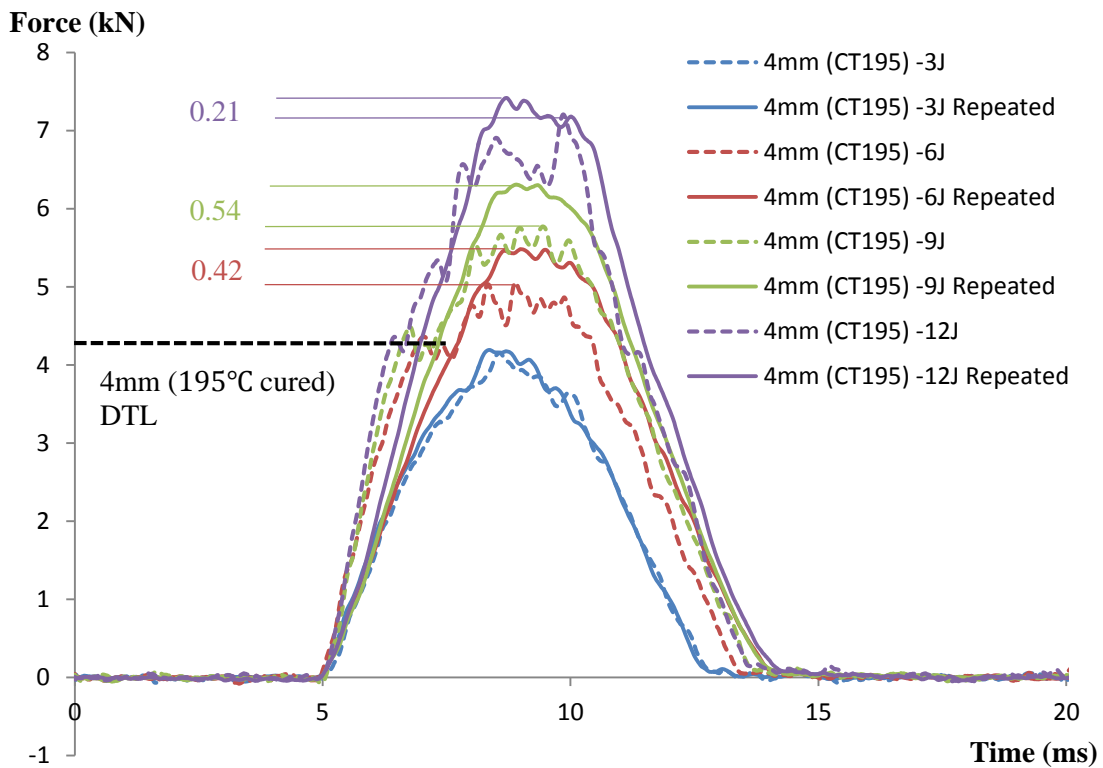


Figure 5.25 Filtered first and repeated impact force histories of 4mm specimens cured at 195°C.

Figure 5.25 shows the filtered first and repeated impact force histories of the 4mm specimens cured at 195°C. The repeated impact force history deviates from the first impact force history once the DTL value is exceeded by the first impact. It is however worth noting that the peak force increment in the deviated repeated impact force history for the 195°C cured specimen is less than the increment obtained from the specimen cured at 180°C. This result indicates that the release of residual thermal stress does affect the response of the laminates but in a way different to the initial expectation in which the release of the residual stress is the main factor contributing to the increase of the peak force during the repeated impact. Based on the initial expectation, if the release of the residual thermal stress is the main factor causing the increase of the peak force during the repeated impact, the specimen cured at 195°C should have a larger peak force increment compared with the specimen cured at 180°C as the higher curing temperature should generate more thermal residual stress in the specimen. As a result, the reduction or even the elimination of the load drop phenomenon due to the improved flexibility of the specimen and the additional energy absorption mechanisms caused by the multiple delaminations in the first impact might be the main reason for the increase of the peak impact force during the repeated impact.

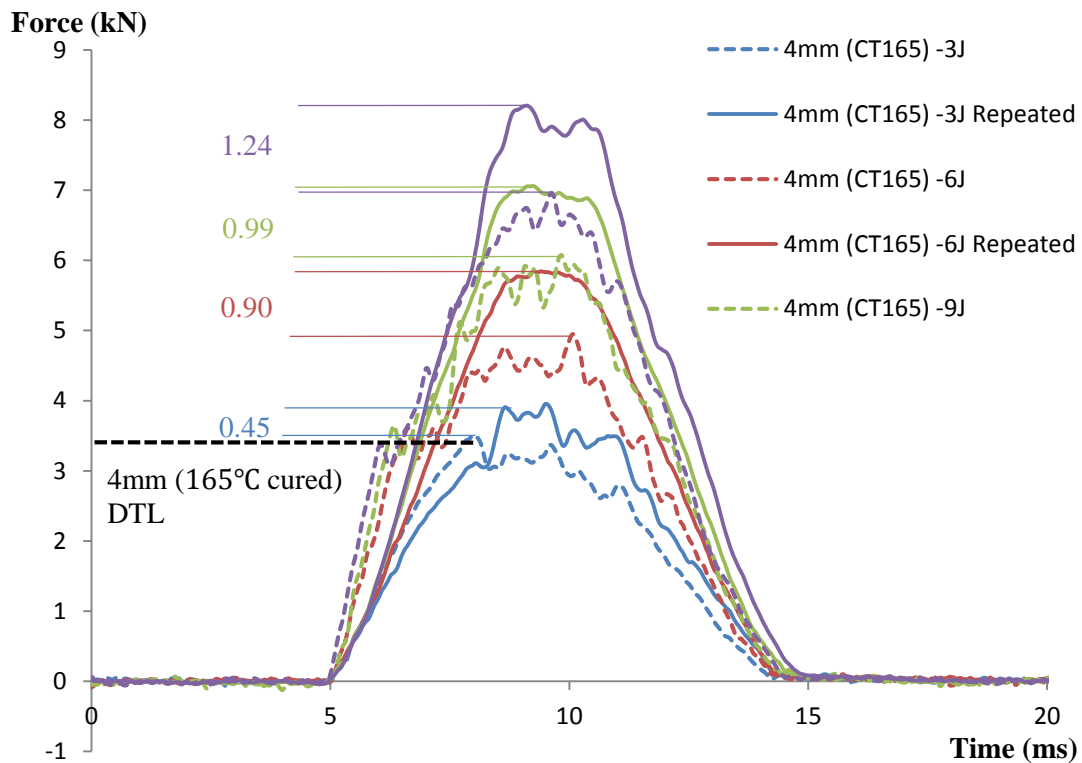


Figure 5.26 Filtered first and repeated impact force histories of 4mm specimens cured at 165°C.

The repeated impact test was also conducted on the 165°C cured 4mm specimen and the test results are shown in Figure 5.26. The phenomenon of the increased impact force appears in the 3J test result, which demonstrates that the initial delamination is indeed introduced into the laminates at the low energy level of 3J. Moreover, it is noticed that the increments in the repeated impact forces of the 165°C cured specimens, which range from 0.45kN to 1.24kN, are considerably larger than the increments of the specimens cured at the normal temperature of 180°C, which are around 0.7kN. Following on the discussion for the specimens cured at 195°C, the result indicates again that the release of residual stress does affect the response of the laminates but in a way different to the initial expectation in which the release of residual thermal stress is the main factor contributing to the increase of the peak force during the repeated impact. It is also interesting to notice that the repeated impact force history under 3J impact is not as smooth as the other repeated impact force histories, which indicates the delamination initiation during the first impact may be further developed under the following repeated loads in the test condition of 3J impact. It can be explained that since the DTL value is just exceeded by the peak force of the first impact, the delamination may not be completely initiated. Therefore, the following repeated impact under the same 3J impact energy may still initiate the delamination.

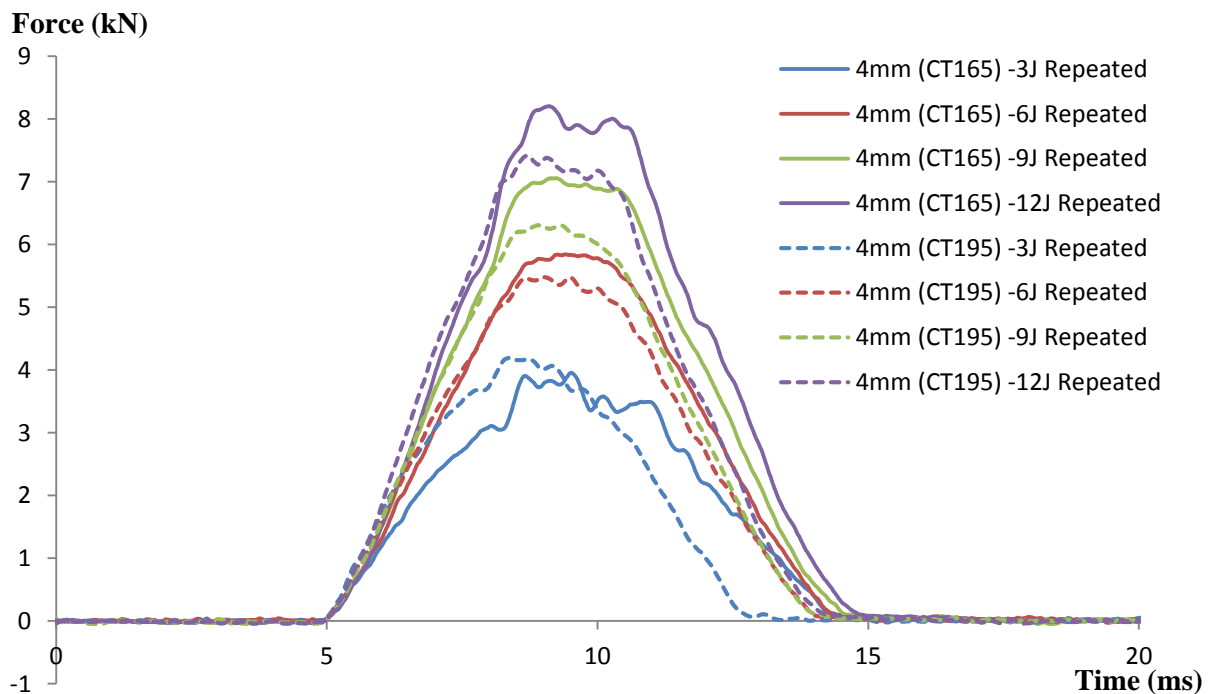


Figure 5.27 Filtered repeated impact force histories of 4mm specimens cured at 165°C and 195°C.

Figure 5.27 summaries the filtered repeated impact force histories achieved from the 4mm specimens cured at 195°C and 165°C. It is noticed that the peak impact force of the 165°C cured specimen is higher than that of the 195°C cured specimen in most test conditions, excepted for the lowest 3J case. This finding demonstrates further that the release of thermal residual stress in the thick laminate is not the reason for the increase of the peak impact force observed in the repeated impact force history. It has been suggested that the reduction or even the elimination of the load drop phenomenon due to the improved flexibility of the specimen and the additional energy absorption mechanisms caused by the multiple delaminations in the first impact might be the main reasons for the increase of the peak impact force during the repeated impact. Further investigation should be carried out to explain the consistently observed phenomenon that the existence of the initial delamination does not reduce the load bearing capacity of composite laminates if the repeated impact energy level is not too high.

5.2 Numerical Simulation

In the numerical simulation, the dynamic process of composite laminates under low-velocity impact was simulated by the FE simulation software ANSYS/LS-DYNA. The model was created in the pre-processor package of LS-PREPOST by defining the model geometry, element type, mesh scheme, material property, contact definition and other global simulation setting. Once the simulation model was created, the defined model file was put to the ANSYS/LS-DYNA solver for solving. After the solution, the simulation result file was read and processed by the post-processor package of LS-PREPOST.

To ensure the comparability between the simulation results and the test results, the material properties of the UD material in the simulation were assigned by the data determined from the test as presented in Chapter 4. Two different modelling strategies were employed in the current study: one without the consideration of damage and one considering the damage.

In the modelling strategy without the consideration of damage mechanism, the laminated composite was modelled as a single layer of shell element by defining the total thickness and the equivalent laminates stiffness. The equivalent stiffness was defined by the ABD stiffness matrix determined from the mechanical analysis as described in Section 2.2.3. The damage mechanism was not considered in the ABD matrix modelling strategy due to absence of the failure criterion and degradation scheme. Therefore, the simulation result only reflects the

elastic response of composite laminates. Nevertheless, the ABD matrix modelling strategy is still the most commonly used method to have a quick estimation of the overall behaviour of composite laminates, due to the simple model creation and low computational cost.

The damage mechanism was considered in the advanced modelling strategy by including the failure criterion and degradation scheme in material property model. It employs the tie-break contact/cohesive element method to predict the interlaminar damage at the interface between adjacent layers with different fibre orientations. The laminated composite was modelled as a stack of orthotropic linear elastic laminas according to the lay-up configuration. To save computational time, the layers with the same fibre orientation were treated as a single lamina in the geometry model. Each lamina was modelled separately by defining the individual thickness and material property model. The physical material properties, material elasticity, failure criterion, geometrical features and degradation scheme factors were specified in the material property model. After that, the adjacent laminas were connected by the tie-break contact to simulate the possible interlaminar damage at the interface of different fibre orientations. It has been found that the solution time and accuracy are highly sensitive to the model parameters such as the element size, degradation scheme factor, and contact definition [122]. Therefore, an extensive parametric study of these parameters was conducted to achieve a better understanding of the FE simulation of composite laminates under low-velocity impact.

5.2.1 Model Creation without Consideration of Damage Mechanism

The rectangular composite test specimen (150mm by 100mm) was treated as a lamina with a dimension of 125mm × 75mm, which is attributed to the fact that the specimen was clamped on the fixture base with a 125mm by 75mm cut-out in practice. In LS-PREPOST, the creation of simulation model is conducted by specifying various definition cards. The dimensions and mesh scheme of the lamina were defined in the 4N_Shell mesh card. The shell element used to model the lamina was defined by the Section_SHELL card, in which the total thickness of laminate was specified. It is however worth to noting that the created shell element only represents the mid-plane of lamina. As a result, the top surface of lamina is actually above the created shell element by a half of the defined thickness. The SPC definition card was used to define the boundary condition. The simply supported boundary conditions (fixed X, Y, and Z) were applied to the four edges of lamina to reflect the physical support condition of experimental test. Furthermore, the material property model of lamina was defined by the

117_COMPOSITE_MATRIX material card, in which the ABD stiffness matrix determined from the mechanical analysis was employed.

For the 2mm laminates with cross-ply lay-up configuration of $[0/90_2/0]_s$, the detailed analysis process to determine the [A], [B], and [D] stiffness matrices is presented in Appendix II, and the calculation results are shown as below

$$\begin{aligned}
 [A] &= \begin{bmatrix} 1.40 \times 10^8 & 3.82 \times 10^6 & 0 \\ 3.82 \times 10^6 & 1.40 \times 10^8 & 0 \\ 0 & 0 & 8.3 \times 10^6 \end{bmatrix} && \text{Pa}\cdot\text{m} && \text{extensional stiffness matrix,} \\
 [B] &= \begin{bmatrix} 0 & 0 & 0 \\ 0 & 0 & 0 \\ 0 & 0 & 0 \end{bmatrix} && \text{Pa}\cdot\text{m}^2 && \text{coupling stiffness matrix,} \\
 [D] &= \begin{bmatrix} 54.45 & 1.27 & 0 \\ 1.27 & 38.48 & 0 \\ 0 & 0 & 2.77 \end{bmatrix} && \text{Pa}\cdot\text{m}^3 && \text{bending stiffness matrix.} \quad (5.4)
 \end{aligned}$$

Thus, the ABD matrix for the 2mm laminate was

$$\begin{aligned}
 \begin{bmatrix} N_x \\ N_y \\ N_{xy} \\ M_x \\ M_y \\ M_{xy} \end{bmatrix} &= \begin{bmatrix} A_{11} & A_{12} & A_{16} & B_{11} & B_{12} & B_{16} \\ A_{12} & A_{22} & A_{26} & B_{12} & B_{22} & B_{26} \\ A_{16} & A_{26} & A_{66} & B_{16} & B_{26} & B_{66} \\ B_{11} & B_{12} & B_{16} & D_{11} & D_{12} & D_{16} \\ B_{12} & B_{22} & B_{26} & D_{12} & D_{22} & D_{26} \\ B_{16} & B_{26} & B_{66} & D_{16} & D_{26} & D_{66} \end{bmatrix} \begin{bmatrix} \varepsilon_x^0 \\ \varepsilon_y^0 \\ \gamma_{xy}^0 \\ \kappa_x \\ \kappa_y \\ \kappa_{xy} \end{bmatrix} \\
 &= \begin{bmatrix} 1.40 \times 10^8 & 3.82 \times 10^6 & 0 & 0 & 0 & 0 \\ 3.82 \times 10^6 & 1.40 \times 10^8 & 0 & 0 & 0 & 0 \\ 0 & 0 & 8.3 \times 10^6 & 0 & 0 & 0 \\ 0 & 0 & 0 & 54.45 & 1.27 & 0 \\ 0 & 0 & 0 & 1.27 & 38.48 & 0 \\ 0 & 0 & 0 & 0 & 0 & 2.77 \end{bmatrix} \begin{bmatrix} \varepsilon_x^0 \\ \varepsilon_y^0 \\ \gamma_{xy}^0 \\ \kappa_x \\ \kappa_y \\ \kappa_{xy} \end{bmatrix} \quad (5.5)
 \end{aligned}$$

Figure 5.28 shows the input data for the 2mm laminates in the MAT_117 card by involving the ABD matrix. It is worth mentioning that the base units of the current simulation were mm, N, and ms.

*MAT_COMPOSITE_MATRIX_(TITLE) (117) (1)

TITLE								
ABBD Matrix for 2mm Laminates								
1	MID	RO						
	1	1.580e-006						
2	C11	C12	C22	C13	C23	C33	C14	C24
	140.00000	3.8199999	140.00000	0.0	0.0	8.3000002	0.0	0.0
3	C34	C44	C15	C25	C35	C45	C55	C16
	0.0	54.450001	0.0	0.0	0.0	1.2700000	38.480000	0.0
4	C26	C36	C46	C56	C66	AOPT		
	0.0	0.0	0.0	0.0	2.7700000	0.0		

Figure 5.28 Input data for the 2mm laminates with cross-ply lay-up configuration in MAT_117_COMPOSITE_MATRIX material card.

Following the same procedure as the 2mm laminates, the ABD matrix for the 3mm laminates with cross-ply lay-up of $[0_2/90_3/0]_s$ was

$$\begin{bmatrix} N_x \\ N_y \\ N_{xy} \\ M_x \\ M_y \\ M_{xy} \end{bmatrix} = \begin{bmatrix} 2.10 \times 10^8 & 5.73 \times 10^6 & 0 & 0 & 0 & 0 & 0 \\ 5.73 \times 10^6 & 2.10 \times 10^8 & 0 & 0 & 0 & 0 & 0 \\ 0 & 0 & 1.25 \times 10^7 & 0 & 0 & 0 & 0 \\ 0 & 0 & 0 & 215.93 & 4.30 & 0 & 0 \\ 0 & 0 & 0 & 4.30 & 98.91 & 0 & 0 \\ 0 & 0 & 0 & 0 & 0 & 9.34 & 0 \end{bmatrix} \begin{bmatrix} \epsilon_x^0 \\ \epsilon_y^0 \\ \gamma_{xy}^0 \\ \kappa_x \\ \kappa_y \\ \kappa_{xy} \end{bmatrix} \quad (5.6)$$

The ABD matrix for the 4mm laminates with cross-ply lay-up of $[0_2/90_3/0_2/90]_s$ was

$$\begin{bmatrix} N_x \\ N_y \\ N_{xy} \\ M_x \\ M_y \\ M_{xy} \end{bmatrix} = \begin{bmatrix} 2.80 \times 10^8 & 7.65 \times 10^6 & 0 & 0 & 0 & 0 & 0 \\ 7.65 \times 10^6 & 2.80 \times 10^8 & 0 & 0 & 0 & 0 & 0 \\ 0 & 0 & 1.66 \times 10^7 & 0 & 0 & 0 & 0 \\ 0 & 0 & 0 & 458.96 & 10.19 & 0 & 0 \\ 0 & 0 & 0 & 10.19 & 287.33 & 0 & 0 \\ 0 & 0 & 0 & 0 & 0 & 22.13 & 0 \end{bmatrix} \begin{bmatrix} \epsilon_x^0 \\ \epsilon_y^0 \\ \gamma_{xy}^0 \\ \kappa_x \\ \kappa_y \\ \kappa_{xy} \end{bmatrix} \quad (5.7)$$

The ABD matrix for the 5mm laminates with cross-ply lay-up of $[0_2/90_3/0_2/90_2/0]_s$ was

$$\begin{bmatrix} N_x \\ N_y \\ N_{xy} \\ M_x \\ M_y \\ M_{xy} \end{bmatrix} = \begin{bmatrix} 3.50 \times 10^8 & 9.56 \times 10^6 & 0 & 0 & 0 & 0 \\ 9.56 \times 10^6 & 3.50 \times 10^8 & 0 & 0 & 0 & 0 \\ 0 & 0 & 2.08 \times 10^7 & 0 & 0 & 0 \\ 0 & 0 & 0 & 841.92 & 19.91 & 0 \\ 0 & 0 & 0 & 19.91 & 615.68 & 0 \\ 0 & 0 & 0 & 0 & 0 & 43.23 \end{bmatrix} \begin{bmatrix} \epsilon_x^0 \\ \epsilon_y^0 \\ \gamma_{xy}^0 \\ \kappa_x \\ \kappa_y \\ \kappa_{xy} \end{bmatrix} \quad (5.8)$$

Those ABD matrices were used to determine elastic behaviours of the laminates with different thicknesses.

Furthermore, the projectile (impactor + support frame) was artificially modelled as a rigid sphere with a diameter of 20mm. Solid elements were used to simulate the ball by specifying the Section_SOLID card. The dimensions and mesh scheme of the ball were defined in the Sphere_Solid mesh card. It is also worth mentioning that the sphere centre was set to a specific position, which was 11mm above the top surface of lamina, to ensure the clearance between the sphere and the lamina in the initial simulation condition as shown in Figure 5.29. Further, a concentrated mass was assigned to the rigid ball to represent the total mass of the projectile (11.8kg) by defining an increased mass density of $2.817042 \times 10^6 \text{ kg/m}^3$ in the 20_RIGID material card. The initial velocity of the rigid sphere, V , was defined in the Initial_VELOCITY_RIGID_BODY card to simulate different impact energy levels. Figure 5.29 shows the initial condition of the simulation, in which the initial velocity of the sphere

is $\sqrt{\frac{2E}{m} - 2gh}$.

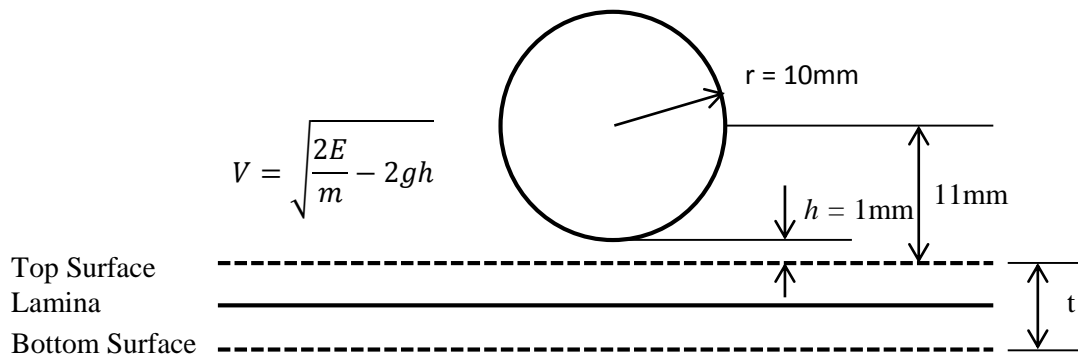


Figure 5.29 Initial condition of the projectile in the FE simulation.

Figure 5.30 shows the geometry model for the FE simulation of a 2mm composite laminates under low-velocity impact using the ABD modelling strategy. The lamina was meshed into 125×75 , which generated 9375 shell elements. The mesh density of the rigid ball was 10, which generated 7000 solid elements. Further, the operations conducted in the PartD

definition card helped to assign the defined material properties and sections to the ball and the lamina modal.

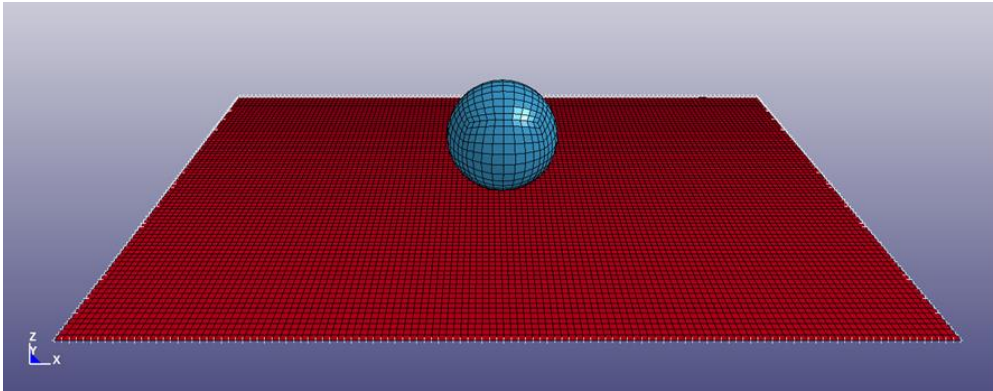


Figure 5.30 Geometry model for the FE simulation of the 2mm laminates under low-velocity impact.

In the simulation, the low-velocity impact event was treated as a contact pair between the rigid ball and the lamina. The contact definition was created using the keyword command `CONTACT_AUTOMATIC_SURFACE_TO_SURFACE`, in which the sphere was the master segment, and the lamina was the slave segment. Moreover, the gravitational acceleration of the model was specified by defining a specific load curve in the `Define_CURVE` card, and then applying the load curve to the model by activating the `Load_BODY_Z` card.

The termination time of simulation was set to 20ms using the `Control_TERMINATION` card. The time-step of the simulation was defined as 0.1ms in the `Dbase_BINARY_D3PLOT` card. The global setting of simulation result was defined in the `Dbase_ASCII_option` card, in which the interval time of the output result was set to 0.2ms and the required output data categories were selected.

5.2.2 Simulation Results without Consideration of Damage Mechanism

Follow the procedure as described in Section 5.2.1, various simulation models were created. The simulation model file (.k file) was inputted to the ANSYS/LS-DYNA solver for calculation. The simulation result file (d3plot file) was read by LS-PREPOST to analyse the simulation result.

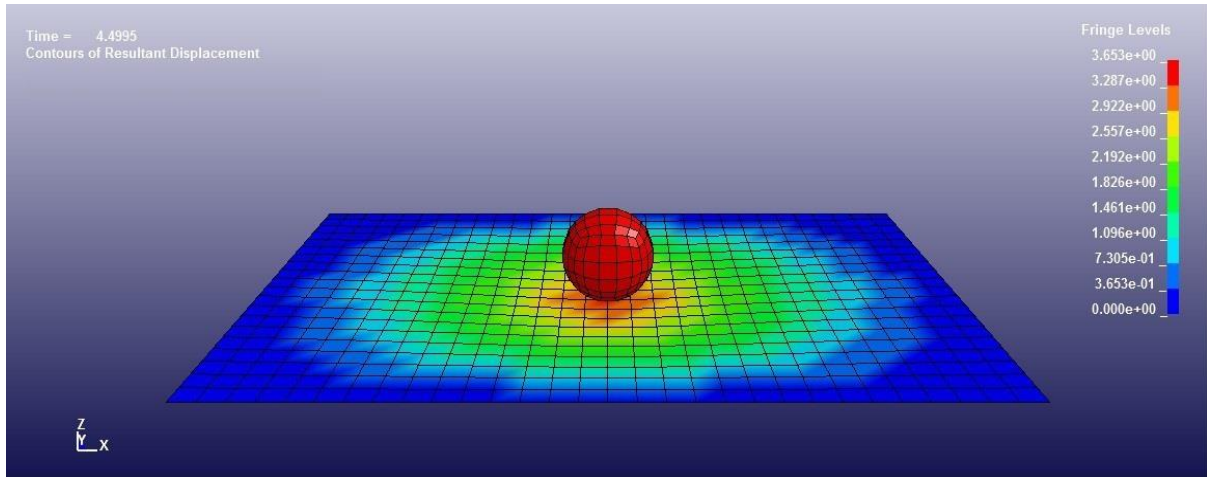


Figure 5.31 Computed displacement of the 3mm laminates under 6J impact energy level.

Figure 5.31 shows a typical result visualisation of the 3mm laminates subjected to the 6J impact, in terms of the resultant displacement at 4.5ms. The visualized simulation result indicates that the maximum deformation of the lamina (3.65275mm) occurs under the impactor. In this model, the lamina was meshed into 600 shell elements (30×20); and the sphere was meshed into 875 solid elements (default mesh density of 5). The solution time of the model with current mesh setting was around one minute. The solution time would be increased dramatically with the increase of the total number of elements. The mesh density of the lamina was increased to 60×40 and 125×75 to investigate the convergence of simulation results.

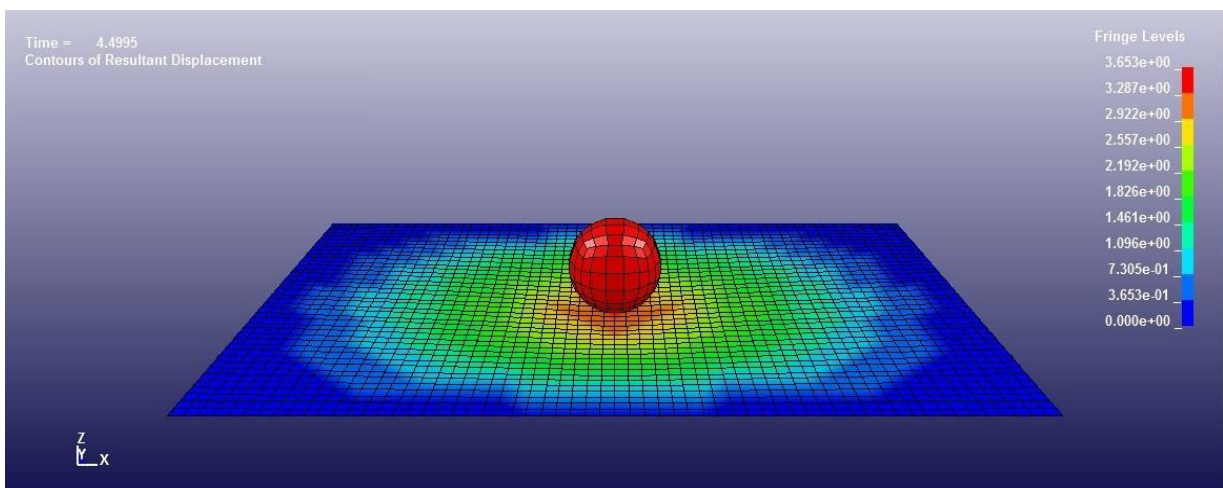


Figure 5.32 Simulation result of the model with 60×40 mesh scheme for laminates.

Figure 5.32 shows the simulation result of the model including 2400 shell elements in the lamina. The result of the resultant displacement agrees well with the one achieved from the

model with smaller mesh density, which indicates that the element size of lamina does not significantly affect the simulation result. It is however noticed that the solution time increased to around half an hour due to the increased mesh density. Similar scenario was found in the simulation result of the model with 9375 shell elements in the lamina and 7000 solid elements in the sphere. The solution time of the model including more elements was increased to a few minutes. The mesh scheme was set to having 600 shell elements in the lamina and 875 solid elements in the sphere, as it offers a good balance between the simulation accuracy and solution cost.

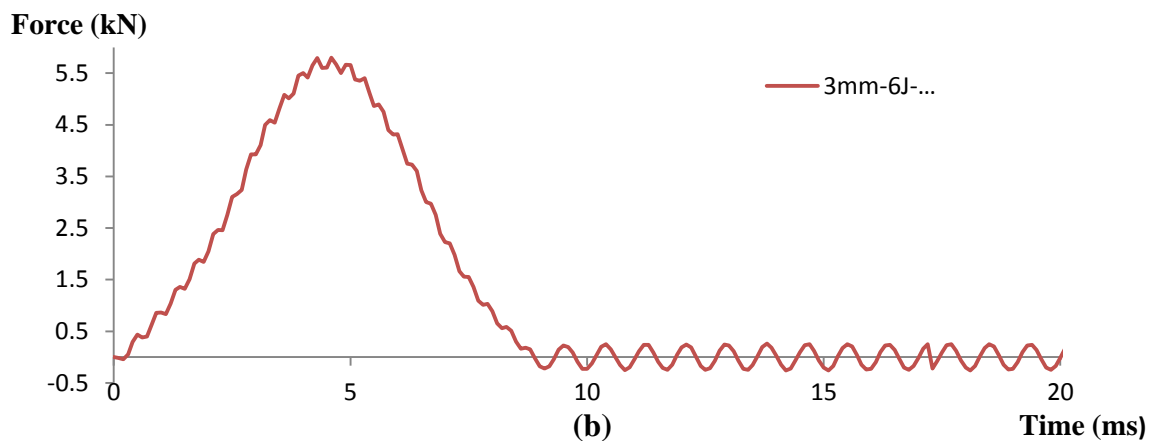
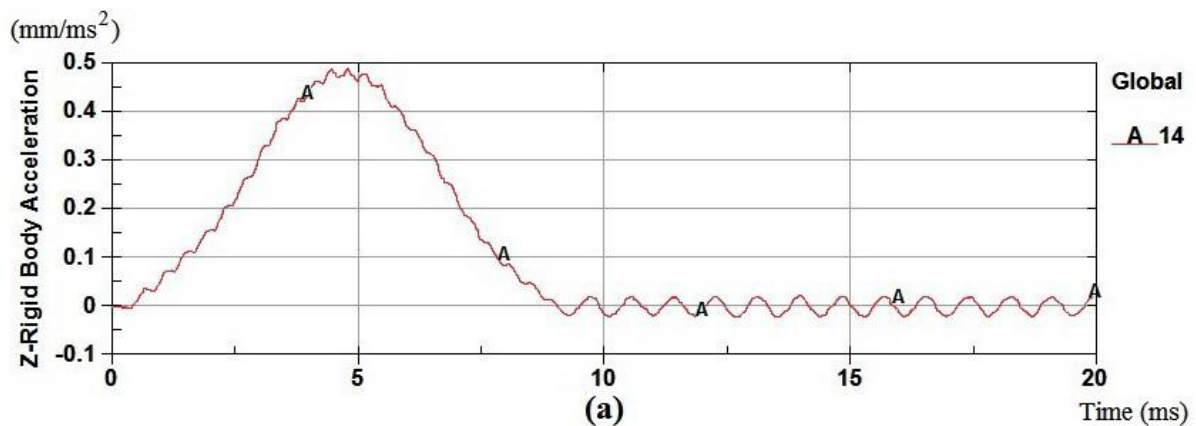


Figure 5.33 Determination of impact force history from a simulation result.

The impact force history can be determined from the simulation result by converting the acceleration of the rigid ball to the reaction force. Figure 5.33(a) shows a typical result of the Z-Rigid body acceleration history obtained from the simulation of a 3mm laminates subjected to the 6J impact. The impact force, as the reaction force applied on the impactor, is equal to the deceleration of the impactor (Z-Rigid body) multiplied by the mass of the impactor (11.8kg). The impact force history so determined is shown in Figure 5.33(b).

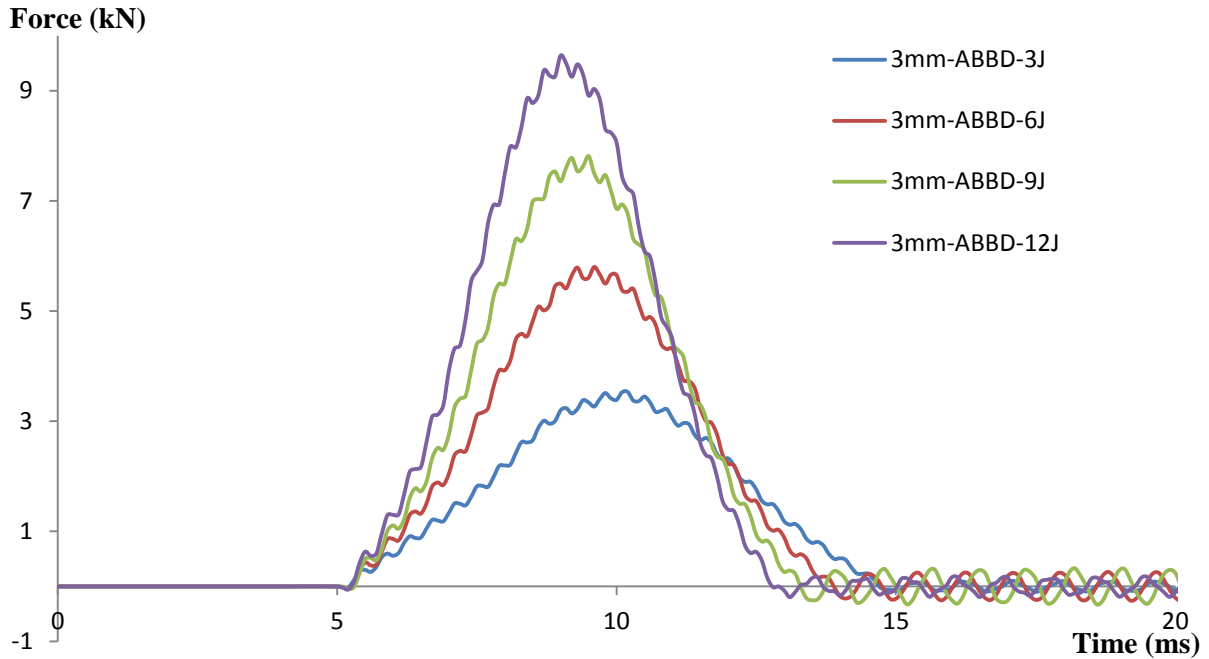


Figure 5.34 Unfiltered simulation results of impact force histories of 3mm laminates under various impact energy levels.

Figure 5.34 shows the simulation results, in terms of the impact force history, obtained from the models of the 3mm composite laminates under various impact energy levels by using the ABD modelling strategy. The typical elastic impact response of the laminates can be clearly found from the load curves since the irregular fluctuation is not significant. This can be explained by the absence of damage mechanism in the ABD matrix modelling strategy, in which the stiffness matrix only reflects the elastic behaviour of the lamina without any damage induced stiffness degradation. Moreover, it is also clear that correlations among the impact force, the impact duration, and the impact energy level are similar to those observed in the experimental tests. The higher impact force and the shorter impact duration were introduced by the impact with higher impact energy.

Apart from the simulations of the 3mm laminates, more impact events, in which the composite laminates with different thicknesses were subjected to impacts with various impact energies, were simulated. The simulation results, especially for the impact force histories, were compared with the experimental results to investigate the impact response of composite laminates.

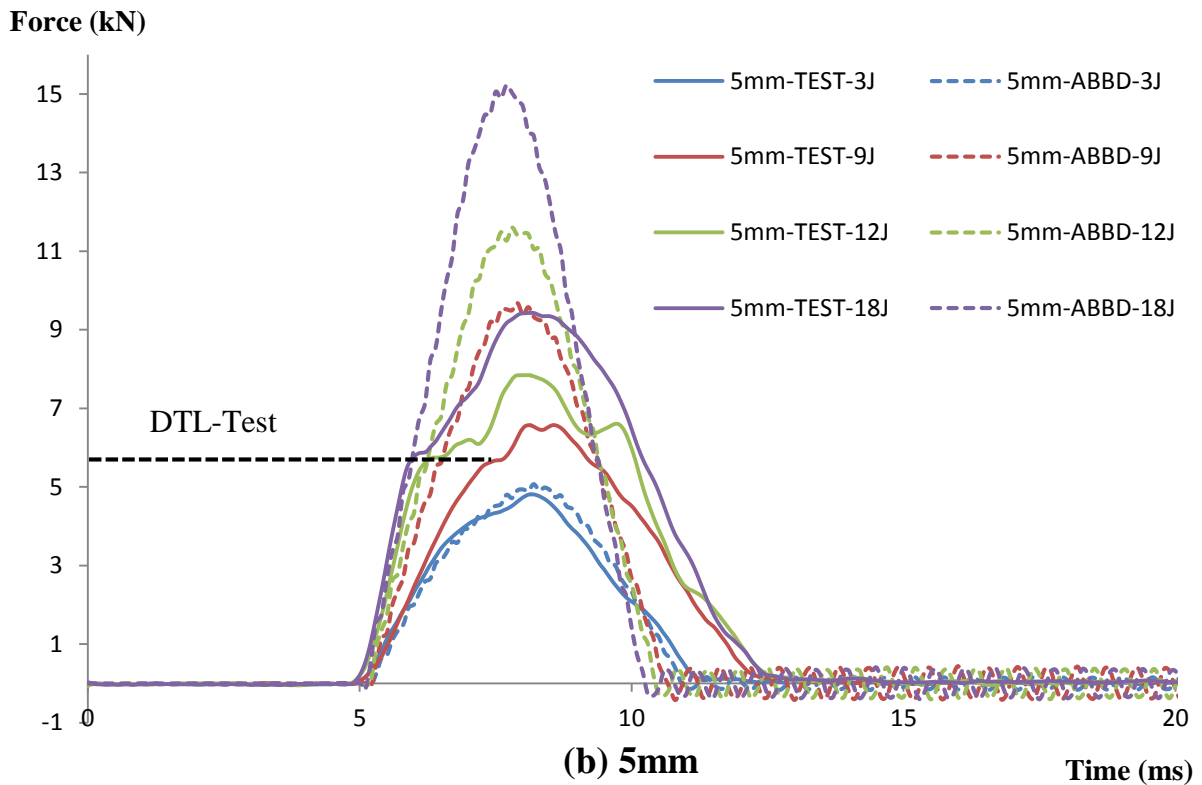
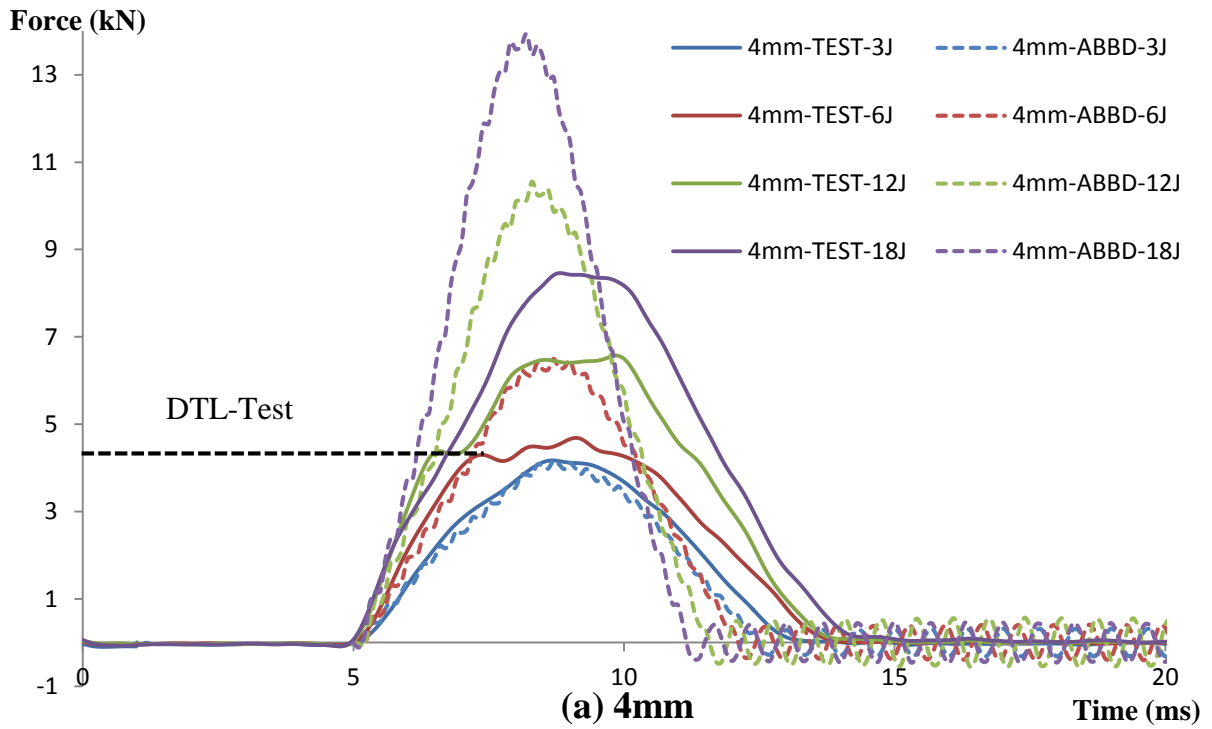


Figure 5.35 Comparison between simulation results employing ABD matrix modelling strategy and test results: (a) 4mm and (b) 5mm laminates.

The comparison between the impact force histories obtained from the numerical and experimental studies of the 4mm composite laminate is shown in Figure 5.35(a). It can be

seen clearly that the initiation of delamination significantly affects the correlation between the simulation and test results. If the maximum impact force in the simulation result is less than the DTL value determined from the experimental test (*e.g.* 4mm laminates under 3J impact), the impact force histories of the numerical simulation and the experimental test agree well with each other. The good correlation between the test result and the simulation result also indicates the model stiffness in the FE model is close to the real stiffness of laminates. Once the maximum impact force in the simulation result exceeds the critical load (*e.g.* 4mm laminates subjected to impact with 6J or higher energy), the simulation result will deviate significantly from the test result, in terms of the higher peak force and shorter impact duration. It is noticed that the difference between the simulation result and the test result is proportional to the impact energy level. Similar scenario was also observed in the comparison between the simulation results and the test results for the 5mm laminates as shown in Figure 5.35(b).

The consistent general trend in the correlation between the numerical simulation result and the experimental test result further proves the concept of the DTL. The ABD matrix modelling strategy employed model does not consider the damage mechanism in the simulation approach. As a result, the ABD matrix model can only reflect the elastic response of the laminates, but cannot simulate the impact damage and the damage induced stiffness degradation. However, the laminates stiffness is reduced significantly when the delamination is initiated during the experimental test. In one word, the differences in the impact force and duration between the simulation result and the test result are attributed to the un-reduced stiffness in the simulation and the reduced stiffness in the test.

Figure 5.36 shows the comparison between the simulation results and the test results from the 3mm laminates. It was found that the delamination initiation phenomenon, in terms of the sudden load dip, could not be easily observed from the impact test result. This was explained by the greater flexibility of the laminates of the relatively thinner laminates. The sudden load drop phenomenon cannot therefore be used to indicate the existence of the delamination. However, it is suggested that the simulation results agree well with the test results from the impact cases of 1J and 3J. For the impact cases of 6J and 9J, a distinct difference between the simulation result and the test result was observed, which indicates the degradation in the laminates stiffness due to the impact. This could lead to an alternative method to estimate the value of DTL.

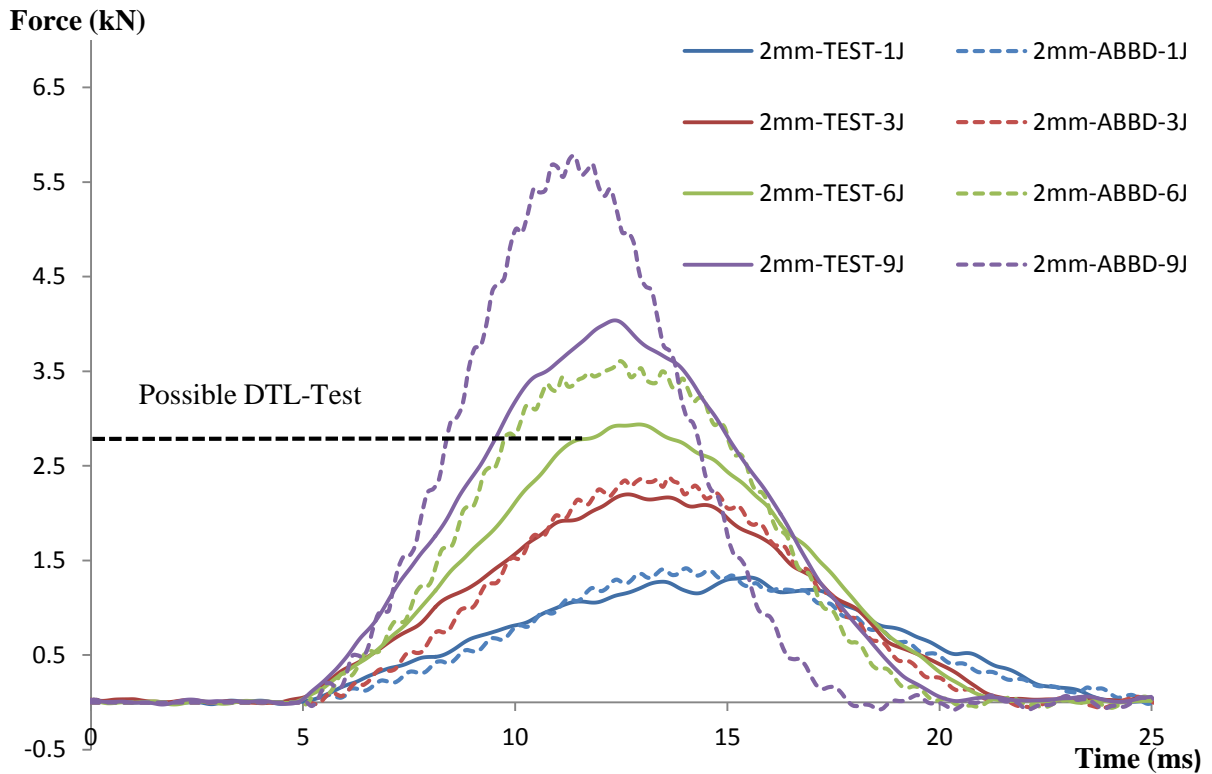


Figure 5.36 Comparison between simulation results and test results for 3mm laminates.

In conclusion, the simulation results with the ABD matrix modelling strategy provides further evidence on the existence of delamination and leads to an alternative method to estimate the value of DTL. The DTL value can be determined from the experimental study, through the comparison between the simulation result and the test result. However, it still cannot predict the initiation of delamination and the corresponding DTL value directly when the damage mechanism is not considered in the current simulation model. A comprehensive model should therefore be developed by the advanced modelling strategy to predict the impact response and the impact induced damage of composite laminates under low-velocity impact.

5.2.3 Model Generation with Consideration of Damage Mechanism

On completion of the simulation without considering damages in the laminates, various simulation models considering the damage mechanism were created to simulate the impact events of composite laminates with different lay-up configurations and impact energy levels. The 4mm laminates with the quasi-isotropic lay-up configuration of $[\pm 45/0_2/90_2/\pm 45]_s$ was selected as the example to illustrate the model creation procedure.

In general, the simulation model considering the damage mechanism was created in a similar procedure as described in Section 5.2.1. The projectile was modelled as a rigid sphere with a diameter of 20mm by defining the Sphere_Solid mesh card. A significant difference in the simulation model here was that the specimen was modelled as a stack of orthotropic laminas. Eleven shell laminas were created in the thickness direction to represent the 4mm composite laminates with the lay-up of $[\pm 45/0_2/90_2/\pm 45]_s$, as illustrated in Figure 5.37.

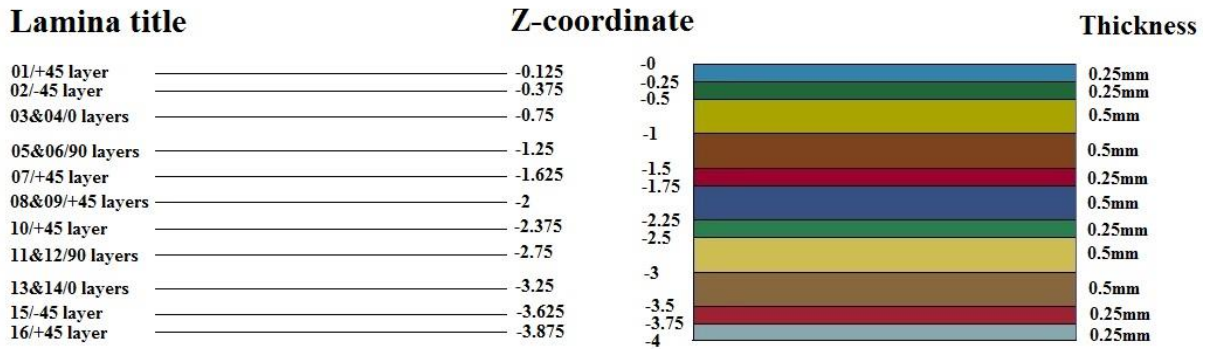


Figure 5.37 Schematic illustration of the stack of 11 laminas to simulate the 4mm quasi-isotropic laminates.

The laminas were created by defining the coordinate information in the 4N_Shell mesh card. It is however worth mentioning that the Z-coordinate of the lamina should be determined considering the laminates lay-up and the corresponding individual lamina thickness since the created shell lamina only represents the mid-plane of lamina as shown schematically in Figure 5.37. Different mesh schemes were employed to study the element size sensitivity of the simulation result. The maximum mesh scheme was set to 75×50 for the 4mm lamina and mesh density of 15 for the sphere, as a result of the limitation of the number of elements of the ANSYS/LS-DYNA academic research licence available for the project.

Figure 5.38 shows the geometry model of the FE simulation of the 4mm composite laminates impacted by a rigid sphere with the maximum mesh scheme. With the maximum mesh scheme, there were 41250 ($75 \times 50 \times 11$) shell elements in the laminates, and 23625 solid elements in the sphere. Different geometry models were created with different lamina mesh schemes (including 15×10 , 30×20 , and 60×40) and rigid sphere mesh densities (including 7 and 10).

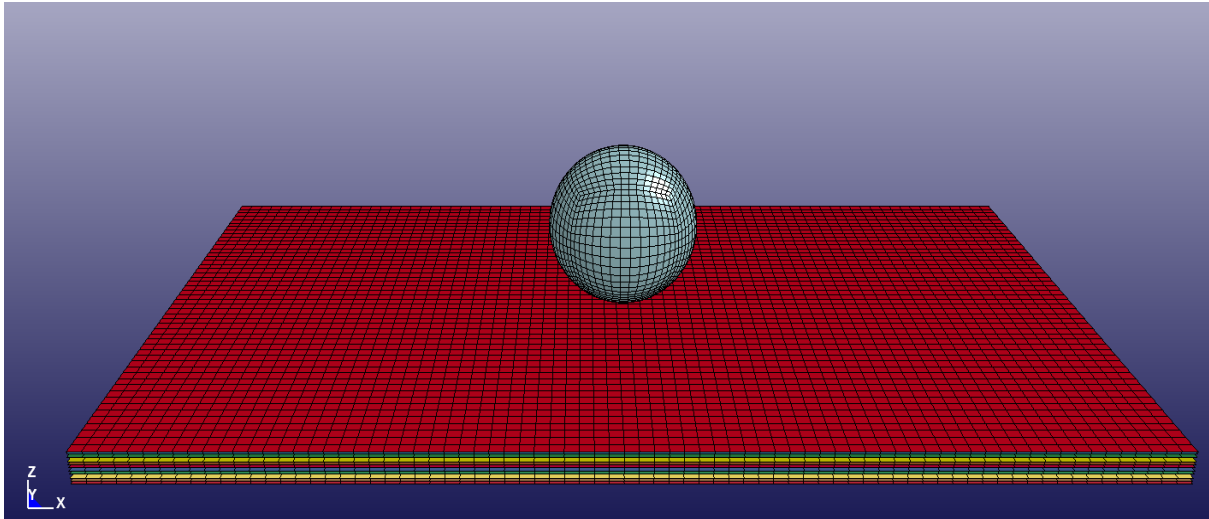


Figure 5.38 Geometry model for the FE simulation of the 4mm laminates under low-velocity impact.

Once the geometry model was created, the impact induced damage was simulated by employing the advanced modelling strategy considering the damage mechanism. In the advanced modelling strategy, the intralaminar and interlaminar damages were predicted by the specific material model, including the failure criterion and degradation scheme, and the tie-break contact/cohesive element method, respectively.

Intralaminar Damage Simulation

In LS-DYNA/LS-PREPOST, a variety of material models are available for simulating the intralaminar damage of composite laminates. Depending on the specific degradation law used, these material models are divided into either progressive failure models (PFM), such as MAT_22 and MAT_54/55, or continuum damage mechanics (CDM), such as MAT_58 and MAT_162 [122]. Considering both of the complexity of model creation and the solution efficiency, the MAT_54/55_ENHANCED_COMPOSITE_DAMAGE was used in this project to predict the progressive intralaminar damage of composite laminates.

Figure 5.39 shows the input data for the +45° prepreg in the MAT_54/55 material card. These input parameters are not detailed in the LS-PREPOST software user manual and it is therefore necessary to summarize the definitions and defined values of these parameters. Table 5.2 shows the input value determined from the literatures [81, 102, 122, 128] and tests as presented in Chapter 4.

NewID	RefBy	Pick	Add	Accept	Delete	Default	Done
<input type="checkbox"/> Use *PARAMETER (Subsys: 1) Setting							
*MAT_ENHANCED_COMPOSITE_DAMAGE_(TITLE) (054/055) (4)							
TITLE							
+45 Prepreg							
1	MID	RO	EA	EB	(EC)	PRBA	(PRCA) (PRCB)
	1	0.0015800	1.320e+005	7530.0000	0.0	0.0127000	0.0 0.0
2	GAB	GBC	GCA	(KF)	AOPT		
	4150.0000	4150.0000	4150.0000	0.0	3.0000000		
3	XP	YP	ZP	A1	A2	A3	MANGLE
	0.0	0.0	0.0	0.0	0.0	0.0	45.000000
4	V1	V2	V3	D1	D2	D3	DFAILM DFAILS
	0.0	1.0000000	0.0	0.0	0.0	0.0	0.1000000 0.0300000
5	TFAIL	ALPH	SOFT	FBRT	YCFAC	DFAILT	DFAILC EFS
	1.000e-007	0.0100000	0.5000000	0.5000000	2.0000000	0.0160000	-0.0111000 0.0
6	XC	XT	YC	YT	SC	CRIT	BETA
	-1465.0000	2116.6001	-236.00000	44.599998	84.629997	54.0	0.0

Figure 5.39 Input data for +45° prepreg in MAT_54/55 material card.

From the Table 5.2, it is clear that the MAT_54/55 contains two main kinds of parameters, which are the material properties and code-specific parameters. The material property related parameters are physical property (mass density), elasticity properties (Young’s modulus and Poisson’s ratio), and failure criterion (failure strength and strain to failure). The code-specific parameters include material axes parameters (AOPT, MANGLE, *et.al.*), failure criterion parameters (ALPHA, BETA and CRIT), degradation scheme factors (FBRT and YCFAC), and other simulation required non-physical parameters (SOFT and TFAIL) [122].

Table 5.2 MAT_54/55 input parameter definitions and values [122]

LS-DYNA parameter	Definition	Defined value
MID	Material ID	1 (can be any integer)
RO	Mass density	1580 kg/m ³
EA	Young’s modulus in longitudinal direction	131.95GPa
EB	Young’s modulus in transverse dirction	7.53GPa
EC	Young’s modulus in thickness direction	Not used
PRBA	Minor Poisson’s ratio, $\nu_{ba} = \nu_{21}$	0.0127

PRCA	Minor Poisson's ratio, $\nu_{ca} = \nu_{31}$	Not used
PRCB	Minor Poisson's ratio, $\nu_{cb} = \nu_{32}$	Not used
GAB	Shear modulus, G_{ab}	4.15GPa
GBC	Shear modulus, G_{bc}	4.15GPa (assumed equal to G_{ab})
GCA	Shear modulus, G_{ca}	4.15GPa (assumed equal to G_{ab})
KF	Bulk modulus of material	Not used
AOPT	Material axes option	3.0
XP YP ZP	Vector components to define the material axes for AOPT = 1.0	Not used
A1 A2 A3	Vector components to define the material axes for AOPT = 2.0	Not used
D1 D2 D3	Vector components to define the material axes for AOPT = 2.0	Not used
V1 V2 V3	Vector components to define the material axes for AOPT = 3.0	Unit vector in y-direction: $V1 = 0 \ V2 = 1 \ V3 = 0$
MANGLE	Material angle in degrees for AOPT = 3.0	+45 (range of -90 to +90)
DFAILM	Maximum strain for matrix straining in tension and compression	0.01 (\geq the max value of (YT/EB) or (YC/EB))
DFAILS	Maximum shear strain	0.03 ($0 < DFAILS \leq 0.1$)
DFAILT	Maximum strain for fibre tension	0.016 (XT/EA)
DFAILC	Maximum strain for fibre compression	-0.011 (XC/EA)
EFS	Effective failure strain	0.0
TFAIL	Time step size criteria for element deletion	1E-7 (very small but nonzero)
ALPH	Shear stress non-linear term	0.01 ($1E-3 \leq ALPH \leq 1$ and calibrated by trial and error)
SOFT	Crush front strength reducing parameter	0.5 (calibrated by trial and error)
FBRT	Softening factor for fibre tensile strength after matrix failure	0.5 ($0 \leq FBRT \leq 1$ and calibrated by trial and error)
YCFAC	Softening factor for fibre compressive strength after matrix failure	2.0 ($0 \leq YCFAC \leq (XC/YC)$ and calibrated by trial and error)
XC	Longitudinal compressive strength	-1465MPa
XT	Longitudinal tensile strength	2117MPa
YC	Transverse compressive strength	-236MPa
YT	Transverse tensile strength	44.60MPa

SC	Shear strength	84.63MPa
CRIT	Failure criterion selected	54 (CRIT = 54: Chang-Chang; CRIT = 55: Tsai-Wu)
BETA	Weighting factor for shear term in tensile fibre mode	0.0 (0 ≤ BETA ≤ 1)

In the MAT_54/55 material model, two main phases are involved in simulating the progressive damage process. One is the elastic phase, and the other is the failure phase. In the elastic phase, the material behaviours, in terms of the stress-strain relation, in the longitudinal, transverse, and shear directions are given by

$$\begin{aligned}\varepsilon_1 &= \frac{1}{E_1}(\sigma_1 - \nu_{12}\sigma_2) \\ \varepsilon_2 &= \frac{1}{E_2}(\sigma_2 - \nu_{21}\sigma_1) \\ 2\varepsilon_{12} &= \frac{1}{G_{12}}\tau_{12} + \alpha\tau_{12}^3\end{aligned}\quad (5.4)$$

where, α is the input parameter, ALPH, in MAT_54/55. It is a weighting factor for the nonlinear shear stress term, which cannot be measured experimentally and needs to be calibrated by trial and error.

In the failure phase, different failure criteria were employed in the material model by assigning the parameter value of CRIT. The MAT_54 uses the Chang-Chang failure criterion, while the MAT_55 uses the Tsai-Wu failure criterion. The individual layer failure was thus determined by the strength-based failure criterion. Once the failure strength was reached, a layer discount method will be used to degrade the material properties from the undamaged state to the fully damaged state. The progressive failure model worked through the ply-by-ply failure within the lamina, and after all layers had failed the element was deleted [122].

Compared with the Chang-Chang failure criterion described in Section 2.3.4, the failure criterion employed in the MAT_54 material model introduces a new shear stress weighting factor β (as BETA in MAT_54) to define the shear stress interaction in the fibre tensile failure mode (where $\sigma_1 \geq 0$)

$$e_f^2 = \left(\frac{\sigma_1}{X_t}\right)^2 + \beta \left(\frac{\tau_{12}}{S_{12}}\right)^2 = \begin{cases} \geq 1 & \text{failure} \\ < 1 & \text{no failure} \end{cases} \quad (5.5)$$

if BETA = 1.0, the Hashin failure criterion is implemented; if BETA = 0.0, the maximum failure criterion without interaction is activated.

Furthermore, the degradation scheme of the MAT_54/55 model was defined by the degradation scheme factors and the simulation required some non-physical parameters. The FBRT and YCFAC are the strength reduction parameters in the MAT_54/55 material model. They are used to degrade the original fibre strengths of the remaining layers, once the specific elastic material properties of a layer are set to zero when one of the failure criterion is reached in that layer within the element. The degradation schemes are based on the following equations:

$$\begin{aligned} XT^* &= XT * FBRT \\ XC^* &= YC * YCFAC \end{aligned} \quad (5.6)$$

where, the FBRT is the percentage reduction of the fibre tensile strength from its original value; the YCFAC is the correlation facator between the original matrix strength YC and the damaged fibre compressive strength. It is also necessary to mention that the values of FBRT and YCFAC cannot be determined from tests and need to be determined by trial and error [122].

In addition, the TFAIL and SOFT are the required non-physical simulation parameters. The value of TFAIL defines whether and what a minimum time step for element deletion is considered in the simulation. By defining a minimum time step allowed for element deletion, the computational cost of the simulation of the highly distorted element that no longer carry load but do not fail from the element deletion criterion can be effectively avoided. When the value of TFAIL is less than or equal to 0, no element would be deleted by time step size. When the value of TFAIL is between 0 and 1, the element with smaller time step compared with the defined TFAIL value would be deleted. When the value of TFAIL is larger than 1, the element would be deleted once the ratio between current time step and original time step is less than the defined TFAIL value. The SOFT parameter is a mathematical expedient to reduce the strength of element immediately ahead of the crush front. This parameter helps to improve the stability of the crushing, when the load is transferred from the crushed row of

elements to the next one. Similarly, this non-physical parameter cannot be measured experimentally neither, and should be determined by trial and error [122].

The other code-specific parameters, including the AOPT, MANGLE, etc., are used to specify the material axes. The AOPT is the indicating parameter to activate the material axes defining method. The principles of the material axis defining methods are shown schematically in Figure 5.40.

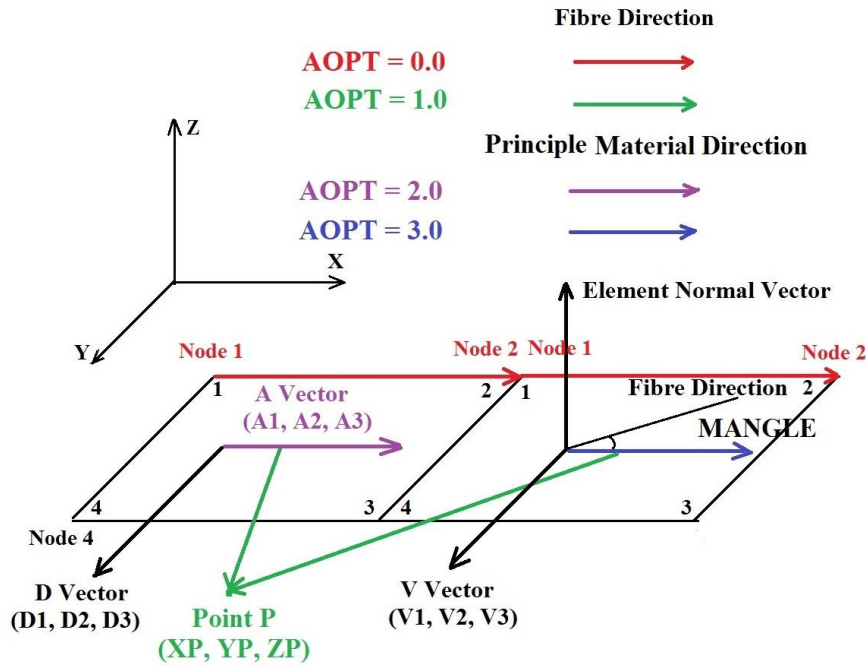


Figure 5.40 Schematic illustration of different material axis defining methods in MAT_54/55 material model.

For AOPT = 0.0, the fibre direction is directly determined by the element nodes. The fibre direction of each element is in the element edge from node 1 to node 2. However, it is difficult to specify the fibre directions of all the elements in general by this method. For AOPT = 1.0, the material axes is determined by the global location of the element centre and a point in the space by specifying the coordinates of this P point (XP, YP, and ZP) in the MAT_54/55 material card. In this method, different elements might have different fibre directions, if just one P point was defined as shown in Figure 5.40. As a result, numerous P points need to be defined to ensure correct fibre direction is assigned to the element.

Apart from the methods with directly defined fibre orientation, several other methods are available to specify the material axes by defining the principal material direction and the rotation angle (as MANGLE). For AOPT = 2.0, two vectors (A vector and D vector) need to

be defined in the MAT_54/55 material card. The A vector is the principal material direction, and D vector is perpendicular to the A vector as shown in Figure 5.40. For AOPT = 3.0, the principal material direction is the cross product of the element normal vector and the defined V vector as illustrated in Figure 5.40. Once the principal material direction is defined, the fibre direction is determined by specifying the MANGLE that is the rotation angle in degrees from the principal material direction to the fibre direction.

In this study, the AOPT was set to 3.0 to activate the corresponding material axes defining method. It is known that the shell element in the geometry model was in x-y plane with a resultant normal vector in z-direction. Therefore, to ensure the principal material direction is in x-direction, the V vector was defined as the unit vector in y-direction. Furthermore, different values of MANGLE were specified to have different material models with different fibre directions (0° , 90° , $+45^\circ$, and -45°).

Interlaminar Damage Simulation

In the current simulation, the tie-break contact is adopted to simulate the interlaminar failure, i.e. a separation of adjacent laminas, although various material models with cohesive element are also available in LS-DYNA/LS-PREPOST to simulate the interlaminar damage. It is mainly because of the more complex model creation and higher computational cost by inserting the cohesive element between adjacent shell elements with a specific traction-separation law to simulate the progress of interlaminar damage. It is also noticed that different layers of cohesive elements may not share common nodes. As a result, the cohesive elements in a multilayer shell model with more than one layer of cohesive elements must be connected by the additional contact definitions, making this modelling strategy rather complex [103]. Therefore, the tie-break contacts are employed in the current multilayer shell model to bond the adjacent laminas.

As it has been suggested in Section 2.4.3, the tie-break contact is capable of simulating the interlaminar damage based on the cohesive zone model. The tie-break contact formulation (CONTACT_AUTOMATIC_ONE_WAY_SURFACE_TO_SURFACE_TIEBREAK) was applied to the nodes which are initially in contact of adjacent laminas. Therefore, the progression of interlaminar damage was reduced to determine the force-displacement relation between pairs of coincident nodes connected by the tie-break contact.

*CONTACT_AUTOMATIC_ONE_WAY_SURFACE_TO_SURFACE_TIEBREAK_(ID/TITLE/MPP)_ (THERMAL) (1)

CID	TITLE							
1	interface 01							
<input type="checkbox"/> MPP1 <input type="checkbox"/> MPP2								
IGNORE	BUCKET	LCBUCKET	NS2TRACK	INITITER	PARMAX	UNUSED	CPARM8	
0	200		3	2	1.0005		0	
UNUSED	CHKSEGS	PENSE	GRPABLE					
	0	1.0	0					
1	SSID	MSID	SSTYP	MSTYP	SBOXID	MBOXID	SPR	MPR
2	1	1	3	3	0	0	0	0
2	FS	FD	DC	VC	VDC	PENCHK	BT	DT
	0.0	0.0	0.0	0.0	0.0	0	0.0	1.000e+020
3	SFS	SFM	SST	MST	SFST	SFMT	FSF	VSF
	0.1000000	0.1000000	0.0	0.0	1.0000000	1.0000000	1.0000000	1.0000000
4	OPTION	NFLS	SFLS	PARAM	ERATEN	ERATES	CT2CN	CN
	8	0.0446000	0.0829100	0.0242152	0.0	0.0	0.0	0.0
<input type="checkbox"/> Thermal <input type="checkbox"/> T_Friction <input checked="" type="checkbox"/> A <input type="checkbox"/> AB <input type="checkbox"/> ABC <input type="checkbox"/> ABCD								
CF	FRAD	HTC	GCRIT	GMAX	CD_FACT	BC_FLG	ALGO	
					1.0			
LCFST	LCFDT	FORMULA	a	b	c	d		
A	SOFT	SOFSCL	LCIDAB	MAXPAR	SBOPT	DEPTH	BSORT	FRCFRQ
	2	0.1000000	0	1.0250000	2.0	2	0	1

Figure 5.41 Input data for the tie-break contact card.

Figure 5.41 shows the input data for the tie-break contact card. The normal and shear failure stresses (NFLS and SFLS) were defined to check the bond failure. The test results of the transverse tensile strength and interlaminar shear stress were assigned to the NFLS and SFLS, respectively. During the loading, the bond failure of the tie-break contact was checked based on the following criteria [81]

$$\left(\frac{|\sigma_n|}{\text{NFLS}}\right)^2 + \left(\frac{|\sigma_s|}{\text{SFLS}}\right)^2 \geq 1 \quad (5.7)$$

The interlaminar damage was a linear function of the distance of the two nodes which are initially in contact. A critical crack opening (CCRIT) was also defined by specifying the PARAM parameter in the tie-break contact definition card. This parameter was linked to the NFLS and the mode I critical energy release rate ($G_{IC} = 500 \text{ J/m}^2$, as presented in Chapter 4) as follow [103]

$$G_{IC} = \frac{1}{2} * NFLS * CCRIT \quad (5.8)$$

Once the defined critical opening was reached, the tie-break contact would degrade into a regular surface-to-surface contact between two separate surfaces to prevent the penetrations. Meanwhile, the OPTION parameter was set equal to 8.0 to active the above mentioned tie-break contact behaviour.

Several contact penalty stiffness parameters are also available to further define the tie-break contact behaviour. These parameters, including the SOFT in the A optional card, SFS and SFM in mandatory card, may significantly affect the simulation result. The SOFT is the soft constraint option. In this study, the value of SOFT was set to 2 to activate a pinball segment based contact algorithm developed by Belytschko *et al.* [129]. By employing the specific contact algorithm, the common node-to-segment contact treatment is replaced with the specific segment-to-segment contact treatment, which helps to make the forces distribution more realistically and invoke all the nodes from both segments to resist segment penetration [81]. The contact stiffness in this case with SOFT = 2 was calculated by taking the nodal mass divided by the square of the time step size with a scale factor, SOFSCL, to ensure stability [81, 103]

$$k = SOFSCL * \frac{m}{\Delta t^2} \quad (5.9)$$

where, the value of SOFSCL was set to the default value 0.1 in the current study.

Moreover, the SFS and SFM are the penalty stiffness scale factors for the slave and master elements, respectively. The default values of these two parameters were 1.0. However, in this study these parameters were set to 0.1. This is based on the parametric study conducted by Heimbs *et al.* [103] in which the reduced value of SFS/SFM (in the range of 0.01 to 0.1) provided acceptable simulation result. The elements in contact were not eroded to make the master segment penetrated through the slave segment.

Lastly, it should be noticed that different contact definitions were used between components in the current simulation model. The AUTOMATIC_SURFACE_TO_SURFACE contact was used between the impactor and the first lamina of the stacked laminas to simulate the impact event. The AUTOMATIC_ONE_WAY_SURFACE_TO_SURFACE_TIEBREAK contacts were used between the adjacent laminas of composite laminates to simulate the interlaminar failure.

5.2.4 Preliminary Simulation Results with Consideration of Damage Mechanism

The low-velocity impact event between the impactor and the 4mm composite laminates with quasi-isotropic lay-up configuration was simulated by employing the modelling strategy with the consideration of the damage mechanism. The simulation models were created following the creation procedure as described in Section 5.2.3. It is however worth noting that both the mesh scheme and the definition of the simulation related model parameters might significantly affect the simulation results [103, 122, 128]. The optimised mesh scheme should be derived by considering the balance between the simulation result convergence and the computational efficiency while the definition of the model parameter should be calibrated by the simulation results. Therefore, it is necessary to derive the optimised mesh scheme for the simulation model, before more impact conditions were simulated in this numerical study.

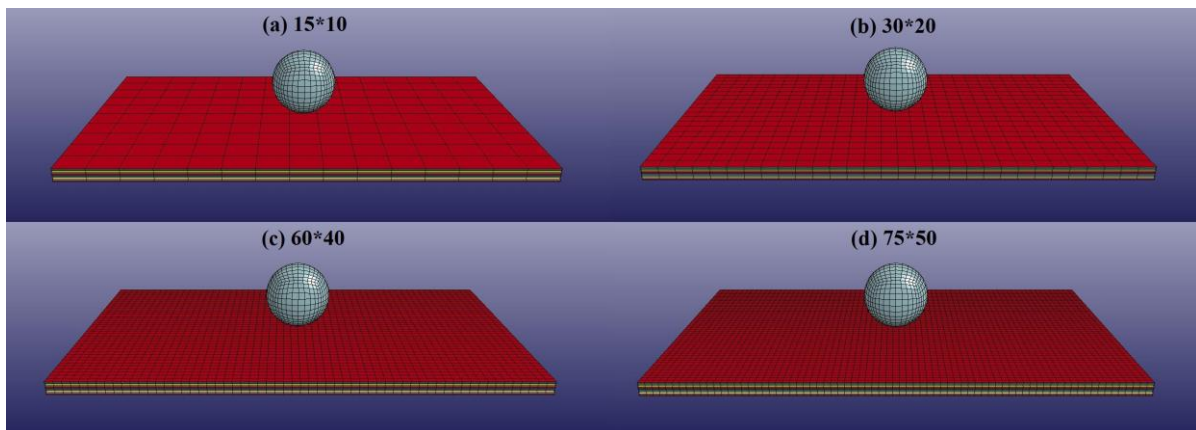


Figure 5.42 Simulation models with different mesh schemes for the laminates.

Figure 5.42 shows four simulation models with various mesh schemes of the plate, which were created to determine the optimised mesh scheme for the laminates. The model with 15*10 plate mesh scheme was solved in several minutes, while the solving time for the model with 75*50 plate mesh scheme was increased to several hours.

Figure 5.43 shows the comparison between the experimental result and the numerical results obtained from different simulation models with different plate mesh schemes, which helped to derive the optimised mesh scheme for the plate. It is found that the simulation results deviated from the experimental impact force history. It is caused mainly by the unexpected load fluctuation in the early stage of simulation result. In addition, the sudden load drop phenomenon due to the delamination initiation could not be found in the simulation results

either. These differences indicate that some parameters of the simulation model need to be adjusted further to achieve the appropriate simulation result of the internal damage.

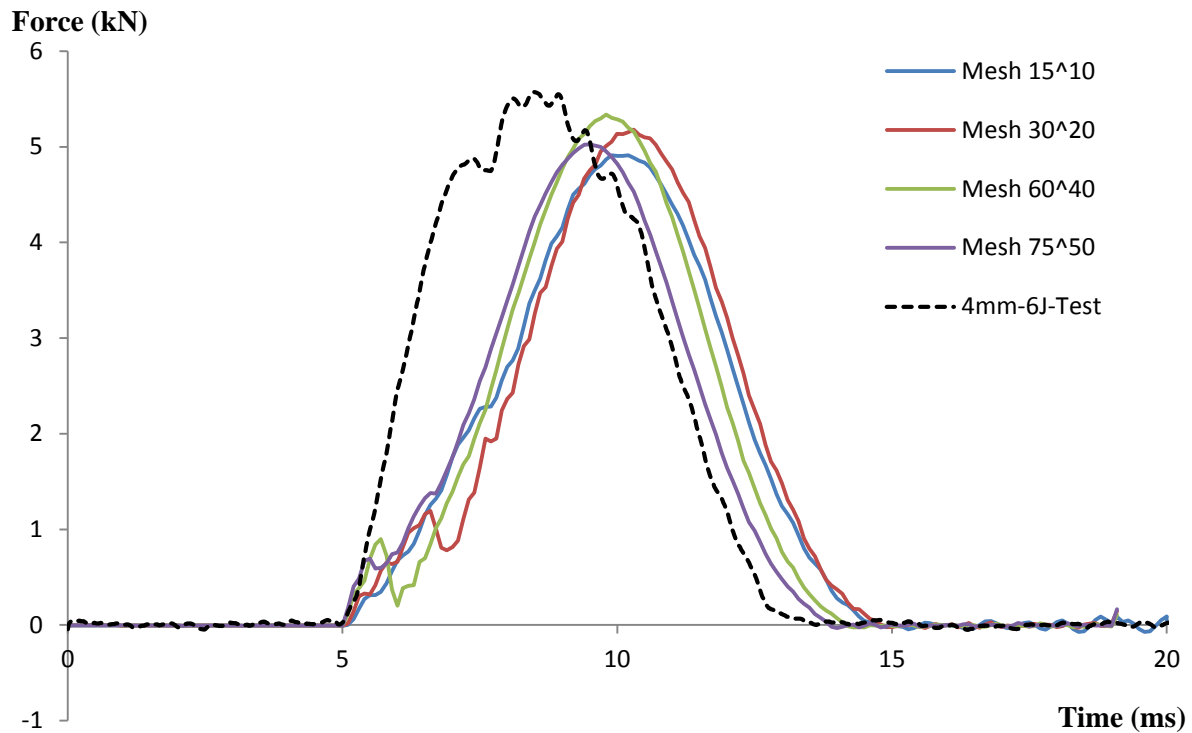


Figure 5.43 Comparison between experimental result and simulation results obtained from models with different plate mesh schemes.

Moreover, it is noticed that there was no clear trend among the simulation results. To be specific, the simulation model with the largest element size generated the lowest peak force and longest impact duration, while the highest peak force and the shortest impact duration were obtained from the simulation models with 60×40 and 75×50 plate mesh schemes, respectively. This result demonstrated that the convergence of the simulation result had not been achieved by the current model setup. As a result, the optimised mesh scheme for the plate could not be evaluated based on the current simulation result. However, considering the computational efficiency, the mesh scheme of 60×40 was selected as the preliminary optimised mesh scheme for the plate and was used in the following study to obtain the optimised mesh density for the impactor.

Figure 5.44 shows the simulation models with same mesh scheme for the plate (as 60×40) and different mesh densities for the impactor.

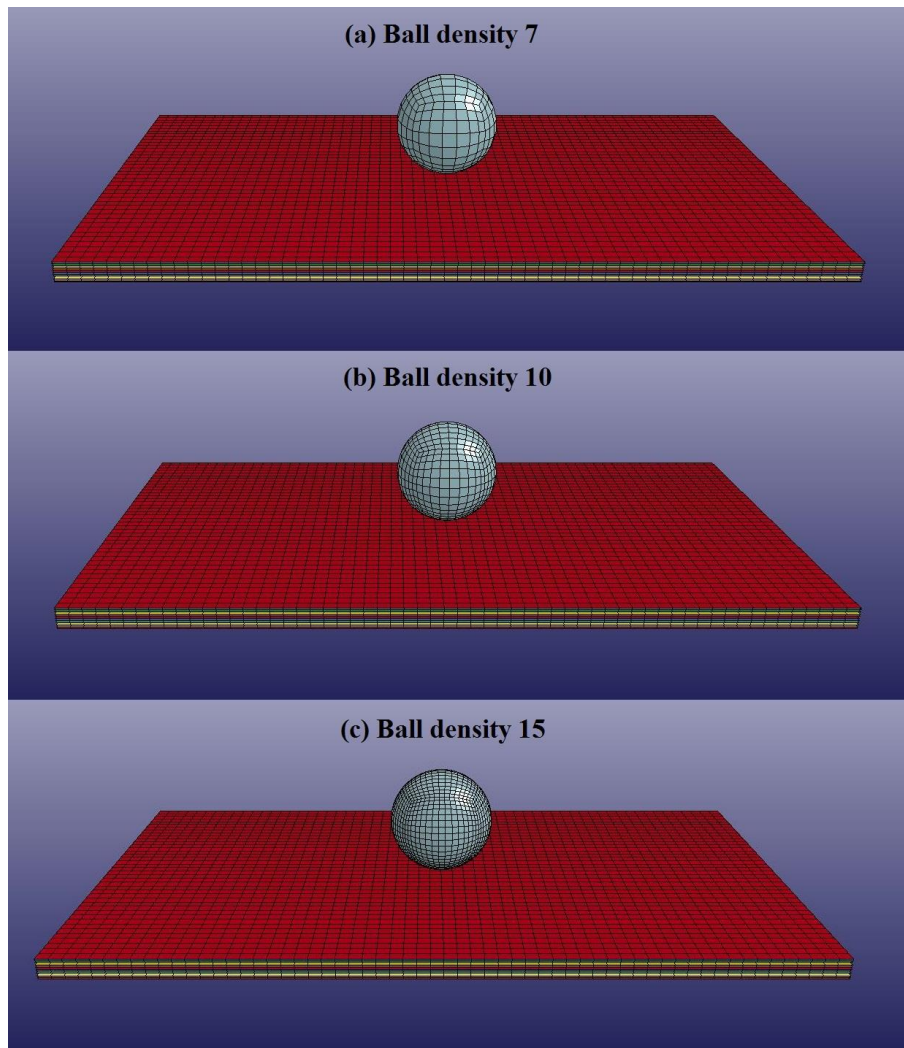


Figure 5.44 Simulation models with different mesh densities for the impactor.

Figure 5.45 shows the comparison between the experimental result and simulation results obtained from the simulation models with different mesh densities for the impactor. It is noticed that the impact peak force and the early stage load fluctuation phenomenon were both affected by the mesh density of the impactor, while the impact duration was hardly influenced by the parameter. Specifically, the simulation results achieved from the simulation models with mesh density of 10 and 15 for the impactor agreed well with each other. However, the simulation result of the simulation model with mesh density of 7 for the impactor deviated from others with a lower peak impact force and a more significant early stage load fluctuation phenomenon. This result indicated that the convergence of simulation result was reached for the simulation model with the mesh density of 10 and 15 for the impactor. The optimised mesh density for the impactor was hence selected to be 10 for the simulation model in this study.

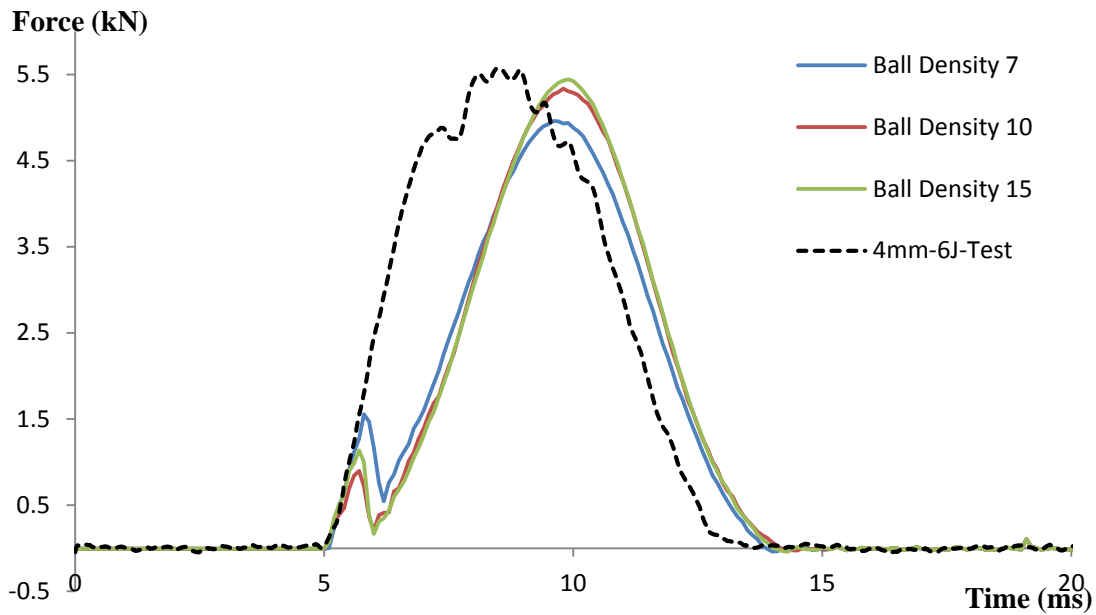


Figure 5.45 Comparison between experimental result and simulation results obtained from models with different mesh densities for impactor.

The optimised mesh scheme for the simulation model, with the mesh scheme of 60×40 for the plate and mesh density of 10 for the impactor, was used in the subsequent simulation investigations to simulate impacts under various impact energy levels. The simulation results were compared with the experimental results as shown in Figure 5.46.

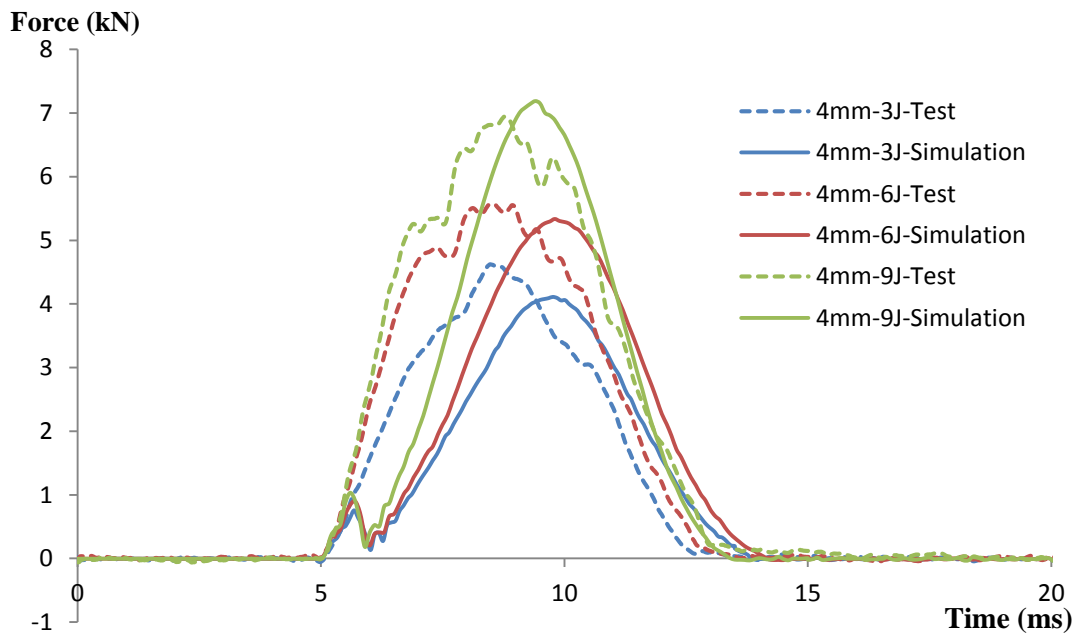


Figure 5.46 Comparison between simulation results employing modelling strategy with consideration of damage mechanisms and test results.

It can be found clearly that the simulation result deviates significantly to the test result, although the experimental results and the numerical results show the similar impact duration and impact peak force. The deviation was mainly related to the unexpected load fluctuation phenomenon in the early stage of the impact force history. It was speculated that the load fluctuation phenomenon in the early stage was caused by the improper definition of material properties as the Chang-Chang theory employed in the MAT_54 material model was sensitive to the matrix crack [66]. Efforts have been made to evaluate the matrix cracking effect on the simulation result. Various transverse compressive strengths had been used in different simulation models. But it was found that the simulation result is independent of the value of the transverse compressive strength (YC). Later on, it was found that the early stage load fluctuation still existed even if the Chang-Chang failure criterion was effectively switched off in the simulation models under lower impact energy levels (3J and 6J) by defining several artificially high values of the related matrix material properties. As a result, it was proved that the load fluctuation in the early stage is not related to the initiation of matrix crack under the low impact force.

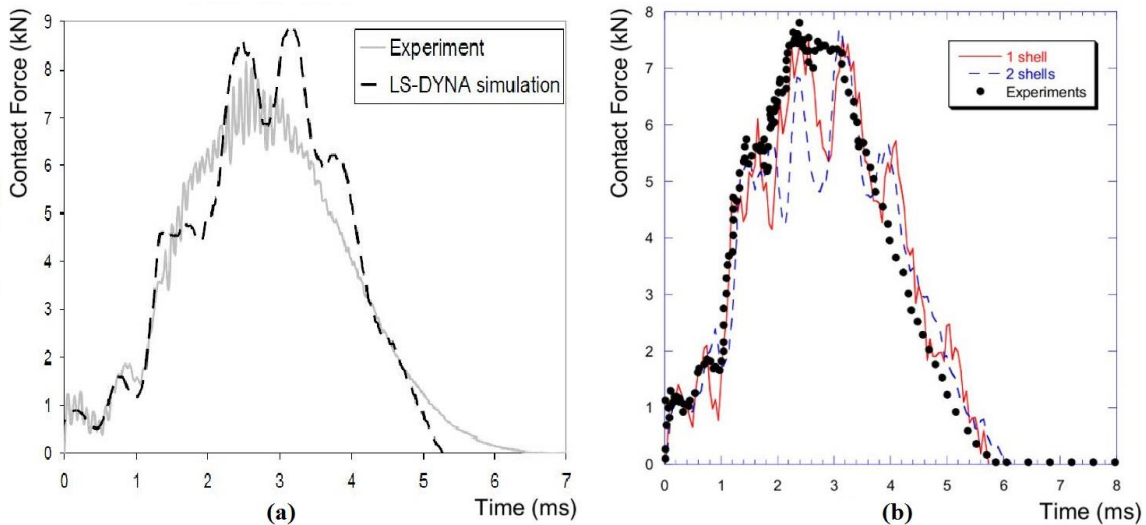


Figure 5.47 Literature simulation results: (a) an impact event with preload [103]; and (b) a simulation using thin shell element and tie-break contact [81].

It is however interesting to note that the early stage load fluctuation phenomenon can also be seen in literature results. Figure 5.47 shows the literature simulation results presented by different researchers [81, 103]. MAT_54 material model and the tie-break contact were also employed in their models. This finding demonstrated that the early stage load fluctuation phenomenon might be an inherent simulation noise induced by the specific material model

and contact definition involved in the specific modelling strategy. More efforts should be made to improve the model setup in order to minimise such simulation noise.

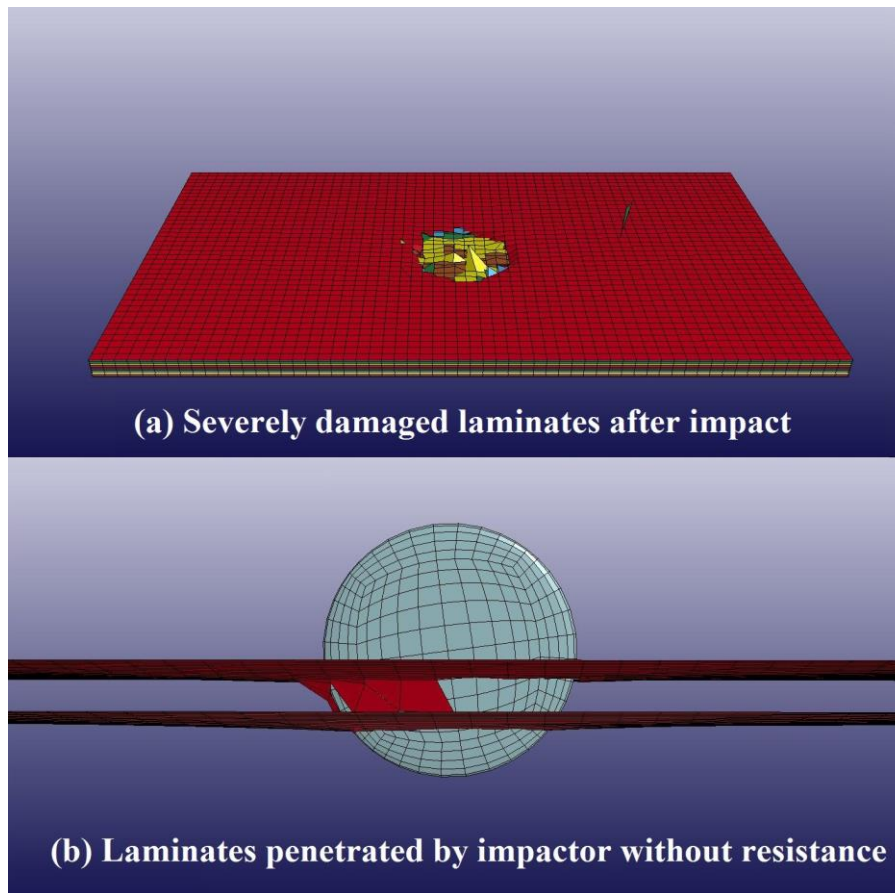


Figure 5.48 Simulation result of the simulation model with 12J impact energy.

Moreover, it was noticed that no significant element deletion could be observed in the results of the simulation models under relatively low impact energy levels as presented in Figure 5.46. Severe damage was found in the simulation result of the simulation model under high impact energy of 12J as illustrated in Figure 5.48(a). The dramatic element deletions were introduced like a chain reaction after the first element deletion. This behaviour was however against the experimental observation since the damage was induced following a specific damage pattern in reality. After carefully reviewing the simulation result, it was found that the impactor actually penetrated the whole laminates without any further material resistance once the elements in the first layer under the impactor were damaged due to the material failure as shown in Figure 5.48(b).

This behaviour is explained by the fact that the impact contact definition, which is `AUTOMATIC_SURFACE_TO_SURFACE` contact, was only applied to the contact pair

between the impactor and the first layer in the current simulation model. As a result, once the elements in the first layer were damaged, the impactor was able to go through the second layer and the subsequent layers as there was no proper contact definition between the impactor and these layers. Therefore, it is necessary to define several extra impact contact pairs between the impactor and the first several layers of the simulation model under relatively high impact energy level.

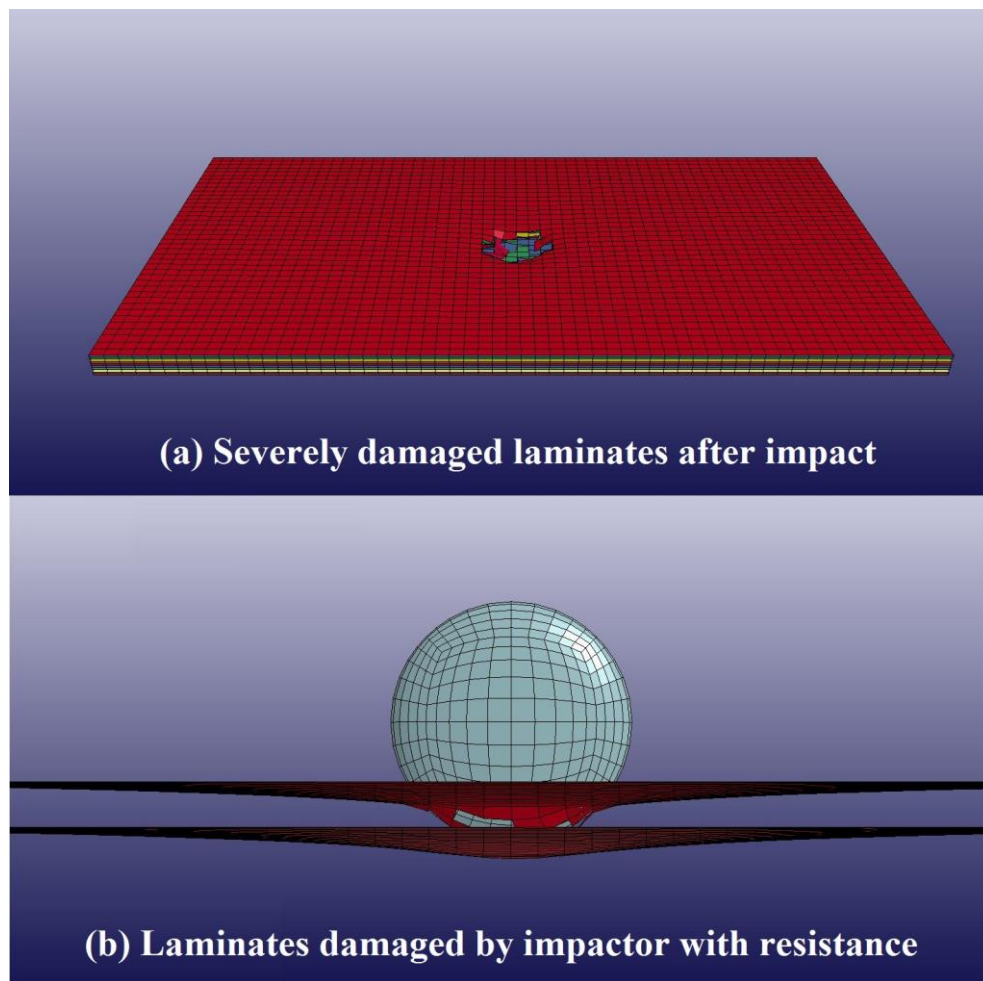


Figure 5.49 Simulation result of the modified simulation model with 12J impact energy.

To verify above explanation, the current simulation model under 12J impact energy was modified by applying four more impact contact definitions to the contact pairs between the impactor and the second to the fifth layers. The simulation result of the modified simulation model is shown in Figure 5.49.

It can be seen that the laminates still suffered a severe damage in the simulation result of the modified simulation model. The damage was however not as significant as that shown in Figure 5.48(a) since more layers had been involved in resisting the impact event. It could be

observed from Figure 5.49(b) that the impactor did not penetrate the laminates, but induced significant deformation in the bottom layer. This result showed that the modification of the extra contact pairs did improve the overall resistance of the laminates. The individual lamina inside the laminates had been combined together with strong interactions to resist the impact event.

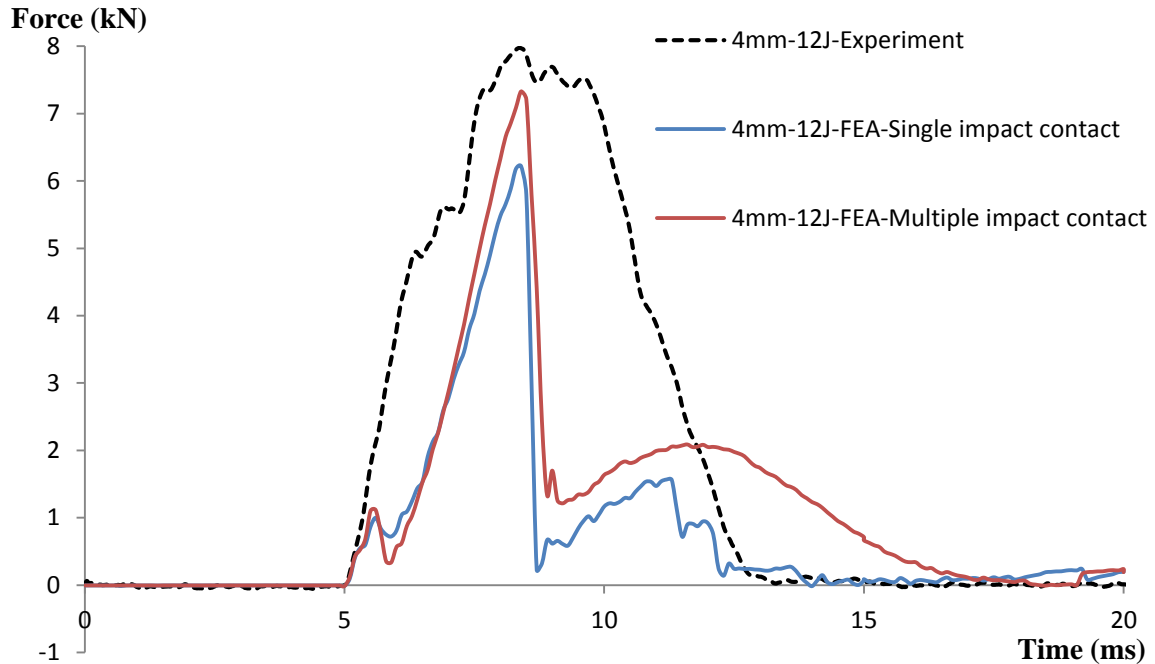


Figure 5.50 Comparison between test result and simulation results with different impact contact definitions.

Fig.5.50 shows the comparison of the impact force history between the experimental and simulation results. In addition to the early load drop mentioned earlier, the simulation results significantly deviate from the test result, as a result of the existence of the tremendous load drop due to the un-controlled element deletion at high impact force. It is also noticed that the simulation efficiency was significantly reduced due to the un-controlled element deletion, in which case the simulation time-step was reduced to an extremely small level once the first element was deleted. As a result, the solution time of a simulation model with such un-controlled element deletion would be increased dramatically or even be stuck in an infinite loop. Such unexpected element deletion had to be further investigated and overcome to achieve acceptable simulation results. Moreover, it was noticed that the simulation results had been slightly improved by defining extra contact pairs. The laminates with multiple impact contact definitions was stiffer than that with single impact contact definition, referring to the

higher peak force before the tremendous load drop was introduced by the unexpected element deletion.

In conclusion, the simulation involving advanced modelling strategy with the consideration of damage mechanism was far from straightforward. The simulation result could easily be affected by improper parameter setup. Therefore, it is necessary to carry out a rigorous parametric study in the future, in order to setup the proper simulation model and to obtain reliable simulation results.

5.3 Summary

This chapter presents the results obtained from both the experimental and numerical approaches to characterise the damage mechanisms and impact response of composite laminates subjected to low-velocity impact.

In the experimental approach, the damage mechanisms and impact response of composite laminates under low-velocity impact were investigated through instrumented drop weight tests. The existence of the DTL, shown as a sudden load drop in the impact force history, was clearly observed in some of the test results. The laminates thickness was found to significantly affect the reliability of the detection of the DTL via the impact force history. Current results indicate that there exists a suitable range of ratio of the impact energy to the laminates stiffness/thickness to determine the DTL value when the impact force history is used.

The effect of repeated impact on the impact response of composite laminate was investigated in details. Interesting findings include that the impact force curve is smoother and the peak impact force is higher in the repeated impact force history compared with the first impact force history when the DTL has not been exceeded. The repeated impact force histories and the first force history are almost identical if the delamination has not been initiated by the first impact. These results further demonstrated the existence of the DTL and offered an alternative approach in detecting the DTL for the case that the sudden load drop phenomenon is not significant in the impact force history. The results have also implied that the influence of delamination initiation on the reduction of the load bearing capacity of the impacted composite laminates might be overestimated considering the increment in the peak force of the repeated impact history of the delaminated composite laminates. While delamination may

be initiated under relatively low impact force, the delamination would not propagate further during the repeated impact due to the improved flexibility of the laminates and additional energy absorption mechanisms offered by multiple delamination initiation sites under the first impact. The good damage tolerance capacity of the impacted composite laminates demonstrated in the current study is valuable in reducing the conservatism in design philosophy of composite laminates in aerospace industry.

Moreover, similar trends, in terms of the effects of laminates thickness and repeated impact on the damage mechanisms and impact response of composite laminates, were observed from a series of low-velocity impact tests conducted on the composite laminates with different lay-up configurations. It is suggested that the lay-up configuration did affect the damage mechanisms and impact response of composite laminates as a result of the changed laminates stiffness. However, such effect was not as dominant as other parameters including the laminates thickness and repeated impact. Moreover, the residual thermal stress effect on the damage mechanisms and impact response of composite laminate was also investigated through a series of impact tests conducted on the specimens cured at different curing temperatures. It is suggested that the release of thermal residual stress in composite laminate was not the reason for the increase of the peak impact force observed in the repeated impact force history. It is suspected that the improved flexibility of the specimen and the additional energy absorption mechanisms caused by the multiple delaminations in the first impact might be the main reasons for the increase of the peak impact force during the repeated impact. More evidences had been achieved in the research and would be presented in the following chapter to support the above opinion.

In the numerical approach, the low-velocity impact event between the impactor and composite laminates was simulated by two different simulation strategies. In the modelling strategy without consideration of damage mechanisms, only the total thickness and the equivalent ABD stiffness matrix were defined for the composite laminates. It is found that the correlation between the simulation result and test result are strongly affected by the delamination initiation. Since no damage mechanism was included in the model, the material degradation in the damaged composite could not be taken into account by the simulation. The simulation results in terms of the impact force history agree well with the experimental result when the peak impact force is below the DTL of the laminates. The predicted impact force history was higher than the experimentally measured impact force history when the DTL was exceeded. The simulation results validated the DTL value detected in experimental work.

The composite laminates was also simulated with the modelling strategy with consideration of damage to account for the damage mechanisms. Failure criterion and degradation scheme were defined in the material model for each individual layer to simulate the intralaminar damage while the tie-break contact was used to connect the adjacent layers to simulate the interlaminar damage. Simulated impact responses in terms of the impact peak force and impact duration were similar to those obtained from the drop weight test. It is however found that the simulation result deviated from the test result due to the existence of the early stage load drop and un-reliably controlled material degradation. It is caused by the fact that the simulation was sensitive to several parameters with some parameters being calibrated by trial and error without any obvious physical meaning. Therefore, the simulation model needs to be further calibrated to generate reliable simulation results, in terms of the damage initiation and propagation under low-velocity impact.

CHAPTER 6 Results of Composite Laminates under QSI

It is established from the literature review that quasi-static indentation test could be used to replace the low velocity impact test to investigate the damage mechanisms and structural response of composite laminates. This Chapter presents the results of QSI using experimental, numerical and analytical approaches to achieve further understanding on the damage mechanisms and process of composite laminates under low-velocity impact. The feasibility of establishing a relation between the internal damage and a visually inspectable parameter is also explored.

6.1 Instrumented Quasi-static Indentation Test

The instrumented quasi-static indentation tests were carried out on the specimens same as those tested in Chapter 5 to maintain the comparability between the LVI results and QSI results. The tests were conducted using ASTM D6264-98 test standard [120] to investigate the contact behaviour of composite laminates.

Two loading approaches, one for a continuous loading and one for a step-by-step loading, were used for the indentation test. The effects of damage initiation and propagation on the contact behaviour were investigated via detailed assessments on relations among the indentation force, indenter displacement, total indentation and dent depth. Different damage phases were proposed to characterise the damage process of composite laminates under low-velocity impact.

6.1.1 Quasi-static Indentation Test Set-up

Figure 6.1 shows the schematic of quasi-static indentation test as described in the ASTM standard [120]. The indentation force is applied to the simply supported specimen by slowly pressing a hemispherical indenter into the top surface of the specimen. In order to maintain the comparability between the results achieved from the LVI and QSI tests, the same indenter and support fixture as used in the LVI tests were employed in the QSI tests.

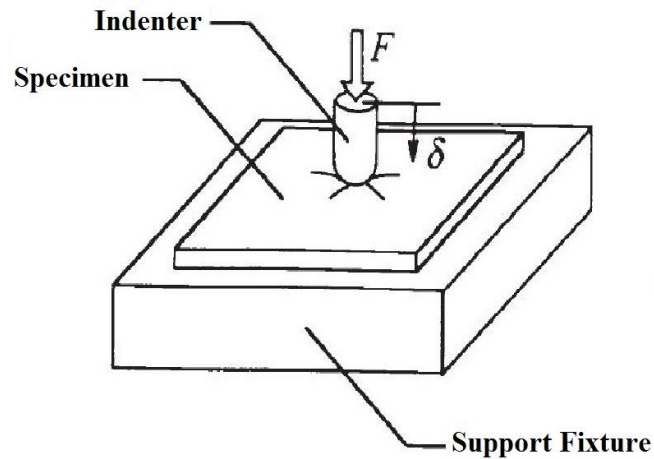


Figure 6.1 Schematic illustration of the quasi-static indentation test [120].

Figure 6.2 shows the instrumented quasi-static indentation test facility. The indenter was gripped by the Hounsfield 10kN universal test machine to apply an indentation force under the displacement control of 1 mm/min. The specimen was carefully placed on the support fixture by making sure that the centre of the specimen was aligned with both the centre of the fixture cut-out and the centreline of the indenter. The alignment was checked against the alignment marks to ensure that the distance between the centreline of the indenter and centres of the specimen and fixture cut-out does not exceed 1.0mm. Moreover, to measure the specimen back-face displacement, the support fixture was supported on two aluminium blocks, and a dial gauge was placed underneath the indenter as shown in Figure 6.2(b).

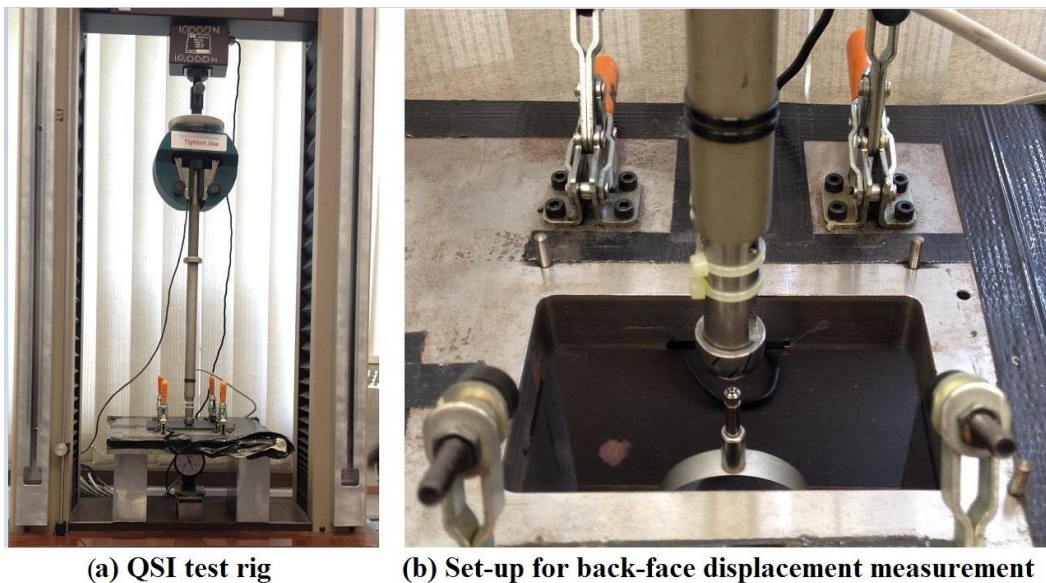


Figure 6.2 Instrumented quasi-static indentation test facility.

The specimens with lay-up configurations of $[\pm 45/0/90]_s$ and $[\pm 45/0_2/90_2/\pm 45]_s$ corresponding to laminates thicknesses of 2mm and 4mm were indented in two different loading approaches.

In a continuous loading approach, an indentation force was applied continuously until either the final failure of the specimen or the maximum load of the test machine was reached. Meanwhile, the indentation force and the indenter displacement were automatically recorded by the same computer-aided data acquisition system as described in Chapter 4.

However, the dent depth is a function of contact force but cannot be measured when the specimen is loaded. Therefore, a step-by-step loading approach was used to take the measurements including the dent depth and the back-face displacement. In the step-by-step loading approach, the specimen was loaded up to a predetermined load to measure the back-face displacement. And then the specimen was unloaded and removed from the support fixture to measure the dent depth within a consistent period (about 1-2 minutes). In this case, the effect of the relaxation of resin matrix was assumed as the similar case for all the dent depth measurements. After the measurement, the same specimen was centred on the fixture again using the alignment marks and loaded up to the next higher predetermined loading level. The process was repeated until the final failure of the specimen or maximum load of the test machine was reached.

In addition, the dent depth was measured immediately after the load was removed from the specimen. Figure 6.3 shows the dent depth measurement performed by a depth dial gauge with a resolution of $\pm 0.01\text{mm}$. The depth dial gauge and the specimen were placed on a calibrated horizontal table. The measuring probe had a hemispherical tip with a diameter of 2mm. It is noticed that the effect of the surface roughness of the laminates plate can be ignored in the dent depth measurement, considering the fact that the surface roughness of the plate is much smaller than the dent depth measurement and the diameter of the measuring probe. In this study, the dent depth was assumed as the local measurement excluding the plate deformation. As a result, the dent depth is the difference between the lowest point in the dent and the dent edge plane. Due to the difficulty in identifying the edge plane for individual dent, the dent depth was taken as the average value of 8 measurements spaced 45° apart and at 10mm from the indentation point.



Figure 6.3 Depth dial gauge to measure dent depth.

6.1.2 Composite Laminates under a Continuous Indentation Approach

In the continuous loading approach, the 4mm and 2mm specimens were tested until either the maximum load of test machine or the ultimate failure of specimen was reached. The indentation force and indenter displacement were recorded and shown in Figure 6.4.

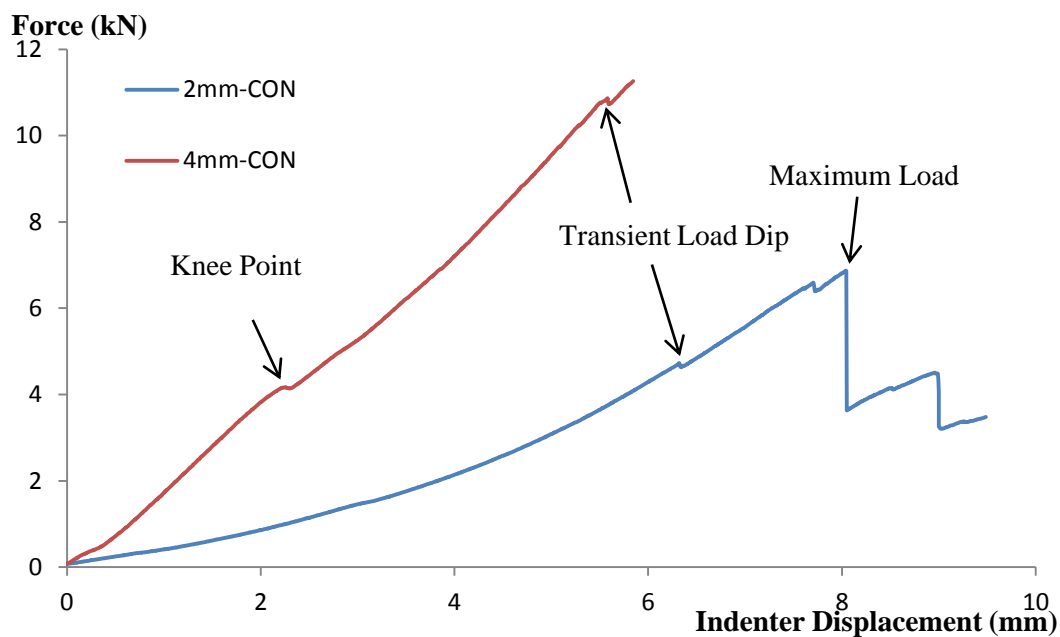


Figure 6.4 Indenter displacement curves of 2mm and 4mm specimens under the continuous loading approach.

From the indentation history of the 4mm specimen, it can be seen clearly that a knee point occurred at around 4.2kN, which was believed to be related to delamination initiation. The explanation for the appearance of knee point was that the indenter displacement was increased under the same indentation force due to the sudden reduction of laminates stiffness caused by the delamination initiation. The knee point phenomenon was however not clear in the indenter displacement history of the 2mm specimen, which agreed well with the finding discussed in Section 5.1.2 that the delamination initiation was not the dominant mechanism in the impact response of the thinner specimen (*e.g.* 2mm). Moreover, the transient load dips, compared with the knee point of delamination initiation, were recorded in both indenter displacement histories of 2mm and 4mm specimens. Sound of fibre breakage was heard for the first time when the transient load dip occurred during the indentation process. It is therefore reasonable to relate the first transient load dip to the initial fibre breakage. The final failure of the 2mm specimen was reached at around 6.7kN.

6.1.3 Comparison between Results of QSI and LVI Tests

It is necessary to compare the results achieved from the LVI test and QSI test, in order to validate the feasibility of employing the QSI test to characterise the damage mechanisms of composite laminates under LVI. However, the indenter displacement history obtained from the QSI test is the relationship between the indentation force and indenter displacement. Therefore, the impact force history recorded during the LVI test needed to be converted to the same relationship between the impact force and impactor displacement to maintain the comparability. The conversion was achieved by integrating the deceleration history of the impactor twice against the impact time.

Figure 6.5 shows the comparison between LVI and QSI test results of 2mm specimen. It can be seen clearly that the result curves of LVI tests with different energy levels followed the same trend, especially for the loading phase of impact process. The trend line was therefore applied to characterise the material behaviour of composite laminates.

The trend line of LVI test result still deviated from the indenter displacement history from the QSI test. This difference was however considered to be acceptable in the current study for the following two reasons. One is the inherent difference between the LVI and QSI events so that some difference between the LVI and QSI tests is expected. The difference should however be small considering the larger impactor mass (11.8kg) and the resultant longer impact

duration in the study. The other reason is the accumulated error introduced by recording the impact force history in LVI test and the conversion from deceleration to displacement. Overall, the QSI test result agreed well with the LVI test result in terms of the initial fibre breakage. A transient load dip was occurred around 5kN from the indenter displacement history of QSI test. The LVI test result of 12J also showed a load fluctuation around 5kN. This correlation further proved the capability of QSI test to study the damage mechanism of composite laminates under LVI.

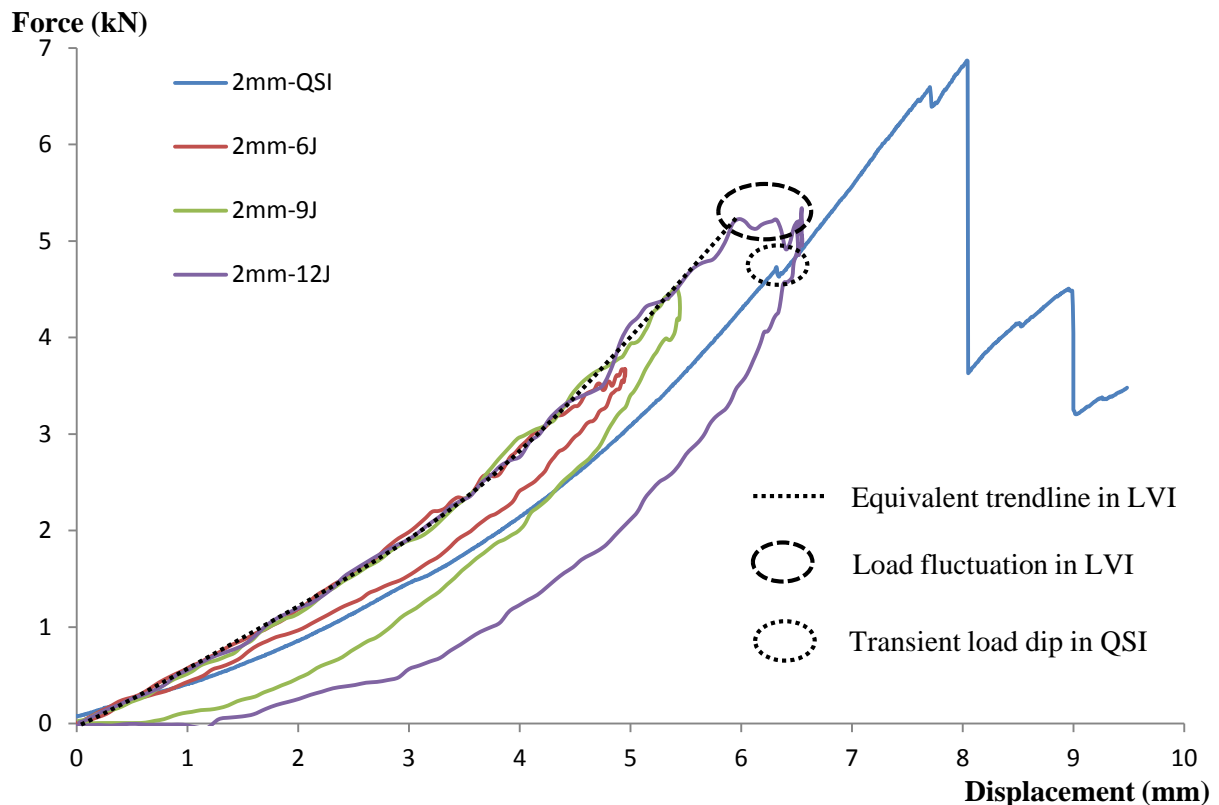


Figure 6.5 Comparison between LVI and QSI test results of 2mm specimens.

Figure 6.6 shows the comparison between the LVI and QSI test results of the 4mm specimen. The knee point value in the QSI result is 4.2kN, which is close to the DTL value (4.9kN) determined by the LVI test. The 15% difference was considered acceptable considering the reasons mentioned earlier and the complexity in determining the DTL. Further investigation is however required to validate the link between the existence of the knee point in the indentation history and the delamination initiation due to the limited data available in this study.

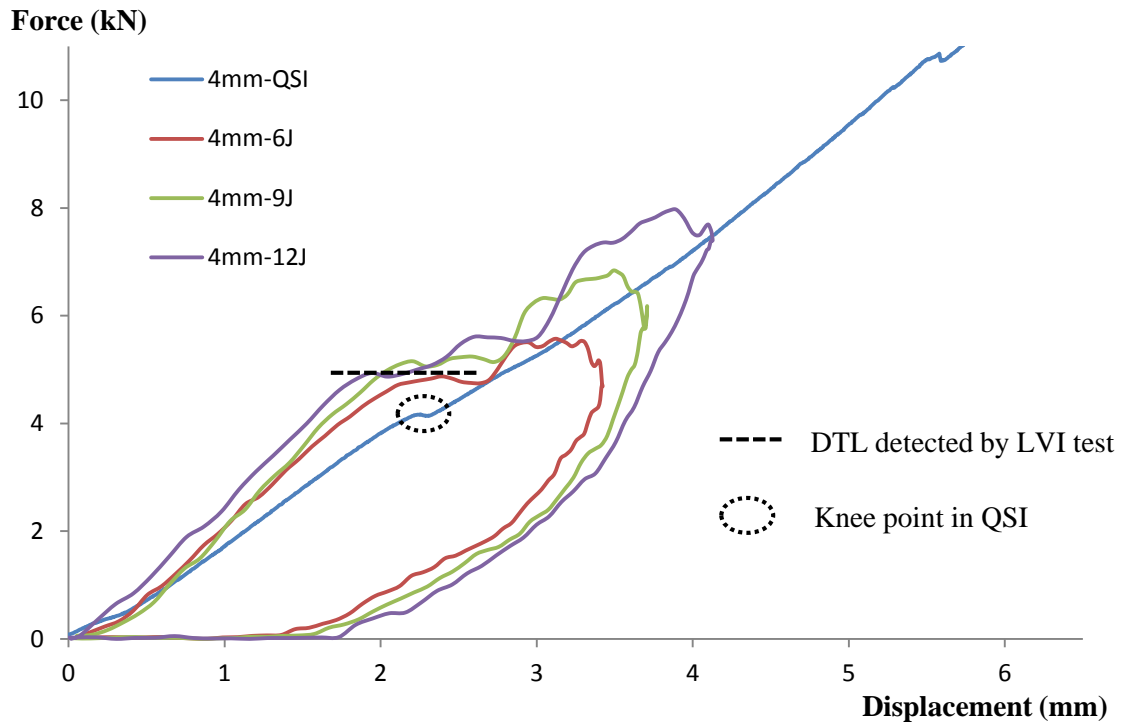


Figure 6.6 Comparison between LVI and QSI test results of 4mm specimens.

6.1.4 Composite Laminates under a Step-by-step Indentation Approach

The 4mm and 2mm specimens were also tested under a step-by-step indentation approach as described in Section 6.1.1 to achieve more information about the indentation response of composite laminates.

Figure 6.7 shows the indenter displacement histories of the 4mm specimen. It is found that the indenter displacement histories of 1kN, 2kN, 3kN, and 4kN followed the same trend, which indicates that no damage has been induced by the indentations under relatively lower load levels. The indenter displacement history of 4.25kN also followed the same trend with a knee point observed at around 4.2kN. It is clear that the indenter displacement history of 5kN deviated significantly from the indenter displacement history of 4.25kN. The smaller curve slope of 5kN load cycle is related to the reduced laminates stiffness due to the delamination initiation. Once the delamination was initiated, it was found consistently that the indenter displacement history of latter load cycle deviated from the indenter displacement history of former load cycle, as a result of the reduced laminates stiffness. This result may indicate that the initial damage in the composite laminate has been propagated under the increased indentation load levels.

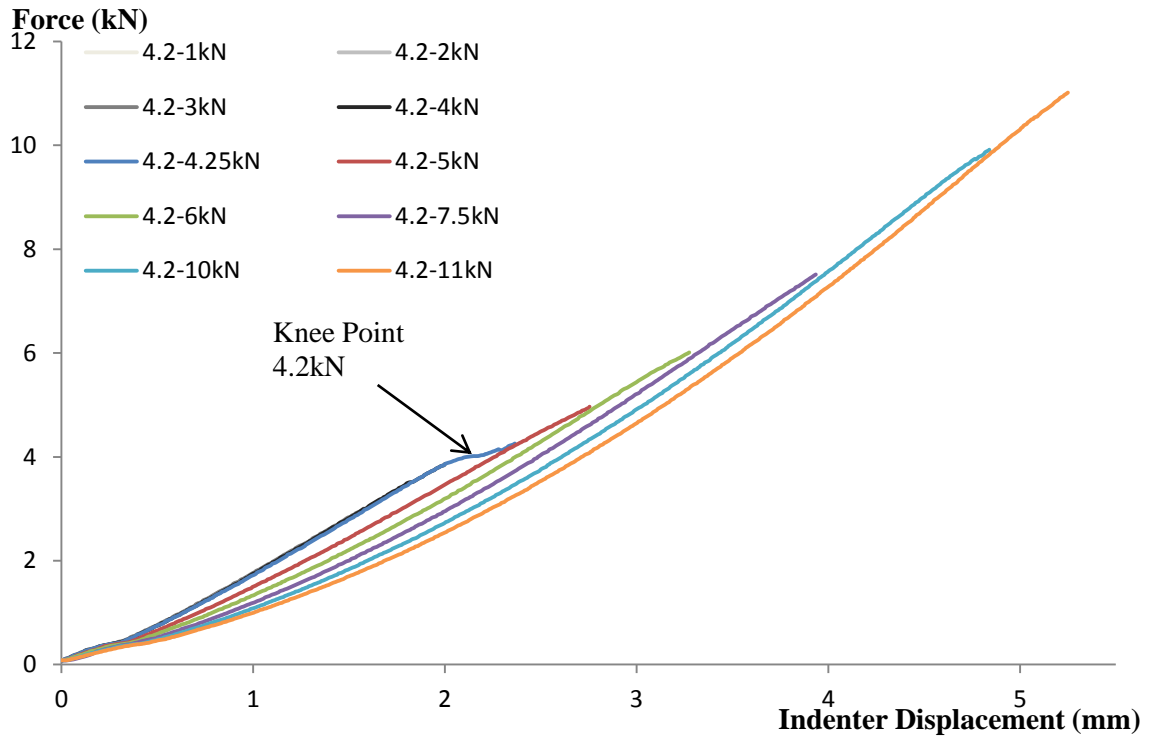


Figure 6.7 Indenter displacement histories of a 4mm specimen under the step-by-step loading approach.

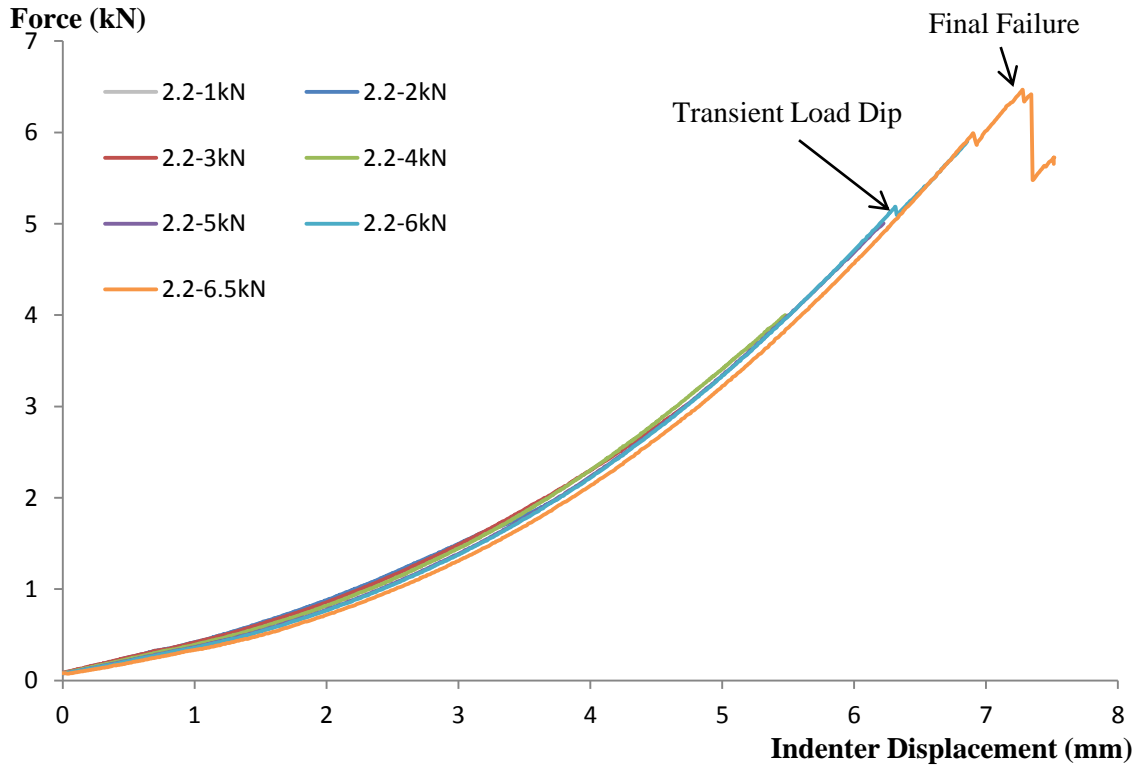


Figure 6.8 Indenter displacement histories of a 2mm specimen under the step-by-step loading approach.

Figure 6.8 shows the indentation histories of the 2mm specimen obtained from indentation tests with a step-by-step loading approach. It is clearly found that the indentation response of the 2mm specimen is different from that of the 4mm specimen. There was no clear knee point and the indenter displacement histories of different load levels were almost identical (except the indentation curve of 6.5kN). These results suggest that the delamination initiation is not the dominant mechanism affecting the contact response of 2mm specimen, and the laminates stiffness was not significantly reduced by the indentation loads.

However, a clear transient load dip can be seen at around 5kN in the indenter displacement history of 6kN, which was related to the appearance of initial fibre breakage. In addition, the indenter displacement history of the 6.5kN deviated from the indenter displacement history of the previous load cycle (6kN). This result demonstrated that the laminates stiffness was reduced by the existence of the initial fibre breakage. The final failure of the 2mm specimen occurred at around 6.5kN.

For the damaged specimens under indentation test, it was interesting to note that the slope of the indenter displacement history curve of the subsequent load cycle was actually gradually changed. In the beginning, the indenter displacement history curve slope of the latter load cycle was smaller than it of the former indentation load cycle. But the slope of the indenter displacement history curve was increased gradually when the indentation load was increased. As a result, the indenter displacement history of the latter load cycle was approaching to the indenter displacement history of the former load cycle. And the latter indenter displacement history would cross the former indenter displacement history at its end, when the indentation load exceeded the maximum indentation load of the former load cycle.

The test results under the step-by-step loading approach were characterised by the overall loading curve by piecing together all the individual load curves under different loading levels in the step-by-step loading approach as shown in Figure 6.9.

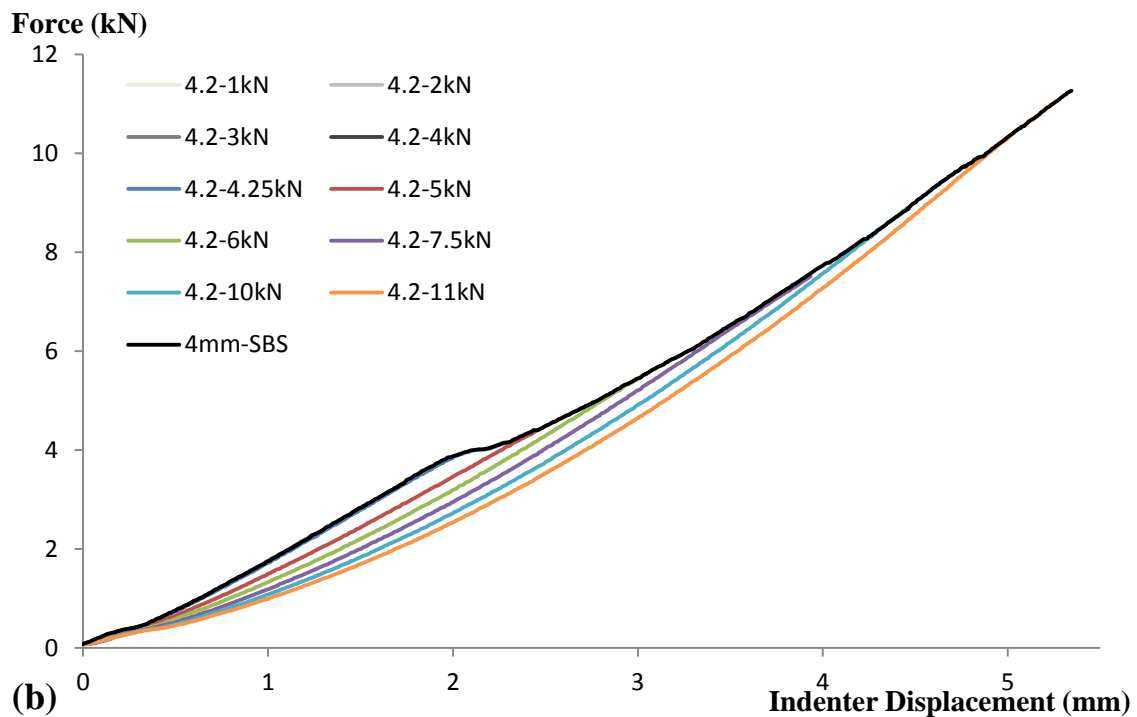
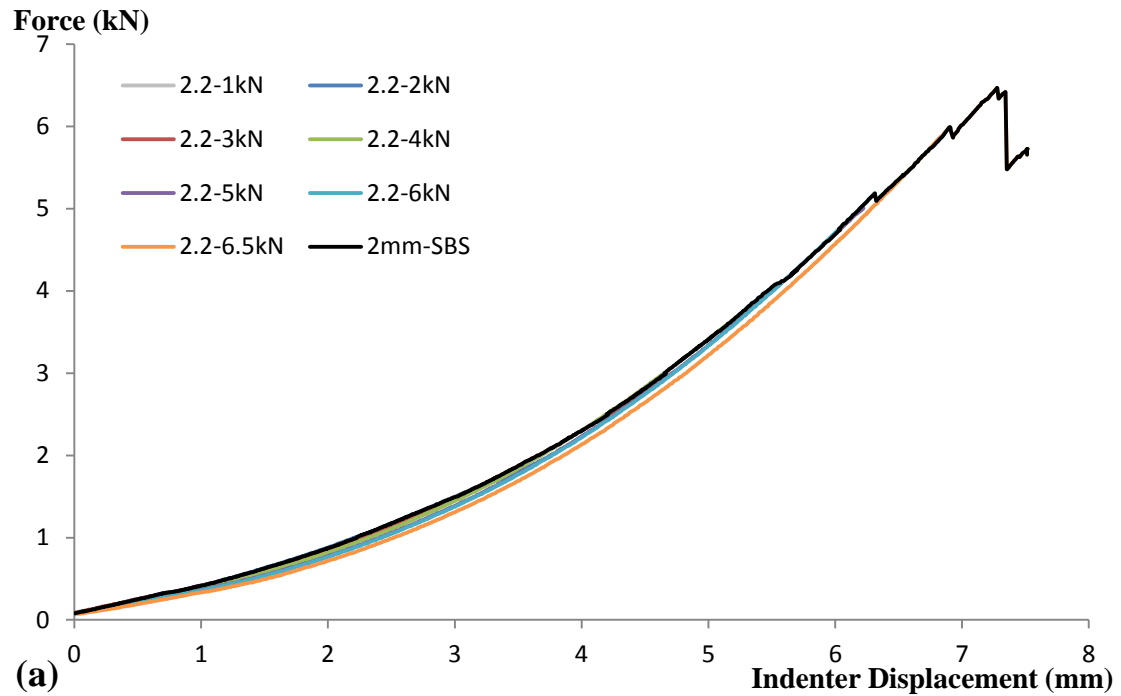


Figure 6.9 Determination of overall indenter displacement histories of (a) 2mm and (b) 4mm specimens under the step-by-step loading approach.

After the overall loading curve of the tested specimen under the step-by-step loading approach was determined, the equivalent step-by-step indenter displacement histories were compared with the indenter displacement histories achieved from the continuous loading approach as shown in Figure 6.10.

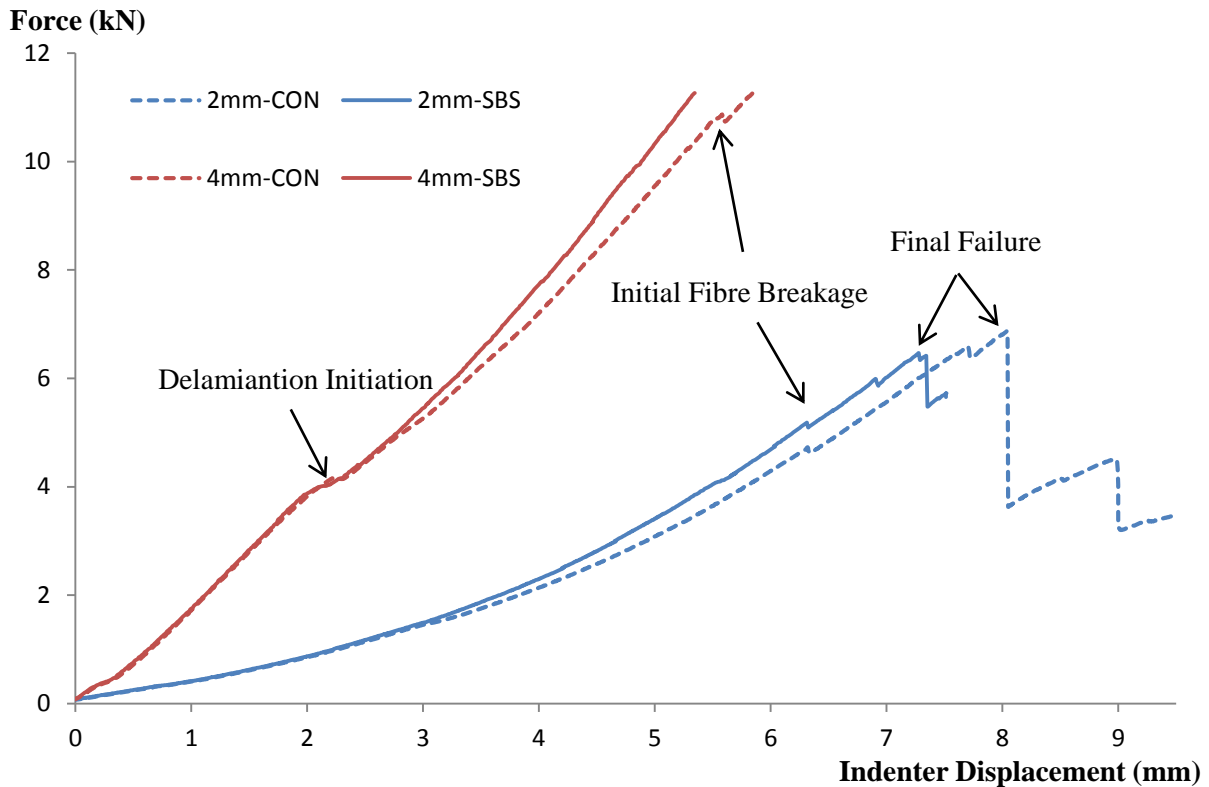


Figure 6.10 Comparison among indenter displacement histories of 4mm and 2mm specimens under continuous and step-by-step loading approaches.

From Figure 6.10, it is found that the indentation response of composite laminate is significantly affected by the laminates thickness, but not by the different loading approaches. The indenter displacement histories obtained from different loading approaches show the similar trend in characterisation of indentation response of composite laminates.

Same knee point value was measured from the indentation tests conducted on the 4mm specimens under different loading approaches, which demonstrated that the quasi-static indentation test method was capable of detecting the delamination initiation. Moreover, similar final failure and initial fibre breakage points were observed from the indentation tests conducted on the 2mm specimens under different loading approaches, which further proved the capability of quasi-static indentation test to characterise the damage mechanism of composite laminates under low-velocity impact.

6.1.5 Dent Depth Measurement

The local dent depth (excluding the global plate deformation) was measured as described in Section 6.1.1 during the QSI test following the step-by-step loading approach. It provides some key information to characterise the indentation response of composite laminates.

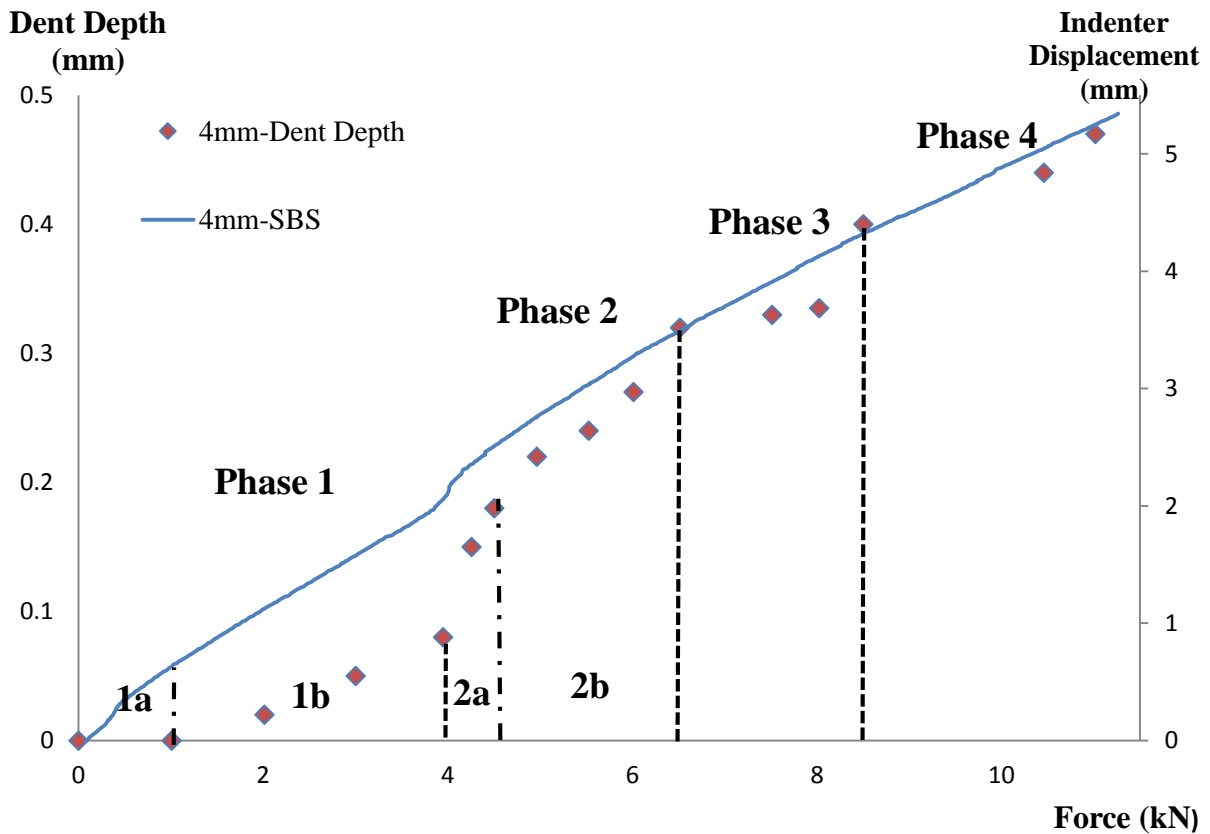


Figure 6.11 Indentation force vs. dent depth/indenter displacement of a 4mm specimen.

Figure 6.11 shows the QSI test results of the indentation force against the dent depth (with ± 0.01 mm error bar) and indenter displacement of the 4mm specimen. The dent depth increases as the indentation force increases to its maximum. The rate of increase in the dent depth is however quite different over the whole indentation process. Based on the test result shown in Figure 6.11, the whole indentation response of the 4mm laminates can be divided into four phases, which are non-damage, local damage, global damage, and final failure, respectively.

The first phase of the indentation response, as the non-damage phase, can be further divided into two sub-phases. When the indentation load is below a certain load level, which is about 1kN for the 4mm laminates, the matrix material resistance to plastic deformation is high

enough to prevent any dent. There is no detectable dent in Phase 1a as a result. Phase 1b has the indentation load greater than 1kN under which the contact stress has exceeded the yielding stress of the matrix in the upper layer. The dent depth increases linearly with the indentation force in Phase 1b, but has no influence on the overall material performance of the laminates.

The second phase of the indentation response is the local damage phase, when the local damage including the local delamination initiation and propagation is introduced in the laminates. Phase 2a is the sub-phase when delamination is initiated after the DTL value has been exceeded. The local stiffness of the material under the indenter is significantly reduced due to the initiation of local delamination, which explains the sharp increase of the dent depth in Phase 2a. This result agrees well with the knee point phenomenon in the result curve of the indentation force against indenter displacement and its explanation as suggested previously. However, it is noticed that there is no direct evidence supporting the link between the reduced local stiffness and the significant material degradation. The correlation between the local delamination initiation and the overall material behaviour needs to be further clarified. After the damage initiation, the damage propagates stably in Phase 2b and the local delamination has been extended from a local region under the indenter to the whole laminates. The damage mechanisms including the delamination initiation and propagation are the dominant energy absorption mechanisms in this phase.

The third phase is the global damage phase, which shows a plateau in the dent depth. This phenomenon is linked to the global stiffness reduction triggered by the cumulative damage from previous phases. The reduction in global stiffness makes the laminates more flexible which increases the contact area between the indenter and the laminates under the same dent depth. Moreover, the plastic deformation of laminates as also becomes an additional energy absorption mechanism when the accumulated damage reaches a certain critical level. All of these mechanisms have contributed to the plateau phenomenon in the dent depth under the increase of the indentation load.

The last phase is the final failure phase in which the matrix has been extensively damaged under the high indentation load. The fibre breakage is triggered by the high flexural stress after the carbon fibre loses the support from the matrix material. Once the fibres are damaged, the material load bearing capacity is tremendously reduced, which results in the final failure of composite laminates. To further validate the mechanism of the above damage phases, the

results of the CAI test and the internal damage observation achieved from different samples suffered different maximum loads would be presented in Section 6.2 and Section 6.3, respectively.

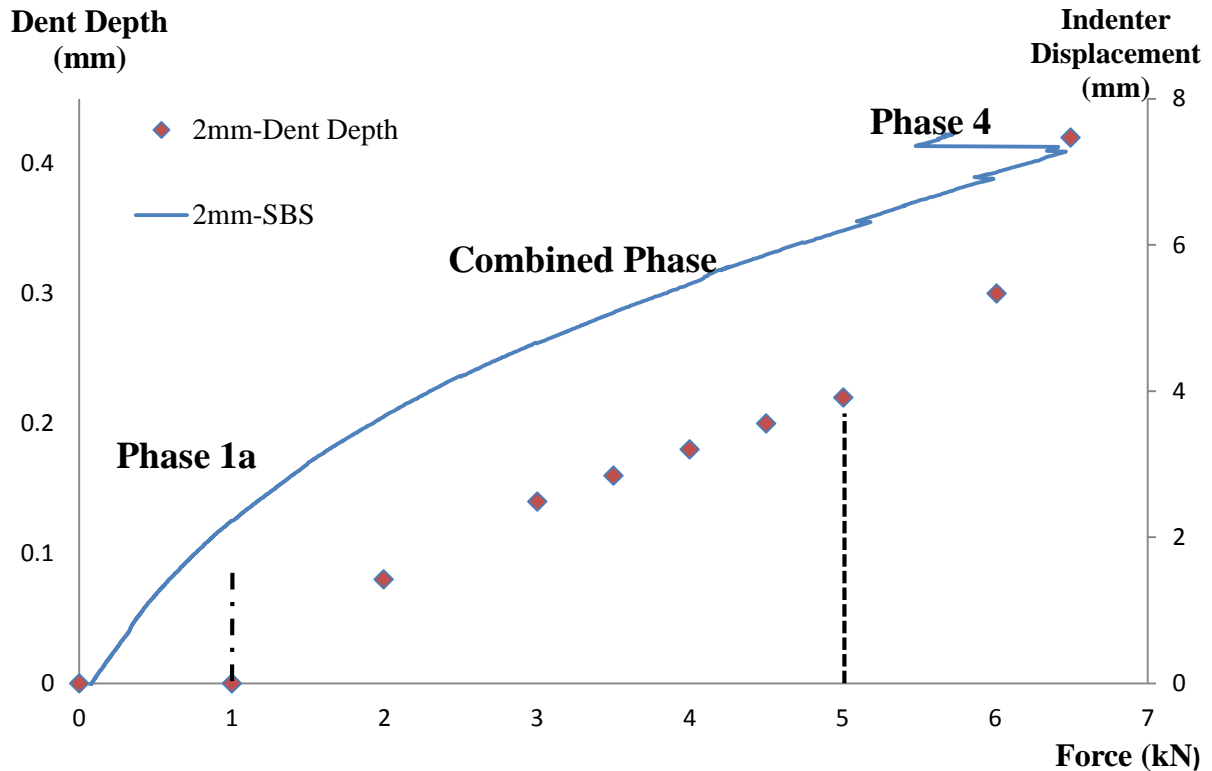


Figure 6.12 Indentation force vs. dent depth/indenter displacement of a 2mm specimen.

Figure 6.12 shows a similar study for the 2mm composite laminates. It is found that the indentation response of the thinner specimen is different from that of the 4mm thicker specimen. The damage process of the 2mm specimen can be separated into three phases.

The first phase is the same as the first sub-phase of the 4mm laminates. The matrix material resistance to the plastic deformation is high enough to prevent any damage. As a result, no dent has been introduced in this phase. It is suggested that the maximum load of the no-dent sub-phase was independent of laminates thickness and is only related to the matrix material property of the upper layer. Furthermore, it is worth noting that the contribution in energy absorption due to the delamination in thinner laminate is relatively small compared with that in thick laminates. The elastic deformation, plastic deformation, and damages all contribute to the absorption of impact energy. As a result, the effect of delamination initiation and propagation on the indentation response of the 2mm thin laminate is less obvious (in other words, difficult to separate) compared with that of the 4mm laminates. Consequently, the

second phase of the 2mm laminate is a combination of local and global damage phases as in the indentation response of the 4mm specimen. The last phase of the 2mm specimen is the same as that of the 4mm specimen in which widespread fibre breakage and severe delamination occur after the fibre loses the support from the matrix.

6.1.6 Back-face Displacement Measurement

The back-face displacement of specimen was also measured during the QSI test following the step-by-step loading approach. The measurement provided some further information to characterise the indentation response of composite laminates.

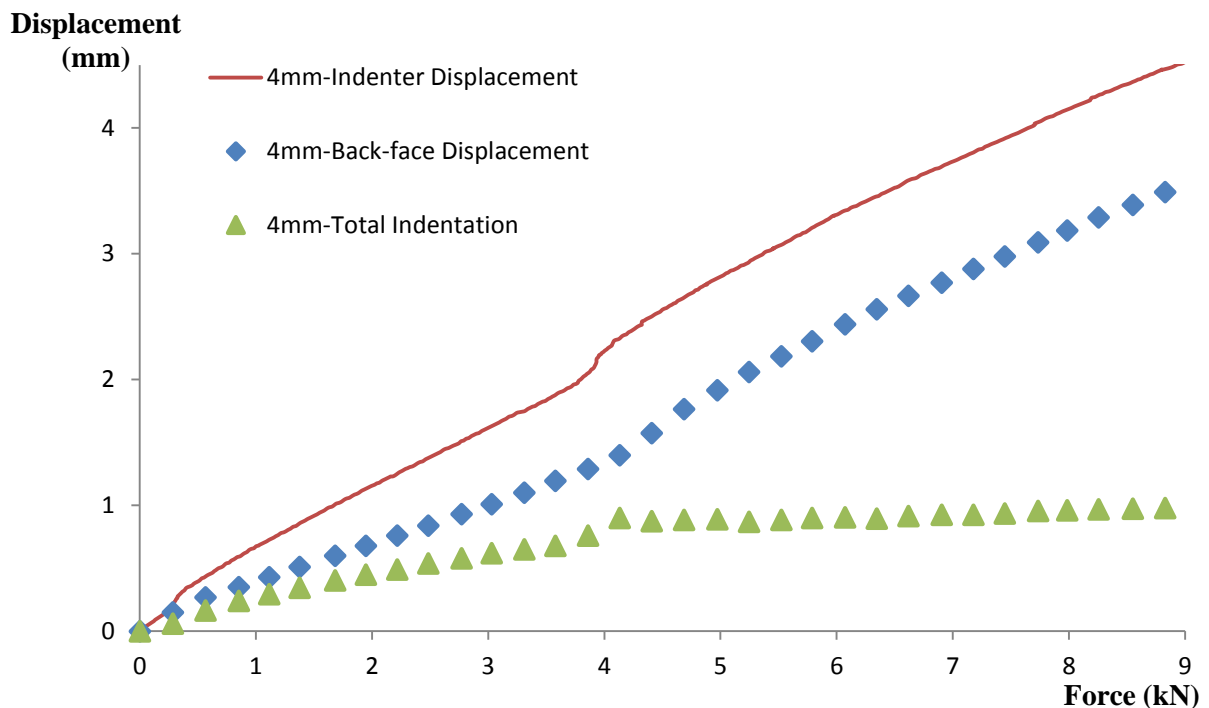


Figure 6.13 Result of total indentation of a 4mm specimen.

Figure 6.13 shows the result of total indentation of the 4mm specimen. The total indentation, as the press-in distance of the loaded indenter, is the key parameter widely used in most Hertz contact law based theories related to the contact force. Assuming the indenter is a rigid body, the total indentation is the difference between the indenter displacement and the back-face displacement as shown in Figure 6.14. During the test, the indenter displacement was recorded automatically by the tester, and the back-face displacement was measured manually at various load levels. The total indentation was determined by subtracting the back-face displacement from the indenter displacement.

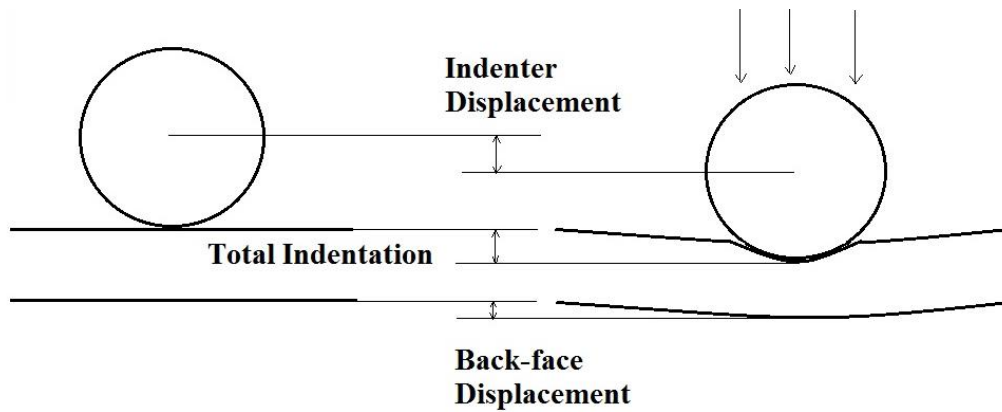


Figure 6.14 Schematic illustration of total indentation.

The indenter displacement and back-face displacement show a general trend that the displacement increases with the indentation force. Noticeable increments in measurements of both the indenter displacement and the back-face displacement were observed around the DTL level. It is however interesting to note that the trend of the total indentation is different to the displacement. In the initial stage (less than 4kN) of the loading process, the total indentation increases slowly. This linear increment can be explained by the material linear elasticity in resisting the press-in of indenter. However, an increment of the total indentation is introduced when the DTL is reached. This increment of total indentation is mainly caused by the increased indenter displacement. Once the delamination is initiated, the local material stiffness would be reduced, which leads to the increase of the indenter displacement. Furthermore, it is interesting to find that the total indentation does not increase substantially after the delamination initiation period. The possible explanation for the phenomenon is that the specimen deformation (including both elastic and plastic deformations) is large enough to increase the contact area between the indenter and the specimen after the delamination initiation. As a result, the contact stress might not be increased with the increased indentation force, which will prevent the indenter from being pressed into the laminates further.

It is suggested that the specimen deformation affected the indentation response of composite laminates. The existence of plastic deformation was however only supported by some indirect evidences, such as the plateau in the total indentation. To get the direct evidence on the plastic deformation of the whole laminates, the permanent back-face deformation was measured during the QSI test conducted on 4mm specimen. The permanent back-face deformation was measured after the indentation load was removed from the specimen at different load levels.

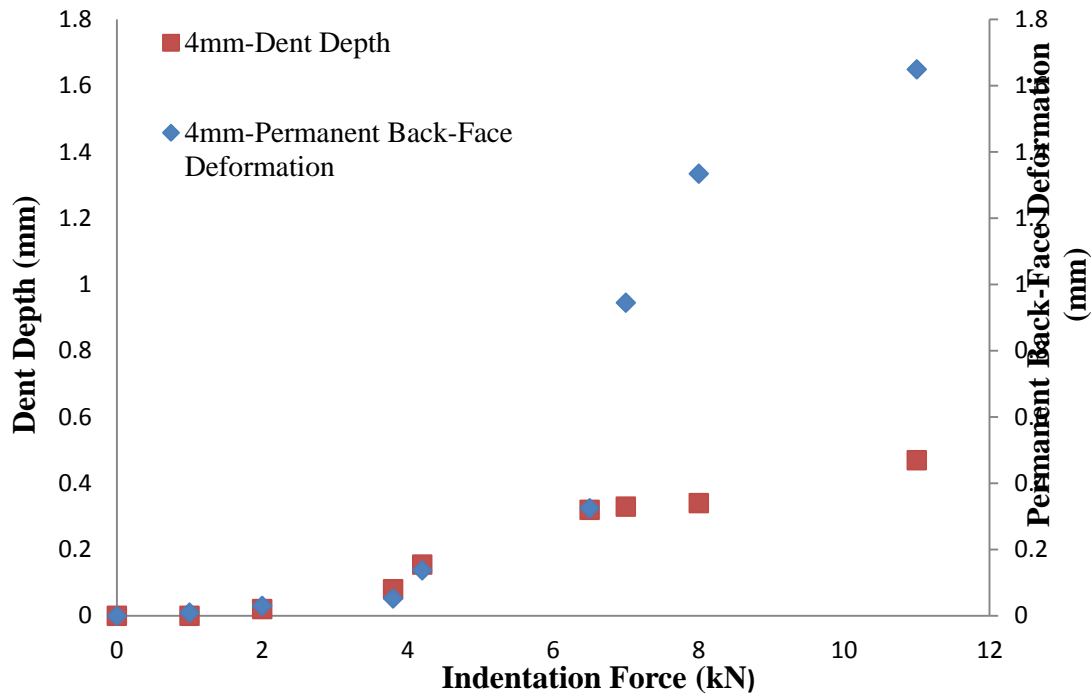


Figure 6.15 Comparison between permanent back-face deformation and dent depth.

Figure 6.15 shows the comparison between the permanent back-face deformation and the dent depth measured from the same 4mm specimen. The permanent back-face deformation is the back-face displacement of laminates measured after the load is removed from the sample and the elastic deformation is released. It is found that the correlation between the two measurements is dependent on the indentation load. For the first three data points, the dent depth and permanent back-face deformation are rarely detectable. For the following two data points around 4kN, the permanent back-face deformation and dent depth correlate well. For the data point under 6.5kN, which is treated as the beginning of the global damage phase, the dent depth is still very close to the permanent back-face deformation. It is however found that these two measurements are significantly different from each other when the load exceeds 6.5kN. The permanent back-face deformation increases sharply, which proves the existence of plastic deformation.

6.2 Compression-after-impact Test

In the current study, the indentation response of composite laminate was divided into different phases according to the difference in rate of dent depth increment. However, the assumption of the damage process was only derived from the indirect measurements such as

the dent depth. Direct evidence associated with the internal damage is therefore required to further prove the damage process assumption proposed in Section 6.1. The compression-after-impact test is a valuable approach to provide the direct evidence associated with the internal damage in terms of the damage tolerance of composite laminates subjected to quasi-static indentation under different loading levels.

6.2.1 Compression-after-impact Test Set-up

For the compression-after-impact (CAI) test, 4mm test specimens with quasi-isotropic lay-up configuration were prepared following the same procedure as described in Section 5.1.1. The test specimens were subjected to the out-of-plane quasi-static-indentation at the centre of specimen under predetermined loading levels. On the basis of the damage process assumption proposed in Section 6.1.4, several predetermined loading levels were selected to represent the key transition points in the damage process as summarised in Table 6.1.

Series of compression-after-impact tests were conducted on the indented specimens in accordance with ASTM D7137/D7137M-12 test standard [121] to determine the residual strength of composite laminates after specific indentation load. The CAI test was performed on the Avery Dension 500kN hydraulic testing machine. The specimen was supported properly to avoid buckling.

Table 6.1 Summary of specimens prepared for CAI tests and the corresponding applied loads

Specimen Number	Applied Load Level (kN)	Description
Ref.1-Ref.3	0	Reference of the initial strength
4.1-4.2	3.8	Just below the DTL
4.3-4.4	4.2	Just above the DTL
4.5-4.6	6.5	End of local damage phase
4.7-4.8	7	Beginning of global damage phase
4.9-4.10	8	End of global damage phase
4.11-4.12	11	In the final failure phase

Figure 6.16(a) shows the schematic of the fixture support suggested by ASTM test standard. A top assembly and a base assembly were included in the standard recommended fixture

support. Figure 6.16(b) shows the real support fixture used in the current CAI test. The support fixture, consisted of one top block, one bottom block and two side plates, was adjustable to tolerate small variations in specimen dimensions. The top and bottom clamp blocks were used to provide some rotational restraint and prevent the crashing at the specimen ends. Two side plates, both including a side rail, were used to resist the specimen buckling and guide the specimen movement in loading direction. When the specimen was fixed to the support fixture, it should be checked to ensure that the specimen was held perpendicular to the base and could slide freely along the side rails.

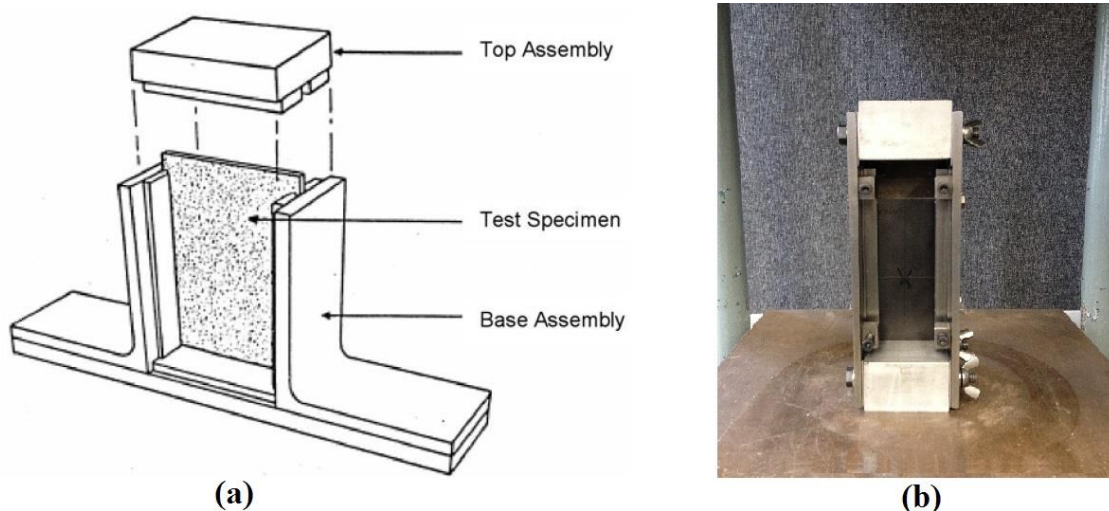


Figure 6.16 (a) Schematic illustration of the support fixture suggested by test standard [121]; (b) the support fixture used in practice.

6.2.2 CAI Test

The prepared CAI test specimens were compressed by the 500kN testing machine under the displacement-control until the final failure. The speed of testing was set to 4 mm/min to produce failure within 1 to 10 min as suggested by the standard [121].

Figure 6.17 shows the top and side views of the failed specimen after a CAI test. It can be seen clearly that the failure occurred where the indentation was applied. But such good agreement between the indentation location and failure location was only valid for the specimens suffered high indentation load, in which case the final failure occurred exactly where the damage existed. On the contrary, the final failure could be introduced to any location of the undamaged specimen as there was no obvious weak section. As a result, the reference specimen (0kN) and the specimen suffered 3.8kN indentation load had experienced

a relatively high number of undesirable failure locations such as the end-crushing or the failure near the clamped edge instead of the failure at the specimen centre; even though the support fixture was used to prevent the end-crushing and guide the failure position. ASTM D6641/D6641M [130] test method was recommended to obtain the compressive strength of the undamaged specimen. However, considering the support fixture availability, the compressive strength of undamaged specimen determined by the current method was still used as the relatively conservative reference data in the CAI study.

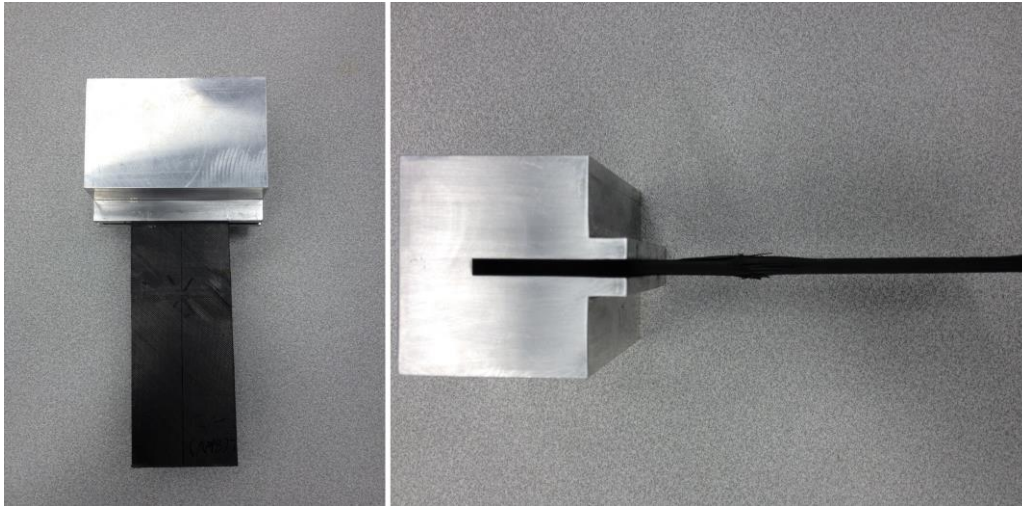


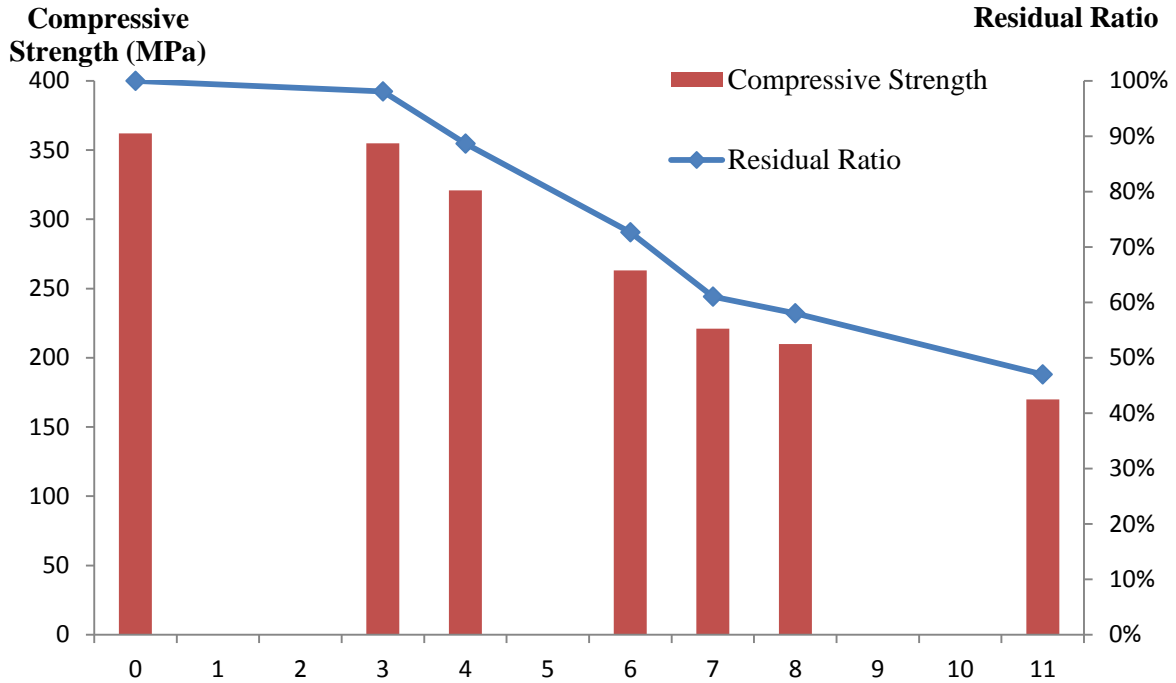
Figure 6.17 Top and side views of a failed specimen after a CAI test.

Once the failure load of each specimen was measured through the CAI test, the compressive strength of each specimen was calculated by dividing the failure load by the cross-section area of each specimen. The residual ratio is the ratio between the compressive strength and the reference strength. The compressive strength and the residual ratio of different specimens indented to different load levels are shown in Figure 6.18(a).

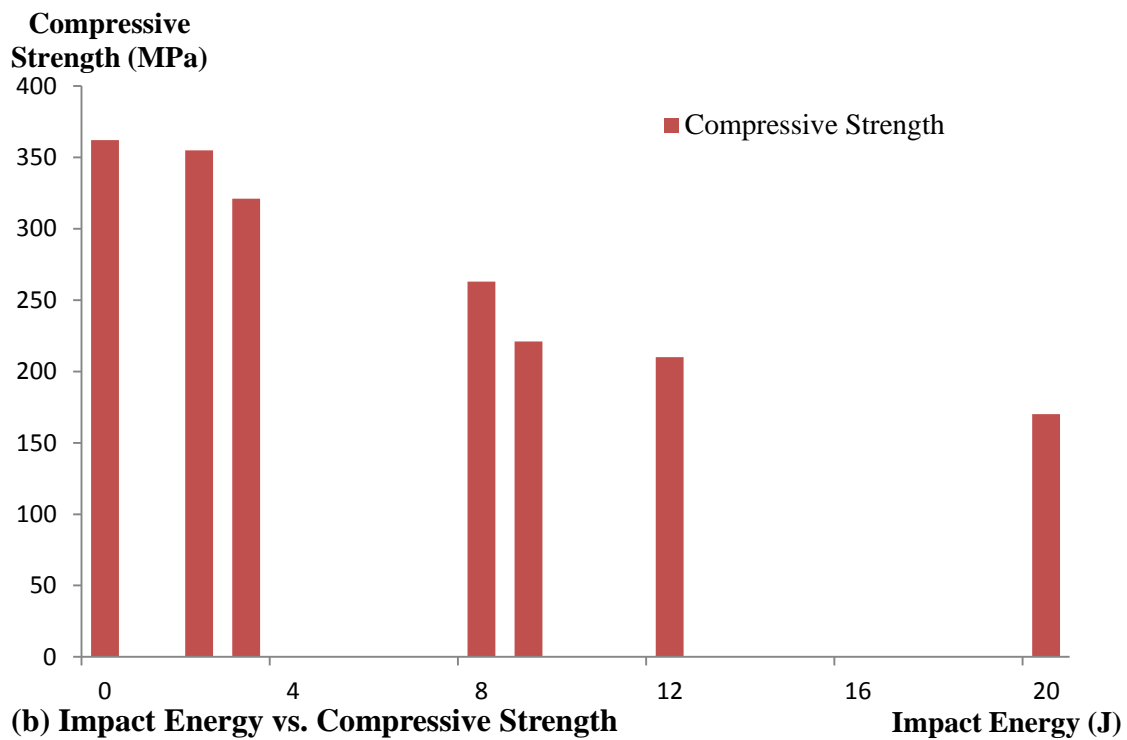
In general, the compressive strength and residual ratio of the specimen are related to the maximum indentation load applied to the specimen. The original compressive strength of the reference specimen is about 365MPa. The residual compressive strength of the specimen under 3.8kN indentation load is about 355MPa. The less than 2% difference is more likely caused by the scattering in measurement, which suggests that the laminates strength has not been really reduced before 3.8kN (up-end of Phase 1).

Once the maximum indentation load has been increased to 4.2kN, which is the DTL value of the 4mm specimen, clear reduction in the compressive strength (321MPa) and the residual ratio (88.7%) are observed. This result demonstrates that the delamination initiation does

reduce the laminates strength. This reduction is however not very critical, which agrees well with the current understanding on the effect of delamination initiation on the structural performance of the laminates mentioned earlier.



(a) Maximun Force vs. Compressive Strength/Residual Ratio Maximun Force (kN)



(b) Impact Energy vs. Compressive Strength

Figure 6.18 Summary of CAI test results.

The compressive strength and the residual ratio of the specimen under 6.5kN are about 263MPa and 72.7%, respectively. It is suggested that the 6.5kN indentation load level is at the end of the local damage phase. This result indicates that the residual strength has been reduced gradually during the local damage phase.

The residual strengths of the specimens under 7kN and 8kN are about 220MPa and 210MPa, respectively. The load levels of 7kN and 8kN are at the beginning and the end of the global damage phase, in which phase the global plastic deformation has been induced as a result of the accumulated stiffness reduction. The strength reduction is more significant in the specimen under 7kN load compared with that of 6.5kN. It is also interesting to note that the residual strength reduction of the specimen under 8kN is not as significant as that of the specimen under 7kN. This can be explained by the fact that the plastic deformation becomes an important energy absorption mechanism in the global damage phase and the proportion of energy absorbed by the damage mechanism becomes less significant. As such, the growth of damage is not that significant, which leads to the smaller reduction rate of the compressive strength.

Significant material strength reduction was observed in the specimen under 11kN indentation load. The compressive strength has been reduced to about 170MPa, which is about 47% of the original compressive strength. This result indicates that the laminate has lost most of the material strength due to the introduction of the severe damage (*e.g.* fibre breakage) during the final failure damage phase.

Moreover, as the compressive strength is normally compared with the impact energy to indicate how the strength reduction varies with the impact energy; the measured compressive strength of each specimen are also compared with the corresponding estimated equivalent impact energy as shown in Figure 6.18(b). However, it should be noticed that the compressive strength was measured from the specimen suffered quasi-static indentation load, in which case only the maximum applied load rather than the impact energy level is available. Therefore, the equivalent impact energy level was estimated from the maximum indentation load based on the relationship between the impact energy level and the maximum impact force of the 4mm quasi-isotropic laminates as shown in Figure 5.20. Furthermore, it is also suggested that the estimated impact energy is not the exact value due to the lack of data series to determine the comprehensive relation between the impact energy and the induced

maximum impact force. In this particular study, the estimated impact energy values are only treated as a series of indirectly determined reference data.

It is suggested that the relation of the compressive strength and the impact energy as shown in Figure 6.18(b) shows the similar trend compared with the relationship between the compressive strength and the maximum indentation load as shown in Figure 6.18(a). The first significant strength reduction occurs at the data point of 3J, in which case the compressive strength is reduced from 355MPa to 321MPa. Then the compressive strength continuously decreases to 170MPa while the impact energy level increases to 20J.

6.3 Internal Damage Characterisation

By conducting the CAI tests on the damaged specimens, the damage tolerance of composite laminates suffered different indentation loads has been assessed. However, the indentation induced internal damages still need to be further characterised in terms of the internal damage distribution and internal damage mode. Therefore, the specimens indented up to the same predetermined load levels as indicated in Section 6.2 were examined under optical microscope (OM) and scanning electron microscope (SEM) to obtain direct information about the internal damage to support the damage process assumption proposed in Section 6.1.

6.3.1 Optical Microscope Observation Set-up

To get the cross-section view of internal damage near the indentation position, the indented specimens were cut along the longitudinal centreline. A slow and constant cutting speed of 5 mm/s was applied to prevent the secondary damage introduced by the cutting process.

The optical microscope observation was conducted on the Motic SMZ168 series microscope with built-in Moticam 2300 3.0M pixel USB 2.0 connected camera as shown in Figure 6.19. The optical microscope system has a binocular stereo with 6x, 12x, 25x, and 50x magnification. The Photonic F1 LED light source was used to supply the supplementary lighting during the optical microscope observation.

The specimen was placed on the microscope stage under the microscope, so that the field of view could be reliably moved. The field of view was set to cover about a 5mm by 5mm area by using the 12x magnification lens. For each field of view, the microscope was individually

focused and a photograph was taken by the built-in camera. After that, the specimen was precisely shifted a distance of 5mm by using the microscope stage to access the new field of view next to the previous one. The operation was repeated from one end of specimen to the other end to cover the whole cross-section of the specimen. Once the images of all the observations were obtained, they were merged into one single image for the whole cross-section view of the specimen by the professional image stitching component in the Motic observation image management software.



Figure 6.19 Motic microscope system and its built-in Moticam camera.

6.3.2 Optical Microscope Observation Results

Different 4mm specimens, loaded up to load levels of 0kN, 3.8kN, 4.2kN, 6.5kN, 7kN, 8kN, and 11kN, were examined by the optical microscopy. A clear trend in the existence of internal damage can be found through the analysis of the observation results.

Figure 6.20 shows the optical microscope observation results of the reference specimen and the specimen loaded up to 3.8kN. It should be noted that all the observation results presented in this section only covered the middle part (30mm width) of the centreline cross-section, considering that this particular area was the mostly damaged area of the whole cross-section.

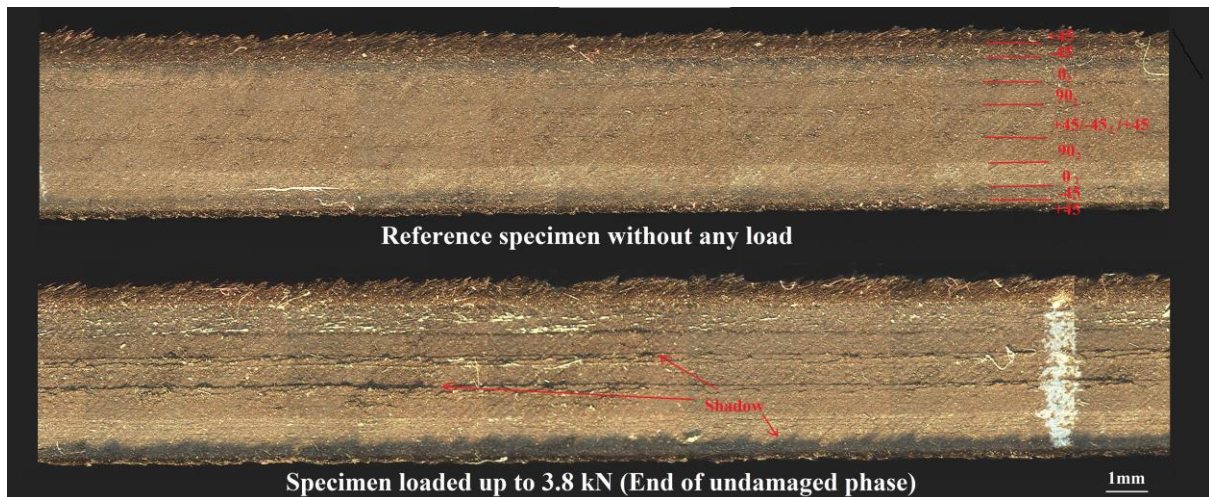


Figure 6.20 Optical microscope observation results of the reference specimen and the specimen loaded up to 3.8kN.

The observation result of the reference specimen, with no indentation load applied, provides the original state of the cross-section of the undamaged specimen. While the interface between layers with different fibre orientations is clearly visible in the thickness direction, there is no detectable crack or gap in the smooth and homogeneous cross-section. This observation result demonstrates that the controlled cutting process is satisfactory since no secondary damage has been introduced.

Similarly, no delamination could be identified in the optical microscope observation of the specimen under the 3.8kN maximum load, even though several dark lines along the interface direction were observed. Further detailed checks were carried out and the dark lines were proved to be the shadow of tiny bulge on the cross-section caused by the illuminating angle of the supplementary light. The load level of 3.8kN was supposed to be the end of the undamaged phase in the proposed damage process assumption, and this is supported by the optical microscope observation result. Moreover, the indentation dent was barely visible, which agreed well with the previous assumption that the dent depth during the non-damage phase was mainly linked to the material elastic deformation. The existence of other damage modes, such as matrix crack, needs to be investigated under higher magnification using SEM and will be presented in Section 6.3.3.

Figure 6.21 shows the optical microscope observation results of the specimens subjected to 4.2kN and 6.5kN indentation loads, respectively. The internal damages, especially for the delamination, can easily be found from both observation results.

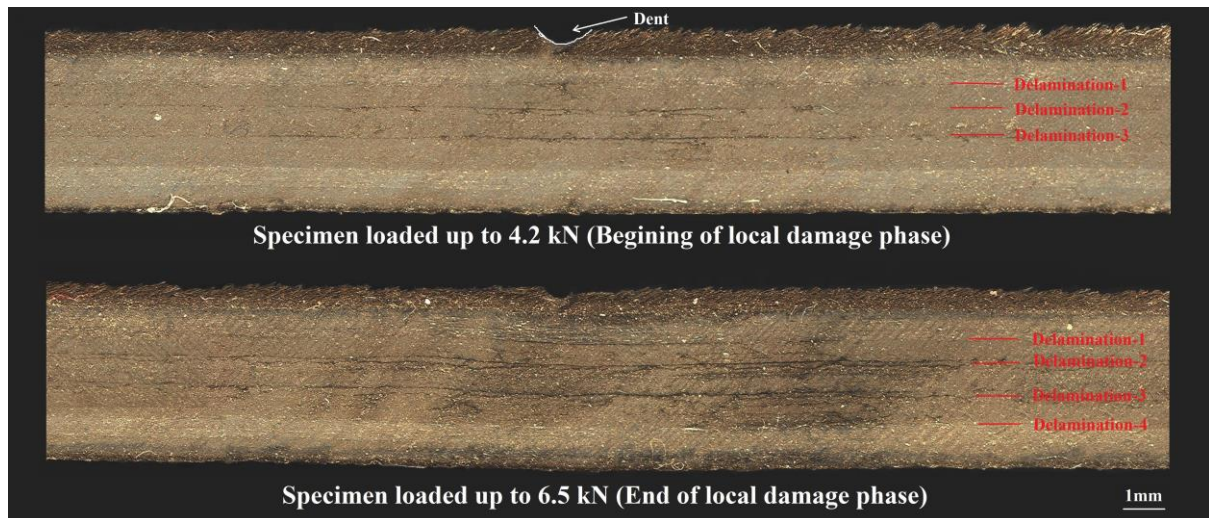


Figure 6.21 Optical microscope observation results of the specimens loaded up to 4.2kN and 6.5kN.

There are three delamination sites found in the specimen loaded up to 4.2kN which is just over the DTL. It is noticed that the initial delamination is restricted within a relatively local area (less than 15mm wide). The top delaminated interface with the shortest delamination length is located at the interface of 0° and 90° laminas. The second delamination is at the interface of 90° and $+45^\circ$ laminas. The third delamination is the longest and located at the interface near the mid-plane, which could be related to the shear stress. It is interesting to note that all these delaminations were roughly distributed in a pine tree shape from the point under the indentation dent to the mid-plane, with no delamination initiated in the bottom half of the specimen. It is also noticed that the indentation dent of the delaminated specimen does increase significantly compared with that of the specimen without delamination (loaded up to 3.8kN), which shows that the initiation of delamination is strongly linked to the dent depth increment. As a result, the dent depth could be used as an important visually inspectable parameter to indicate the initiation of delamination.

By comparing the observation results of the specimens loaded up to 4.2kN and 6.5kN, it is found that the internal damage has experienced a stable growth during the local damage phase. A new delamination was initiated at the interface of 0° and 90° laminas at the bottom half of the specimen due to the increased tensile stress. Meanwhile, the three initial delaminations had propagated (more than 20mm wide) during the local damage phase in the specimen subjected to 6.5kN load. In addition, it is found that the matrix was also significantly damaged with matrix cracks close to the delaminated interfaces. All these results suggest that

the local damage phase is a period of stable growth to propagate the internal damage from a local level to an accumulated level which may trigger the subsequent global damage and final failure.

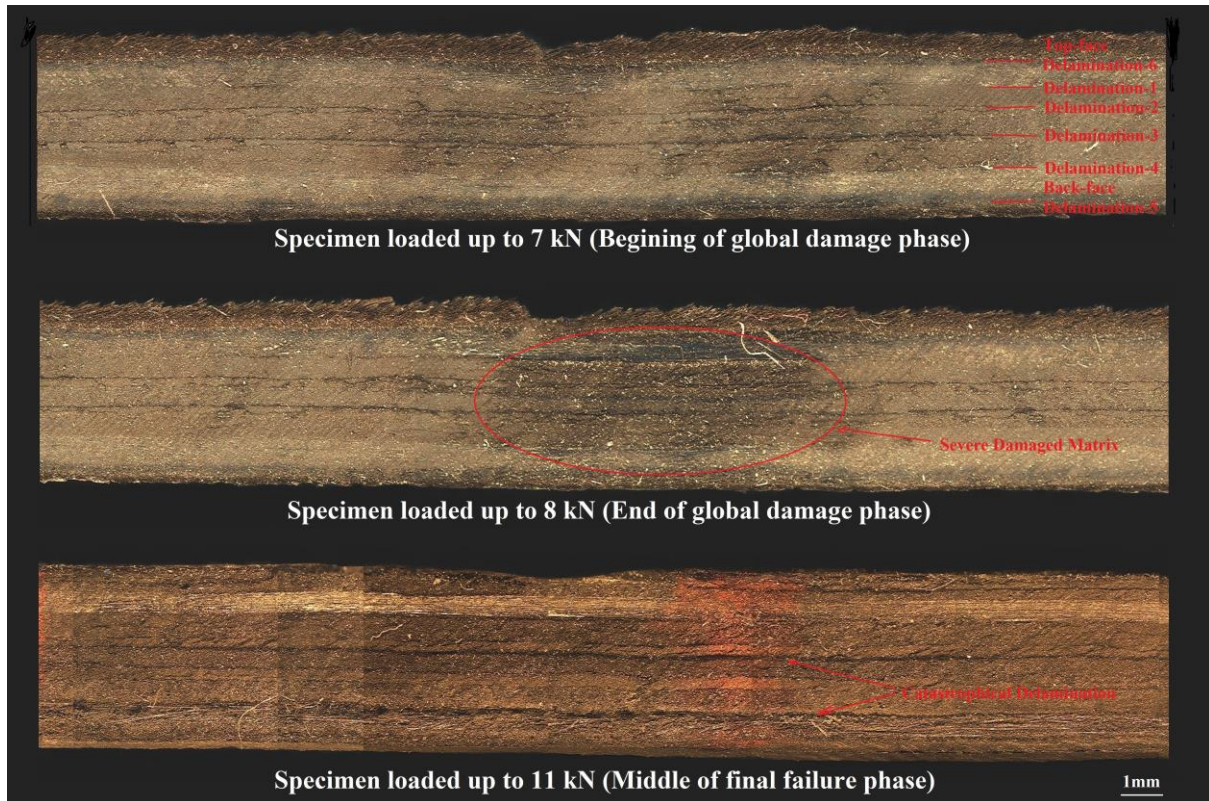


Figure 6.22 Optical microscope observation results of the specimens loaded up to 7kN, 8kN and 11kN.

Figure 6.22 shows the optical microscope observation results of the specimens subjected to 7kN, 8kN, and 11kN, respectively. Under such high loading levels, the specimens were severely damaged with wide-spread matrix crack and delaminations.

For the specimen loaded to 7kN (beginning of the global damage phase), it is noticed that the new delaminations were initiated at the top-face interface of -45° and 0° laminas and the back-face interface of $+45^\circ$ and -45° laminas. The two initial delaminations near the mid-plane were extended to a global level (more than 70mm wide). These observations agree well with the damage process assumption proposed in Section 6.1 that the cumulative damage from the previous damage phases triggers the global stiffness reduction and plastic deformation of laminates. The large deformation of laminates introduces high back-face tensile stress and mid-plane stress mismatch causing the back-face delamination initiation and mid-plane delamination propagation.

Comparing the observation results of the specimens loaded up to 7kN and 8kN (end of the global damage phase), it is obvious that the matrix was severely damaged under 8kN load as a result of the large deformation of laminates. Meanwhile, although the delamination has propagated under the increasing indentation load, the amount of growth is not significant. In addition, there is no newly initiated delamination during the global damage phase. These findings demonstrate that the global plastic deformation has become important energy absorption mechanism along with other damage mechanisms in this specific damage phase. Large deformation of laminates introduces more matrix cracking rather than the growth of delamination.

The final failure phase was introduced into the specimen under the 11kN indentation load. Since the matrix was tremendously damaged in the previous global damage phase, the fibre breakage occurred in the final failure phase when the support from the matrix was lost. Once the carbon fibre started to break, the load bearing capacity of the laminate was catastrophically reduced. As a result, the delamination would grow significantly. Massive fibre breakage and even penetration could be introduced into the laminates when the ultimate failure was reached.

6.3.3 Scanning Electron Microscope Observation Set-up

While much useful information in terms of the internal damage distribution has been obtained from a series of optical microscope observations, the internal damage still cannot be characterised in detail. This is due to the insufficient magnification and the inherent drawback of the optical observation system that the observation might be disturbed by the luminous environment. As a result, the specimens need to be further examined by the scanning electron microscopy under higher magnification and excluding possible observation noise caused by the improper lighting setup.

The SEM observation was conducted on the JCM-5700 Carry Scope as shown in Figure 6.23(a), which delivered the high resolution image and analytical capacities. The digitally recorded sharp imaging, including 8x to 300,000x magnifications and up to 5.0nm resolution, made it possible to conduct high precision measurements on the sub-micron features (such as the matrix crack and delamination). Moreover, the specimen was placed on the motorized specimen stage to achieve required precise movement. Specimens were cut into dimensions of 90mm by 15mm from the vertical centreline to fit the size of the specimen stage.

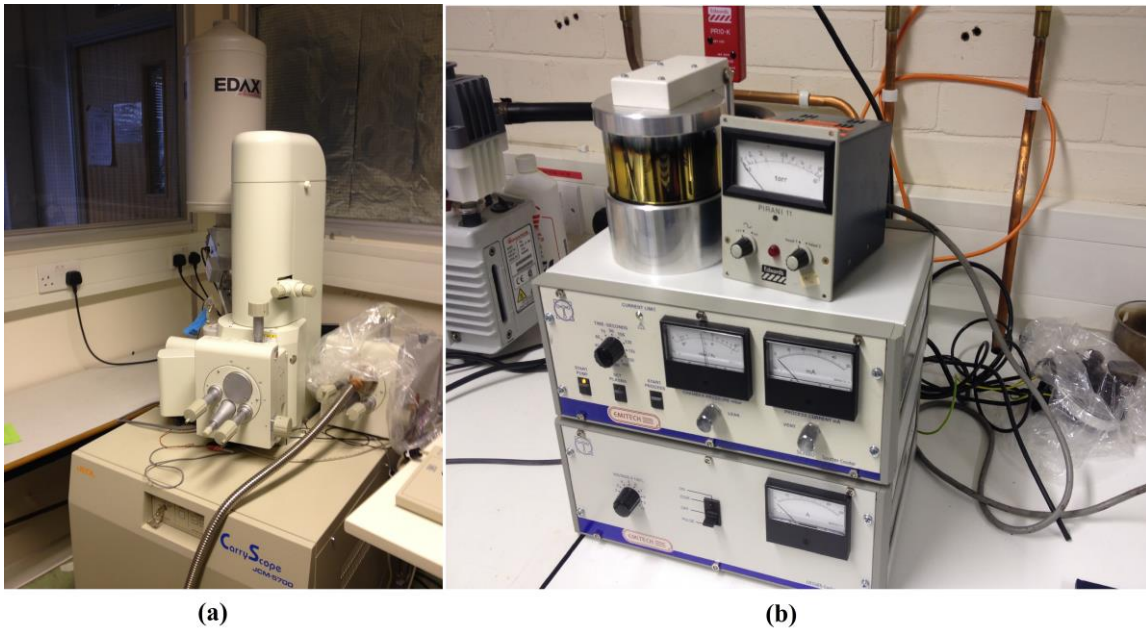


Figure 6.23 Facilities used in SEM observation: (a) SEM and (b) sputter coater.

In addition, gold coating was applied to cross-section to be examined by using the Emitech sputter coater as shown in Figure 6.23(b), to achieve the best SEM image quality. The several micron thick gold coating helped to improve the electrical conductivity of the carbon fibre/epoxy composite laminates.

6.3.4 Scanning Electron Microscope Observation Results

The scanning electron microscope observations were carried out on the same specimens as observed under the optical microscope. The SEM observation was conducted under high magnification on the area which is needed to be further observed based on the microscopic observation.

The cross-section of the reference specimen was observed under SEM as shown in Figure 6.24. The SEM image under 250x magnification shows little detectable discontinuities, which agrees well with the OM observation result.

The cross-section of the specimen subjected to 3.8kN load as shown in Figure 6.25 was found to be fairly smooth and continuous under the SEM, which is different to the image obtained by optical microscope. This is because the disturbance of shadow associated with the OM observation was avoided during the SEM observation.

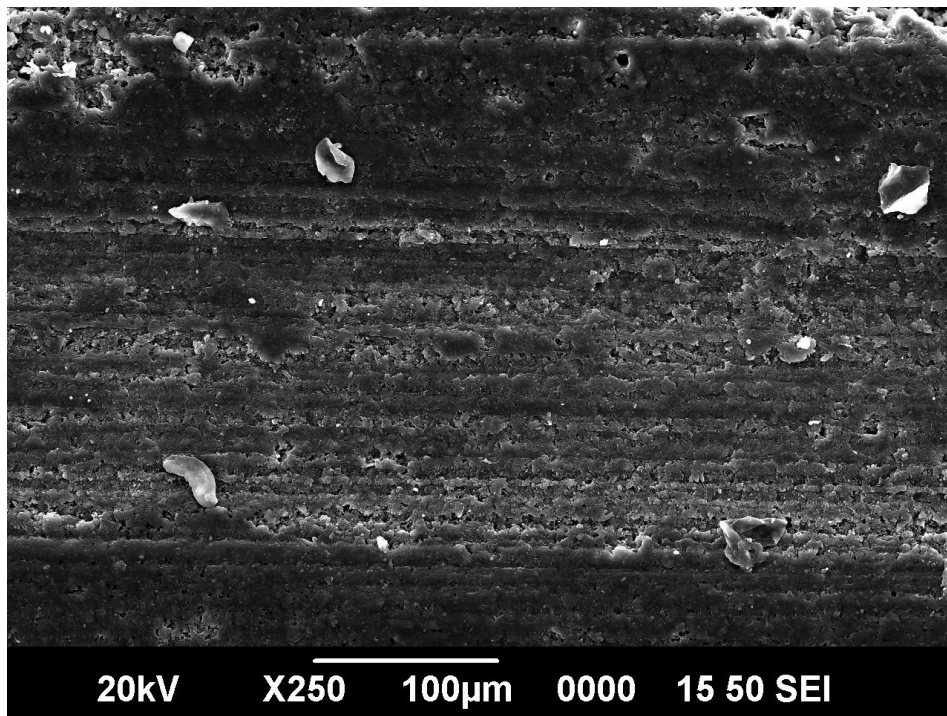


Figure 6.24 SEM image of the reference specimen.

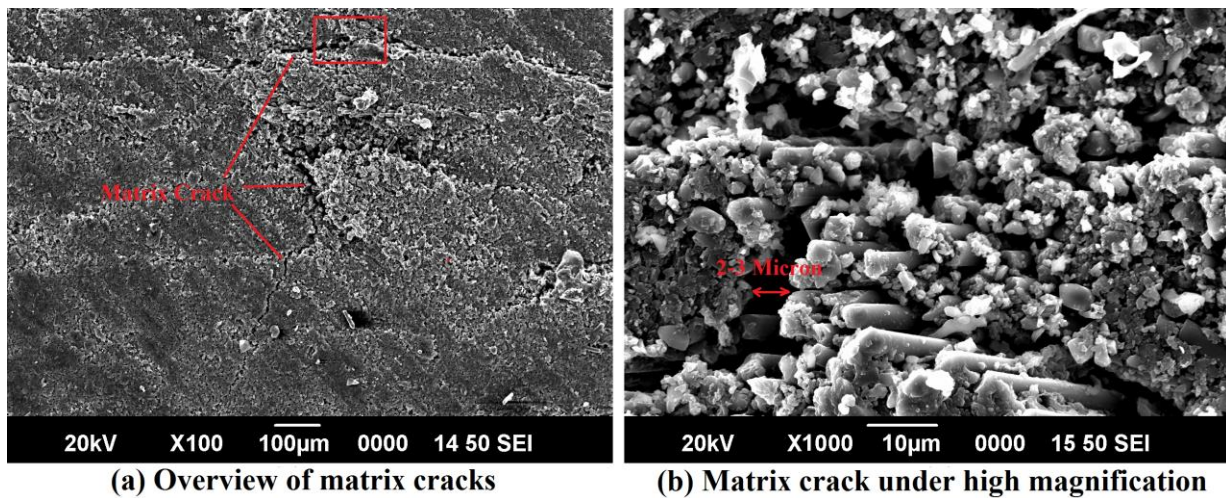


Figure 6.25 SEM images of the specimen loaded up to 3.8kN.

Based on various literatures [10, 11, 47, 48], it is suggested that the matrix crack is the discontinuity within the matrix resin and occurs parallel to the fibre direction, while the delamination is the separation between adjacent laminas with different fibre orientations. Tiny discontinuities, in the form of matrix crack, can be found within the lamina as shown in Figure 6.25(a). No discontinuity was however found at the interface between adjacent laminas with different fibre orientations, which indicates that no delamination is initiated by the indentation load below the DTL value. Figure 6.25(b) shows the SEM image of a matrix

crack under high magnification, which demonstrates that matrix crack with an opening of 2-3 microns does exist inside the lamina with the same fibre orientation.

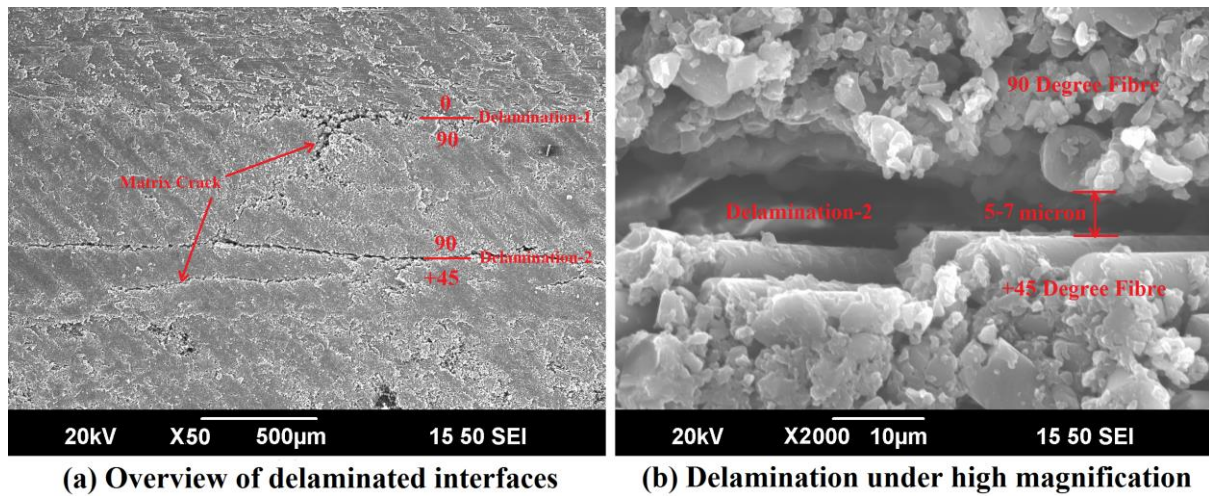


Figure 6.26 SEM images of the specimen loaded up to 4.2kN.

The specimen subjected to 4.2kN load was also examined under the SEM, in which case the distributed delaminations were found parallel to each other. Figure 6.26(a) shows the overview of the area containing such delaminations. It is noticed that the possible initial delamination exists at the interface of laminas with different fibre orientations. To validate this, the delamination was further examined by the SEM under high magnification as shown in Figure 6.26(b). It shows clearly that the delamination does exist at the interface of the laminas with different fibre orientations. In addition, the width of the initial delamination is about 5-7 micron, which is wider than the matrix crack. The matrix crack and the initial delamination can therefore be identified based on the location and the gap width of the discontinuity in the SEM image. Delamination only exists at the interface of laminas with different fibre orientations. The opening of matrix crack (2-3 micron) is smaller than that of delamination (5-7 micron for the initial delamination) based on the observation in this study.

From the OM observation, it is suggested that the internal damage (especially the delamination) suffered a stable propagation after the initiation of delamination. The SEM observation results have been used to examine this suggestion further.

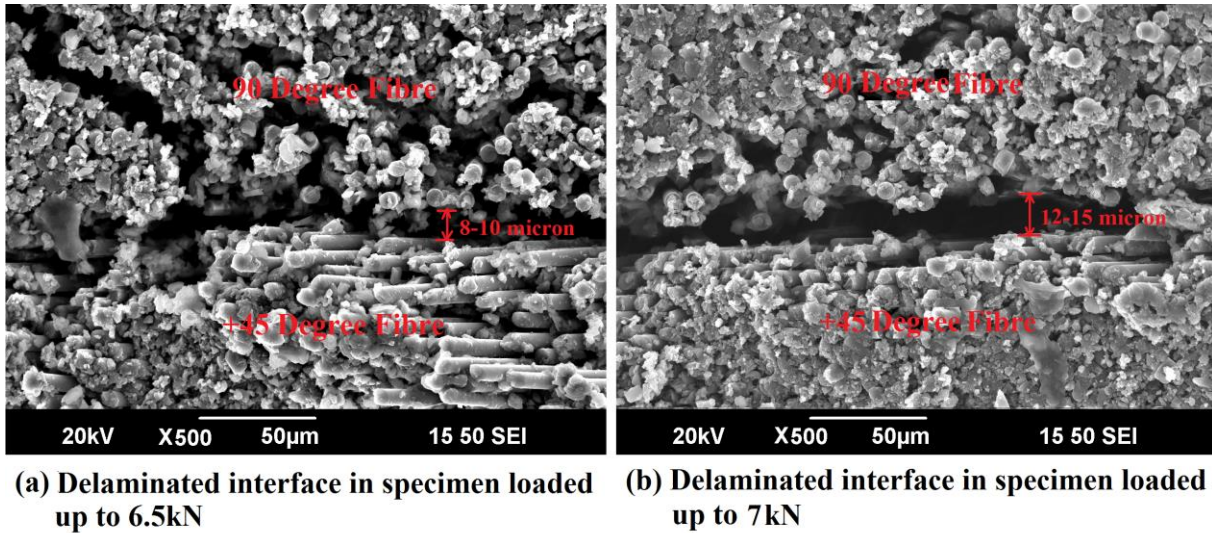


Figure 6.27 Comparison between delaminations in the specimens subjected to 6.5kN and 7kN loads.

Figure 6.27(a) shows the SEM image of the delaminated interface in the specimen loaded up to 6.5kN. It is clear that the delamination spreads along the interface of laminas with 90° and +45° fibre orientations. It is found that the delamination width increases to 8-10 micron compared with that of the initial delamination (5-7 micron), but the increment is not significant. This agrees well with the suggestion that the delamination in the current specimen is still regarded as the local delamination and the applied load is at the transition level between the local and global damage phases. On the contrary, the same delamination damage under 7kN load has increased its opening from 8-10 micron to 12-15 micron, and propagated to a global level as shown in Figure 6.27(b). These results suggest that the transition period from initial local delamination to the global delamination is quite short and occurs when the plastic deformation is introduced into the specimen due to the cumulative damages from the previous damage phases.

Figure 6.28 shows the SEM image of the specimen subjected to 8kN which is close to the end of the global damage phase in the proposed damage process. It is clear that the laminate was deformed by looking at the curved interface of the laminates, which proves the existence of the plastic deformation of the indented specimen. However, the delamination did not significantly propagate or open compared with the specimen subjected to 7kN load. The possible explanation is that the proportion of the energy absorbed by the delamination becomes relatively small when the plastic deformation is introduced to absorb the energy. The relatively larger laminates deformation however causes severe damage in the matrix. As

a result, the matrix cracks become widespread in the area between the delaminated interfaces. Furthermore, once the matrix has been severely damaged under such a high load, the fibre breakage will be easily initiated due to the inherent brittleness of carbon fibres.

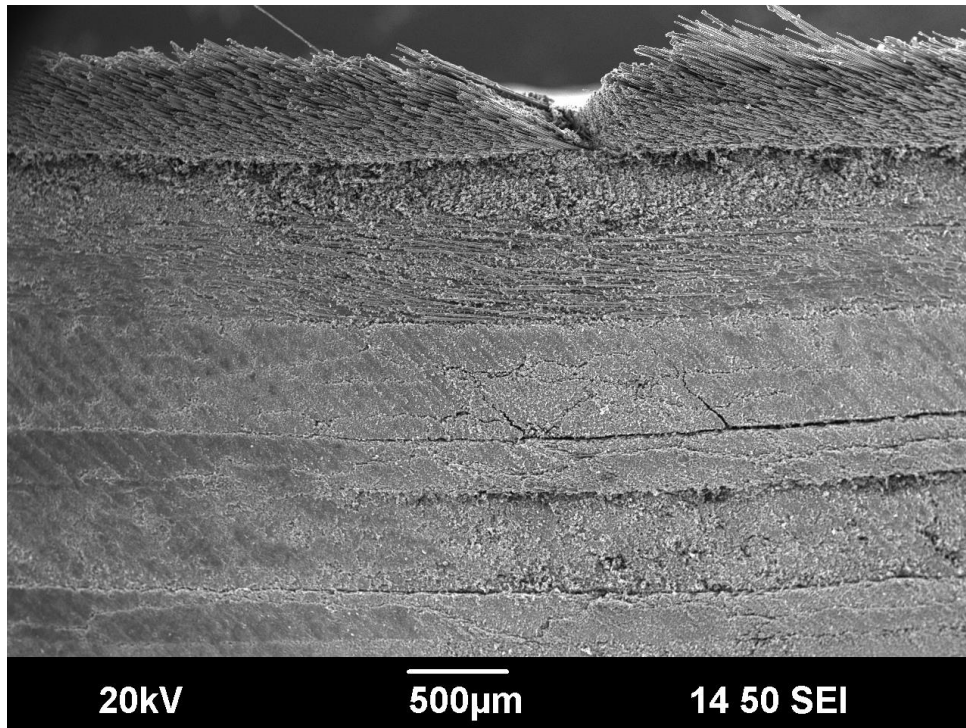
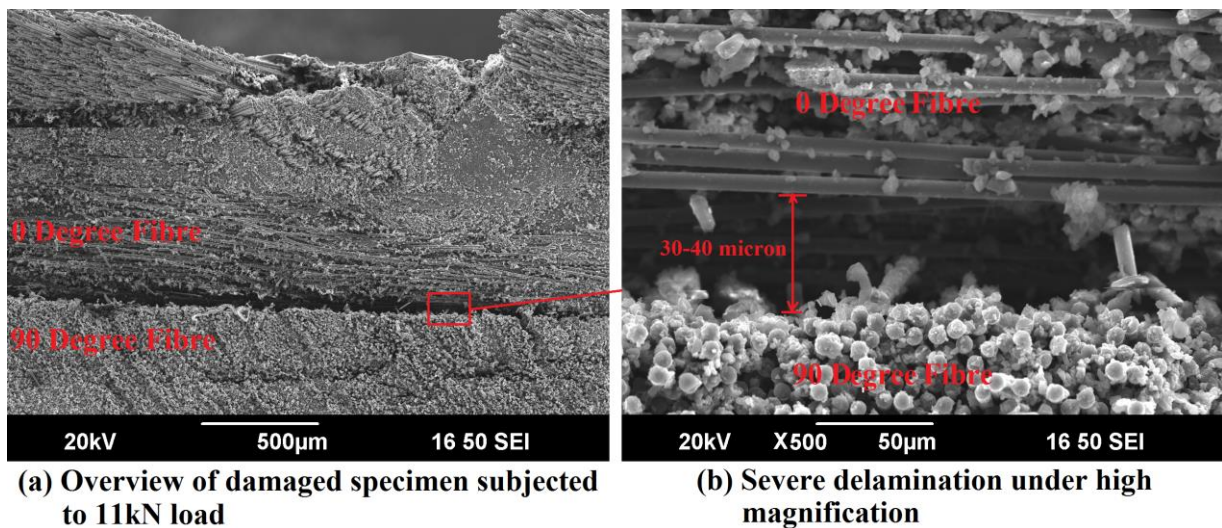


Figure 6.28 SEM image of the specimen loaded up to 8kN.



(a) Overview of damaged specimen subjected to 11kN load

(b) Severe delamination under high magnification

Figure 6.29 SEM observation result of the specimen loaded up to 11kN.

Figure 6.29 shows the SEM images of the specimen loaded up to 11kN under which the final failure phase is assumed to be triggered. The images show that the specimen was severely damaged under the applied indentation load. It is found that the opening of the delamination

has increased to 30-40 microns, which is much larger than the values measured from the specimen under lower indentation loads. Meanwhile, initial fibre breakage is believed to be introduced into the laminates at such high indentation load. Unfortunately, the existence of the initial fibre breakage could not be clearly shown from the SEM image as the SEM observation only characterises the cross-section of specimen. The specimen was cut through the centreline to get such a cross-section for SEM examination. However, the possible discontinuity in the fibre could still be found within the lamina with 0° fibre, in which case the fibre direction of lamina is perpendicular to the cutting direction. The severely propagated delamination and the possible fibre breakage observed from the SEM further prove the existence of the final failure phase.

6.4 Numerical Simulation

In the numerical simulation, the quasi-static indentation process between the composite laminates and the indenter was simulated by the commercial FE analysis software ANSYS/Workbench version 14.5. The indentation induced local permanent deformation was particularly focused on in the current simulation. The comparison between the numerically simulated local permanent deformation and the experimentally measured dent depth can provide very useful information on the indentation behaviour and damage process of composite laminates.

6.4.1 Model Creation

The simulation was conducted in the ANSYS/Workbench environment to perform a static structural analysis. It has been reported that the structural behaviour of composite laminates in the transverse direction was governed by the material properties of the matrix [123, 124]. The local permanent deformation was introduced into the composite laminates when the indentation load exceeded a certain critical value associated with the laminates thickness and the matrix material properties. Therefore, the composite laminate was modelled as a block of pure resin in the current simulation to predict the indentation induced permanent local deformation.

The geometry model for the simulation was created in the CAD software CATIA V5. The created geometry model (.stp file) was then imported to the ANSYS/Workbench to specify

detailed definitions, in terms of the mesh scheme, material property, boundary condition, contact definition and load definition.

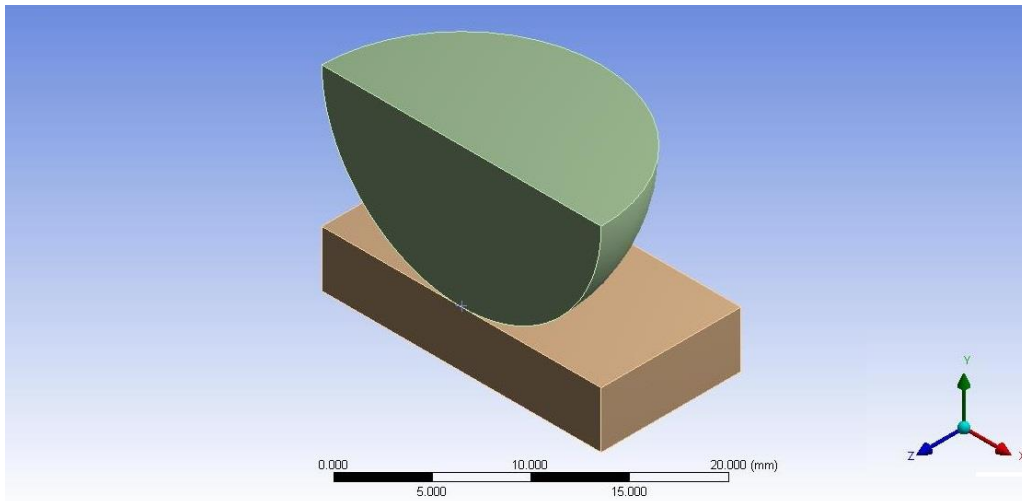


Figure 6.30 Geometry model for the indentation event of the 4mm thick laminates.

In the geometry model, only half of the plate and quarter of the spherical indenter (both were symmetric to the x-y plane) were created as shown in Figure 6.30. Moreover, considering the fact that the indentation was a relatively local phenomenon, the global elastic deformation of plate was not the dominant parameter in relation to the simulation of the local permanent deformation. Therefore, the plate was assumed to be bonded to a rigid substrate to avoid the possible global elastic deformation. Based on this assumption, the simulation was less sensitive to the plate size. As a result, the plate size was reduced to 20mm by 10mm to further simplify the geometry model. Two geometry models with different plate thicknesses were created to simulate the indentation events between the indenter and composite specimens with thicknesses of 2mm and 4mm.

The mesh scheme of the plate was manually controlled by defining the number of mesh divisions of each edge, while automatic body mesh was applied to the quarter-spherical indenter by defining the element size. Figure 6.31 shows the example of the meshed 4mm thick plate (mesh size of 0.5mm) and the quarter-spherical indenter (mesh size of 1mm).

The rigid material properties of the indenter were defined by modifying the existing structural steel material model in the software built-in engineering data library. The original Young's modulus and Poisson's ratio of the structural steel were set to 20000 GPa (100 times larger) and 0, respectively. Therefore, the modified structural steel material model effectively behaved as a rigid material. Similarly, the non-linear material behaviour of the M21 resin was

defined by modifying the material properties of the existing non-linear material model (structural steel NL) to the input data as shown in Figure 6.32. It is noticed that the non-linear material behaviour of the M21 matrix is dominated by the bilinear isotropic hardening parameters including the yield strength and the tangent modulus.

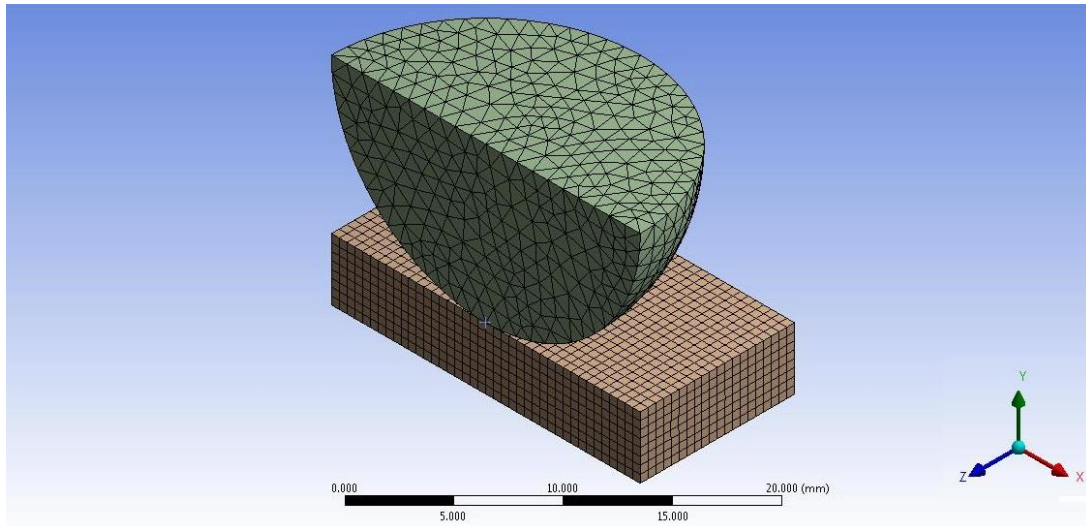


Figure 6.31 Meshed 4mm thick plate and indenter in simulation.

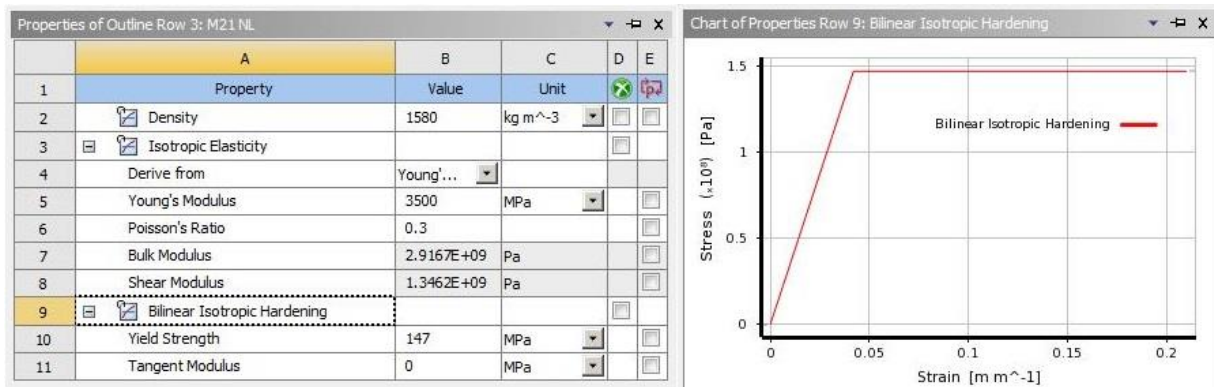


Figure 6.32 Material properties outline of the nonlinear M21 resin.

The model boundary condition was specified by applying different support conditions on different faces. The plate is assumed to be bonded to a rigid substrate. The fixed support is applied to the bottom face of the plate. Fixed supports are also applied to the three side faces of the plate to simulate the local deformation of the laminates. Moreover, the simulation model is symmetric to the x-y plane in the coordinate system. The symmetric regions in the plate and the quarter sphere are firstly selected, and then the z axis is defined as the symmetric axis of the symmetric regions.

The contact between the plate and indenter is defined by inserting a frictional contact definition. The spherical face of the indenter is assigned to be the contact face, while the top face of the plate is assigned to be the target face. The frictional coefficient is set to 0.35, which is the general frictional coefficient between the steel and polymer.

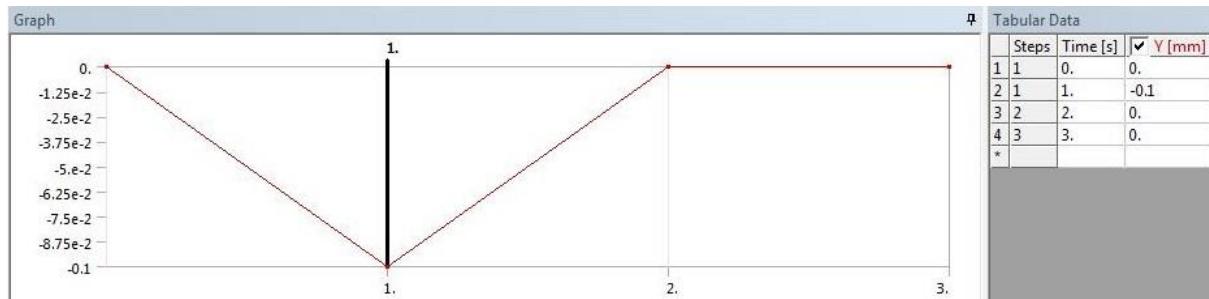


Figure 6.33 Input data for a typical 0.1mm displacement control.

The indentation process (including the loading and the unloading phases) was simulated by controlling the displacement of the top face of the quarter spherical indenter in the y direction. Figure 6.33 shows the input data for a typical 0.1mm displacement control for the indentation process lasted for 3 seconds. In the first second, the indenter was pressed into the plate by 1mm from its initial contact position. The indenter was then back to its initial position in the following second. The indenter was held in the initial position for one more second to get the value of permanent indentation excluding the elastic deformation.

In ANSYS/Workbench, different aspects of solution results could be effectively extracted from the simulation by specifying different solution outputs during the model setup. For instance, the indentation load and the resultant permanent deformation are obtained by activating the force reaction and the directional deformation solution outputs, respectively. It is also worth mentioning that the large deflection option was activated in the solver controls to take the plasticity into account.

6.4.2 Simulation Results

Follow the creation procedure described in Section 6.4.1, different geometry models with different plate thicknesses (2mm & 4mm) were created. Various indenter displacements were specified to simulate the resultant maximum reaction forces and the permanent local deformations. During the solving process, the solution converge was monitored in real-time by means of the graphical plot, after switching on the force convergence function in the

solution output option. Once the model was solved, the indentation force and the permanent deformation were read from the force reaction and directional deformation solution options, respectively. The total reaction force obtained from the simulation result is multiplied by a factor of two to obtain the indentation force as the simulation model only represents one half of the physical objects. The permanent local deformation is equal to the absolute value of the final minimum y-directional deformation from the simulation result.

The mesh size sensitivity was firstly studied to determine the optimised mesh scheme. Four different simulation models were created with element sizes of 2mm, 1mm, 0.5mm and 0.25mm in the plate and the same element size of 1mm in the quarter sphere. In these models, same indenter displacement of 0.4mm was applied. The simulation results, in terms of the final y-directional deformation, obtained from the four different simulations are shown in Figure 6.34.

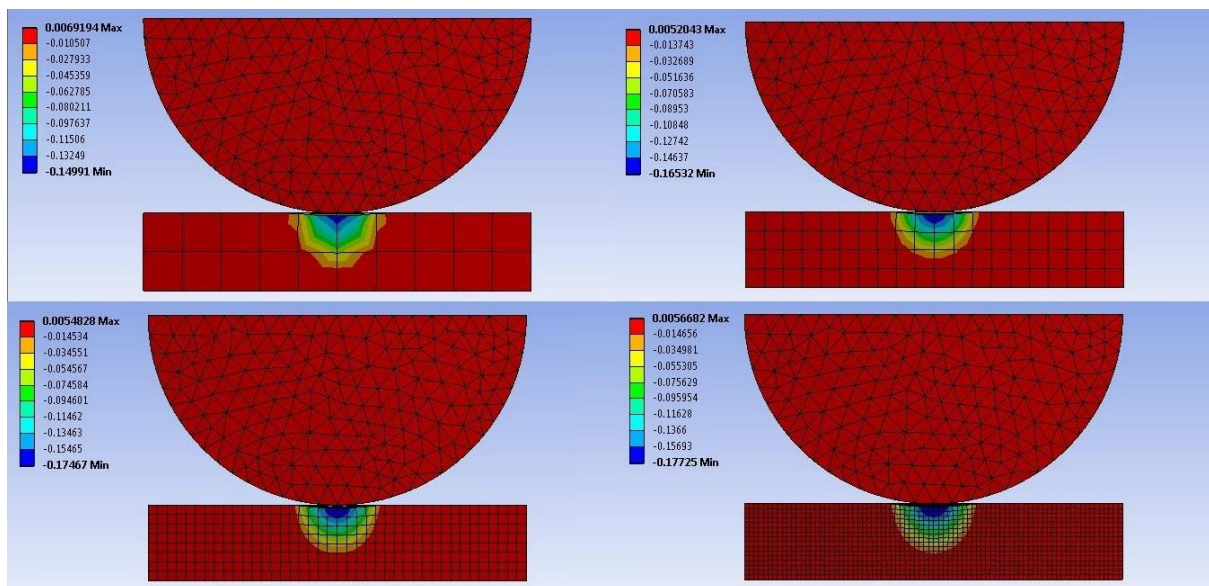


Figure 6.34 Simulation results obtained from different models with different plate mesh schemes.

It is found that the simulation is sensitive to the element size. The simulation solving time is also dependent on the element size. The final minimum deformation in the y-direction for the model with 2mm elements is -0.14991mm and the simulation was completed within several minutes. When the element size was reduced to 1mm, the permanent deformation is increased to 0.16532mm and the simulation solving time was increased to around 10 minutes. For the models with 0.5mm and 0.25mm element sizes, the simulations were completed in about half an hour and over one hour, respectively. The simulation result convergence was improved

with the permanent deformations being 0.17467mm and 0.17725mm, respectively. Considering the simulation convergence and the computational efficiency, the mesh scheme with the 0.5mm elements in the plate was selected as the optimised element scheme in this study.

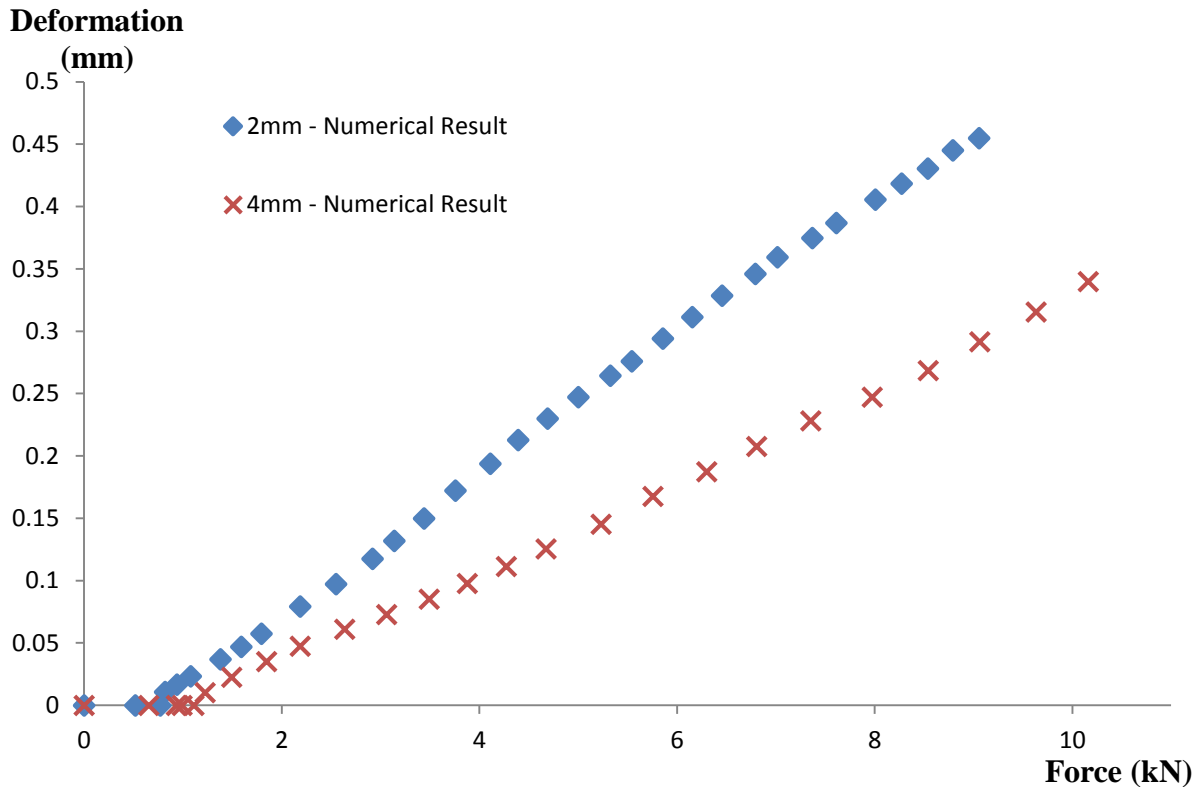


Figure 6.35 Simulation results of models with 2mm and 4mm plate thicknesses.

Different indenter displacements were specified to cover the indentation load range in practice. The simulation results of the models with 2mm and 4mm plate thicknesses, in terms of the correlation between the indentation force and the permanent deformation, are shown in Figure 6.35. It is found that the simulation results of plates with different thickness show a similar trend. In general, correlations between the permanent deformation and the indentation force are linear for both models before permanent deformation is introduced at a critical indentation load. The critical load for the 2mm thick plate is about 0.8kN and permanent deformation is introduced into the 4mm thick plate at around 1.1kN. It is also found that more permanent deformation is introduced in the thinner specimen compared with the thicker specimen under the same indentation load. For instance, the deformation of the 2mm laminates at 4kN is about 0.18mm that is larger than the deformation of 4mm laminates (about 0.11mm) at the same 4kN load.

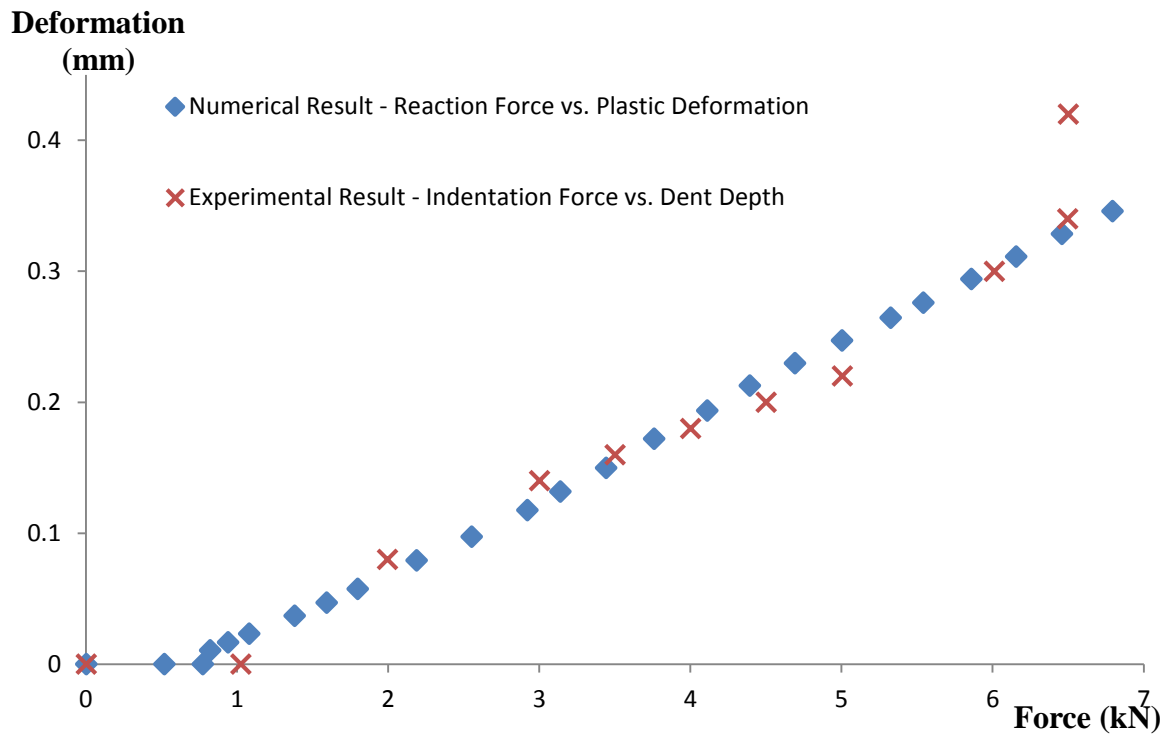


Figure 6.36 Comparison between results achieved from numerical simulation and experimental test for the 2mm specimen.

Figure 6.36 shows the comparison between results obtained from the numerical simulation and the experimental test for the 2mm specimen. It is found that permanent deformations were introduced into the specimen at around 0.8kN and 1.0kN in the numerical simulation and the experimental test, respectively. This proves the existence of the no-dent stage in which the material resistance is high enough to prevent the initiation of the plastic deformation. The numerical simulation result agrees well with the experimental test result in general, which demonstrates that the indentation of composite laminate is governed by the material properties of the matrix. Therefore, the numerical simulation proposed here can be an effective approach to establish the correlation between the contact force and the resultant plastic dent of the thin composite laminates. However, it should be noticed that the simulation result could not capture all the features of the experimental test result due to the simplification in the simulation model. This is down to the inherent complexity associated with the structural behaviour of composite laminates. The structural behaviour of composite laminates under indentation is also influenced by the damage mechanisms and plate deformation as discussed earlier although the influence of these is less significant for the 2mm thin specimen compared with the 4mm specimen. The experimental test result included a sharp dent depth increment when the final failure of composite laminate was reached, while the simulation

result could not capture this. This is because the current simulation only performed an elastoplastic analysis without considering the effect of damage due to the absence of damage mechanisms. However, considering the simplicity of the simulation model and the good general behaviour mentioned above, the current simulation approach is considered successful and provides a useful tool to establish a relation between the contact force and the dent depth of the thin composite laminates.

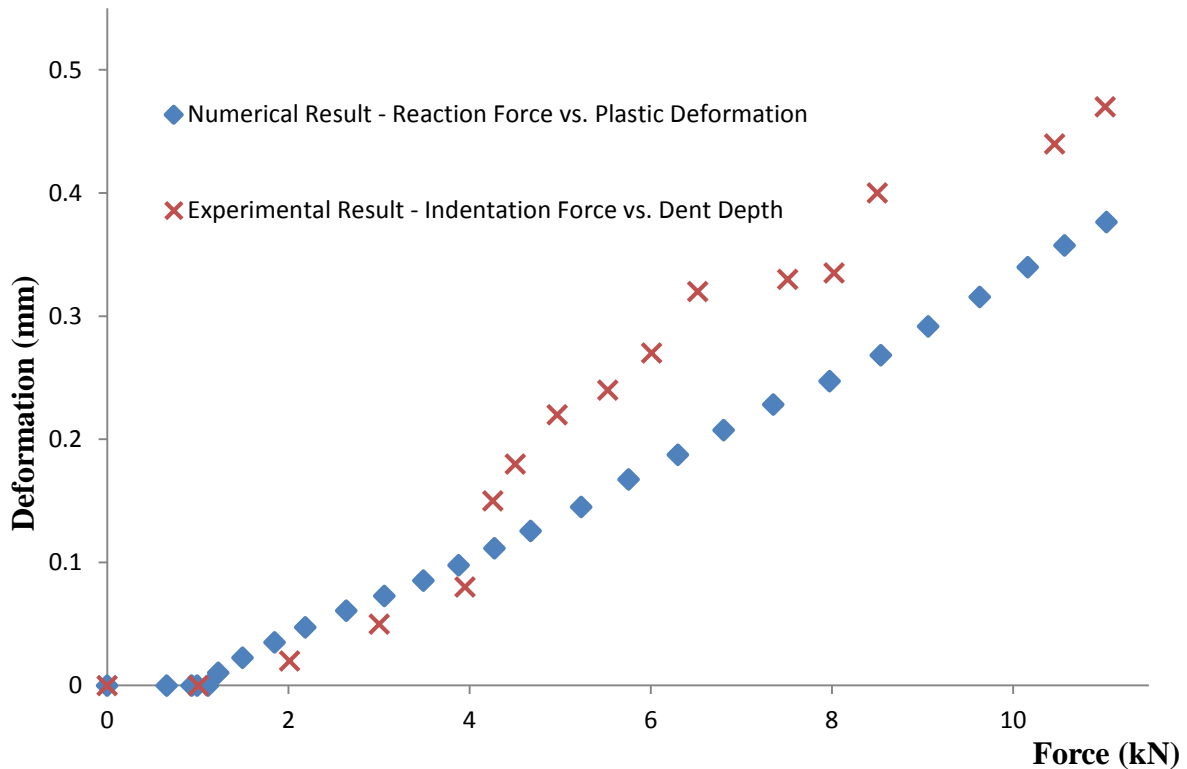


Figure 6.37 Comparison between results achieved from numerical simulation and experimental test for the 4mm specimen.

Figure 6.37 shows a similar comparison between the results obtained from the numerical simulation and the experimental test on the 4mm thick specimen. The simulation result deviates quite significantly from the test result for the indentation force greater than 4kN even though they agree with each other well in the no-dent stage. This suggests that the structural behaviour of the 4mm thick composite laminate is affected more strongly by the damage mechanism and the plate deformation compared with the 2mm thin specimen, which is consistent to the discussions in earlier sections.

Prior to the initiation of the delamination when the indentation force is below 4kN, the simulation result agrees well with the test result. This result suggests that the structural

behaviour of the thick composite laminates follows the elastoplastic behaviour of the matrix material properties until the delamination was initiated.

Once the delamination is initiated, the material resistance to the local indentation is significantly reduced in practice while the simulation model still follows the same elastoplastic behaviour. As a result, the local dent depth measured from the experimental test is much larger than the permanent deformation predicted by the numerical simulation. Effect of damages on structural response becomes more important in thick composite laminates compared with thin laminates. Moreover, the phenomenon of the plateau in the dent depth measurements, which was related to the global plastic deformation of the specimen, also could not be predicted by the current simulation model. All of these demonstrate that the current simulation strategy needs to be developed further to improve simulation result for thick laminates.

6.5 Result of Analytical Prediction

An analytical study was conducted to characterise the correlation between the contact force and various contact parameters using simple contact models. Analytical predictions obtained from different contact models were compared with the experimental measurements to assess the capability of each contact model to predict the structural behaviour of composite laminates. Possible modifications to the existing contact model were explored to enhance the model performance.

6.5.1 Hertz Contact Theory based Contact Model

The modified Hertz contact theory based contact model, which was suggested by Turner [114], was employed in the current analytical prediction. The contact model, as reviewed in Section 2.5.3, replaces the isotropic modulus with an effective transversely isotropic modulus to extend its applicable range to the transversely isotropic materials, such as the quasi-isotropic composite laminates.

The effective modulus, E_{TI}^* , is a combination of the three-dimensional elastic property of the transversely isotropic composite laminates, referring to Equation 2.54. Once the effective modulus has been determined, the relationship between the contact force and the contact

indentation can be determined by substituting the effective modulus and the radius of the rigid spherical indenter into Equation 2.53. The detailed analysis presented in Appendix III.

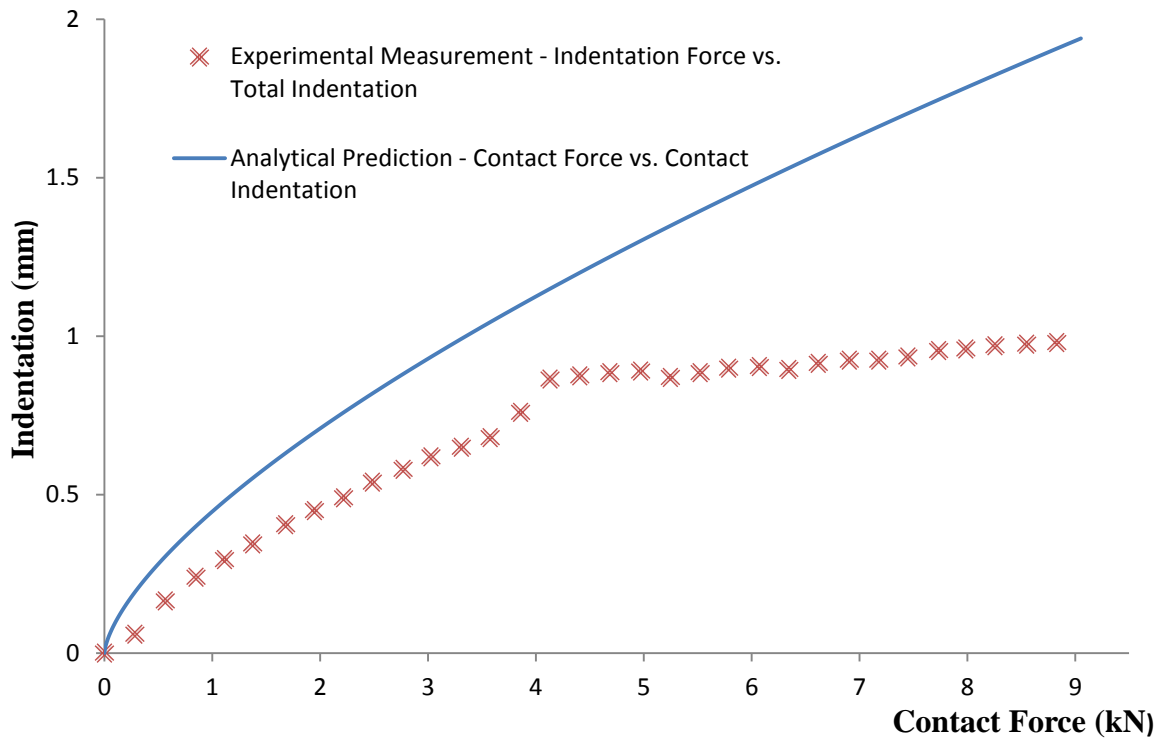


Figure 6.38 Comparison between analytical prediction and experimental measurement.

Figure 6.38 shows the comparison between the analytical prediction calculated from the elastic material properties of the transversely isotropic composite laminates and the experimental measurement obtained from the test of the 4mm thick quasi-isotropic composite laminates.

It is found that the analytical prediction deviates significantly from the experimental measurement. The analytical prediction, showing a non-linear relationship between the contact force and the contact indentation with a power index of 1.5, failed to capture the complex correlation between the indentation force and the total indentation in the experimental measurement. Such deviation is related to the drawback of the classic Hertz contact theory which only considers the material elastic behaviour. The real structural behaviour of the thick composite laminate is affected by multiple mechanisms including the damage mechanisms and the plastic deformation.

It is interesting to note that the experimental measurement follows a non-linear relationship similar to the analytical prediction before the delamination threshold load is reached. The

difference is possibly caused by the error in the determination of the effective modulus. As a result, the early stage structural behaviour of composite laminates could be predicted by the analytical contact model with modification to the determination of the effective modulus. However, once the delamination is initiated, the effects of damage mechanisms and plastic deformation become significant and the structural behaviour of the delaminated composite laminates does not follow the non-linear trend of the analytical prediction. This indicates that the structural behaviour of the delaminated composite laminates could not be reliably predicted with the current contact model unless the damage mechanism and the plastic deformation were included.

6.5.2 Elastoplastic Response based Contact Model

The Hertz contact theory based contact model links the contact force to the total indentation under the loading, not the permanent indentation which is easy to check. The elastoplastic response based contact model [4] is however capable of linking the contact force to the permanent contact parameter such as the dent depth and is explored in this section.

In the contact model, the layer of material is firstly assumed to deform elastically until a critical indentation was reached. The contact area is then divided into a plastic zone immediately under the indenter and an elastic zone surrounding the circular plastic zone as the loading increases. The structural behaviour of composite laminate is governed by the elastic-perfectly-plastic stress-strain behaviour of the matrix material. The correlation between the contact force and the plastic deformation of the composite laminate is derived based on the analysis (using Equation 2.57-Equation 2.64) as presented in Appendix IV.

The analytical predictions were compared with the results obtained from the experimental tests of the 2mm and 4mm quasi-isotropic composite laminates as shown in Figure 6.39. The result of the analytical prediction represents the relation between the contact force and plastic deformation, while the experimental measurement result is the indentation force against dent depth.

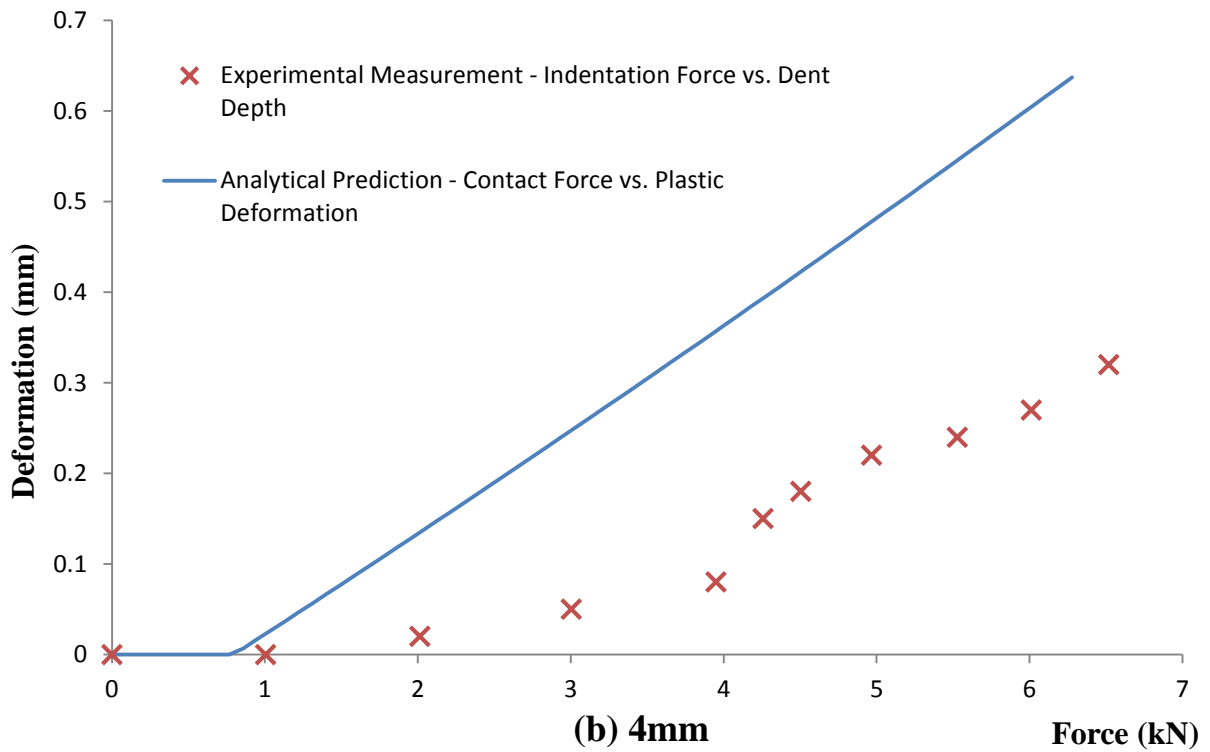
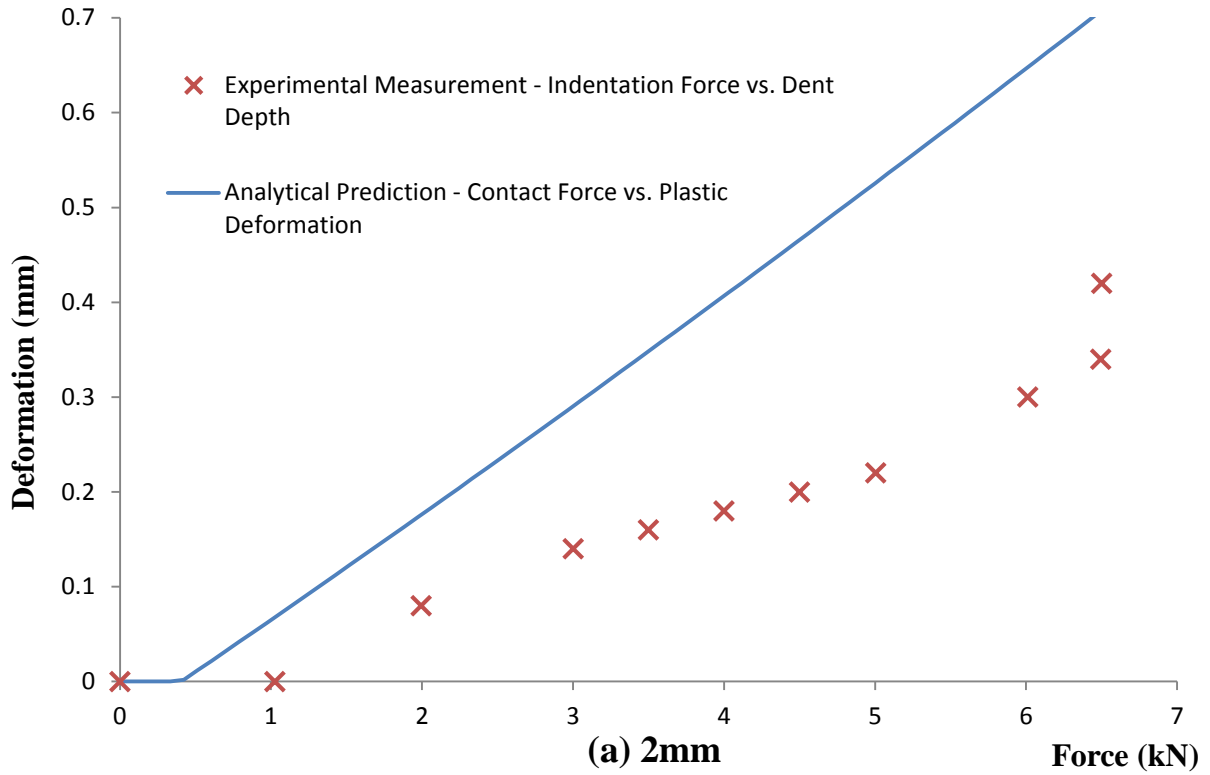


Figure 6.39 Comparison between analytical prediction and experimental measurement: (a) 2mm and (b) 4mm composite laminates.

The analytical prediction deviates significantly from the experimental measurement for both the 4mm and 2mm composite laminates. The elastoplastic contact model overestimates the plastic deformation compared with the result of dent depth measured from the quasi-static indentation test. However, the existence of the no-dent phase is illustrated in both results, which demonstrates further that the dent is introduced to the laminates at a specific critical load level linked to the matrix material property and the laminates thickness. The analytical prediction, which shows a linear relationship between the contact force and the plastic deformation, however, fails to capture the complex relation between the indentation force and the dent depth in the experimental measurement.

It is however worth noting that the elastoplastic response based contact model shows great potential in predicting the correlation between the dent depth and contact force associated with the LVI/QSI events. This is due to the fact that a very simple elastoplastic material model is used for the material properties of composite laminates in the current study. The performance of the analytical model is expected to be improved significantly when more comprehensive material model is adopted. Such a comprehensive material model should account for more realistic stress-strain behaviour such as strain hardening/softening for the matrix material, the reinforcing effect of the fibre to the matrix material in the transverse direction, and the effect of damages at different phases identified in Section 6.1.5. Detailed research is however required to implement these changes to the current model properly.

6.6 Summary

Presented in this chapter are the experimental, numerical and analytical investigations to achieve further understanding on the damage mechanisms and structural response of composite laminates under low-velocity impact.

In the experimental approach, the damage mechanisms and structural response of composite laminates under low-velocity impact were investigated through a series of instrumented quasi-static indentation tests. It is found that the indentation load curve is capable of characterising the damage mechanisms and structural response of composite laminates under low-velocity impact, in terms of the delamination initiation, initial fibre breakage and ultimate failure.

Moreover, the dent depth, as an externally inspectable parameter, is the key in the investigation. Results show that the indentation response of composite laminates can be divided into several damage phases in accordance to the difference in rate of dent depth increment. The indentation response of the 4mm composite laminates can be divided into the undamaged, local damage, global damage, and final failure phases, respectively. The indentation response of the 2mm composite laminates can be divided into the no-dent, combined damage, and final failure phases, respectively. The effect of delamination initiation and propagation is not significant in the indentation response of the more flexible 2mm thin laminates. The measurement of the back-face displacement of the 4mm composite laminates demonstrates that the effect of the plastic deformation on the indentation response needs to be considered when the global damage phase is introduced to the thick specimen due to the accumulative damage induced stiffness degradation.

To validate the damage process assumption proposed above, a series of CAI tests and internal damage observations were conducted on the 4mm composite laminates loaded up to different loading levels. The test results provide direct evidences, in terms of the residual strength and internal damage distribution, to support the damage process assumption.

In the numerical approach, particular attention was given to the result of indentation induced local plastic deformation. The composite specimen indented by the indenter was simplified to a contact between a rigid quarter sphere and a layer of material characterised by the elastoplastic material properties of the matrix material. It is found that the current elastoplastic simulation model was capable of predicting the relation between the indentation force and dent depth when the effect of damage on structural behaviour is not significant. The simulation result could not however capture all the features of the experimental test result, due to the absence of the damage mechanisms in the simulation model. The dent depth measurements of the 4mm specimen after the delamination initiation are much bigger than the simulation prediction. The delamination induced local stiffness reduction could not be simulated by the current elastoplastic material behaviour dominated simulation model.

In the analytical approach, the indentation response of composite laminate was predicted by two different contact models. For the Hertz contact theory based contact model, the analytical prediction could not predict the nearly flat increment in the total indentation after the delamination initiation since the damage mechanism and the plastic deformation were not considered in the current elastic material properties based contact model. For elastoplastic

response based contact model, the analytical prediction deviates significantly from the experimental measurement, which is consistent to the numerical simulation. However, the elastoplastic response based contact model is still considered to have great potential in predicting the relation between the dent depth and contact force if more realistic material behaviour can be employed in the material model.

CHAPTER 7 Discussion

In this PhD project, a series of investigations have been conducted to achieve a further understanding on the damage mechanisms and impact response of composite laminates under low-velocity impact. The feasibility of assessing the internal damage with a visually inspectable parameter has been explored by working on the relation between the contact force and the dent depth. While investigation results have been presented and discussed, it is necessary to discuss and compare the investigation results from the project point of view in order to achieve a further understanding.

In this chapter, systematic discussions are mainly focused on the following three topics. The first one is about the reliable detection of the DTL, which is related to a suitable range of ratio of the impact energy to the laminates stiffness/thickness. The second one is about the effect of delamination initiation on structural performance, which might have been overestimated based on the evidence collected in this project. The final one is about the newly proposed damage process assumption, which could be used in structural health monitoring of the post-impact composite laminates in the future.

7.1 Reliable Detection of DTL

The delamination threshold load, as an important parameter to characterise the damage resistance of composite laminates, has been the focus throughout this project. It is widely reported that the DTL value can be determined by locating the sudden load drop in the impact force history [4, 10, 13, 14, 67].

As it has been presented in Chapter 5, a series of instrumented drop-weight tests have been conducted on various impact test specimens under various impact energy levels to determine the DTL values of the tested composite laminates. These impact test specimens have different laminates thicknesses and different lay-up configurations, which helps to evaluate the influence on the DTL value and detectability of DTL value.

Table 7.1 summarizes the DTL values of different composite laminates. It is found that the existence of the load drop phenomenon is strongly affected by the laminates thickness. To be specific, the sudden load drop phenomenon can be consistently observed in most of the

impact force histories obtained from the impact tests conducted on the thick specimen (4mm & 5mm) when the peak impact force exceeds the threshold level. On the contrary, the DTL phenomenon is not obvious in the impact force histories from the thin specimens (2mm & 3mm). In addition, it is interesting to note that the DTL phenomenon is also less obvious for the 4mm cross-ply laminates under 12J or higher impact energy. The DTL phenomenon can however be detected for the 4mm quasi-isotropic specimen and 5mm cross-ply specimen subjected to the 12J impact. As it is suggested in Chapter 5, the detectability of the DTL value via the impact force history is related to a suitable range of ratio of the impact energy level to the laminates stiffness/thickness.

Table 7.1 Summary of DTL values of different composite laminates

	Cross-ply Lay-up Configuration	Quasi-isotropic Lay-up Configuration
2mm	No detectable DTL	No detectable DTL
3mm	Possible DTL: 3.3kN	
4mm	Clear DTL: 4.3kN	Clear DTL: 4.9kN
5mm	Clear DTL: 5.8kN	

For a thin composite laminates, it should be noted that the specimen is more flexible due to its relatively low stiffness. As a result, the elastic deformation is easier to be induced by the low-velocity impact and becomes a dominant impact energy absorption mechanism. The delamination initiation may not occur easily under the low energy impact as most of the energy may be dissipated through the elastic deformation, rather than via the damage mechanism. The delamination will however still be initiated in the thin specimen when the impact energy increases to a certain level. Meanwhile, it is noticed that severe damages, such as the fibre breakage and delamination propagation, are introduced into the specimen immediately after the delamination initiation due to the large specimen deflection. As a consequence, the DTL phenomenon may be eliminated due to the dramatic laminates stiffness reduction triggered by several failure mechanisms occurred simultaneously. It is however worth mentioning that the repeated impact force history will consistently deviate from the first impact force history as a result of the existence of delamination for all the laminates tested as presented in Section 5.1.3-5.1.4. In other words, the DTL value cannot be reliably detected from the first impact force histories of thin specimens; the repeated impact test result

may provide an alternative method in detecting the DTL value for the case when the delamination initiation effect is not significant in the impact force history of the first impact.

For the thick composite laminates, the specimen is stiffer compared with the thin specimen, which makes the elastic deformation not easy to occur under the impact. As a result, the damage mechanism, such as the delamination initiation, plays a significant role in energy dissipation. The DTL phenomenon can therefore be detected in most of the impact force histories of thick specimens. Moreover, damage propagation can also be clearly found as discussed in the damage process assumption in Section 6.1.5. However, when the impact energy has been increased to a certain level, severe damages are introduced immediately after the delamination initiation and the separation of delamination initiation and other damage mechanisms becomes difficult. This is the case when the 4mm cross-ply specimen is under the 12J impact, which is similar to the behaviour of the thin specimen suffered high energy impact. Hence the load drop phenomenon can be reliably detected from the impact force history of a thick specimen when the impact energy/laminates thickness ratio is within a reasonable range.

The quasi-static indentation test results presented in Chapter 6 agree well with the low-velocity impact test results. The delamination initiation can be clearly found, as a knee point, in the indenter displacement history of the thick specimen. The knee point phenomenon is however not clear in the indenter displacement history of the thin specimen. Moreover, the DTL value determined by the QSI test is close to that determined by the LVI test. As such, the QSI test can be used as a good supplementary method to enhance the reliability of the DTL measurement via the LVI test.

Based on the investigation results obtained from this project, it is found that the reliable determination of the DTL value of composite laminates via the low-velocity impact test is far from straightforward. The existence of the sudden load drop phenomenon in the impact force history is strongly affected by the ratio of the impact energy and the laminates thickness/stiffness. A good DTL derivation procedure should consist of two parts: one for the QSI test and one for the LVI test. The existence of the load drop phenomenon should be firstly checked by the QSI test. If the knee point phenomenon can be found in the indenter displacement history, which indicates that the sudden load drop phenomenon also should be obvious in the impact force history, the exact DTL value should then be determined by more LVI tests. Moreover, the load level determined by the QSI test should be used for the

estimation of the DTL value and the impact energy selection for the LVI test. This is to ensure that the load drop phenomenon associated with the delamination initiation may not be eliminated by the improper selection of impact energy level and its resultant excessive impact force. If the knee point phenomenon cannot be clearly identified on the indenter displacement history, which demonstrates that the delamination initiation effect is not significant in the impact response of the tested specimen, the repeated impact test should then be considered as an indirect method to determine the possible DTL value of the tested specimen. A number of repeated impact tests under various impact energy levels should be carried out to locate the transition point related to the DTL by examining the impact force histories of the laminates under the first and repeat impacts.

7.2 Potential Menace of Delamination Initiation

It is widely reported that the delamination initiation is a hallmark event representing a significant increase of delamination and thus a large reduction of the residual compressive strength of composite laminates. It is suggested that the matrix crack and delamination may contribute up to 60% loss in the compressive strength of composite laminates under low-velocity impact [4, 9, 17, 24]. The influence of the delamination initiation on the structural performance of composite laminate has been investigated in details in this project to characterise the damage resistance and damage tolerance of this type of materials.

Based on the repeated impact test results presented in Section 5.1, it is found that the repeated impact force history under the same impact energy level is much smoother than the first impact force history, which suggests that the existing delamination has not been significantly propagated during the repeated impact if the impact energy level is not too high. This result demonstrates a good damage tolerance of the composite laminates to the initial delamination as the composite laminate is able to resist the further propagation of delamination. It can be explained by the fact that the existence of the multiple initial delaminations acts as additional sources for impact energy absorption and hence improves the damage tolerance of composite laminates under the repeated impact. The initial delamination may also improve the flexibility of the original brittle carbon fibre epoxy composite material and thus enhance the capacity of the composite laminates in absorbing impact energy. Figure 7.1 shows a SEM image of the tip of the initial delamination under high magnification. There is an opening area at the tip of the delamination which not only may absorb certain impact energy but also can reduce the

stress concentration. As a result, the initial delamination is difficult to propagate under the repeated impact when the impact energy level is not too high.

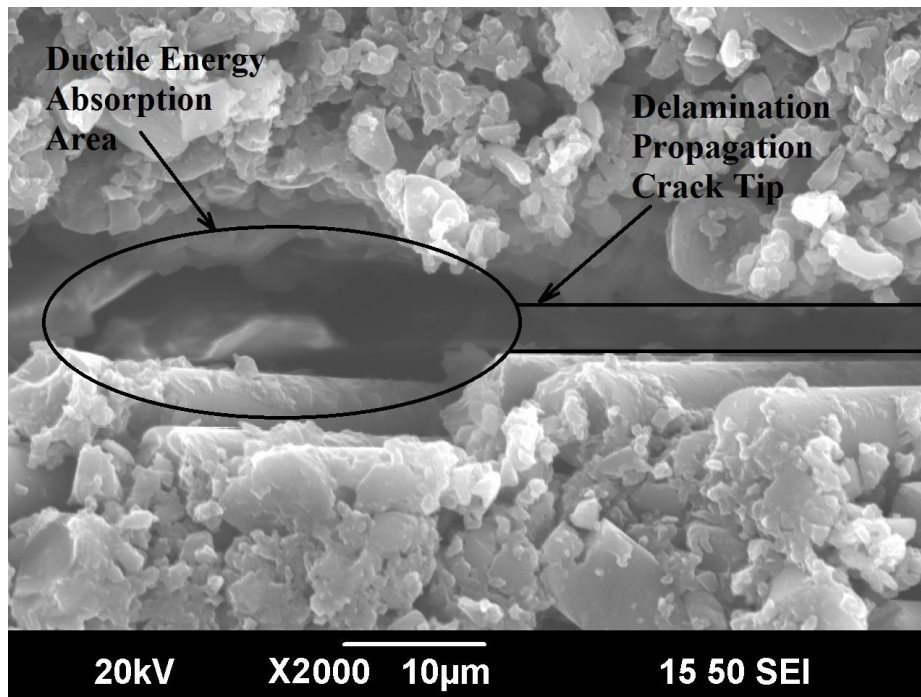


Figure 7.1 SEM image of the initial delamination propagate tip.

Moreover, the phenomenon of peak force increment is consistently observed in the repeated impact force history for the specimen that has been delaminated in the first impact. This indicates that the delaminated laminate is able to withstand the repeated impact under the same energy level and the structural integrity of the laminate has not been reduced after the initiation of the delamination. The higher peak force in the repeated impact force history may be caused by the elimination of the load drop related to the delamination initiation due to the enhanced damage tolerance mentioned earlier.

The CAI test results presented in Section 6.2 also confirm that the load bearing capacity of composite laminates with initial delamination has not been reduced significantly. Figure 7.2 shows the CAI test results of the 4mm specimens in the form of the relation between the maximum applied load and the residual compressive strength.

It is found that the residual compressive strength of the specimen with the initial delamination is reduced by about 10% compared with that of the reference specimen and the specimen without initial delamination. It shows that the existence of initial delamination does cause a reduction in the residual strength. However, it should be noticed that this reduction is not as

significant as the prediction based on the traditional understanding on the effect of delamination initiation. The initial delamination might not be as severe as originally suggested in the literature. This should be reflected in the service and maintenance process of a composite laminates component, bearing in mind the good damage tolerance capacity of the delaminated laminates and the safety factor employed in the design process. Furthermore, it is interesting to note that the residual strength of the damaged laminates experiences a gradual decline after the 10% reduction in the residual strength caused by the delamination initiation. Another 20% of residual strength is reduced while the initial delamination is propagating. These results indicate that the delamination propagation is not an instantaneous event after the delamination initiation, but follows a stable damage propagating process. Details of such a damage process will be discussed in the next section. In addition, it is found that the introduction of the global plastic deformation of the laminates leads to a sudden reduction in the residual strength at the magnitude of about 60% of the reference strength. The composite laminates with the obvious plastic deformation is no longer capable to withstand the load and should be replaced or repaired immediately.

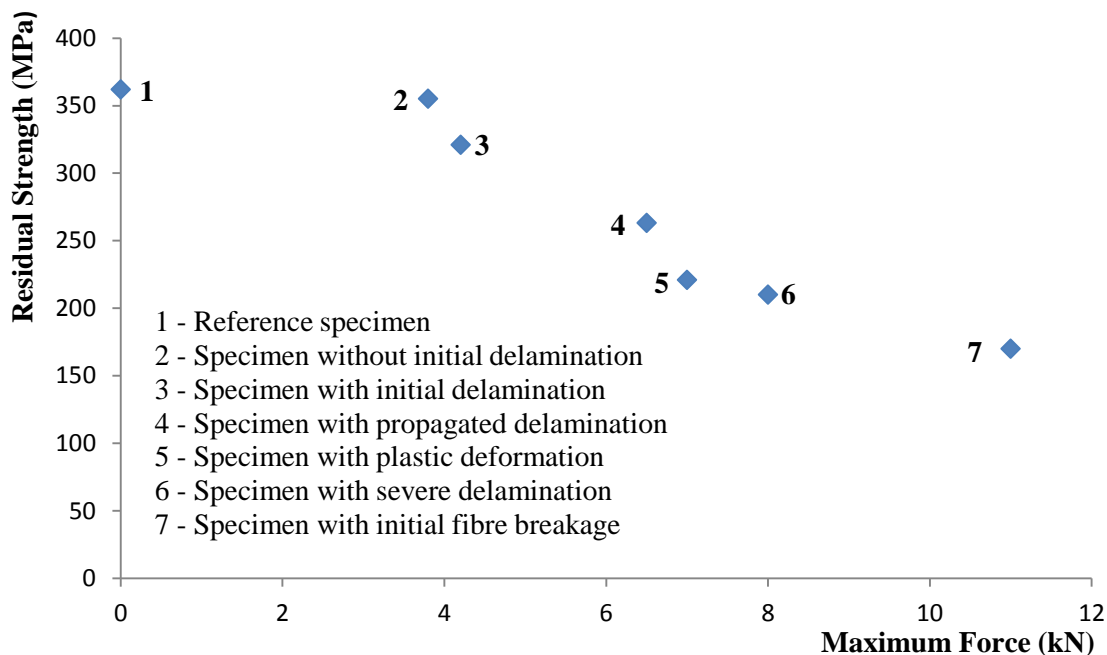


Figure 7.2 CAI test results of various 4mm specimens suffered different maximum loads.

Based on the above discussion, it can be concluded that the potential menace of the delamination initiation under DTL may be overestimated by the traditional understanding on the delamination initiation. Damage resistance and the damage tolerance of composite laminates are two independent concepts and should be considered separately in a design

process to achieve more effective design. The material may have low damage resistance but exhibit very good damage tolerance capacity. Moreover, in the service and a maintenance process of composite laminates, the delamination initiation should not be treated as the only criterion to assess the performance of the post-impact composite laminates. The plastic deformation of the laminate is usually associated with severe internal damage and significant reduction of the load bearing capacity. The finding on the influence of delamination initiation on structural performance of composite laminates may reduce the conservatism in design and lead to a great save in the cost of replacing or repairing post-impact composite components.

7.3 Damage Process Assumption

Traditionally, an impact damage process of composite laminate is believed to be dominated by the material brittleness, in which the damage is initiated in the brittle composite laminates immediately after the impact force exceeds a critical level and followed by a rapid damage propagation [4-7, 24]. Based on the investigations conducted in this project, it is however found that several other mechanisms also play important roles in the impact damage process of composite laminates. A damage process assumption was proposed in Chapter 6 to characterise the damage initiation and propagation process of composite laminates.

As illustrated in Figure 7.3, the damage process can be divided into several phases according to the difference in the increasing rate of dent depth. Figure 7.3(a) shows the damage process assumption for the 4mm composite laminates, in which the delamination initiation phenomenon can be clearly observed in the indentation force curve. It is proposed that the damage initiation and propagation process of 4mm specimen can be divided into four phases corresponding to non-damage, local damage, global damage, and final failure, respectively.

The non-damage phase is further divided into two sub-phases, which is controlled by the yield strength of the matrix material. If the contact stress is less than the yield strength, the material resistance to yielding is high enough to prevent any permanent dent. As a result, no detectable dent is introduced into the laminates in the no-dent sub-phase (as Phase 1a). If the contact stress exceeds the yield strength, the dent depth increases linearly with the increasing load. Only the local crush dent and matrix crack are introduced into the laminates during this sub-phase (as Phase 1b), and the overall material performance of the laminate is not affected.

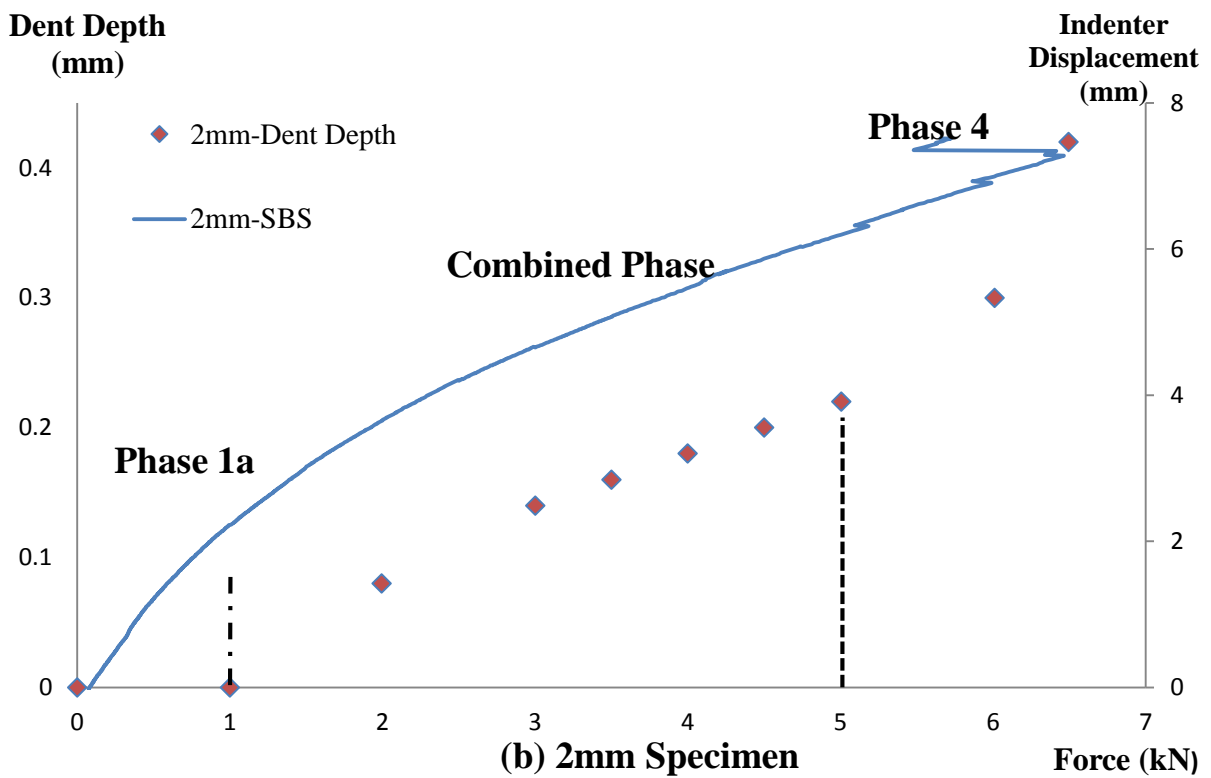
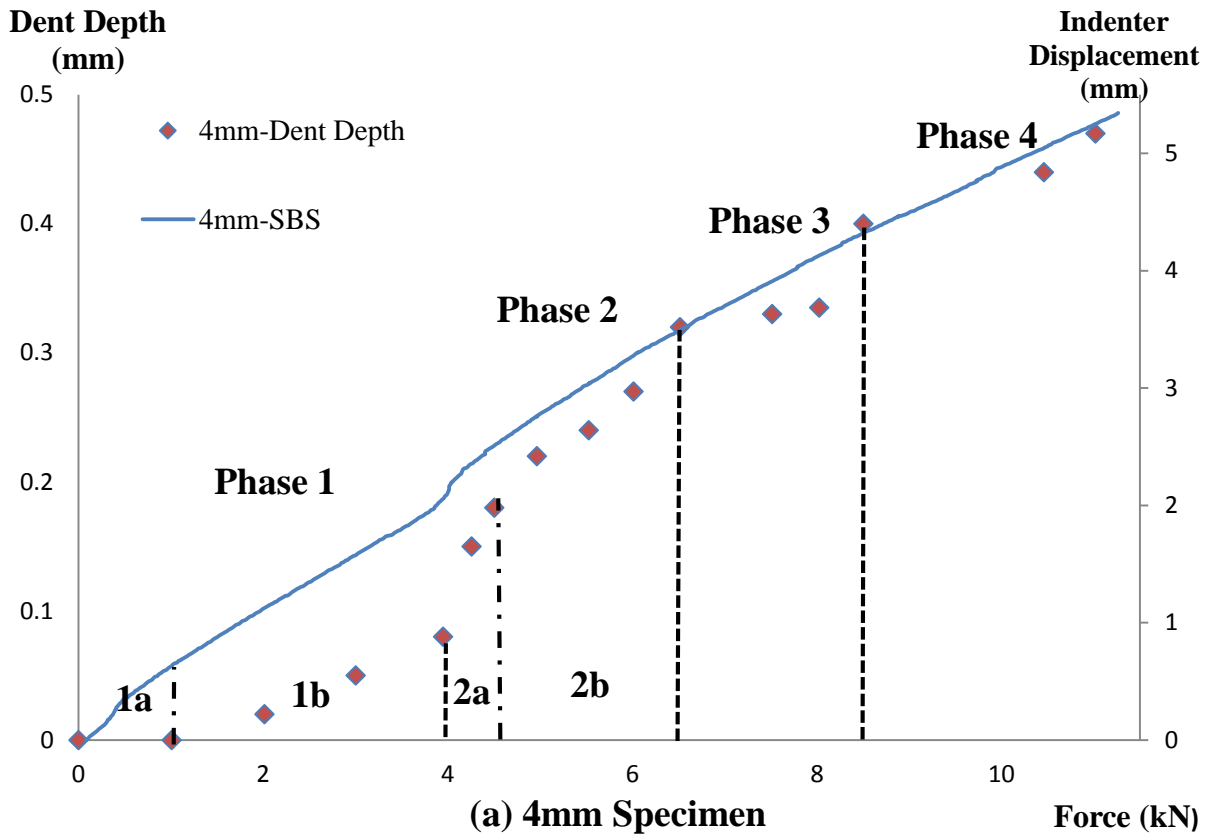


Figure 7.3 Damage process assumption for (a) 4mm and (b) 2mm specimens.

The local damage phase is divided into two sub-phases representing the delamination initiation (as Phase 2a) and the delamination propagation (as Phase 2b). If the contact load is over the DTL, the delamination is initiated in the composite laminates. The local stiffness is significantly reduced due to the delamination initiation, which explains the sharp increase in the dent depth in Phase 2a. It is however worth mentioning that the initial delamination only exists in a local area under the indentation position based on the internal damage characterisation results presented in Section 6.3. The overall material performance is not significantly degraded by referring to the 10% reduction in the residual strength presented in Section 6.2. Moreover, the damage tolerance capacity is improved due to the additional energy absorption mechanisms from the delamination opening and the improved laminates flexibility. As a result, the propagation of the initial delamination does not exhibit the behaviour of brittle material. The initial delamination experiences a stable growth as shown in Phase 2b, in which the initial delamination extends to a global level under the increased loads. This finding indicates that the carbon fibre epoxy composite material cannot be simply regarded as a complete brittle material. The plasticity of the matrix material and the existence of the initial delamination also affect the damage mechanism of such material.

The accumulative damages from the first two damage phases finally reduce the stiffness of the laminates to a certain level, which triggers the plastic deformation of the laminates during the global damage phase (as Phase 3). This assumption may seem like in contradiction to the typical behaviour of the brittle material. But the global permanent deformation of the damaged laminates is proved by the back-surface displacement measurement in Section 6.1.6. Moreover, the internal damage observation results in Section 6.3 provide more supporting evidence for the existence of the global permanent deformation. The wide spread matrix cracks and delaminations make the original brittle matrix system to be more flexible. The plastic deformation of the laminates acts as another energy absorption mechanism in addition to the elastic deformation and other damage mechanisms during the global damage phase. Finally, severe damages such as serious delamination and fibre breakage are introduced into the laminates during the final failure phase (as Phase 4). As a result, the composite laminates loses most of its load bearing capacity as proved by the CAI test result presented in Section 6.2.

Figure 7.3(b) shows a similar damage process for the 2mm composite laminates. Because the effect of delamination initiation is less significant in the damage process of the thin specimen, the damage process is divided into the no-dent, combined damage, and final failure phases.

It is found that the 2mm thin laminates experiences the same no-dent damage sub-phase as occurred in the damage process of the 4mm thick laminates when the contact stress is lower than the yield strength of the matrix material. It is however noticed that elastic deformation is more dominant in energy absorption in the thin laminates compared with that of the thick laminates, which makes the effect of delamination initiation on contact response of the thin laminates less significant. The second damage phase of the thin laminate is a complicated damage phase during which interactions among the elastic deformation, plastic deformation, and other damage mechanisms occur. It is difficult to separate damage initiation and damage propagation for the thin laminates with the indentation curve. The 2mm laminates shares the same final failure damage phase with the 4mm laminates, during which fibre breakage and severe delamination are introduced into the laminates.

In conclusion, the damage process of composite laminates should not be regarded as a simple process with instant damage initiation and subsequent rapid damage propagation, which only occurs in an ideal brittle material system. The damage process of composite laminate is influenced by multiple mechanisms, including the material elasticity and plasticity. The damage process assumption as proposed in this project has great potential to improve the efficiency and accuracy of both the analytical prediction and the structural health monitoring for damages in composite laminates under a low-velocity impact. Different material degradation factors can be used in the analytical contact model corresponding to different damage statuses, which will improve the accuracy of the current analytical prediction. Meanwhile, a dent depth based internal damage monitoring technique can be developed on the basis of the damage process assumption proposed in this project.

CHAPTER 8 Conclusions and Recommended Work

This PhD project aims to develop further knowledge on the impact response and damage mechanisms of composite laminates under low-velocity impact, and to explore the feasibility of assessing the internal damage with a visually inspectable parameter. This chapter summarises the main conclusions derived from the systematic experimental, numerical, and analytical investigations conducted in this project. Further work is recommended to continue the research associated with this project.

8.1 Conclusions

The damage mechanism and impact response of composite laminates under low-velocity impact have been investigated experimentally and numerically. Delamination, as a dominant damage mode, and delamination threshold load, as a key parameter to characterise the low-velocity impact damage resistance of composite laminates, were particularly focused in this project. The following conclusions can be derived from the LVI related investigation results:

- The effect of the delamination initiation on the impact response of the thin laminate is less significant than that of the thick laminates. Most of the impact energy is dissipated through elastic deformation rather than by being absorbed by the damage mechanism due to the structural flexibility of the thin laminates.
- The existence of DTL is clearly shown on the impact force history of the thick specimen, while the sudden load drop phenomenon is not obvious in the impact force history of the thin specimen. The results also suggest that there is a suitable range of ratio of the impact energy to the laminates stiffness/thickness to determine the DTL value reliably via the impact force history.
- The correlation between the impact force histories of the first impact and the repeated impact under the same energy is strongly affected by the existence of the initial delamination. The repeated impact force history differs from the first impact force history by showing a smoother impact force curve and a higher peak force, if the delamination is initiated by the first impact. The impact force history under repeated impact is otherwise identical to those of the first impact if no delamination is initiated during the first impact.

- The repeated impact test can be used as an alternative approach to determine the upper limit of the delamination threshold load, for the case when the sudden load drop is not clear from the impact force history in the first impact.
- The composite laminates used in the current project demonstrates good damage tolerance capacity referring to the smoother impact force history and the higher peak force when the laminate is under repeated impact.
- The existence of multiple initial delaminations acts as an additional source of impact energy absorption and hence has the potential to improve the damage tolerance capacity of the composite laminates under a repeated impact. The opening area at the tip of the delamination may not only absorb a certain amount of the impact energy but can also reduce the stress concentration.
- The simulation strategy employing the ABD matrix is capable of simulating the structural behaviour of composite laminates subjected to low-velocity impact before any damage is introduced into the laminates.
- The simulation strategy employing the progressive damage model and the tie-break contact/cohesive element shows great potential in simulating the interlaminar and intralaminar damages and the damage induced material degradation of composite laminates. The simulation result is highly sensitive to the model setup and some parameters need to be carefully defined and calibrated by trial and error.

The feasibility of assessing the internal damage with a visually inspectable parameter has also been explored by a series of experimental, numerical, and analytical investigations. The quasi-static indentation was used to represent the low-velocity impact in order to achieve more reliable control of the contact event. The internal damage has been successfully linked to the dent depth via the QSI force. The following conclusions can be drawn from the QSI related investigation results:

- The low-velocity impact damage of a composite laminates including the delamination initiation, initial fibre breakage and final failure can be studied with the QSI test result.
- The DTL can be determined from the curve of the indentation force against the displacement of the indenter based on the knee point phenomenon. The initial fibre breakage and the final failure are related to the transient load dip and the ultimate load drop on the indentation load curve, respectively.

- The dent depth can be used as a visually inspectable parameter to monitor the internal damage of a composite laminates. Based on the differences in the increase rate of the dent depth, the contact process of a composite laminates can be separated into a number of phases corresponding to different damage status of the laminates.
- The effect of damage initiation and propagation on the contact response of composite laminate is dependent on the thickness/stiffness of the laminates. The damage status of the thick laminate is divided into the no-damage, local damage, global damage, and final failure. The damage status of the thin laminate is divided into the no-dent, combined damage, and final failure.
- The plastic deformation of composite laminate is shown to be an important energy absorption mechanism in addition to the elastic deformation and damage mechanisms. The plastic deformation is introduced into the damaged composite laminates when the laminates stiffness is reduced to a critical level due to the accumulation of damage.
- The residual strength of the indented/impacted composite laminate is a direct indication of the damage status. No significant reduction in the residual strength is found until delamination is initiated. The initial delamination causes about 10% reduction in the residual strength, which is further reduced to 45% with the damage propagation.
- The internal damage, in terms of the damage modes and damage distribution, can also be related to the damage status. The matrix crack, as a small discontinuity in the resin with 2-3 microns in width (opening), distributes inside the lamina. The delamination distributes at the interface between adjacent laminas with a width greater than 5 microns. The initial delamination is propagated from a local area to a global area with its opening increased from 5-7 microns to around 30-40 microns.
- Numerical and analytical predictions, which are obtained with the elastoplastic response based contact model, show great potential in correlating the dent depth to the contact force. However, the elastoplastic response based contact model needs to be further developed by considering strain hardening/softening of the stress-strain curve of the matrix material, the fibre reinforcement effect on the material behaviour in the transverse direction, and the effect of damage on the model behaviour.

Among the conclusions listed above, there are three key findings that need to be highlighted:

- 1. The ratio between the impact energy and the laminates stiffness/thickness may affect the reliable determination of the DTL value via the impact force history.** The DTL phenomenon, as the sudden load drop in the impact force history, may not be detectable in the case of thin specimens or thick specimens under high energy impact. For the thin specimens, the elastic deformation is the dominant energy dissipation mechanism due to the structural flexibility of the specimens. As a result, the delamination is not easily initiated under low energy impact. Under high energy impact, severe damage (*e.g.* delamination propagation and fibre breakage) is introduced into the specimen immediately after the delamination initiation, which might eliminate the load drop phenomenon. The behaviour of thick specimens under high energy impact is similar to that of thin specimens under high energy impact. The repeated impact test can be used as an alternative approach to determine the upper limit of the DTL when the load drop phenomenon is not clear from the impact force history.
- 2. The potential menace of the delamination initiation is overestimated.** The composite laminates demonstrate good damage tolerance capacity under low-velocity impact when the energy level is not too high. This observation is explained by the fact that the existence of the initial delamination provides additional energy absorption mechanisms by improving the flexibility of the laminates and the requirement of the opening process for the delamination to propagate. As a result, the delaminated composite is capable of resisting further propagation of the existing delamination, unless the repeated impact energy is too high. The CAI test result showing that residual compressive strength of composite laminates with the initial delamination is only reduced by 10-15% is further proof that the severity of delamination initiation may not be as high as has been reported in the literature. Damage resistance and damage tolerance of composite laminates are two independent concepts and need to be characterised carefully. The effect of delamination initiation on structural performance of composite structures should be re-examined, and not just treated as a severe potential menace to structural integrity with an over-conservative design philosophy.
- 3. The damage process of composite laminates can be divided into different damage phases based on the difference in the increasing rate of dent depth.** The damage process is affected by multiple mechanisms. For thick laminates, the delamination initiation and the subsequent delamination growth and plastic

deformation are the main mechanisms absorbing the impact energy. The damage process can be divided into no-damage, local damage, global damage, and final failure damage phases. For thin laminates, the effect of elastic deformation is more significant in energy absorption compared with the effect of delamination initiation. As a result, the damage process can be divided into the no-dent, combined damage, and final failure phases. The result of the study has demonstrated that the dent depth is closely related to the damage status of composite laminates. The internal damage can therefore be assessed with this visually inspectable parameter, which has great potential for the structural health monitoring of damage in composite laminates under low-velocity impact.

8.2 Recommended Work

Damage characterisation of composite laminates under low-velocity impact is a complex engineering problem and proves to be a big challenge to the industry. While much effort has been made in the project to improve the knowledge in this field, there are still many areas that need to be investigated further. The following work is recommended for future research associated with this project:

1. The experimental investigation could be extended to consider the difference in composite material system, support condition, impactor weight and shape. This is to validate the universality of the results achieved from the current study in terms of the damage mechanisms and impact response of composite laminates under low-velocity impact.
2. In the internal damage characterisation part, the C-scan and thermal deply techniques could be involved to further characterise the internal damage. The C-scan result can provide detailed information on the damaged area and width while the thermal deply technique can provide further information on the damage distribution and specific damage mode such as fibre breakage.
3. Numerical simulation could be further conducted, especially for the simulation employing advanced modelling strategy and include the damage based material model and the tie-break contact/cohesive element, both of which can be further developed to improve the model setup and simulation accuracy and efficiency.

4. The contact model used in the analytical prediction could be further modified by considering the effect of the plate plastic deformation and the proposed damage process assumption.
5. An engineering applicable internal damage monitoring technique, which is based on the relation between the internal damage status and a visually inspectable parameter, could be developed based on the results obtained from the project.

References

- [1] A. B. Strong, *History of Composite Materials - Opportunities and Necessities*, Brigham Young University, 2002.
- [2] AIRBUS, *A350 XWB Launch Press Conference*, 2006.
- [3] Boeing, *787 Dreamliner: Program Fact Sheet*, 2012, Available from: <http://www.boeing.com/boeing/commercial/787family/programfacts.page>.
- [4] S. Abrate, *Impact on Composite Structures*, Cambridge University Press, 1998.
- [5] A. K. Kaw, *Mechanics of Composite Materials*, Taylor & Francis Group, LLC, 2006.
- [6] V. V. Vasiliev and E. V. Morozov, *Mechanics and Analysis of Composite Materials*, Elsevier Science Ltd, 2001.
- [7] D. Hull and T. W. Clyne, *An Introduction to Composite Materials*, Cambridge University Press, 1996.
- [8] A. R. Bunsell and J. Renard, *Fundamentals of Fibre Reinforced Composite Materials*, Taylor & Francis, 2005.
- [9] B. Harris, *Engineering Composite Materials*, Maney Materials Science, 1999.
- [10] G. A. O. Davies and X. Zhang, "Impact damage prediction in carbon composite structures," *International Journal of Impact Engineering*, vol. 16, pp. 149-170, 1995.
- [11] X. Zhang, "Impact damage in composite aircraft structures - experimental testing and numerical simulation," *Journal of Aerospace Engineering*, vol. 212, pp. 245-259, 1998.
- [12] X. Zhang, F. Bianchi, and H. Q. Liu, "Predicting low-velocity impact damage in composites using a cohesive fracture model," *Aeronautical Journal*, vol. 116, pp. 1367-1381, 2012.
- [13] R. Olsson, M. V. Donadon, and B. G. Falzon, "Delamination threshold load for dynamic impact on plates," *International Journal of Solids and Structures*, vol. 43, pp. 3124-3141, 2006.
- [14] G. A. Schoeppner and S. Abrate, "Delamination threshold loads for low velocity impact on composite laminates," *Composites Part A: Applied Science and Manufacturing*, vol. 31, pp. 903-915, 2000.
- [15] G. H. Staab, *Laminar Composites*, Butterworth-Heinemann Press, 1999.

-
- [16] M. F. Ashby, S. F. Bush, N. Swindells, R. Bullough, et al., "Technology of the 1990s: advanced materials and predictive design," *Philosophical Transactions of the Royal Society of London*, vol. 322, pp. 393-407, 1987.
- [17] E. J. Barbero, *Introduction to Composite Materials Design*, Taylor and Francis Group, 2011.
- [18] P. K. Mallick, *Fiber Reinforced Composites Materials Manufacturing and Design*, Taylor & Francis Group, LLC., 2007.
- [19] F. C. Campbell, *Manufacturing Processes for Advanced Composites*, New York: Elsevier, 2003.
- [20] P. D. Soden, M. J. Hinton, and A. S. Kaddour, "Lamina properties, lay-up configurations and loading conditions for a range of fibre-reinforced composite laminates," *Composites Science and Technology*, vol. 58, pp. 1011-1022, 1998.
- [21] L. J. Hart-Smith, "The ten-percent rule for preliminary sizing of fibrous composite structures," in *51st SAWE Annual Conference*, Hartford, Connecticut, 1992.
- [22] L. J. Hart-Smith, "Expanding the capabilities of the ten-percent rule for predicting the strength of fibre-polymer composites," *Composites Science and Technology*, vol. 62, pp. 1515-1544, 2002.
- [23] L. J. Hart-Smith, "Comparison between theories and test data concerning the strength of various fibre-polymer composites," *Composites Science and Technology*, vol. 62, pp. 1591-1618, 2002.
- [24] W. J. Cantwell and J. Morton, "The impact resistance of composite materials - a review," *Composites*, vol. 22, pp. 347-362, 1991.
- [25] P. O. Sjoblom, J. T. Hartness, and T. M. Cordell, "On low-velocity impact testing of composite materials," *Journal of Composite Materials*, vol. 22, pp. 30-52, 1988.
- [26] K. N. Shivakumar, W. Elber, and W. Illg, "Prediction of low-velocity impact damage in thin circular laminates.," *AIAA Journal*, vol. 23, pp. 442-449, 1985.
- [27] P. Robinson and G. A. O. Davies, "Impactor mass and specimen geometry effects in low velocity impact of laminated composites," *International Journal of Impact Engineering*, vol. 12, pp. 189-207, 1992.
- [28] S. P. Joshi and C. T. Sun, "Impact induced fracture in a laminated composite," *Journal of Composite Materials*, vol. 19, pp. 51-66, 1985.
- [29] D. Liu and L. E. Malvern, "Matrix cracking in impacted glass/epoxy plates," *Journal of Composite Materials*, vol. 21, pp. 594-609, 1987.

- [30] W. J. Cantwell and J. Morton, "Detection of impact damage in CFRP laminates," *Composite Structures*, vol. 3, pp. 241-257, 1985.
- [31] D. Delfosse, G. Pageau, R. Bennett, and A. Poursartip, "Instrumented impact testing at high velocities," *Journal of Composites Technology & Research*, vol. 15, pp. 38-45, 1993.
- [32] S. T. Jenq, H. S. Jing, and C. Chung, "Predicting the ballistic limit for plain woven glass/epoxy composite laminate," *International Journal of Impact Engineering*, vol. 15, pp. 451-464, 1994.
- [33] Y. Aoki, H. Samejima, H. Suemasu, and Y. Nagao, *Effect of Thickness on Impact Damage and CAI Behavior*, Tokyo.
- [34] E. Sevkat, B. Liaw, F. Delale, and B. B. Raju, "Drop-weight impact of plain-woven hybrid glass-graphite/toughened epoxy composites," *Composites Part A: Applied Science and Manufacturing*, vol. 40, pp. 1090-1110, 2009.
- [35] R. Hosseinzadeh, M. M. Shokrieh, and L. Lessard, "Damage behavior of fiber reinforced composite plates subjected to drop weight impacts," *Composites Science and Technology*, vol. 66, pp. 61-68, 2006.
- [36] L. S. Kistler and A. M. Waas, "Experiment and analysis on the response of curved laminated composite panels subjected to low velocity impact," *International Journal of Impact Engineering*, vol. 21, pp. 711-736, 1998.
- [37] M. A. Perez, X. Martinez, S. Oller, L. Gil, et al., "Impact damage prediction in carbon fibre-reinforced laminated composite using the matrix-reinforced mixing theory," *Composite Structures*, vol. 104, pp. 239-248, 2013.
- [38] X. Zhang, L. Hounslow, and M. Grassi, "Improvement of low-velocity impact and compression-after-impact performance by z-fibre pinning," *Composites Science and Technology*, vol. 66, pp. 2785-2794, 2006.
- [39] S. Heimbs, S. Heller, P. Middendorf, F. Hähnel, et al., "Low velocity impact on CFRP plates with compressive preload: test and modelling," *International Journal of Impact Engineering*, vol. 36, pp. 1182-1193, 2009.
- [40] G. Zhou, "The use of experimentally-determined impact force as a damage measure in impact damage resistance and tolerance of composite structures," *Composite Structures*, vol. 42, pp. 375-382, 1998.
- [41] T. Mitrevski, I. H. Marshall, R. Thomson, R. Jones, et al., "The effect of impactor shape on the impact response of composite laminates," *Composite Structures*, vol. 67, pp. 139-148, 2005.

- [42] T. Mitrevski, I. H. Marshall, R. Thomson, and R. Jones, "Low-velocity impacts on preload GFRP specimens with various impactor shapes," *Composite Structures*, vol. 76, pp. 209-217, 2006.
- [43] T. Mitrevski, I. H. Marshall, and R. Thomson, "The influence of impactor shape on the damage to composite laminates," *Composite Structures*, vol. 76, pp. 116-122, 2006.
- [44] K. M. Lal, "Low velocity transverse impact behaviour of 8-ply, graphite-epoxy laminates," *Journal of Reinforced Plastics and Composites*, vol. 2, 1983.
- [45] K. M. Lal, "Residual strength assessment of low velocity impact damage of graphite-epoxy laminates," *Journal of Reinforced Plastics and Composites*, vol. 2, 1983.
- [46] R. Olsson, "Modelling of impact damage zone in composite laminates for strength after impact," *Aeronautical Journal*, vol. 116, pp. 1349-1365, 2012.
- [47] M. O. W. Richardson and M. J. Wisheart, "Review of low-velocity impact properties of composite materials," *Composites Part A: Applied Science and Manufacturing*, vol. 27, pp. 1123-1131, 1996.
- [48] D. Liu, "Impact-induced delamination - a view of bending stiffness mismatching," *Journal of Composite Materials*, vol. 22, pp. 674-692, 1988.
- [49] S. M. Lee and P. Zahuta, "Instrumented impact and static indentation of composites," *Journal of Composite Materials*, vol. 25, pp. 204-222, 1991.
- [50] H. Y. Choi, H. Y. T. Wu, and F. K. Chang, "A new approach towards understanding damage mechanisms and mechanics of laminated composites due to low-velocity impact: part II - analysis," *Journal of Composite Materials*, vol. 25, pp. 1012-1038, 1991.
- [51] C. J. Jih and C. T. Sun, "Prediction of delamination in composite laminates subjected to low velocity impact," *Journal of Composite Materials*, vol. 27, pp. 684-701, 1993.
- [52] S. R. Finn and G. S. Springer, "Delamination in composite plates under transverse static or impact loads - a model," *Composite Structures*, vol. 23, pp. 177-190, 1993.
- [53] W. J. Cantwell and J. Morton, "Geometrical effects in the low velocity impact response of CFRP," *Composite Structures*, vol. 12, pp. 39-59, 1989.
- [54] H. Y. Choi and F. K. Chang, "A model for predicting damage in graphite/epoxy laminated composites resulting from low-velocity point impact," *Journal of Composite Materials*, vol. 26, pp. 2134-2169, 1992.

- [55] G. Dorey, *Impact Damage in Composites - Development, Consequences, and Prevention*, in 6th International Conference on Composite Materials & 2nd European Conference on Composite Materials, Imperial College, London, 1988, pp.3.1-3.26.
- [56] H. M. Wen, "Penetration and perforation of thick FRP laminates," *Composites Science and Technology*, vol. 61, pp. 1163-1172, 2001.
- [57] F. Erdogan and G. C. Sih, "On the crack extension in plane loading and transverse shear," *Journal of Basic Engineering*, vol. 85, pp. 519-527, 1963.
- [58] M. E. Waddoups, "Characterization and design of composite materials," *Composite Materials Workshop*, vol. pp. 254-308, 1968.
- [59] R. Hill, *The Mathematical Theory of Plasticity*, Oxford University Press, 1950.
- [60] O. Hoffman, "The brittle strength of orthotropic materials," *Journal of Composite Materials*, vol. 1, pp. 200-206, 1967.
- [61] S. W. Tsai and E. M. Wu, "A general theory of strength for anisotropic materials," *Journal of Composite Materials*, vol. 5, pp. 58-80, 1971.
- [62] R. B. Pipes and B. W. Cole, "On the off-axis strength test for anisotropic materials," *Journal of Composite Materials*, vol. 7, pp. 246-256, 1973.
- [63] Z. Hashin, "Failure criteria for unidirectional fibre composites," *Journal of Applied Mechanics*, vol. 47, pp. 329-334, 1980.
- [64] C. G. Davila, P. P. Camanho, and C. A. Rose, "Failure criteria for FRP laminates," *Journal of Composite Materials*, vol. 39, pp. 323-345, 2005.
- [65] A. Puck and H. Schurmann, "Failure analysis of FRP laminates by means of physically based phenomenological models," *Composites Science and Technology*, vol. 58, pp. 1045-1067, 1998.
- [66] F. K. Chang and K. Y. Chang, "A progressive damage model for laminated composites containing stress concentrations," *Journal of Composite Materials*, vol. 21, pp. 834-855, 1987.
- [67] Y. G. Xu, Z. Shen, W. Tiu, Y. Z. Xu, et al., "Delamination threshold load of composite laminates under low-velocity impact," *Key Engineering Materials*, vol. 525-526, pp. 521-524, 2013.
- [68] D. Liu, *Delamination in Stitched and Nonstitched Composite Plates subjected to Low Velocity Impact*, in Proceeding of the American Society for Composites, 2nd Technical Conference, Newark, DE, 1987, pp.147-155.
- [69] W. J. Cantwell and J. Morton, "Comparison of the low and high velocity impact response of CFRP," *Composites*, vol. 20, pp. 545-551, 1989.

- [70] W. J. Cantwell and J. Morton, "The influence of varying projectile mass on the impact response of CFRP," *Composite Structures*, vol. 13, 1989.
- [71] G. A. O. Davies, D. Hitchings, and G. Zhou, "Impact damage and residual strengths of woven fabric glass/polyster lamiantes," *Composites Part A: Applied Science and Manufacturing*, vol. 27, pp. 1147-1156, 1996.
- [72] R. Olsson, "Mass criterion for wave controlled impact response of composite plates," *Composites Part A: Applied Science and Manufacturing*, vol. 31, pp. 879-887, 2000.
- [73] R. Olsson, "Analytical model for delamination growth during small mass impact on plates," *International Journal of Solids and Structures*, vol. 47, pp. 2884-2892, 2010.
- [74] R. Olsson, "Analytical prediction of large mass impact damage in composite laminates," *Composites Part A: Applied Science and Manufacturing*, vol. 32, pp. 1207-1215, 2001.
- [75] P. O. Sjoblom, *Simple Design Approach against Low Velocity Impact Damage*, in Proceedings of 32nd SAMPE Symposium, Anaheim, CA, 1987, pp.529-539.
- [76] E. V. Gonzalez, P. Maimí, P. P. Camanho, C. S. Lopes, et al., "Effect of ply clustering in laminated composite plates under low-velocity impact loading," *Composites Science and Technology*, vol. 71, pp. 805-817, 2011.
- [77] T. E. Tay, "Characterisation and analysis of delamination fracture in composites: an overview of developments from 1990 to 2001," *Applied Mechanics Reviews*, vol. 56, pp. 1-32, 2003.
- [78] R. Borg, L. Nilsson, and K. Simonsson, "Simulation of delamination in fibre composites with a discrete cohesive failure model," *Composites Science and Technology*, vol. 61, pp. 667-677, 2001.
- [79] T. K. O'Brien, *Characterization, Analysis and Prediction of Delamination in Composites using Fracture Mechanics*, in ICF10, Honolulu, USA, 2013.
- [80] A. Hillerborg, M. Modeer, and P. E. Petersson, "Analysis of crack formation and crack growth in concrete by means of fracture mechanics and finite elements," *Coment and Concrete Research*, vol. 6, pp. 773-781, 1976.
- [81] F. Dogan, H. Hadavinia, T. Donchev, and P. S. Bhonge, "Delamination of impacted composite structures by cohesive zone interface element and tiebreak contact," *Central European Journal of Engineering*, vol. 2, pp. 612-626, 2012.
- [82] C. Shet and N. Chandra, "Analysis of energy balance when using cohesive zone models to simulate fracture processes," *Journal of Engineering Materials and Technology*, vol. 124, pp. 440-450, 2002.

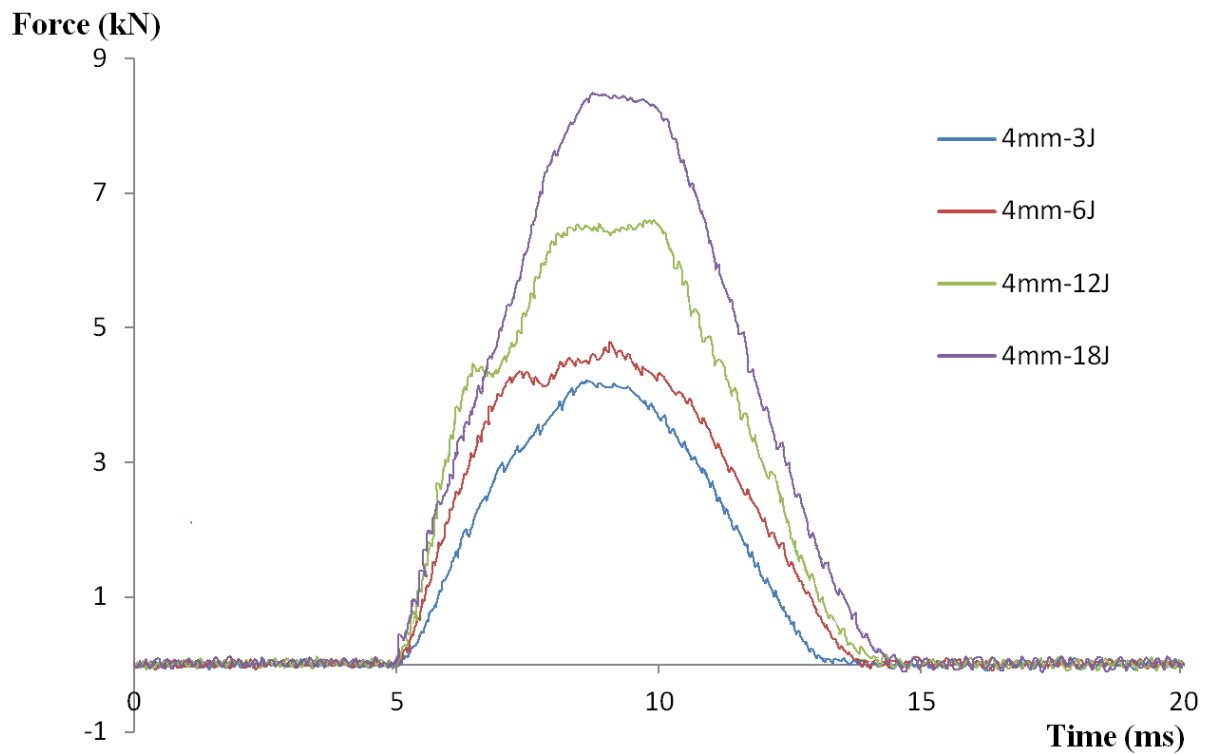
- [83] J. G. Williams and H. Hadavinia, "Analytical solutions for cohesive zone models," *Journal of the Mechanics and Physics of Solids*, vol. 50, pp. 809-825, 2002.
- [84] R. Borg, L. Nilsson, and K. Simonsson, "Simulation of low velocity impact on fibre laminates using a cohesive zone based delamination model," *Composites Science and Technology*, vol. 64, pp. 279-288, 2004.
- [85] F. Aymerich, F. Dore, and P. Priolo, "Simulation of multiple delaminations in impacted cross-ply laminates using a finite element model based on cohesive interface elements," *Composites Science and Technology*, vol. 69, pp. 1699-1709, 2009.
- [86] G. T. Camacho and M. Ortiz, "Computational modelling of impact damage in brittle materials," *International Journal of Solids and Structures*, vol. 33, pp. 2899-2938, 1996.
- [87] A. M. Elmarakbi, N. Hu, and H. Fukunaga, "Finite element simulation of delamination growth in composite materials using LS-DYNA," *Composites Science and Technology*, vol. 69, pp. 2383-2391, 2009.
- [88] M. F. S. F. De Moura, J. P. M. Goncalves, J. A. G. Chousal, and R. D. S. G. Campilho, "Cohesive and continuum mixed-mode damage models applied to the simulation of the mechanical behaviour of bonded joints," *International Journal of Adhesion & Adhesives* vol. 28, pp. 419-426, 2008.
- [89] B. R. K. Blackman, H. Hadavinia, A. J. Kinloch, and J. G. Williams, "The use of a cohesive zone model to study the fracture of fibre composites and adhesively-bonded joints," *international Journal of Fracture*, vol. 119, pp. 25-46, 2003.
- [90] A. Needleman, "A continuum model for void nucleation by inclusion debonding," *Journal of Applied Mechanics*, vol. 54, pp. 525-531, 1987.
- [91] P. H. Geubelle and J. S. Baylor, "Impact-induced delamination of composites: a 2D simulation," *Composites Part B: Engineering*, vol. 29, pp. 589-602, 1998.
- [92] E. F. Rybicki and M. F. Kanninen, "A finite element calculation of stress intensity factors by a modified crack closure integral.," *Engineering Fracture Mechanics*, vol. 9, pp. 931-938, 1977.
- [93] R. Krueger, "Virtual crack closure technique: history, approach, and applications," *Applied Mechanics Reviews*, vol. 57, pp. 109-143, 2004.
- [94] J. R. Reeder, K. Demarco, and K. S. Whitley, *The use of Doublers in Delamination Toughness Testing*, in The American Society for Composites 17th Technical Conference, Purdue University, West Lafayette, IN, 2002.

- [95] B. R. K. Blackman and A. J. Kinloch, *Protocol for the Determination of the Mode I Adhesive Fracture Energy (GIC) of Structure Adhesives using the Double Cantilever Beam (DCB) and Tapered Double Cantilever Beam (TDCB) Specimens*.
- [96] T. K. O'Brien, W. M. Johnston, and G. J. Toland, *Mode II Interlaminar Fracture Toughness and Fatigue Characterization of a Graphite Epoxy Composite Material*, NASA Center for AeroSpace Information, 2010.
- [97] G. C. Tsai, *Design of Composite ENF Specimens and Conduct Three-point Test to Calculate Mode II Fracture Toughness*, in 9th International Conference on Engineering Education, San Juan, PR, 2006.
- [98] J. L. Wang and P. Z. Qiao, "Novel beam analysis of end notched flexure specimen for Mode-II fracture," *Engineering Fracture Mechanics*, vol. 71, pp. 219-231, 2004.
- [99] M. L. Benzeggagh and M. Kenane, "Measurement of mixed-mode delamination fracture toughness of unidirectional glass/epoxy composites with mixed-mode bending apparatus," *Composites Science and Technology*, vol. 56, pp. 439-449, 1996.
- [100] A. B. De Morais, A. B. Pereira, M. F. S. F. De Moura, and A. G. Magalhaes, "Mode III interlaminar fracture of carbon/epoxy laminates using the edge crack torsion (ECT) test," *Composites Science and Technology*, vol. 69, pp. 670-676, 2009.
- [101] J. G. Ratcliffe, *Characterization of the Edge Crack Torsion (ECT) Test for Mode III Fracture Toughness Measurement of Laminated Composites*, NASA/Technical Memorandum, 2004.
- [102] H. Hadavinia, F. Dogan, A. M. Elmarakbi, and S. M. R. Khalili, "Modelling of low velocity impact of laminated composite structures," *International Journal of Vehicle Structures & Systems*, vol. 3, pp. 96-106, 2011.
- [103] S. Heimbs, S. Heller, and P. Middendorf, *Simulation of Low Velocity Impact on Composite Plates with Compressive Preload*, in LS-DYNA Anwender Forum, Bamberg, 2008.
- [104] H. Kaczmarek and S. Maison, "Comparative ultrasonic analysis of damage in CFRP under static indentation and low-velocity impact," *Composites Science and Technology*, vol. 51, pp. 11-26, 1994.
- [105] A. T. Nettles and M. J. Douglas, *A Comparison of Quasi-static Indentation to Low-velocity Impact*, NASA, 2000.
- [106] S. Abrate, "Modeling of impacts on composite structures," *Composite Structures*, vol. 51, pp. 129-138, 2001.

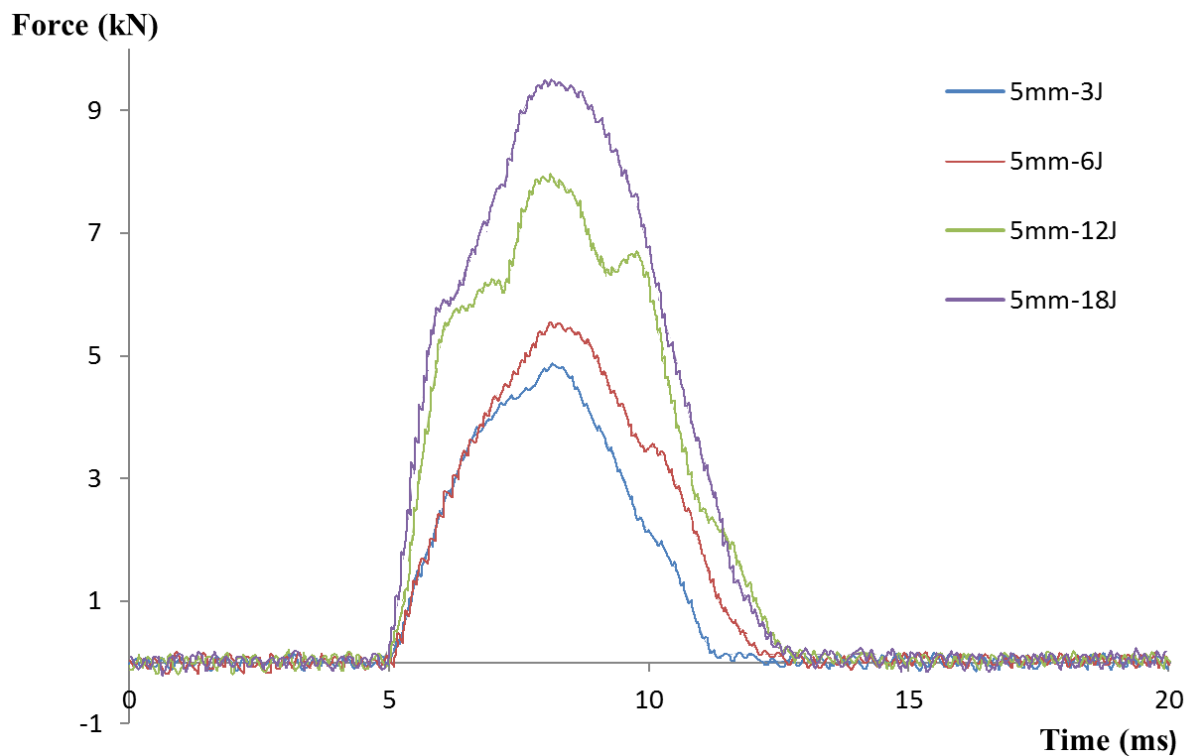
- [107] C. T. Lim, V. P. W. Shim, and Y. H. Ng, "Finite-element modeling of the ballistic impact of fabric armor," *International Journal of Impact Engineering*, vol. 28, pp. 13-31, 2003.
- [108] K. N. Shivakumar, W. Elber, and W. Illg, "Prediction of impact force and duration during low velocity impact on circular composite laminates," *Journal of Applied Mechanics*, vol. 52, pp. 674-80, 1985.
- [109] A. Brindle and X. Zhang, "Predicting compression-after-impact performance of carbon fibre composites based on impact response," in *International Conference on Composite Materials*, Edinburgh, UK, 2009.
- [110] L. Yan, X. F. An, and X. S. Yi, "Comparison with low-velocity impact and quasi-static indentation testing of foam core sandwich composites," *International Journal of Applied Physics and Mathematics*, vol. 2, pp. 58-62, 2012.
- [111] P. H. Chen, Z. Shen, J. J. Xiong, S. C. Yang, et al., "Failure mechanisms of laminated composites subjected to static indentation," *Composite Structures*, vol. 75, pp. 489-495, 2006.
- [112] H. R. Hertz, "Über die berührung fester elastischer körper," *Journal für die reine und angewandte Mathematik*, vol. 92, pp. 156-171, 1881.
- [113] S. H. Yang and C. T. Sun, *Indentation Law for Composite Laminates*, NASA, 1981.
- [114] J. R. Turner, "Contact on a transversely isotropic half-space, or between two transversely isotropic bodies," *International Journal of Solids and Structures*, vol. 16, pp. 409-419, 1980.
- [115] P. H. Chen, J. J. Xiong, and Z. Shen, "Thickness effect on the contact behavior of a composite laminate indented by a rigid sphere," *Mechanics of Materials*, vol. 40, pp. 183-194, 2008.
- [116] ASTM, "ASTM D3039-07 standard test method for tensile properties of polymer matrix composite materials," West Conshohocken, PA, USA, 2007.
- [117] ASTM, "ASTM D3846-02 standard test method for in-plane shear strength of reinforced plastics," West Conshohocken, PA, USA, 2002.
- [118] ASTM, "ASTM D3518-01 standard test method for in-plane shear response of polymer matrix composite materials by tensile test of a $\pm 45^\circ$ laminate," West Conshohocken, PA, USA, 2001.
- [119] ASTM, "ASTM D7136-05 standard test method for measuring the damage resistance of a fiber-reinforced polymer matrix composite to a drop-weight impact event," West Conshohocken, PA, USA, 2005.

- [120] ASTM, "ASTM D6264-98 standard test method for measuring the damage resistance of a fiber-reinforced polymer-matrix composite to a concentrated quasi-static indentation force," West Conshohocken, PA, USA, 1998.
- [121] ASTM, "ASTM D7137-12 standard test method for compressive residual strength properties of damaged polymer matrix composite plates," West Conshohocken, PA, USA, 2012.
- [122] P. Feraboli, B. Wade, F. Deleo, M. Rassaian, et al., "LS-DYNA MAT54 modeling of the axial crushing of a composite tape sinusoidal specimen," *Composites Part A: Applied Science and Manufacturing*, vol. 42, pp. 1809-1825, 2011.
- [123] D. S. Cairns, "A simple, elasto-plastic contact law for composites," *Journal of Reinforced Plastics and Composites*, vol. 10, pp. 423-433, 1991.
- [124] A. P. Christoforou, "On the contact of a spherical indenter and a thin composite laminate," *Composite Structures*, vol. 26, pp. 77-82, 1993.
- [125] HexPly, *HexPly M21 180°C (350°F) Curing Epoxy Matrix Product Data*, 2010.
- [126] P. Prombut, *Caractérisation de la propagation de délaminage des stratifiés composites multidirectionnels*, Ph.D. thesis, Université de Toulouse, 2007.
- [127] AIRBUS, "UD prepreg lay-up criteria," Airbus Operations Ltd, UK.
- [128] B. Wade, P. Feraboli, and M. Osborne, *Simulating Laminated Composites using LS-DYNA Material Model MAT54 Part I - [0] and [90] Ply Single-element Investigation*, University of Washington: Seattle, WA.
- [129] T. Belytschko and I. S. Yeh, "The splitting pinball method for contact-impact problems," *Computer Methods in Applied Mechanics and Engineering*, vol. 105, pp. 375-393, 1993.
- [130] ASTM, "ASTM D6641-09 standard test method for compressive properties of polymer matrix composite materials using a combined loading compression (CLC) test fixture," West Conshohocken, PA, USA, 2009.

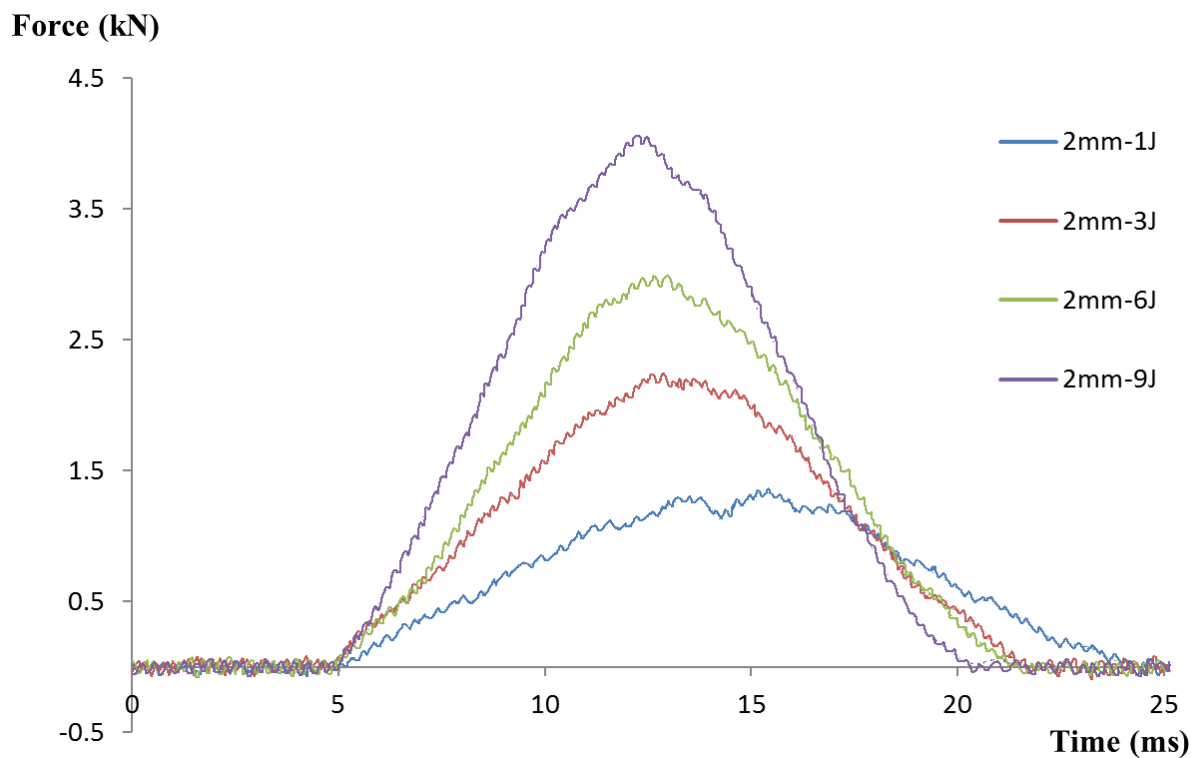
Appendix I Un-filtered Impact Force History



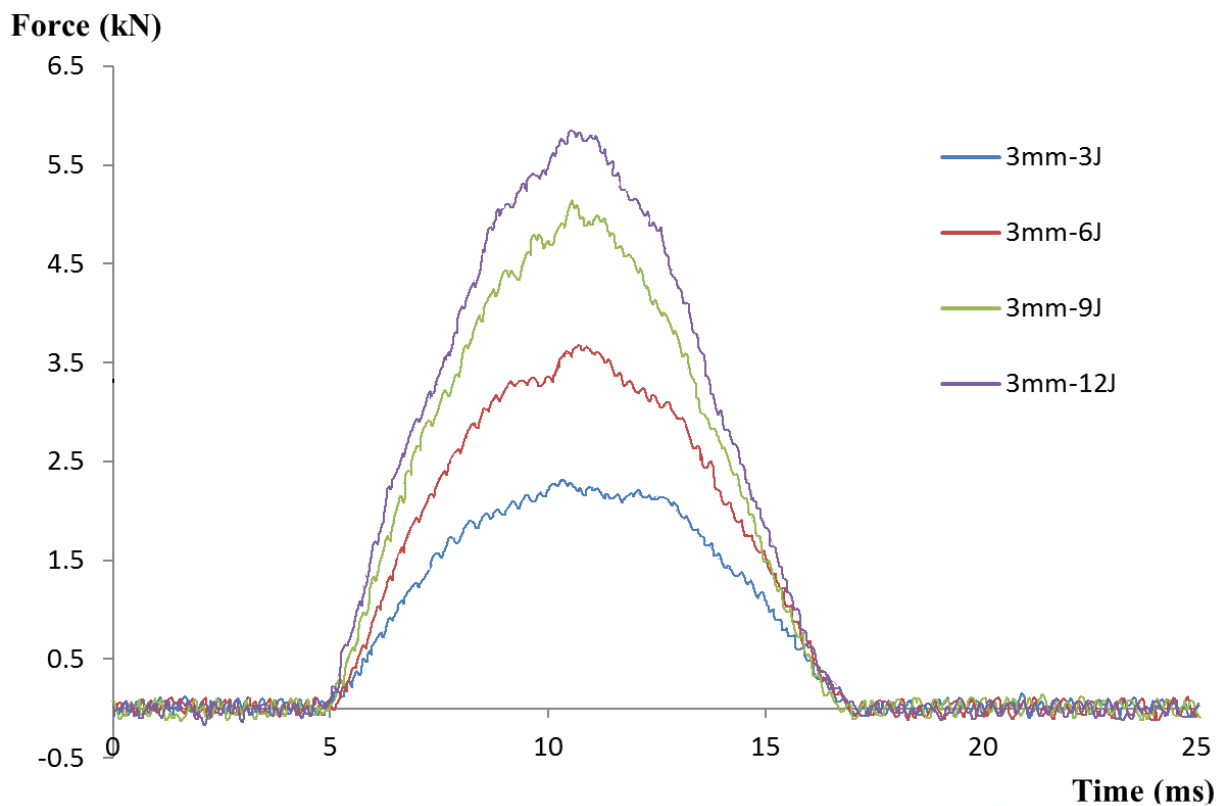
Un-filtered impact force histories of 4mm specimens with cross-ply lay-up configuration.



Un-filtered impact force histories of 5mm specimens with cross-ply lay-up configuration.



Un-filtered impact force histories of 2mm specimens with cross-ply lay-up configuration.



Un-filtered impact force histories of 3mm specimens with cross-ply lay-up configuration.

Appendix II Derivation of ABD Matrix

To determine the ABD matrix, it is necessary to determine the stiffness matrix, $[Q]$, by the engineering elasticity constants of the M21/T700 UD material as shown below

$$E_1 = 131.95\text{GPa}; E_2 = 7.53\text{GPa}; \nu_{12} = 0.253; \nu_{21} = 0.0127; G_{12} = 4.15\text{GPa}.$$

The individual stiffness coefficient, Q_{ij} , is determined by

$$Q_{11} = \frac{E_1}{1-\nu_{21}\nu_{12}} = \frac{131.95}{1-0.0127 \times 0.253} = 132.375\text{GPa}$$

$$Q_{12} = \frac{\nu_{12}E_2}{1-\nu_{21}\nu_{12}} = \frac{0.253 \times 7.53}{1-0.0127 \times 0.253} = 1.911\text{GPa}$$

$$Q_{22} = \frac{E_2}{1-\nu_{21}\nu_{12}} = \frac{7.53}{1-0.0127 \times 0.253} = 7.554\text{GPa}$$

$$Q_{66} = G_{12} = 4.15\text{GPa}$$

Then the new stiffness matrix, $[\bar{Q}]$, is determined for the analysis of an θ angle lamina with an off-axis configuration.

For the 0° lamina, $m = \cos \theta = \cos 0^\circ = 1$, and $n = \sin \theta = \sin 0^\circ = 0$.

The individual stiffness coefficient, \bar{Q}_{ij} , is determined by

$$\bar{Q}_{11} = Q_{11}m^4 + 2(Q_{12} + 2Q_{66})m^2n^2 + Q_{22}n^4 = 132.375\text{GPa}$$

$$\bar{Q}_{12} = (Q_{11} + Q_{22} - 4Q_{66})m^2n^2 + Q_{12}(m^4 + n^4) = 1.911\text{GPa}$$

$$\bar{Q}_{22} = Q_{11}n^4 + 2(Q_{12} + 2Q_{66})m^2n^2 + Q_{22}m^4 = 7.554\text{GPa}$$

$$\bar{Q}_{16} = (Q_{11} - Q_{12} - 2Q_{66})m^3n - (Q_{22} - Q_{12} - 2Q_{66})mn^3 = 0$$

$$\bar{Q}_{26} = (Q_{11} - Q_{12} - 2Q_{66})mn^3 - (Q_{22} - Q_{12} - 2Q_{66})m^3n = 0$$

$$\bar{Q}_{66} = (Q_{11} + Q_{22} - 2Q_{12})m^2n^2 + Q_{66}(m^2 - n^2)^2 = 4.15\text{GPa}$$

For the 90° lamina, $m = \cos \theta = \cos 90^\circ = 0$, and $n = \sin \theta = \sin 90^\circ = 1$.

The individual stiffness coefficient, \bar{Q}_{ij} , is determined by

$$\bar{Q}_{11} = Q_{11}m^4 + 2(Q_{12} + 2Q_{66})m^2n^2 + Q_{22}n^4 = 7.554\text{GPa}$$

$$\bar{Q}_{12} = (Q_{11} + Q_{22} - 4Q_{66})m^2n^2 + Q_{12}(m^4 + n^4) = 1.911\text{GPa}$$

$$\bar{Q}_{22} = Q_{11}n^4 + 2(Q_{12} + 2Q_{66})m^2n^2 + Q_{22}m^4 = 132.375\text{GPa}$$

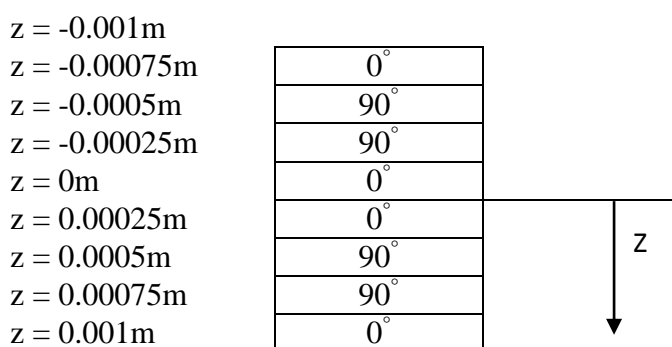
$$\bar{Q}_{16} = (Q_{11} - Q_{12} - 2Q_{66})m^3n - (Q_{22} - Q_{12} - 2Q_{66})mn^3 = 0$$

$$\bar{Q}_{26} = (Q_{11} - Q_{12} - 2Q_{66})mn^3 - (Q_{22} - Q_{12} - 2Q_{66})m^3n = 0$$

$$\bar{Q}_{66} = (Q_{11} + Q_{22} - 2Q_{12})m^2n^2 + Q_{66}(m^2 - n^2)^2 = 4.15\text{GPa}$$

The ABD matrix for each laminates can be determined based on the thickness and lay-up configuration, once the stiffness matrix is determined.

For the 2mm laminates with the lay-up configuration of $[0_2/90_3/0]_s$, the location of each lamina in the coordinate system is shown as:



And the individual coordinate for each lamina is determined as

$$h_0 = -0.001 \quad h_1 = -0.00075 \quad h_2 = -0.0005$$

$$h_3 = -0.00025 \quad h_4 = 0 \quad h_5 = 0.00025$$

$$h_6 = 0.0005 \quad h_7 = 0.00075 \quad h_8 = 0.001$$

The ABD matrix for the $[0_2/90_3/0]_s$ laminate is determined by

$$\begin{bmatrix} N_x \\ N_y \\ N_{xy} \end{bmatrix} = \begin{bmatrix} A_{11} & A_{12} & A_{16} \\ A_{12} & A_{22} & A_{26} \\ A_{16} & A_{26} & A_{66} \end{bmatrix} \begin{bmatrix} \varepsilon_x^0 \\ \varepsilon_y^0 \\ \gamma_{xy}^0 \end{bmatrix} + \begin{bmatrix} B_{11} & B_{12} & B_{16} \\ B_{12} & B_{22} & B_{26} \\ B_{16} & B_{26} & B_{66} \end{bmatrix} \begin{bmatrix} k_x \\ k_y \\ k_{xy} \end{bmatrix}$$

$$\begin{bmatrix} M_x \\ M_y \\ M_{xy} \end{bmatrix} = \begin{bmatrix} B_{11} & B_{12} & B_{16} \\ B_{12} & B_{22} & B_{26} \\ B_{16} & B_{26} & B_{66} \end{bmatrix} \begin{bmatrix} \varepsilon_x^0 \\ \varepsilon_y^0 \\ \gamma_{xy}^0 \end{bmatrix} + \begin{bmatrix} D_{11} & D_{12} & D_{16} \\ D_{12} & D_{22} & D_{26} \\ D_{16} & D_{26} & D_{66} \end{bmatrix} \begin{bmatrix} k_x \\ k_y \\ k_{xy} \end{bmatrix}$$

where,

$$\begin{aligned} [A_{ij}] &= \sum_{k=1}^n [(\bar{Q}_{ij})]_k (h_k - h_{k-1}) \\ &= \begin{bmatrix} 132.375 & 1.911 & 0 \\ 1.911 & 7.554 & 0 \\ 0 & 0 & 4.15 \end{bmatrix} \times (10^9) \times [(-0.00075) - (-0.001)] \\ &+ \begin{bmatrix} 7.554 & 1.911 & 0 \\ 1.911 & 132.375 & 0 \\ 0 & 0 & 4.15 \end{bmatrix} \times (10^9) \times [(-0.0005) - (-0.00075)] \\ &+ \begin{bmatrix} 7.554 & 1.911 & 0 \\ 1.911 & 132.375 & 0 \\ 0 & 0 & 4.15 \end{bmatrix} \times (10^9) \times [(-0.00025) - (-0.0005)] \\ &+ \begin{bmatrix} 132.375 & 1.911 & 0 \\ 1.911 & 7.554 & 0 \\ 0 & 0 & 4.15 \end{bmatrix} \times (10^9) \times [0 - (-0.00025)] \\ &+ \begin{bmatrix} 132.375 & 1.911 & 0 \\ 1.911 & 7.554 & 0 \\ 0 & 0 & 4.15 \end{bmatrix} \times (10^9) \times (0.00025 - 0) \\ &+ \begin{bmatrix} 7.554 & 1.911 & 0 \\ 1.911 & 132.375 & 0 \\ 0 & 0 & 4.15 \end{bmatrix} \times (10^9) \times (0.0005 - 0.00025) \\ &+ \begin{bmatrix} 7.554 & 1.911 & 0 \\ 1.911 & 132.375 & 0 \\ 0 & 0 & 4.15 \end{bmatrix} \times (10^9) \times (0.00075 - 0.0005) \\ &+ \begin{bmatrix} 132.375 & 1.911 & 0 \\ 1.911 & 7.554 & 0 \\ 0 & 0 & 4.15 \end{bmatrix} \times (10^9) \times (0.001 - 0.00075) \\ &= \begin{bmatrix} 1.40 \times 10^8 & 3.82 \times 10^6 & 0 \\ 3.82 \times 10^6 & 1.40 \times 10^8 & 0 \\ 0 & 0 & 8.3 \times 10^6 \end{bmatrix} \text{Pa}\cdot\text{m} \end{aligned}$$

$$\begin{aligned} [B_{ij}] &= \frac{1}{2} \sum_{k=1}^n [(\bar{Q}_{ij})]_k (h_k^2 - h_{k-1}^2) \\ &= \frac{1}{2} \begin{bmatrix} 132.375 & 1.911 & 0 \\ 1.911 & 7.554 & 0 \\ 0 & 0 & 4.15 \end{bmatrix} \times (10^9) \times [(-0.00075)^2 - (-0.001)^2] \end{aligned}$$

$$\begin{aligned}
 & + \frac{1}{2} \begin{bmatrix} 7.554 & 1.911 & 0 \\ 1.911 & 132.375 & 0 \\ 0 & 0 & 4.15 \end{bmatrix} \times (10^9) \times [(-0.0005)^2 - (-0.00075)^2] \\
 & + \frac{1}{2} \begin{bmatrix} 7.554 & 1.911 & 0 \\ 1.911 & 132.375 & 0 \\ 0 & 0 & 4.15 \end{bmatrix} \times (10^9) \times [(-0.00025)^2 - (-0.0005)^2] \\
 & + \frac{1}{2} \begin{bmatrix} 132.375 & 1.911 & 0 \\ 1.911 & 7.554 & 0 \\ 0 & 0 & 4.15 \end{bmatrix} \times (10^9) \times [0^2 - (-0.00025)^2] \\
 & + \frac{1}{2} \begin{bmatrix} 132.375 & 1.911 & 0 \\ 1.911 & 7.554 & 0 \\ 0 & 0 & 4.15 \end{bmatrix} \times (10^9) \times (0.00025^2 - 0^2) \\
 & + \frac{1}{2} \begin{bmatrix} 7.554 & 1.911 & 0 \\ 1.911 & 132.375 & 0 \\ 0 & 0 & 4.15 \end{bmatrix} \times (10^9) \times (0.0005^2 - 0.00025^2) \\
 & + \frac{1}{2} \begin{bmatrix} 7.554 & 1.911 & 0 \\ 1.911 & 132.375 & 0 \\ 0 & 0 & 4.15 \end{bmatrix} \times (10^9) \times (0.00075^2 - 0.0005^2) \\
 & + \frac{1}{2} \begin{bmatrix} 132.375 & 1.911 & 0 \\ 1.911 & 7.554 & 0 \\ 0 & 0 & 4.15 \end{bmatrix} \times (10^9) \times (0.001^2 - 0.00075^2) \\
 & = \begin{bmatrix} 0 & 0 & 0 \\ 0 & 0 & 0 \\ 0 & 0 & 0 \end{bmatrix} \text{Pa}\cdot\text{m}^2
 \end{aligned}$$

$$\begin{aligned}
 [D_{ij}] &= \frac{1}{3} \sum_{k=1}^n [(\bar{Q}_{ij})]_k (h_k^3 - h_{k-1}^3) \\
 &= \frac{1}{3} \begin{bmatrix} 132.375 & 1.911 & 0 \\ 1.911 & 7.554 & 0 \\ 0 & 0 & 4.15 \end{bmatrix} \times (10^9) \times [(-0.00075)^3 - (-0.001)^3] \\
 & + \frac{1}{3} \begin{bmatrix} 7.554 & 1.911 & 0 \\ 1.911 & 132.375 & 0 \\ 0 & 0 & 4.15 \end{bmatrix} \times (10^9) \times [(-0.0005)^3 - (-0.00075)^3] \\
 & + \frac{1}{3} \begin{bmatrix} 7.554 & 1.911 & 0 \\ 1.911 & 132.375 & 0 \\ 0 & 0 & 4.15 \end{bmatrix} \times (10^9) \times [(-0.00025)^3 - (-0.0005)^3] \\
 & + \frac{1}{3} \begin{bmatrix} 132.375 & 1.911 & 0 \\ 1.911 & 7.554 & 0 \\ 0 & 0 & 4.15 \end{bmatrix} \times (10^9) \times [0^3 - (-0.00025)^3]
 \end{aligned}$$

$$\begin{aligned}
 & + \frac{1}{3} \begin{bmatrix} 132.375 & 1.911 & 0 \\ 1.911 & 7.554 & 0 \\ 0 & 0 & 4.15 \end{bmatrix} \times (10^9) \times (0.00025^3 - 0^3) \\
 & + \frac{1}{3} \begin{bmatrix} 7.554 & 1.911 & 0 \\ 1.911 & 132.375 & 0 \\ 0 & 0 & 4.15 \end{bmatrix} \times (10^9) \times (0.0005^3 - 0.00025^3) \\
 & + \frac{1}{3} \begin{bmatrix} 7.554 & 1.911 & 0 \\ 1.911 & 132.375 & 0 \\ 0 & 0 & 4.15 \end{bmatrix} \times (10^9) \times (0.00075^3 - 0.0005^3) \\
 & + \frac{1}{3} \begin{bmatrix} 132.375 & 1.911 & 0 \\ 1.911 & 7.554 & 0 \\ 0 & 0 & 4.15 \end{bmatrix} \times (10^9) \times (0.001^3 - 0.00075^3) \\
 & = \begin{bmatrix} 54.45 & 1.27 & 0 \\ 1.27 & 38.48 & 0 \\ 0 & 0 & 2.77 \end{bmatrix} \text{Pa}\cdot\text{m}^3
 \end{aligned}$$

Therefore, the ABD matrix for the $[0_2/90_3/0]_s$ laminate is expressed as

$$\begin{bmatrix} N_x \\ N_y \\ N_{xy} \\ M_x \\ M_y \\ M_{xy} \end{bmatrix} = \begin{bmatrix} A_{11} & A_{12} & A_{16} & B_{11} & B_{12} & B_{16} \\ A_{12} & A_{22} & A_{26} & B_{12} & B_{22} & B_{26} \\ A_{16} & A_{26} & A_{66} & B_{16} & B_{26} & B_{66} \\ B_{11} & B_{12} & B_{16} & D_{11} & D_{12} & D_{16} \\ B_{12} & B_{22} & B_{26} & D_{12} & D_{22} & D_{26} \\ B_{16} & B_{26} & B_{66} & D_{16} & D_{26} & D_{66} \end{bmatrix} \begin{bmatrix} \varepsilon_x^0 \\ \varepsilon_y^0 \\ \gamma_{xy}^0 \\ k_x \\ k_y \\ k_{xy} \end{bmatrix} \\
 = \begin{bmatrix} 1.40 \times 10^8 & 3.82 \times 10^6 & 0 & 0 & 0 & 0 \\ 3.82 \times 10^6 & 1.40 \times 10^8 & 0 & 0 & 0 & 0 \\ 0 & 0 & 8.3 \times 10^6 & 0 & 0 & 0 \\ 0 & 0 & 0 & 54.45 & 1.27 & 0 \\ 0 & 0 & 0 & 1.27 & 38.48 & 0 \\ 0 & 0 & 0 & 0 & 0 & 2.77 \end{bmatrix} \begin{bmatrix} \varepsilon_x^0 \\ \varepsilon_y^0 \\ \gamma_{xy}^0 \\ k_x \\ k_y \\ k_{xy} \end{bmatrix}$$

Moreover, the ABD matrices for more laminates with different lay-up configurations are determined in the similar procedure by employing the same stiffness matrix.

For the 3mm laminates with lay-up configuration of $[0_2/90_3/0]_s$, the ABD matrix is expressed as

$$\begin{bmatrix} N_x \\ N_y \\ N_{xy} \\ M_x \\ M_y \\ M_{xy} \end{bmatrix} = \begin{bmatrix} 2.10 \times 10^8 & 5.73 \times 10^6 & 0 & 0 & 0 & 0 \\ 5.73 \times 10^6 & 2.10 \times 10^8 & 0 & 0 & 0 & 0 \\ 0 & 0 & 1.25 \times 10^7 & 0 & 0 & 0 \\ 0 & 0 & 0 & 215.93 & 4.30 & 0 \\ 0 & 0 & 0 & 4.30 & 98.91 & 0 \\ 0 & 0 & 0 & 0 & 0 & 9.34 \end{bmatrix} \begin{bmatrix} \varepsilon_x^0 \\ \varepsilon_y^0 \\ \gamma_{xy}^0 \\ \kappa_x \\ \kappa_y \\ \kappa_{xy} \end{bmatrix}$$

For the 4mm laminates with lay-up configuration of $[0_2/90_3/0_2/90]_s$, the ABD matrix is expressed as

$$\begin{bmatrix} N_x \\ N_y \\ N_{xy} \\ M_x \\ M_y \\ M_{xy} \end{bmatrix} = \begin{bmatrix} 2.80 \times 10^8 & 7.65 \times 10^6 & 0 & 0 & 0 & 0 \\ 7.65 \times 10^6 & 2.80 \times 10^8 & 0 & 0 & 0 & 0 \\ 0 & 0 & 1.66 \times 10^7 & 0 & 0 & 0 \\ 0 & 0 & 0 & 458.96 & 10.19 & 0 \\ 0 & 0 & 0 & 10.19 & 287.33 & 0 \\ 0 & 0 & 0 & 0 & 0 & 22.13 \end{bmatrix} \begin{bmatrix} \varepsilon_x^0 \\ \varepsilon_y^0 \\ \gamma_{xy}^0 \\ \kappa_x \\ \kappa_y \\ \kappa_{xy} \end{bmatrix}$$

For the 5mm laminates with lay-up configuration of $[0_2/90_3/0_2/90_2/0]_s$, the ABD matrix is expressed as

$$\begin{bmatrix} N_x \\ N_y \\ N_{xy} \\ M_x \\ M_y \\ M_{xy} \end{bmatrix} = \begin{bmatrix} 3.50 \times 10^8 & 9.56 \times 10^6 & 0 & 0 & 0 & 0 \\ 9.56 \times 10^6 & 3.50 \times 10^8 & 0 & 0 & 0 & 0 \\ 0 & 0 & 2.08 \times 10^7 & 0 & 0 & 0 \\ 0 & 0 & 0 & 841.92 & 19.91 & 0 \\ 0 & 0 & 0 & 19.91 & 615.68 & 0 \\ 0 & 0 & 0 & 0 & 0 & 43.23 \end{bmatrix} \begin{bmatrix} \varepsilon_x^0 \\ \varepsilon_y^0 \\ \gamma_{xy}^0 \\ \kappa_x \\ \kappa_y \\ \kappa_{xy} \end{bmatrix}$$

Appendix III Analytical Prediction by Hertz Contact Law Based Contact Model

In the analytical prediction, the relationship between the contact force, F , and the contact indentation, α , is shown as

$$F = \frac{4\sqrt{R}E_{TI}^*}{3} \alpha^{1.5}$$

where, the radius of the indenter tip, R , is 10mm; and the effective modulus, E_{TI}^* , needs to be determined based on the material properties of the transversely isotropic material.

It is known that

$$E_x = 131.95 \text{ GPa}, E_y = E_z = 7.53 \text{ GPa}, G_{xy} = G_{xz} = 4.15 \text{ GPa}, \text{ and } \nu_{xy} = \nu_{xz} = 0.253.$$

Therefore,

$$\alpha_1 = \sqrt{\frac{E_x/E_z - \nu_{xz}^2}{1 - \nu_{xy}^2}} = \sqrt{\frac{131.95/7.53 - 0.253^2}{1 - 0.253^2}} = 4.3189356$$

$$\begin{aligned} \alpha_2 &= \frac{1 + (E_x/2G_{xz} - 1) - \nu_{xz}(1 + \nu_{xy})}{1 - \nu_{xy}^2} \\ &= \frac{1 + (131.95/2 \times 4.15 - 1) - 0.253 \times (1 + 0.253)}{1 - 0.253^2} = 16.6461 \end{aligned}$$

$$\alpha_3 = \frac{1 - \nu_{xy}}{G_{xy}} \sqrt{\frac{\alpha_1 + \alpha_2}{2}} = \frac{1 - 0.253}{4.15} \sqrt{\frac{4.3189356 + 16.6461}{2}} = 0.58278$$

Hence,

$$E_{TI}^* = \frac{2}{\alpha_1 \alpha_3} = \frac{2}{4.3189356 \times 0.58278} = 0.7946$$

As a result, the relationship between the contact force (in kN) and the contact indentation (in mm) is determined as

$$F = \frac{4\sqrt{R}E_{TI}^*}{3} \alpha^{1.5} = \frac{4\sqrt{10} \times 0.7946}{3} \alpha^{1.5} = 3.3503 \alpha^{1.5}$$

Appendix IV Analytical Prediction by Elastoplastic Response Based Contact Model

The elastoplastic response based contact model is dominated by the material properties of the M21 resin and the laminates thickness. The Yield strength, Z_c , the elasticity modulus, E , and the laminates thickness, h , are summarised as below

$$Z_c = 147\text{MPa}, E = 3.5\text{GPa}, \text{ and } h = 4.12\text{mm}$$

Therefore, the critical indentation, α_{cr} , for the 4mm laminate is

$$\alpha_{cr} = \frac{Z_c h}{E} = \frac{147 \times 10^6 \times 4.12}{3.5 \times 10^9} = 0.173\text{mm}$$

And the critical contact force, P_{cr} , is

$$P_{cr} = \frac{\pi E R_i}{h} \alpha_{cr}^2 = \frac{\pi \times 3.5 \times 10^9}{4.12} \times 0.173^2 = 0.799\text{kN}$$

For the plastic deformation, when $\alpha > \alpha_{cr}$,

The radius of the plastic zone, R_p , is expressed as

$$R_p = \sqrt{2R_i \left(\alpha - \frac{Z_c h}{E} \right)} = \sqrt{2 \times 10 \times \left(\alpha - \frac{147 \times 4.12}{3500} \right)} = \sqrt{20\alpha - 3.46} \text{ mm}$$

where, the radius of the indenter, R_i , is 10mm.

The radius of the contact zone, R_c , is expressed as

$$R_c = \sqrt{2\alpha R_i - \alpha^2} = \sqrt{2 \times \alpha \times 10 - \alpha^2} = \sqrt{20\alpha - \alpha^2} \text{ mm}$$

It is known that the relationship between the contact force and the contact indentation is approximated as

$$P = \pi R_p^2 Z_c + \frac{2\pi E}{h} \int_{R_p}^{R_c} \delta(r) r dr$$

And the displacement under the indenter, $\delta(r)$, is expressed as

$$\delta(r) = \alpha - R_i \left[1 - \sqrt{1 - \left(\frac{r}{R_i} \right)^2} \right]$$

Therefore, it is necessary to determine the unknown part, $\int_{R_p}^{R_c} \delta(r)r dr$, in the contact force approximation.

$$\int_{R_p}^{R_c} \delta(r)r dr = \int_{R_p}^{R_c} (\alpha - R_i + R_i \sqrt{1 - \frac{r^2}{R_i^2}}) dr = \frac{1}{2} \int_{R_p}^{R_c} (\alpha - R_i + \sqrt{R_i^2 - r^2}) dr^2$$

Let $x = r^2$, therefore,

$$\frac{1}{2} \int_{R_p}^{R_c} (\alpha - R_i + \sqrt{R_i^2 - r^2}) dr^2 = \frac{1}{2} \int_{R_p^2}^{R_c^2} (\alpha - R_i + \sqrt{R_i^2 - x}) dx$$

Let $t = \sqrt{R_i^2 - x}$, and $x = R_i^2 - t^2$, therefore,

$$\frac{1}{2} \int_{R_p^2}^{R_c^2} (\alpha - R_i + \sqrt{R_i^2 - x}) dx = \frac{1}{2} \int_{R_p^2}^{R_c^2} (\alpha - R_i) dx + \frac{1}{2} \int_{t_p}^{t_c} t d(R_i^2 - t^2)$$

where, $t_c = \sqrt{R_i^2 - R_c^2}$, and $t_p = \sqrt{R_i^2 - R_p^2}$

Therefore,

$$\begin{aligned} & \frac{1}{2} \int_{R_p^2}^{R_c^2} (\alpha - R_i) dx + \frac{1}{2} \int_{t_p}^{t_c} t d(R_i^2 - t^2) \\ &= \frac{1}{2} [(\alpha - R_i)R_c^2] - \frac{1}{2} [(\alpha - R_i)R_p^2] - \frac{1}{3} (R_i^2 - R_c^2)^{1.5} + \frac{1}{3} (R_i^2 - R_p^2)^{1.5} \\ &= \frac{1}{2} [(\alpha - 10)(20\alpha - \alpha^2)] - \frac{1}{2} [(\alpha - 10)(20\alpha - 3.46)] - \frac{1}{3} (100 - 20\alpha + \alpha^2)^{1.5} + \\ & \frac{1}{3} (100 - 20\alpha + 3.46)^{1.5} \end{aligned}$$

As a result, the relationship between the contact force (in N) and contact indentation (in mm) for the 4mm laminate is determined as

$$\begin{aligned} P &= \pi R_p^2 Z_c + \frac{2\pi E}{h} \int_{R_p}^{R_c} \delta(r)r dr \\ &= \pi(20\alpha - 3.46) \times 147 + \frac{2\pi \times 3500}{4.12} \left[\frac{1}{2} (\alpha - 10)(3.46 - \alpha^2) - \frac{1}{3} (100 - 20\alpha + \alpha^2)^{1.5} + \right. \\ & \quad \left. + \frac{1}{3} (100 - 20\alpha + 3.46)^{1.5} \right] \end{aligned}$$

Appendix V Publication List

- 1) Y.G. Xu, **Z. Shen**, W. Tiu, Y.Z. Xu, Y. Chen, G. Haritos, "Delamination threshold load of composite laminates under low-velocity impact," *Key Engineering Materials*, vol. 525-526, pp. 521-524, 2013.
- 2) **Z. Shen**, Y.G. Xu, A. Chrysanthou, "Contact behaviour of composite laminates under quasi-static indentation load," *Key Engineering Materials*, vol. 577-578, pp. 545-548, 2014.
- 3) **Z. Shen**, Y.G. Xu, A. Chrysanthou, "Correlation of dent depth to maximum contact force and damage of composite laminates," accepted for publication on *Key Engineering Materials*.
- 4) **Z. Shen**, Y.G. Xu, A. Chrysanthou, "Effect of delamination initiation on the damage tolerance of low-velocity impacted composite laminates," under preparation.
- 5) **Z. Shen**, Y.G. Xu, A. Chrysanthou, "Characterisation of damage process of composite laminates via quasi-static indentation test," under preparation.